PERFORMANCE ANALYSIS OF FREQUENCY RECONFIGURABLE ANTENNA USING RF MEMS

A THESIS

SUBMITTED IN FULFILLMENT OF THE REQUIREMENT
FOR THE AWARD OF DEGREE OF

DOCTOR OF PHILOSOPHY

IN

ELECTRONICS & COMMUNICATION ENGINEERING

BY

PARAS CHAWLA

SUPERVISIOR

Dr. RAJESH KHANNA

PROFESSOR, DEPARTMENT OF ELECTRONICS & COMMUNICATION ENGINEERING, THAPAR UNIVERSITY, PATIALA

DEPARTMENT OF ELECTRONICS & COMMUNICATION ENGINEERING

THAPAR UNIVERSITY

PATIALA-147004 (INDIA)

2014

Certificate

I, **Paras Chawla** hereby certify that the thesis entitled "**Performance Analysis of Frequency Reconfigurable Antenna using RF MEMS**" which is being submitted by me to **Department of Electronics & Communication Engineering, Thapar University, Patiala** in fulfillment of the requirements for the award of degree of "Doctor of Philosophy" is a record of bonafide research work carried out under the guidance and supervision of **Prof. (Dr.) Rajesh Khanna**. The matter presented in this thesis does not incorporate without acknowledgment any material previously published or written by any other person except where due reference is made in the text.

Paras Chawla

Reg. No. - 950806013 **Dated-: 13/10/2014**

This is to certify that the above statement made by the candidate is correct and true to the best of my knowledge and belief.

Prof. (Dr.) Rajesh Khanna
Department of ECE,
Thapar University, Patiala.

Dated-: 13/10/2014

Abstract

In the present age, the development of reconfigurable multiband antennas (RMA) have great prospective for wireless communication systems and circuits to accomplish the requirement with a single compact element operating better on multiple frequencies and/or generating same/different radiation patterns. Working this way, in future a single RMA shall be able to avoid the need of multiple antennas as used in earlier and also, the present communication devices. Due to the advantage of thin profile, adaption in any shape, low constructional cost, and mass and readily available for bulk integrated circuit (IC) fabrication, microstrip antenna (MA) is suitable contenders for RMA. There are numerous switching elements options are available in market such as PIN diode, FET, varicap/varactor diode, CMOS and MEMS, which can be used to reconfigure the antenna. The prime objective towards the right choice of switching element for the antenna is that it not only has excellent electromagnetic performance but at the same time has also the advantages of micro-size as well as consumption of less power is desired. From all the available options of RF switches, micro-meter MEMS RF switch is the best in this class. Multi-functional RF MEMS is one of the key MEMS application areas that generates communication devices that have the unlimited potential to increase the performance of RF systems and circuits in addition to permitting the understanding of small size automated switches embedded in microelectronic devices. In addition, RF MEMS has the feature of fabrication through standard IC microelectronics technology which allows it's compatibility with other RF and digital signal processing (DSP) devices. In the procedure of realizing low actuated MEMS RF switches, spring constant (*k*) of movable beam essentially be reduced. Design, optimization and analysis of four different proposed MEMS RF switches (includes capacitive, DC shunt, metal-contact, and cantilever film bulk acoustic resonator) are presented to achieve low pull in voltage, current and power consumption as well insertion loss and high isolation. Aforementioned optimized switches are than integrated on three different MAs (includes swastika-shaped, hexagonal fractal and spiral-shaped) for converting into RMA and their electromagnetic post processing characteristics are analyses in next preceding section of thesis. Testing and simulated results of RMAs are also compared and displaying comparatively good agreement with respect to each other.

For complete designing of the RMA structures, the whole methodology is divided into three steps. In first step, to design and study the proposed MEMS switches characteristics, a

commercial multi-physics solver, Coventorware (ver. 2010) is used. In second step, the electromagnetic properties and optimization of MEMS switches is done with the help of EM solver Ansoft HFSS. Optimization algorithms preferred in this work are artificial neural network (ANN), pattern search (PS) and quasi-newton (QN). All these optimization techniques are compatible with HFSS simulator. The parametric analysis of some proposed switches is also performed in EM solver and later on for optimization purpose; its S-parameter results used as an input values of presented ANN model. The advanced ANN algorithm scheme permits the optimization explanations of the MEMS switches to be supported by exchanging repetitive simulations and also be responsible for reduced processing times whilst still keep in mind a unlimited accuracy as related to traditional mathematical formulation. Further, the actual equivalent circuit of proposed MEMS structures is produced by means of HSPICE model file. The HSPICE file from HFSS is exported in advance design system (ADS) RF simulation tool to generate lumped RLC components, validate the results through equivalent circuit and layout approach. In third step, multiband MA is analysed for EM characteristics for RMA. Antenna is fabricated by photo-lithography technology and RF switches are integrated on it for proof of concept. Finally, RMA is tested using vector network analyzer (VNA) in ideal aneochic chamber condition.

The proposed MEMS switches and RMA results presented in this work are broadly and well-studied in the frequency range of 1.0 to 10.0 GHz. Talking about the presented MEMS switches in aforementioned frequency range, lowest pull-in voltage recorded is 0.70 V for serpentine beam. The lowest insertion loss is measured as 0.1 dB again for serpentine beam and highest isolation is 79.8 dB for fixed beam. All switches display negligible power consumption. The results of all three RMAs realizing fairly normalized omni-directional radiation patterns and also presenting well-behaved linearly polarized performance in all possible switching states. The proposed spiral-shaped RMA showing wide bandwidth ranging from 200 MHz to 1.65 GHz at different multiband indicates device contribution in enhancing the mobile TV and internet application speed.

Different MEMS switches have been proposed in this dissertation are mainly divided into four categories and useful for reconfigurable microstrip device applications. The proposed RMAs are designed to cover all the current as well as upcoming wireless and portable communication bands as frequencies lying between 1.5 to 7.5 GHz.

Acknowledgments

Firstly, I bow to Lord Shiva for His blessings. It is through His strength that I could pursue a doctoral degree.

As I discover myself at the tail end of this work, I recollect many indispensable events that enabled its smooth completion.

I am undoubtedly thankful to all those who were of any help to me directly or indirectly, during the course of my research work. I owe them my gratitude.

I feel proud to be a student of Dr. Rajesh Khanna. With great pleasure and a deep sense of gratitude, I wish to thank for his continuous and invaluable guidance as well as his timely advice that contributed greatly to the completion of this dissertation. His profound technical insight, entering effort and vision has helped to give the proper shape to this dissertation. But for his thought-provoking guidance and never-ending encouragement, this dissertation would not have been possible.

I would like to express my sincere gratitude for the entire administration and management of Thapar University for supporting me in achieving one of the most important goals of my life. I have great pleasure in expressing thanks to Director of Thapar University for his constant encouragement, timely advice and support throughout. I greatly acknowledge my doctoral research committee members Dr. Kulbir Singh, Associate Professor, ECED, TU and Dr. Mahesh Kumar Sharma, Associate Professor, Mathematics, TU for closely monitoring and sharing their valuable inputs in completing this work. Their watchful way of analytically promoting and monitoring research activities helped me immensely in completing my assignment.

Special thanks to my colleagues and mates Dr. Rajiv Chechi, Sukhdeep Kaur, and Nitin Saluja for their continuous encouragement, help and advice throughout my entire PhD work. I would like to acknowledge and mention the name of Prof. (Dr.) Randhir Singh, Ex-Director, JMIT, Radaur and Dr. Ved Prakash Sharma, Lecturer, DOE, Govt. of NCT of Delhi, for suggesting minor grammatical corrections so as to improve the content. I am also thankful to all my students (especially M.Tech. ECE students) for patiently bearing with me as they demanding extra time and I used to busy with this work.

I also express my sincere gratitude to my in laws for their never-ending love and firm

support. My parents, Sh. G. K. Chawla and Smt. Raj Chawla, I find no words to convey how happy and contended I feel to acknowledge that it is only your hard work, untiring efforts and confidence in me which made me what I am today and for instilling in me a love of learning. The moral and ethical values which you have imbibed in me always showed me a path in hardships. Further, a special thanks to my brother Er. Deepak Chawla his companion Mrs. Pooja Chawla and my nephew master Vardan who are very excited, eager and interested for completion of my dissertation.

Last but not the least, I understand in addition value all the cooperation, help and the sacrifices my wife, Shweta, as well my sweet children Ms. Sejal & master Parth had to undergo. I would like to thank my wife, Shweta, for enduring a seemingly endless ordeal, for sacrificing some of her best years so that I could finally finish this research work. I wish to tell you something you know it is only now, I am able to complete my work because of your true love, support, patience and caring nature.

Paras Chawla

CONTENTS

LIST OF FIGURES

LIST OF TABLES

ACRONYMS AND ABBREVIATIONS

2D	Two Dimensional
3D	Three Dimensional
2G	Second Generation
3G	Third Generation
4G	Fourth Generation
ADS	Advance Design System
AlN	Aluminum Nitride
ANN	Artificial Neural Network
AM	Amplitude Modulation
AMPS	Advanced Mobile Phone System
ASICs	Application Specific Integrated Circuits
ASIMPS	Application Specific MEMS Processes
BAW	Bulk Acoustic Wave
BPSG	Borophosphosilicate Glass
CAD	Computer Aided Design
CDMA	Code Division Multiple Access
CF	Cost Function
CMOS	Complementary Metal Oxide Semiconductor
CPW	Co-Planar Waveguide
DARPA	Defense Advanced Research Project Agency
D/C	Down Converters
DC	Direct Current
DCS	Digital Cellular System
DTV	Digital Television
EBG	Energy Band Gap
EF	Error Function
EGSM	Extended Global System for Mobile Communication
EM	Electromagnetic
FBAR	Film Bulk Acoustic Resonator

FEM	Finite Element Method
FET	Field Effect Transistor
FFBP	Feed Forward Back Propagation
FM	Frequency Modulation
FRA	Frequency Reconfigurable Antenna
FRMA	Frequency-Reconfigurable Microstrip Antenna
GA	Genetic Algorithm
GPS	Global Positioning System
GSM	Global System for Mobile Communication
HFSS	High-Frequency Structure Simulator
HR	High Resistivity
ICs	Integrated Circuits
IFS	Iterated Function Systems
IEEE	Institute of Electrical and Electronics Engineering
IL	Insertion Loss
IMT-2000	International Mobile Telecommunication Year-2000
ISM radio bands	Industrial, Scientific and Medical radio bands
LAN	Local Area Network
LHCP	Left hand Circular Polarization
LNA	Low Noise Amplifier
LTE	Long Term Evolution
MA	Microstrip Antenna
MEMS	Micro-Electro-Mechanical System
MIMO	Multiple Input Multiple Output
MLP	Multi-Layer Perceptron
MMS	Multimedia Message Service
MSE	Mean Square Error
NEMS	Nano-Electro-Mechanical System
NN	Neural Network
PA	Power Amplifier
PBG	Photonic Band Gap

PC	Personal Communication
PCB	Printed Circuit Board
PCS	Personal Communication System
PCN	Personal Communication Network
PIFA	Planar Inverted-F Antenna
PLF	Polarization Loss Factor
PR	Photo Resist
PS	Pattern Search
PSO	Particle Swarm Optimization
PTFE	Polytetrafluoroethylene
PZT	Lead Zirconate Titanate
QN	Quasi Newton
RA	Reconfigurable Antenna
RBS	Reconfigurable Beam Steering
RF	Radio Frequency
RFS	Reconfigurable Frequency Switches
RHCP	Right hand Circular Polarization
RIE	Reactive Ion Etching
RL	Return Loss
RLSA	Radial Line Slot Array
RSA	Reconfigurable Spiral Antenna
SA	Simulated Annealing
SFA	Swastika Fractal Antenna
SM	Search Method
SMINLP	Sequential Mixed Integer Non-linear Programming
SMS	Short Message Service
SNLP	Sequential Non-linear Programming
SOM	Self-Organizing Map
SPDT	Single Pole Double Throw
STO	Strontium Titanate Oxide
TF	Transfer Function

TV	Television
U/C	Up Converter
UMTS	Universal Mobile Telecommunication System
UWB	Ultra-Wide Band
VNA	Vector Network Analyzer
VSWR	Voltage Standing Wave Ratio
WCDMA	Wideband Code Division Multiple Access
Wi-Fi	Wireless Fidelity
Wi-MAX	Worldwide Interoperability for Microwave Access
ZnO	Zinc Oxide

GLOSSARY OF SYMBOLS

F	Fractal Set
w	Affine Transformation for Fractal
a, b, c, d, e, f	Real Number
r_1, r_2, θ_1, θ_2	Polar Coordinates
ε_r	Relative Permittivity/ Relative Effective Dielectric Constant
t	Thickness of Substrate
S_{21}, $S_{21\text{-off}}$	Isolation
R_a	Addition of Bypass Resistance and the Contact Resistance
w	Angular Frequency
L_p	Parallel Inductance
C	Corrugating Constant
σ_0	Residual Intrinsic Stress
σ	Residual Corrugated Stress
V_{pi}, V_p	Pull-in voltage
g_o	Initial Air Gap/ Relaxed Gap
v	Poisson's Ratio
E	Elasticity
η	Residual Stress Reduction Ratio
R	Radius
nall	Normalized Side/Adjacent Lobe Level
w_1, w_2, w_3	Weight Factors of Equivalent Parameters
hpbw	Beam Width at which Intensity is Half the Maximum Value
addition	Addition of Far-field Radiation Pattern at Different Angles
LAF(Θ)	Linear Array Factor containing only Even Number Elements
D	Directivity
λ	Wavelength
$\beta(n)$	Phase Angle of n^{th} Even Element
W_1, W_2, W_3, W_4	Weighing factors
R_{eff}	Effective Radius

$\alpha_1, \alpha_2, \alpha_3, \alpha_4$	Constant Coefficients of GA
T	Thickness of Material
F_{res}	Resonant Frequency
B_{np}	n^{th} Derivative of Bessel's Function of Order p
c	Free Space Electromagnetics Signal Velocity
$H_{c(x),\, i}$	Size of the Centered Neighborhood on the Best Match Neuron
$a(t)$	Learning coefficient
r_i, r_c	Positions of the Neurons on the Lattice
tanδ	Loss Tangent
Z_o	Characteristics Impedance
k	Spring Constant of the Material
g	Separation between Upper and Bottom Electrode
V	Actuation voltage
G	Torsion Modulus
I_x	Moment of Inertia
J	Torsion Constant
l_a, l_b, w	Primary Length, Secondary Length and Width of the Meander
n	Amount of Meanders
F	Reaction Force
A	Electrode Area
ε_0	Permittivity of the Free Space
Wgnd1, Wgnd2	CPW ground 1 and 2
C_{down}	Down-state Capacitance
C_{up}	Up-state Capacitance
LCR	Inductance-Capacitor-Resistance
L_{down}	Down-state Inductance
L_{up}	Up-state Inductance
S_{11}	Return Loss
R_s	Series Resistance
f	Linear Signal Frequency
$S_{21}, S_{21\text{-ON}}$	Insertion Loss

ρ	Density
e	piezoelectric constant
c_{33}	Stiffness
k_t^2	Coupling Coefficient
$v_{e,,}\ v_p$	Acoustic Velocity
$G_{1,}\ G_2,\ G_3,\ G_{4,}\ G_5$	Generated Resonant Frequencies
I	Number of Iteration
$f_1,\ f_2$	activation function
E_y/E_x	Axial Ratio
w_r	Affine Transformation
a_11, a_22	Controls Scaling
a_12, a_21	Controls Rotation
b_11, b_22	Control Linear Translation
δ	Scale Factor
Θ	Azimuthal Angle
Ø	Elevation Angle

Chapter 1

Introduction

1.1 Evolution and Need of Next-Generation Reconfigurable Communication Devices

The prime goal of next generation reconfigurable wireless communication devices is to meet the requirement of providing various services anywhere in the globe, to anybody, anytime. Further, these devices have led to the current efforts towards integration of different wireless access technologies [1-5]. These services include:–

- Internet
  - Provides user high speed variable and fixed data communication.
  - Compatible with different wireless generations like 2G/3G/4G.
- Communications
  - Global System for mobile communication (GSM) to GSM, GSM to Code Division Multiple Access (CDMA) and vice-versa, mobile to fixed landline voice calling.
  - Video calling.
  - Short Message Service (SMS).
  - Multimedia Message Service (MMS).
  - Push to talk.
  - Emails.
  - Bluetooth.
- Online Shopping
  - Mobile net banking support.
  - Billing option.
- Multimedia
  - Music player.
  - Video clipper and player.
  - Play Movie & TV.

- ❖ Gaming
    - Online gaming and downloading support.
- ❖ Applications
    - World Clock.
    - Navigation through Global Positioning System (GPS).
    - FM/AM Radio.
    - Support to social networking site like WeChat, WhatsApp, Hike, Viber and Line.
- ❖ Security, Networking and Cloud facility
    - Anti-virus, Anti-theft, Anti-spam and optimization of mobile device performance.
    - Central server storage facility through cloud like to backup contacts.
    - Wi-Fi hotspot and Wired-/Wireless- Local Area Network (LAN) sharing.

In addition to aforementioned services, the upcoming reconfigurable devices will be needed to ensure the following requirements also -:

- ❖ Single reconfigurable device operates on multiband frequencies, which include present and future standards of wireless communication systems.
- ❖ Small-sized, high RF efficiency and less power consuming device.
- ❖ Application Specific Integrated Circuits (ASICs), which incorporate micro-/nano-electromechanical system (M/NEMS) and Complementary Metal Oxide Semiconductor (CMOS) technology on the same substrate.

The design of a mobile device equipped with compact size and multiband reconfigurable internal circuit elements is a challenge which telecommunication industry is facing now days. Also, there is a requirement to design a miniaturized version of RF switch which has excellent RF characteristics and is reconfigurable to different sections of mobile devices, as shown in **figure 1.1**. The uses of RF switches avoid the repeatability of internal circuitry, otherwise in present mobile terminal devices as many individual circuits are required as the number of communication frequency bands needed. Further, **figure 1.2** exhibits possible redesign architecture of typical mobile terminal of figure 1.1 using RF MEMS-enabled reconfigurable RF elements. The seven distinct mobile front ends of figure 1.1 have been compacted to two mobile front-end terminals, each with considerably less elements, and the number of microstrip antennas

(MAs) has been decreased from three static elements to a single reconfigurable multiband antenna structure [1].

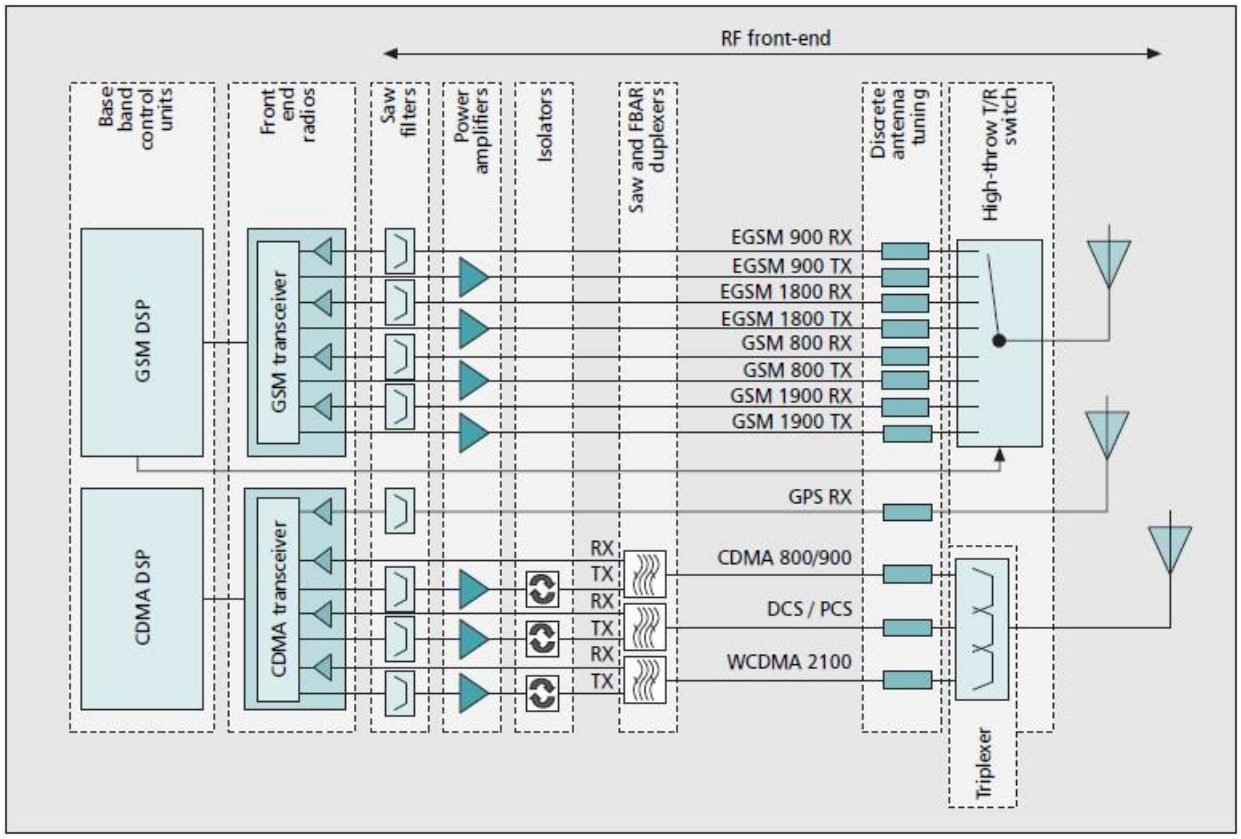

Figure 1.1- Architecture of Typical Multi-Radio Mobile Terminal [1]

The first element of any reconfigurable communication system, to transmit and receive the electromagnetic waves, is antenna. Incorporation of MEMS technology on antenna makes the mobile terminal smaller, inexpensive, and smarter thereby combining the demands of swift advancement of personal communication (PC) market [6]. MEMS RF switches are perfect elements for RF front end [7]. MEMS RF switches can be used in RF front end scheme to vary the particular resonance frequency by actually altering electrical length (w.r.t. wavelength) recognized to inductive and capacitive reactance.

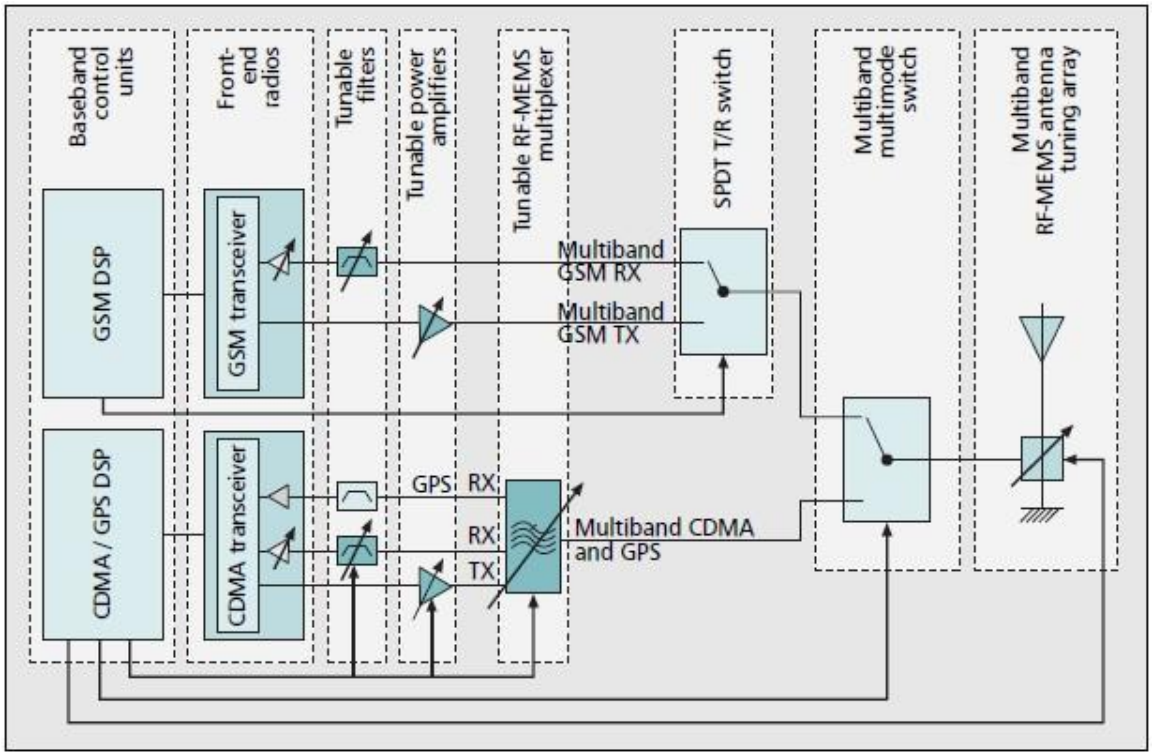

Figure 1.2- Structural Design of Typical Reconfigurable Mobile Terminal [1]

1.2 Origin and History of the Reconfigurable Antennas (RAs)

Almost all antennas are passive in basic nature. These antennas have no ability to adapt to the environment to improve signal strength, variation in resonance (frequency band) and change directionality. The active antenna is one solution but such antenna is very costly and too bulky. So, there is a requirement of one antenna covers all the useful frequency bands and therefore RA is best suited for this purpose.

Definition of RA - Reconfigurable multi-band frequency antennas are prime candidate for numerous commercial and military applications where it is needed to have a particular sole antenna that can be dynamically reconfigured with the help of RF switches and therefore to communicate on multiple frequency bands. All the biasing lines and DC biasing pads are either provided on same printed circuit board of antenna or on the separate substrate. Such type of common-aperture antennas result in significant savings in the weight, size and cost. They find place in mobile communication, air-borne radars, space satellites, electronic intelligence systems, aircrafts and several other PCs as well sensing applications [8,9].

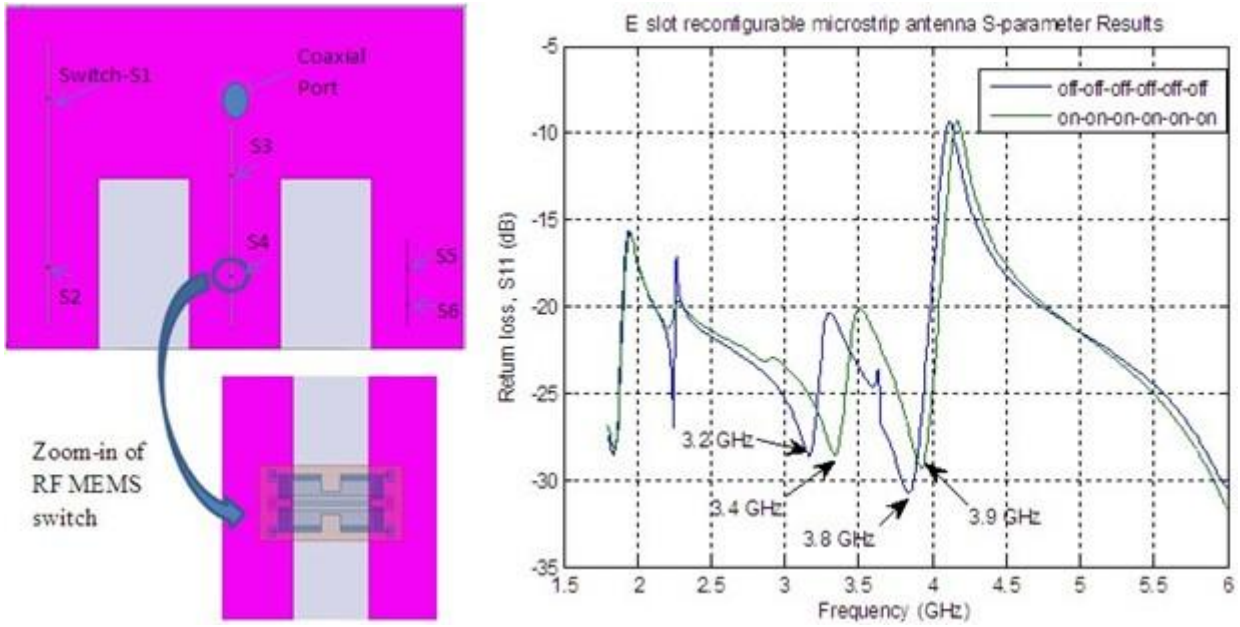

(a)

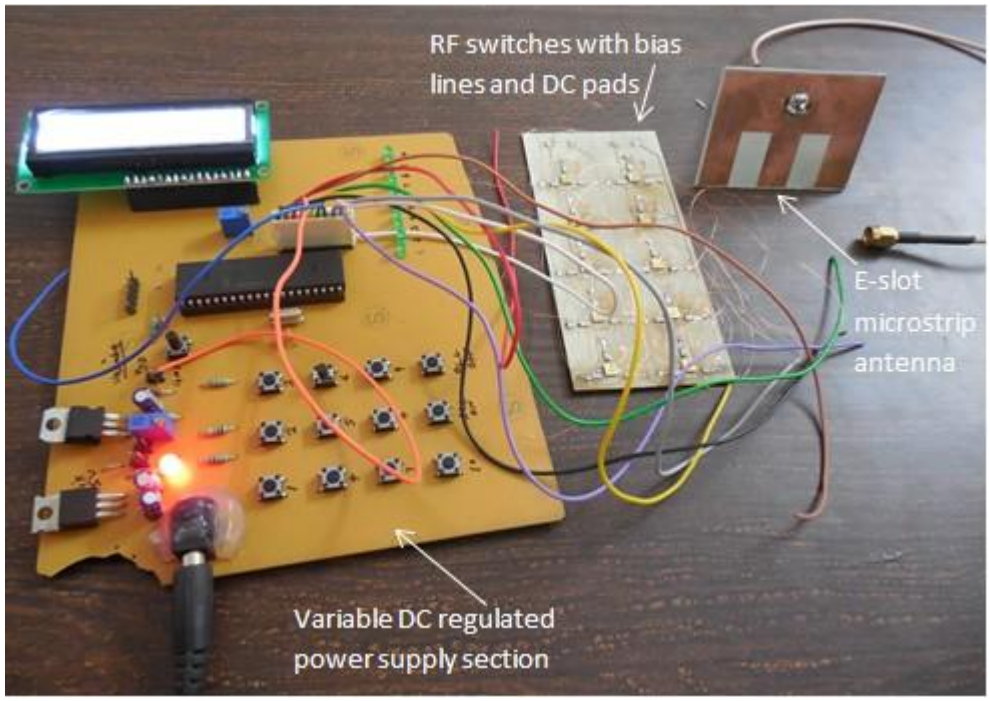

(b)

Figure 1.3- (a) Schematic of E-slot Microstrip RA and Return Loss Results under condition when all Switches are ON- and OFF- positions (b) Fabricated RA complete setup

Figure 1.3 demonstrates the schematic of RA, its S-parameter results and complete setup of fabricated RA.

RA systems using RF MEMS have been first familiarized in 1998 by E. R. Brown [6] and after this development, MEMS based RAs have also been considered by a number of research groups. In [6], the only device that speaks to is the electrostatic actuated micro dimensions switch conceivably the model of RF-MEMS design. Two prospects noticed from the Brown investigation are pseudo optical beam direction-finding and electrically RAs. Considerably these actions has been focused by the capability of MEMS due to micron level size, inexpensive, and improvement in the performance of actuators and transducers as compared to earlier fabricated by hybrid methods. These aids have restricted the compatibility of MEMS design with semiconductor built structure, which followed bulk and surface micromachining.

1.2.1 Suitability of Multiband Microstrip Antennas for RA

MA is the best candidate for designing the efficient RA with following advantages-

- Low construction cost; readily acquiescent to bulk fabrication.
- Light mass, small volume, thin shape/configuration and which can be prepared conformal.
- Circular and linear polarizations characteristics and also conceivable with modest transmission feed line.
- Matching networks and transmission lines can be made-up all together with the antenna design.
- It can be effortlessly incorporated into microwave ICs to give upsurge to integrated active planar antennas.
- It can be combined with the mobile display of the RF-front end terminal.
- With the help of MA approach, dual polarization properties and multi frequency band antennas can be achieved without any problem.

1.1.2.1 Slot and Fractal Antennas

In the present work, the multi-resonance characteristics of the antennas are reported by considering slot and fractal antennas as basic building blocks. All the antennas that are studied in

this work aim towards the miniaturization of actual antenna element size in the 1.0 to 10 GHz range. While antennas have a scaling law that can be engineered, RF MEMS cannot be scaled up in frequency for antenna applications [107]. To understand the behavior of slot and fractal antennas, firstly one has to go through the background, characteristics, definition and their research applications in the various fields of engineering and sciences.

Fractal shapes are those widespread structures that can be seen regularly in our daily life but we do not observe them often. Basically, the fractals are the irregular structures have with the multiple copies of themselves at different scales in a recursive manner. Fractal geometries give the view of seeing everything with an interesting approach. While studying in depth about fractal shapes, a person risks the loss of his childhood vision of trees, clouds, leaves, flowers, fences, carpets, feathers, bricks, and mountains etc. It is likely that a person perception of aforementioned things will never be quite the same again [10].

One can list and observe the development of a number of antennas which are based on different fractal geometries. It is a fact that single fractal geometry cannot be used for all types of communication systems. Some of these fractal designs have been particularly deployed for miniaturization of the antenna elements, while other fractal geometries serve the multiband characteristics for the antennas.

Many of the fractal shapes and curves were identified well before 1970's and were often incorporated in the functions of mathematics to define and understand them in depth. At that time, these fractal geometries were practically abjured to accomplish the electromagnetic behavior of various telecommunication elements due to their chaotic and nebulous patterns, but later on this misconception was dismissed due to the fruitful researches on the fractal shapes to understand them in depth. During 1970's, a French mathematician B.B. Mandelbrot discovered that there are certain special features which were associated with the fractals within their irregular geometric patterns. Mandelbrot gave a number of definitions about the term fractals. All these definitions mainly are concern about the fractal dimensions. A very sophisticated meaning of fractals is a set for which the Hausdorff Besicovich measurement rigorously goes beyond its topological measurement as marked in [11]. Each non-integer measurement set is a fractal but it is worth noting that fractals can have integer measurement. It can be said that fractals have no proper meaning just they have some sequence of properties that could create

interest in researchers to explore them more. In a more generalized way, the fractals can also be defined as a set 'F' such that [12]:-

- 'F' can be explained in a modest recursive way.
- The fractal measurement of 'F' should be more than its topological measurement.
- 'F' has an adequate structure with details on randomly lesser scales.
- 'F' is too asymmetrical to be labeled by the available conventional geometries.
- 'F' must have the same form of self-similarity.

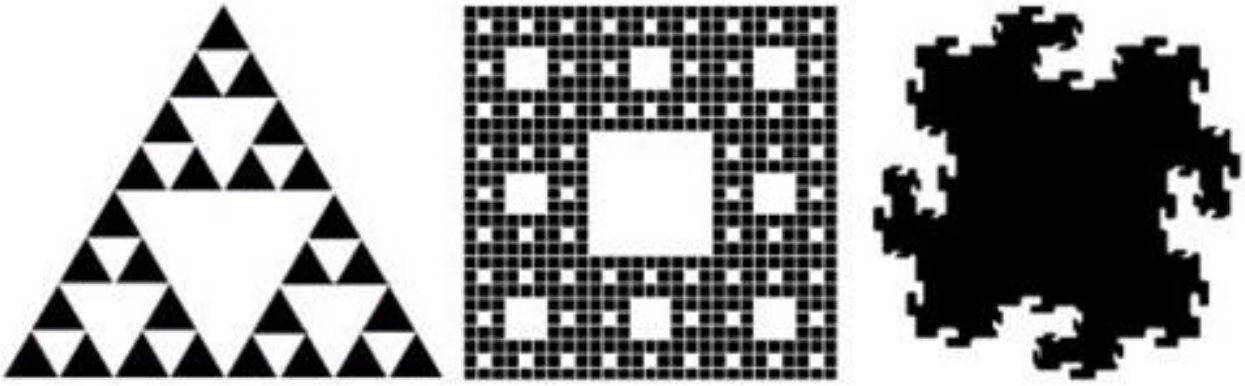

Sierpinski Gasket | Sierpinski Carpet | Giuseppe Peano

Cactus | Hilbert Curves | Hexagonal

Figure 1.4- Examples of the Fractal Geometry [13]

In the bright history of fractals there are an infinite number of shapes which are employed to motivate the research into multiband and compact antenna designs. The Sierpinski gasket better known as a Sierpinski triangle was the first fractal shape that was used for the antenna design

purposes. In later years, this shape i.e. Sierpinski triangle became popular and several experiments were carried out by taking this fractal shape into consideration. After some years, the antenna researchers moved on to other fractal shapes also. Other fractal geometries include the Sierpinski carpet, Hilbert curve, Hexagonal shape, Cactus shape, Giuseppe Peano fractal shapes and many more are there which can be listed here as the very beneficial antenna design elements [13]. The pictorial representation of these popular fractal geometries for antenna designing is given in the **figure 1.4**. All these fractal geometries are intended to design low profile and multi-resonant antennas with considerable gain often with almost similar radiation characteristics in their bands. Although the utility of these different fractal geometries vary in the aspects of performance but when we choose fractal geometry for antenna designing and our ultimate goal must be fulfilled for a better fractal antenna design.

There are some laws on which the fractal geometries rely and collectively they can be known as the language of fractals, because without the knowledge of these laws the fractals are complex to understand, generate and develop. The language of fractals includes mainly three objects on which the theory of fractals rely, which are -: self-affine set, self-similar sets and Iterated Function Systems (IFS).

Definition of fractal [12] **-** A transformation for real (R) valued function, $\mathbf{w}: R^2 \to R^2$ of the form

$$\mathbf{w}(x_1, x_2) = (ax_1 + bx_2 + e, cx_1 + dx_2 + f) \tag{1.1}$$

where a, b, c, d, e, and f has designated as real numbers, is known as a (2D) affine transformation. We often use the following equivalent notations

$$\mathbf{w}(x) = w\begin{pmatrix} x_1 \\ x_2 \end{pmatrix} = \begin{pmatrix} a & b \\ c & d \end{pmatrix}\begin{pmatrix} x_1 \\ x_2 \end{pmatrix} + \begin{pmatrix} e \\ f \end{pmatrix} = Ax + t \tag{1.2}$$

Here $\mathbf{A} = \begin{pmatrix} a & b \\ c & d \end{pmatrix}$ is a two-dimensional, 2 x 2 real matrix and t is the column vector $\begin{pmatrix} e \\ f \end{pmatrix}$, which we do not distinguish from the coordinate pair $(e, f) \in R^2$. Such transformations have important geometrical and algebraic properties. The matrix A can be written in the form

$$\begin{pmatrix} a & b \\ c & d \end{pmatrix} = \begin{pmatrix} r_1\cos\theta_1 & -r_2\sin\theta_2 \\ r_1\sin\theta_1 & r_2\cos\theta_2 \end{pmatrix} \tag{1.3}$$

where (r_1, θ_1) are designated as polar coordinates of mark point (a, c) and $\left(r_2, \theta_{2+\pi/2}\right)$ are the polar coordinates of the point (b, d).

Self-Similar Sets- It is unique set that is made up of scaled down replicas of itself, i.e., reduction in the original copy by the similar scale factors vertically and horizontally. The various fractal shapes that posse self-similarity have been applied to multi-band or miniaturized antenna design.

Self-Affine Sets- A self-affine set is a reduction of the original copy by dissimilar factors, vertically and horizontally.

Affine transformations are important characteristics of fractal geometries. These involve scaling, rotation and translation. These transformations can be expressed in the mathematical form as:

$$w\begin{pmatrix} x_1 \\ x_2 \end{pmatrix} = \begin{pmatrix} r_1\cos\theta_1 & -r_2\sin\theta_2 \\ r_1\sin\theta_1 & r_2\cos\theta_2 \end{pmatrix}\begin{pmatrix} x_1 \\ x_2 \end{pmatrix} + \begin{pmatrix} e \\ f \end{pmatrix} \quad (1.4)$$

In the equation (1.4), r_1 and r_2 are scale factors, θ_1 and θ_2 correspond to rotation angles and x_1 and x_2 are translations involved in the transformation. If r_1 and r_2 both are reductions ($r_1, r_2 < 1$), or both are magnifications ($r_1, r_2 > 1$), the transformation is self-affine. If $r_1 = r_2$ and $\theta_1 = \theta_2$, the transformation is self-similar [12].

1.2.2 Role of RF switches for Designing RA

There are various types of RF switches available which can be used along with MA to achieve the reconfigurabilty. Some of important RF switches include-

- PIN/Schottky Diodes
- GaAs FETs
- RF MEMS

1.2.2.1 Comparisons of various RF Switches

MEMS RF switches demonstrate exceptional performance in upper range of frequency as related to the traditional semiconductor RF switching microelectronics technology, for example,

GaAs based FET and PIN diode switches. The comparisons of MEMS RF switches over semiconductor PIN diode or MOSFET switches are given below [14-17]:

Batch fabrication and low cost- The micro-fabrication technology involves lithography based micromachining for the construction of MEMS structures which allow the production of MEMS devices on the batch basis which reduce the cost as it scales up the volume but much more expensive as compared with other conventional switches. MEMS RF switches are made-up of using surface micromachining methods and can be fabricated on quartz, automated mark high-resistivity (HR) Si or GaAs wafers.

Low insertion loss (IL) - It is easy to make low-resistivity electrode, so that the conductor loss can be reduced. Since the gap between the electrodes is mainly air, dielectric loss can also be reduced easily. MEMS metal-contact resistive and capacitive shunt switches have an IL of around 0.1 dB up to 125 GHz.

High isolation- The flexibility in design of the device structure is high in comparison with semiconductor devices such as diodes or transistors. In addition, air gap is easily introduced around the device. So isolation can be higher than semiconductor devices. MEMS metal-contact resistive switches are made-up of with air gaps between electrodes having very small off-state capacitances (2-4 fico farads) to bring about an outstanding isolation from 0.1-65 GHz. Capacitive MEMS switches with a capacitance ratio of 60-160 offer tremendous isolation from 7-110 GHz.

High Linearity- In the case of switches, the position of movable parts is defined by direct contact of fixed and movable part, so the movable electrode is not moved by electrostatic field of the signal. Since the RF characteristics are determined by the mechanical position of the movable parts, distortion of the signal can be quite low. MEMS perform 30-50 dB improved than FET or PIN switches.

Low Power Consumption- In principle, electrostatic actuation does not consume power after displacement. Metal semiconductor (MES)-FET switching in the cold-FET mode require almost no control power. Magnetic/thermal switches put away a lot of current if not are prepared to latch in the down-position once set in motion. Some commercial cold-FETs can switch at 2.3 V

Despite all of the advantages discussed above, MEMS switches also have some problems associated with them. The main issue at present is that they are not commercially available. Besides this the other issues related to them are [14, 17]-:

Relatively low speed- Most of the MEMS switches have limited switching speed i.e. around 3-40 μs except communication and radar systems where this limit can be acceptable.

Moderate voltage or high current initiative- Electrostatic actuated MEMS have nearly zero power consumption but require 5-80 V for consistent operation, whereas, magnetic /thermal switches can be activated with 2-6 V, but require 9-105 mA of current supply.

Reliability- The consistency of developed MEMS RF switches is 0.2-4 billion cycles. This is acceptable for many applications but switches by means of 30-300 billion cycles are still required as consistency of capacitive MEMS switches is limited by the dielectric charging effect and of metal contact switches due to the interface problems. Cold-FETs are more reliable.

Packaging- MEMS RF switches should be packaged in passive atmosphere and in small humidity which necessitates near hermetic sealed packaging. Due to this the packaging cost becomes high and reliability of MEMS switches may also be adversely affected by the packaging technique used.

Power handling- The RF MEMS cannot handle power larger than 200 mW with high reliability. Highly reliable MEMS switch that can handle 0.1-10 W doesn't exist today. To accommodate high power devices some changes in actuation mechanism and fabrication technique must be made.

1.3 Motivation of Thesis

The desire to have single device to access the additional several services like DCS, PCS, GSM, EGSM, CDMA, WCDMA, GPS, Wi-Fi, Wi-MAX, UMTS, Bluetooth, 802.11a, and 802.11b bands at anytime and anyplace has led to the current efforts towards integration of different wireless access technologies. A mobile device is needed to be equipped with compact size and multiband internal antenna for wireless terminal is an interesting issue of research. Development of latest communication and ICs technologies, lessening in size and bandwidth broadening are becoming significant design attentions for real-world applications of MA. Following are some gaps found in different RF MEMS switches and RA structures available in the literature-:

Capacitive MEMS RF switches of Tantalum material are presented in 2011 [18]. The pull-in voltage measured is lying between 15-20 V. Insertion loss and isolation values at 10 GHz are

0.6 dB and 13 dB, which need to be improved. In [19], the low losses microwave RF switches are designed but the pull-in voltage is quite high i.e. 50 V and not suitable for low power devices.

In [20] the strips of copper as a replacement for closed switches and no filling as an alternative of open switches has been used in the simulations and for testing purpose. This ideal switch (RF MEMS) performance has been used as a proof and added to the planar fractal antenna, while the effect of the DC bias transmission lines on the antenna performance has been mainly ignored.

In [21] the measured voltage standing wave ratio (VSWR) less than 2 at frequency range lying 3.7– 4.2 GHz when the RF MEMS is in OFF state, whereas in the ON position VSWR at less than 2 at frequency range lying 5.9–6.4 GHz. The integrated switch exhibits isolation greater than 40 dB whereas its IL is less than 0.3 dB in the desired frequency band. RF MEMS switch consumes how much power and the value of return loss; it is not experimented in [22].

It can be experimented in [23] that without RF switch the first resonance lies between 1.25–2.22 GHz and along with RF switch the antenna works at 1.16 –2.08 GHz providing a tunability in frequency near to 56%. Similarly, the 2nd resonance frequency proposal without switch lies from 2.45 to 3.68 GHz and by means of switch the antenna offers 2.22 to 3.48 GHz band. The frequency swiftness is nearby 40 and 44%, respectively, which is very less.

Huff et al. [24] uses RF switches to alter the radiation pattern response. The losses generated due to switches are very high. A structurally reconfigurable MEMS Vee-antenna is brought together by Chiao et al. [25], by means of electronically organized microactuators to attain the preferred reconfigurability. However, in these RAs the pattern diversity is not realized.

Based upon the above review and identified gaps, the following research objectives are proposed:-

- To design improved RF MEMS switch in terms of insertion loss, isolation and power consumption. Further, various optimization methods are discussed to optimize the switch performance.

- To design and simulate the frequency reconfigurable antenna using RF MEMS switch proposed above for 1.5-6.5 GHz band.
- Analytical study and fabrication of the proposed frequency reconfigurable antenna (FRA) along with RF MEMS switch. Further, to define the applications of FRA for next generation wireless and mobile communications.

1.4 Methodology

Conventionally, each antenna works at one or two-resonance frequency and if the requirement is more for achieving more frequency band than as many as antennas are needed for attaining different applications. Although 'iPhone-5' antenna is exceptional example out of those entire antenna available in the market. To handle multiband frequency problem, RA using RF MEMS can be used where a single antenna can control at numerous frequency bands. So, the RA using RF MEMS design for handset applications is active research area. To study and design the RA structures following methodology will be used-:

- With the help of softwares coventorware and COMSOL, the RF MEMS switches in terms of multi-Physics properties have been studied, designed and simulated for RA design. The multi-Physics characteristics for MEMS switches generally include the activation/pull-in voltage, squeeze film damping effect/displacement time, Electrostatic force, and ON-OFF capacitance ratio.
- The lumped/equivalent circuits of aforementioned MEMS switches are generated by using Advance Design System (ADS) software with the help of Hspice model. After generation of lumped elements, the mathematical analysis and verification of post-processing simulation results of switches has been performed.
- Further, the Ansoft High frequency structure simulator (HFSS) software is used to find out the electromagnetic (EM) characteristics of MEMS switches and the MA. In case of switches, the important EM post-parameters are IL, return loss (RL) and isolation. This software provides the in-built optimization tools, which are also considered to optimize the EM results. The multiband antenna for FRA is designed and studied by this electromagnetic field solver. For antenna point of view, some of the important

characteristics studied by HFSS software consist of RL, gain, radiation pattern, polarization, current & electric field distribution.

- In next stage of work, the simulated multiband antennas are fabricated by using photo-lithography process. These fabricated antennas are than tested by vector network analyzer (VNA) in anechoic chamber. The simulated results obtained are than compared by tested VNA results.
- After designing the basic building block of FRA, the next step is to study the consequence of proposed MEMS RF switches on multiband antenna. Again HFSS software is used to compute the electromagnetic parameters of FRA. Two approaches are followed to evaluate the performance of antenna along with RF switches – First, the aforementioned proposed RF MEMS switches designed in coventorware software are exported in open and closed positions to 3rd-party electromagnetic field solvers HFSS. Second method involves finding out the equivalent RLC lumped element values of already designed RF MEMS switches in both ON- and OFF- conditions with the help of ADS software. These equivalent values are considered for designing the FRA and EM performance analysis is done by using HFSS software.
- In final stage of work, the FRA is designed by combining the optimized RF switches on the different proposed multiband MA as proof of concept. The proposed RA fabrication and testing setup broadly contains five different sections, which include -:
    - Multiband planar antenna substrate
    - RF switches with biasing circuit board
    - Microcontroller based voltage regulated power supply board to on/off the desired RF switches
    - VNA
    - Anechoic RF chamber

  In this way three different boards are designed to make the FRA.

- After that the analytical evaluation and verification of the proposed RA using RF MEMS structure is examined to the application of next-generation of wireless communication.

The complete procedure of proposed work is summarized with the help of flow diagram by taking an example of proposed Hexagonal-shaped FRA.

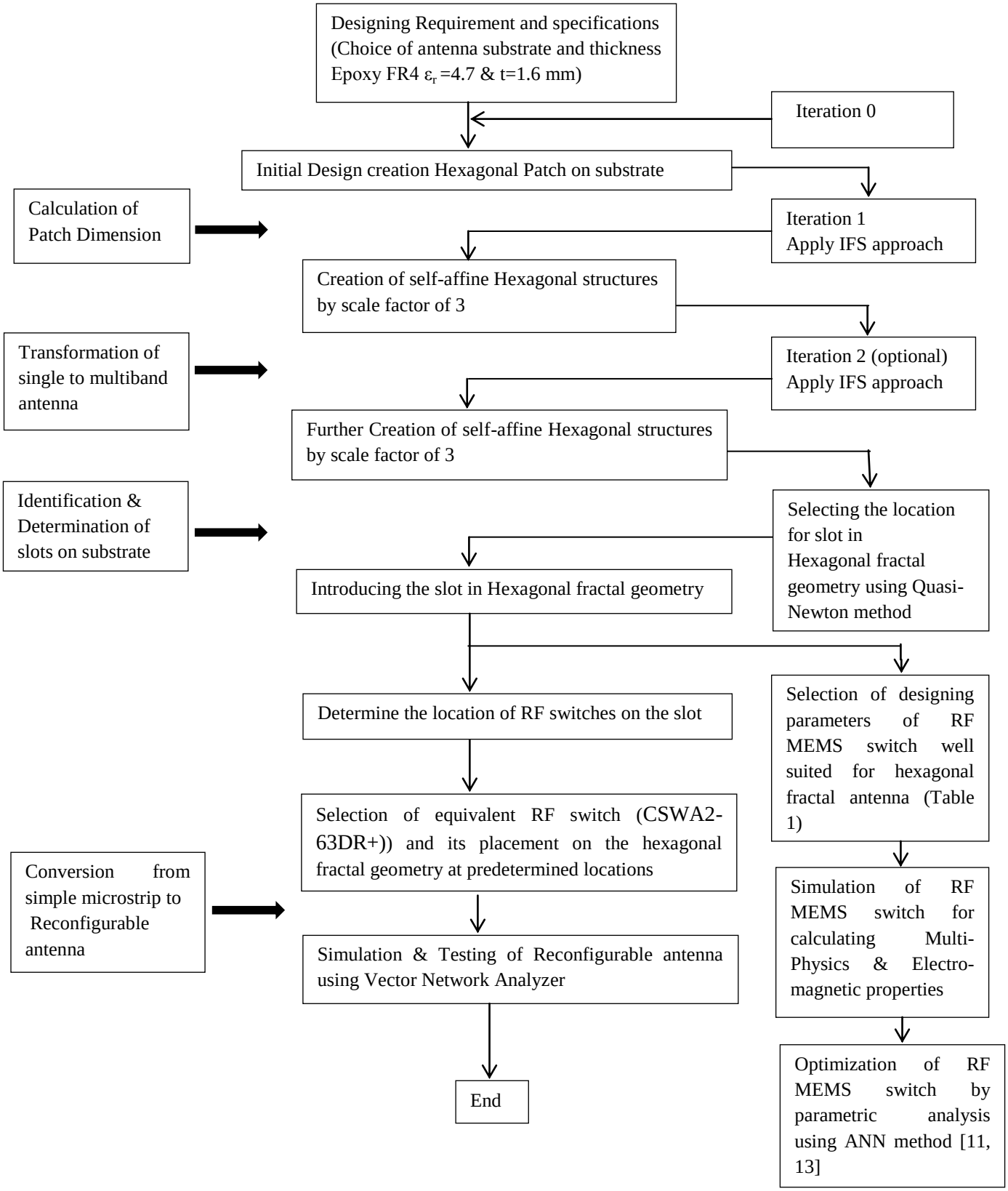
Designing Requirement and specifications (Choice of antenna substrate and thickness Epoxy FR4 ε_r =4.7 & t=1.6 mm)
Iteration 0
Initial Design creation Hexagonal Patch on substrate
Calculation of Patch Dimension
Iteration 1 Apply IFS approach
Creation of self-affine Hexagonal structures by scale factor of 3
Transformation of single to multiband antenna
Iteration 2 (optional) Apply IFS approach
Further Creation of self-affine Hexagonal structures by scale factor of 3
Identification & Determination of slots on substrate
Selecting the location for slot in Hexagonal fractal geometry using Quasi-Newton method
Introducing the slot in Hexagonal fractal geometry
Determine the location of RF switches on the slot
Selection of designing parameters of RF MEMS switch well suited for hexagonal fractal antenna (Table 1)
Selection of equivalent RF switch (CSWA2-63DR+)) and its placement on the hexagonal fractal geometry at predetermined locations
Conversion from simple microstrip to Reconfigurable antenna
Simulation of RF MEMS switch for calculating Multi-Physics & Electro-magnetic properties
Simulation & Testing of Reconfigurable antenna using Vector Network Analyzer
Optimization of RF MEMS switch by parametric analysis using ANN method [11, 13]
End

1.5 Commercial CAD Tools used for Analysis

For present research work, commercial CAD tools are classified either for computing multi-physics properties of MEMS switches or EM properties of both MEMS switches and MA. Four major simulation tools are available in market for designing and analyzing the multi-physics of MEMS device applications, which includes COMSOL [26], Intellisuite [27], ANSYS [28], and Coventorware [29]. Further, the EM properties of planar circuits and MEMS products are well studied by the help of some of the important softwares package available like Ansoft HFSS [30], CST microwave, Zealand IE3D, and Agilent ADS [31]. All these aforementioned softwares are capable and easy to analyze any problem related to RF device applications. Additionally, HFSS, ADS and coventorware softwares are compatible with each other, as all are FEM based, and therefore due to these features they provide the best solution of step by step complete designing and analyzing of RA using MEMS switches.

CoventorWare®

CoventorWare supports the researchers by providing the choice of a physical design method (Designer and Analyzer) or a system-level method (Architect). These methods can provide the solution of MEMS and microfluidics device problems, in combination of each other or alone, and brief flow diagram as shown in following **figure 1.5**.

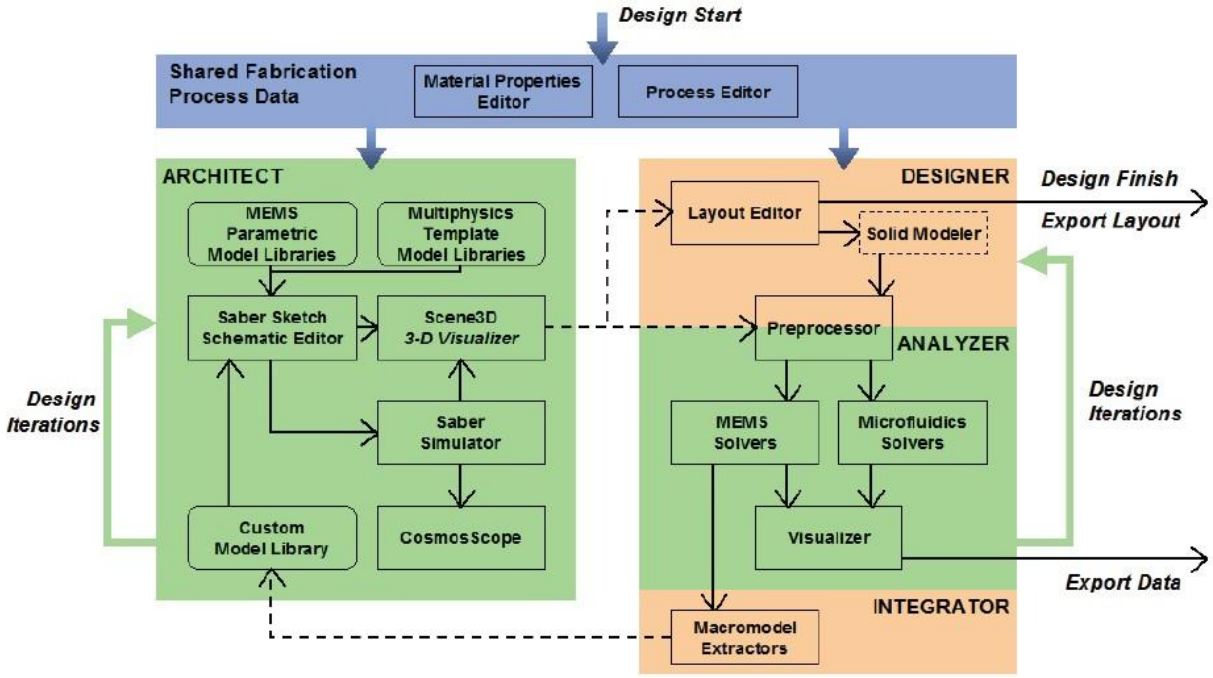

Figure 1.5- Design Flow of Coventorware Simulator [29]

The architect approach follows a "parametric library" technique, which includes various components like microfluidic, electro-mechanical, magnetic, and optical applications in order to develop the MEMS product applications. The architect approach describes the design model by using schematic method as it selects and connects the symbols from pre-defined parametric library. Further, the schematic view can be converted into 3D-layout to verify the properties and proper placement of component.

The Designer and Analyzer approach use FEM/BEM mathematical solving technique, initiated with a 2-D model and consists of building a 3-D layout, creating a mesh structure by dividing the whole geometry into small elementary area, and simulates for calculating multi-physics properties.

In this thesis work designer and analyzer approach is followed for modeling the RF MEMS switches.

Ansoft HFSS™

Ansoft HFSS supports the numerical approach called the FEM. A designed structure is split up into small sub-divisions known as finite element by following meshes for solving 3D electromagnetic problems, which is the same approach used for coventorware software. The shape of finite elements (FEs) used by this software is tetrahedral, and the entire unit of tetrahedral is named as a mesh. The geometry is simulated and the way out is calculated is meant for the fields inside the FEs, and the generated Electric (E-) & Magnetic (H-) fields are interconnected to Maxwell's equations, which further are satisfied through applied inter-element boundaries. It can be used to compute post-processing results such as Scattering (S-), Admittance (Y-), Impedance (Z-) parameters, E- and H-Fields, resonant frequency, current distribution, polarization, 3D-radiation pattern and many more. The latest version of Ansoft HFSS also provided the facility of performing various optimization techniques on designed geometry [30].

In this research work EM properties of RF MEMS switches and antenna have been studied by using HFSS software.

Agilent Technologies ADS®

Advanced design System (ADS) is an excellent product of Agilent Technologies for specially designing and analyzing various problems related to electrical, electronics and

communication engineering. The in-built simulation tool of ADS mainly includes applications like Analog/RF, signal processing, electromagnetic, wireless test benches, HDL and SPICE model generator. The EM tools are useful to calculate the S-parameters for general planar circuits such as slotline, Coplanar Waveguide (CPW), microstrip, stripline, and numerous other topologies by combining FEM and momentum simulators [31]. This particular tool initiates the physical planar design, for example a MA, in three ways-:

- Translate a schematic circuit into a Layout form.
- Design the structure directly in Layout.
- By importing the layout geometry from another compatible simulator like HFSS.

In the present work, the ADS simulator is preferred to compute the RLC lumped equivalent of MEMS switches by importing the HSPICE extension file from HFSS.

1.6 Thesis Organization

Based on the above proposed objectives, the prime focus of this thesis is the performance analysis of frequency RA using RF MEMS switches. This is followed with first simulation and designing of improved RF MEMS switches, than designing of multiband MAs and finally assembling of optimized RF switches over proposed antenna in order to make it RA for next generation wireless and mobile communication applications. The thesis has been organized into seven chapters. The contents of each chapter are briefly described as under:-

The **first Chapter** 'Introduction' provides brief description about the evolution and need of next-generation reconfigurable communication devices. Under the heading, 'origin and history of the RAs, the suitability of multiband MAs for RA, slot and fractal antennas, role of RF switches for designing RA and comparisons of various RF switches has been covered. Further, motivation of thesis, methodology adopted for the present work and thesis organization has also been briefly explained in the next preceding sections.

Chapter 2 covers a comprehensive literature survey which is divided into four different sub-sections. First sub-section covers various series and shunt RF MEMS switches also includes PIN diode, CMOS and FET switches. In the second sub-section, the literature of different multiband slotted and fractal antennas is covered. The next section includes literature of various

RA. Finally, the last sub-section includes the various optimization techniques relating to physical designing of RF switches and MA.

In **chapter 3**, the brief overview of the principles, pre-processing fabrication process and operation of various RF MEMS switches has been given. Various configurations of switches RF have been discussed which show many advantages in terms of manufacturability or working performance. The multi-physics and EM parameters of MEMS switches have been defined in the next section. The first objective of this research work i.e. 'To design improve RF MEMS switch in terms of IL and power consumption.' has been covered in this chapter. Designing of proposed resistive i.e. metal-to-metal resistive or shunt capacitive i.e. metal–insulator–metal switches has also been included in this part of thesis.

Chapter 4 considers the various optimization methods related to optimize the electromagnetic properties of RF MEMS switches and antennas. These methods include artificial neural network, quasi newton, pattern search etc. The advantages and disadvantages of these optimization techniques are also compared. The parametric analysis of physical dimensions (like length, width and air gap) of proposed RF switches and planar antenna also has been part of this chapter.

Chapter 5 deals with achieving the second objective of this dissertation i.e. 'To design and simulate the frequency reconfigurable antenna using RF switch proposed for 1.5-6.5 GHz band.' This chapter includes introduction and working of RA. The proposed RF MEMS switches, and optimization techniques of chapter-3 and chapter-4, respectively have been combined along with MAs in this chapter. The designing, fabrication issues and mathematical modeling of various slotted and fractal antennas have been covered. The brief introduction and suitability of these antennas as RA has also been included in this particular chapter. The proposed RAs analyses which include pre-processing designing steps, simulations, fabrication method, testing procedure and finally results have been discussed. The proposed RA fabrication and testing setup broadly contain five different sections, which include - planar antenna, RF switches with biasing circuit, voltage regulated power supply to on/off the desired RF switches, VNA and the anechoic chamber.

Finally the **Chapter 6** covers the summary and conclusions drawn from all the three objective areas. In this thesis work, it has been concluded that the planar antenna was converted into RA by applying RF MEMS switches. The new novel reconfigurable multiband antenna with RF switches was designed, fabricated and tested. For all possible RF switching states, the results of proposed RA worked well for proposed frequency band. From industrial application point of view, the proposed compact RAs is considered in mobile RF front end terminal which covers maximum present as well as future wireless and mobile communication bands like UMTS (IMT-2000), 4G WiMAX/IEEE 802.16, WLAN (5.8 GHz)/IEEE 802.11a (outdoor) wireless communications and some other personal communication band (PCS) despite the fact that retaining a sensible integrity in its reasonable bandwidth, is described in this chapter. The results obtained by discussed methods are compared very well with simulated results. In the end, the scope of future work has been presented.

1.7 Summary of the Chapter

This chapter includes the scope of the presented research work. An introduction about the evolution and need of the next-generation reconfigurable communication devices is presented, further emphasizing the requirements still to be examined. Role of RF switches and their advantages/disadvantages, suitability of slot and fractal antenna as RMA and conversion procedure of MA into RMA are also discussed in this chapter. Designing of new improved RF MEMS switches, development of new optimization techniques for switches and antenna and analytical study as well fabrication of proposed RA, are identified the major research objective of the thesis. The complete methodology is brief by the help of flow diagram. Commercial softwares used in this work are also introduced. In chapter-2, a comprehensive literature review is presented that has facilitated the author throughout the investigations.

Chapter 2

Review – RF Switches to Reconfigurable Antenna

2.1 Classification of Literature Review

- Recent Developments in MEMS RF Switches
- Advancement in Multiband Antennas Structures
- Latest Optimization Techniques for RF Circuits
- Contemporary Methods of Designing RAs

2.1.1 Recent Developments in MEMS RF Switches

The first ever RF MEMS series switch paper was developed and published by K.E. Peterson (IBM) in 1979 [79]. Then after MEMS RF switch was developed in 1991 by Dr. L. Larson at Research Lab named Hughes and funding provided by DARPA (Defense Advanced Research Project Agency) [8]. The switch was explicitly fabricated for microwave devices. The switch's capability to work well up to 55 GHz was an important advancement over solid-state and mechanically designed switches. One of the key innovations towards reduction in dimensions and bulk production cost is the option of incorporating altogether the radio segments, comprising the antenna; transmit/receive switch, and other RF modules on a packaged unit by means of a monolithic fabrication batch procedure [9].

Generally speaking, MEMS is a novel technology of submissive devices (e.g., switches) and circuit modules (e.g., reconfigurable transmission circuit lines) poised for organized MEMS. The best extensively studied RF MEMS application has been the electrostatically actuated switches made of a metallic cantilever beam, air-bridge structure, diaphragm, or specific other arrangement that when pulled down towards bottom electrode, becomes open, short, or act as load on RF t-line [32].

MEMS switch limitations like low ON-OFF time and high biasing voltage is addressed by applying the method of moving center transmission line of CPW i.e. bottom plate [33]. Authors analyzed the physical characteristics of RF switch by defining the continuity equation of

two movable electrode plates. By enhancing the dimensions of switch, around 20% decrease of ON-OFF time and biasing voltage is possible. It has also been observed that a decrease of 30% in the biasing voltage by maintaining ON-OFF time unchanged and 50% decrease in transient time by maintaining the voltage unchanged can be achieved.

The switching interval of MEMS single RF switch is generally governed by the mechanical reaction of the stimulating beams [34]. Phosphorous-doped hydrogenated amorphous silicon and Chromium (Cr) are the two best mentioned high resistivity (HR) materials that are preferred for designing of dc biasing of MEMS RF switches. This procedure follows seven-mask layer processes for the construction of MEMS products and precisely suitable for creating matrices of MEMS RF switch.

Characterization and production status of micro level devices for microwave applications like polar ceramics is studied in [35]. In this paper it is discussed about bulk acoustic wave (BAW) products with Aluminum Nitride layer, tunable ferroelectrics, and MEMS capacitive RF switches made with high permittivity substrate. The significant characteristics of ferroelectrics materials for microwave devices are brief by highlighting the thin films and composites. In this relevant research, the fabrication, applications, and characteristics of polar ceramics material for MEMS based RF and reconfigurable microwave electronics have been studied.

The piezoelectric actuated shunt-ohmic MEMS switches operated at low voltage and very less power consumption is reported by Hee-Chul Lee [36]. RF wave t-line of the ohmic shunt switches are straightly joined commencing the one to the other port with no break, and further contact plate is connected to entire grounds. Ohmic switch using single piezoelectric cantilever beam (labeled-A) and four piezoelectric based cantilever beams (labeled-B and labeled-C) are demonstrated. Type-B has square shaped center contact plate and Type-C has diamond shape. The usage of additional piezoelectric beams can produce an adequately enormous contacting force among the signal t-line and the contact conductor. An introduction of thin film of Iridium on the gold plate increases the power-handling ability. For the circuit equivalent of shunt DC contact MEMS switch with the transmission line, the isolation can be defined by the next equations:-

$$S_{21-off} = \frac{2(R_a+jwL_p)||Z_o}{(R_a+jwL_p)||Z_o+Z_o} \cong \frac{2(R_a+jwL_p)}{Z_o+R_a+jwL_p} \quad (2.1)$$

where, R_a - addition of bypass resistance and the contact resistance, L_p- shunt inductance, w-angular frequency, and Z_o- characteristics impedance.

A novel low cost powerless MEMS based Osscicular System is designed in [37]. This technique is useful for low power devices.

Mathematical expressions and geometrical model are derived for the actuation mechanism of corrugated structure for a small residual stress is presented by Yo-Tak Songa et al. [38]. The electrostatic actuated corrugated bridge is up in the air above a concave geometry of CPW, using sputtered nickel (Ni) conductor as the physical material designed for the gold and bridge for CPW t-lines, made-up on HR silicon wafer. The corrugated plate on concave geometry needs lesser actuation voltage as compared to flat plate on planar geometry by introducing several values of Ni thickness of MEMS switch. Either reasonably good level of stresses and/or low corrugations, the augmented bending toughness happening a tangential way can be ignored. Under equilibrium, a corrugated thin membrane having residual intrinsic stress (σ_0) turns similar to flat thin membrane having residual corrugated stress (σ). If C is called the corrugation constant, than effective residual tension of a corrugated thin membrane should be defined as $\sigma = C\sigma_0$.

Feixiang Ke et al. [39] also introduced the corrugated diaphragm to reduce the residual stress of the MEMS RF switch and as a result its pull-in voltage is considerably reduced. The calculated voltage is considerably decreased as of 105 V for a flat designed diaphragm to 42 V and 51 V for four-corrugation and two-corrugation designed diaphragms, respectively.

Figure 2.1 displays the schematic view of corrugated diaphragm. A generalized formula to calculate the pull-in voltage for both corrugated and flat diaphragm is given as [39] -:

$$V_{pi} = \sqrt{\frac{6g_o^2}{5_o}\left[\frac{7-v}{81(1-v)(1-v^2)}\left(\frac{Etg_o^2}{R^4}\right) + \frac{4}{9(1-v)(1-v^2)}\left(\frac{Et^3g_o}{R^4}\right) + \frac{4}{3}\frac{\sigma_0 tg_o}{\eta R^2}\right]} \quad (2.2)$$

where g_o- initial air gap, ε_o- permittivity of the free space, v- Poisson ratio, E- Young's modulus, R- circular diaphragm radius, η- residual stress reduction ratio, t- thickness of diaphragm, σ_o- flat membrane initial stress lacking of corrugation.

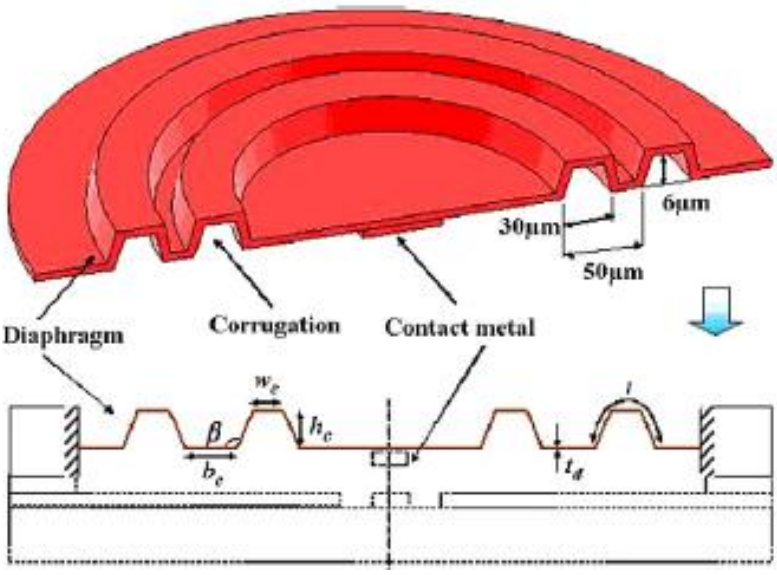

Figure 2.1- Corrugated Circular Diaphragm [39]

2.1.2 Advancement in Multiband Antennas Structures

Some important multiband antennas structures and their advancement are discussed in this section and later on latest multiband antennas are also covered along with the RA in section 2.1.4.

Lee et al. (2002) conceptualized a fractal based novel conformal multiband antenna design which is applicable at three different frequencies. Authors claimed that although a wide range of conventional fractal type monopole and dipole configurations have been designed in the past but they are not well suited for all the applications. In this research they described a Sierpinski gasket type of fractal configuration, printed on a dielectric substrate backed by a ground plane, and propose a novel approach to enhancing its multiband performance in terms of impedance matching characteristics as well as radiation pattern [40].

Varadhan et al. (2013) employed the fractal structures as the radiating elements. Using this concept, two tri-band RFID antennas are proposed, one for the radio frequency identification (RFID) reader and the other for the RFID tag. The antenna is the crucial part in designing any

RFID system. The reader antenna operates at 3.6 GHz, 5.8 GHz, and 8.2 GHz. The tag antenna operating frequencies are 3.9 GHz, 5.9 GHz, and 8.2 GHz. The applications of these frequencies are RFID for logistics management, traffic toll collection and tagometry (telemetry using RFID), respectively. The maximum read range obtained by the reader antenna is 87.5 cm and 85.6 cm by the tag antenna [41].

Patel et al. (2011) designed an E - shaped fractal patch antenna. The antenna is designed to function in multiple bands in the frequency range of 1 - 4 GHz depending on the geometric specifications of antenna. E-shape of different dimensions of area 604 mm^2, 1600 mm^2 and 1720 mm^2 are analyzed. The observed value of VSWR is near to 1 at each frequency band. The design parameters are tuned to have multiple applications like GSM 1800, P-GSM, E-GSM, GPS, UMTS and Wi-MAX [42].

One of the basic building blocks of reconfigurable antenna is fractal antenna. Various types of fractal shapes like Koch curve, Sierpinski gasket, Hilbert curve, Minkowski fractal and Sierpinski carpet have been examined by Ghosh, Sinha and Kartikeyan [13]. Self-similar geometries are given away to be capable in decreasing the resonant frequency of the given aperture is studied.

2.1.3 Latest Optimization Techniques for RF Circuits

In current years, the neural networks (NN) and genetic algorithms (GA) are being preferred for novel reconfigurable multiband antenna (RMA) designs. These techniques not only reduce the computational time and but are at the same time efficient also [106]. The procedures using NN are technologically advanced for characterizing RMA [43]. A multi-layer perceptron (MLP) is used to track down the resonance frequencies of the antenna at altered reconfigured situations. One more NN, named, self-organizing map (SOM) achieves the assignment of track down the RF switches to be configured ON for a preferred frequency response. In further study, an MLP NN is made expert in the back propagation mode to recognize the resonance frequencies of the designed reconfigurable geometry. It considerably decreases the mathematical design complexity as compared to other various numerical techniques used to design or model the whole RA owing to its multi scale structure. The designing stage is close to the clustering problem and a SOM NN is preferred to classify the resonance frequency calculations of the given reconfigurable

geometry. In order to define a new operational frequency, the ON-configuration of the RF switches can be recognized from a cluster of approximate distinctive structures.

The linear array thinning achieved by proper choice of cost function (CF) in the pattern search optimization (PSO) algorithm is studied by Razavi and Forooraghi [44]. By controlling the parameters and appropriate choice of weight factors, the minor increase in the width of main lobe and < -20 dB side lobe is attained as compared to uniform array. Using PSO algorithm, the scanning of main lobe at different angles is also presented in this article. As compared to genetic algorithm, the PSO is more reliable and fast in accomplishment of aforementioned problem. The CF which is to minimize and so as the three parameters are given as -

$$CF = w_1 \times nall + w_2 \times hpbw + w_3 \times addition \tag{2.3}$$

where

nall = normalized side/adjacent lobe level; *hpbw* = Beam width at which intensity is half the maximum value; *addition* = addition of far-field radiation pattern at different angles and w_1, w_2, w_3 = weight factors of equivalent parameters

In another article [45], the pattern search (PS) algorithm is used to optimize the post-processing parameters of antenna array. The prime objectives are to maximize the main beam width in the preferred direction, minimize the side lobe and to get the nulls in the interfering wave directions. Hence the cost/fitness function is well-represented as follows:-

$$CF = w_1 20 \log\left\{\sum_j \int_{l_j}^{u_j} |LAF()d|\right\} + w_2\, 20\, log\left\{\sum_i max\,\{|LAF()|\}_{l_i}^{u_i}\right\} + w_3 20\, log\{\sum_k |LAF(_k)|\} - w_4 20 log D \tag{2.4}$$

where, w_1 to w_4 - weighting coefficients; $_{u_j}$ and $_{l_j}$ are the upper and lower angles of the regions; $_k$ are the directions where the nulls are required; *LAF(Θ)* – Linear array factor containing only even number elements and given as-

$$LAF() = 2\sum_{n=1}^{N} A(n) cos\left[\frac{2\Pi d(n)}{\lambda} cos + \beta(n)\right] \tag{2.5}$$

Here *D* is the directivity, λ is wavelength and $\beta(n)$ is the phase angle of n^{th} even element. *d(n)* and *A(n)* are the inter-element spacing and the excitation amplitudes of n^{th} even element.

Furthermore, it is concluded in this research that convergence is completed in shorter time by using process of seeding by introducing the initialization process of genetic algorithm (GA).

The number of multibands, determining the operational frequency and the amount of parameters increase with the rise in quantity of thin layers in an arranged patch MA. Therefore it turns into a challenging task to enhance all the factors at the same time for definite frequency of bands. In [46], a novel algorithm, named, swarm optimization has been introduced to select the patch sizes of two band squares arranged patch antenna working in the X- or Ku- frequency bands. The CF aimed at the PSO is estimated by means of the trained NN to lessen the lengthy simulation period. The simulation results evaluated by PSO centered CAD tool has been confirmed by the experimental analysis for particularly arranged patch MAs [46].

Gangwar et al. [47] presented ANN approach to find out the resonant frequency of microstrip circular shaped patch antenna. The input for training the feed forward propagation model of ANN is generated by GA. The effective radius (R_{eff}) of circular patch expression is given as-

$$R_{eff} = R + T(\alpha_1 + \alpha_2)\left[\left(\frac{T}{R}\right)^{\alpha_3} + \left(\frac{1}{r}\right)^{\alpha_4}\right] \quad (2.6)$$

where the constant coefficients α_1, α_2, α_3 and α_4 are calculated by the GA. T and ε_r is the thickness of material and relative permittivity. The resonant frequency by using effective circular radius is determined as-

$$F_{res} = \frac{B_{np}c}{2\Pi R_{eff}\sqrt{r}} \quad (2.7)$$

B_{np} – n^{th} derivative of Bessel's function of order p

c – free space electromagnetics signal velocity

So, ANN uses three inputs and one output i.e. 3-15-5-1 model and 45 inputs values for the training purpose. It has been studied that resonant frequency experimented by ANN algorithm showed good agreement with previous related work.

Skinner et al. [48] reported self-organizing clustering maps technique to decrease the necessary computational time to optimize the microstrip feed line based rectangular metallic shaped patch antenna. The whole patch is divided into small elementary parts (32 Δx × 40 Δy grid) and they look like the cluster shape having presence of metal at some places and absence of

metal at some other places. SOM technique takes these subset stochastic unsupervised values for simulation and then mapped the frequency responses on the 2-D grid. The Euclidean distance is used to update the weights and neurons lattice and is given as,

$$H_{c(x),i} = a(t)exp\left(-\frac{\|r_i - r_c\|^2}{2\sigma^2(t)}\right) \quad (2.8)$$

$$w_i(t+1) = w_i(t) + h_{c(x),i}(x(t) - w_i(t)) \quad (2.9)$$

where

$H_{c(x),\,i}$ is the size of the centered neighborhood on the best match neuron; *a(t)* is the learning coefficient; r_i and r_c are the positions of the neurons on the lattice.

In conclusion, the SOM technique significantly reduced the possible configuration from 2^{32x40} to 2^5 the precise configuration for the selected antenna.

Authors [49] have presented a genetic hybrid algorithm for optimum employment of radio ports in application of cellular networks. This paper proposes a two-phase hybrid algorithm for optimal employment of radio ports. The employment scheme reduces the channel dynamic range and therefore decreases the desirable peak transmit power of a mobile handset. The performance analysis of the presented algorithm is related by a simplex algorithm and exhaustive search.

2.1.4 Contemporary Methods of Designing RAs

In the article [50], Majid et al. presented a reconfigurable frequency monopole antenna with ground plane slotted. Two bias circuit lines having series resistance (68 Ω) and inductance (56 nH) are linked to the ground plane over and done with a via and behave as a filter characteristics to block the radio frequency signal accepted through the biasing circuit and via. One line is located at circular patch and another on feed line as shown in **figure 2.2**. The microstrip slot is created at the ground plane of the monopole antenna. The slot bending is located at least a λ/4 distance, from the transmission line so reduces the coupling. The length selection for dimensions *g* and *k* are just about one-eighth of the wavelength of given frequency, and *h* dimension is just about quarter-wavelength of frequency. On chip RF capacitors (= 100 pF) are introduced to provide radio frequency signal joining through the ground. Four PIN diode

switches are integrated on MA. V-shaped slot is introduced to improve return loss characteristics.

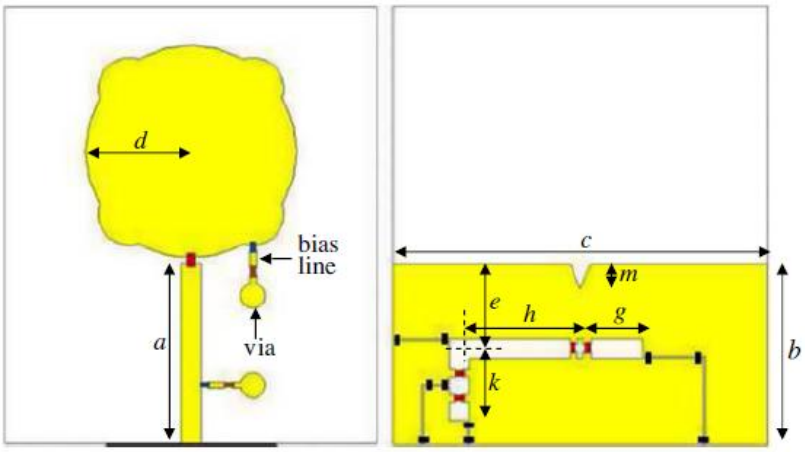

(a)

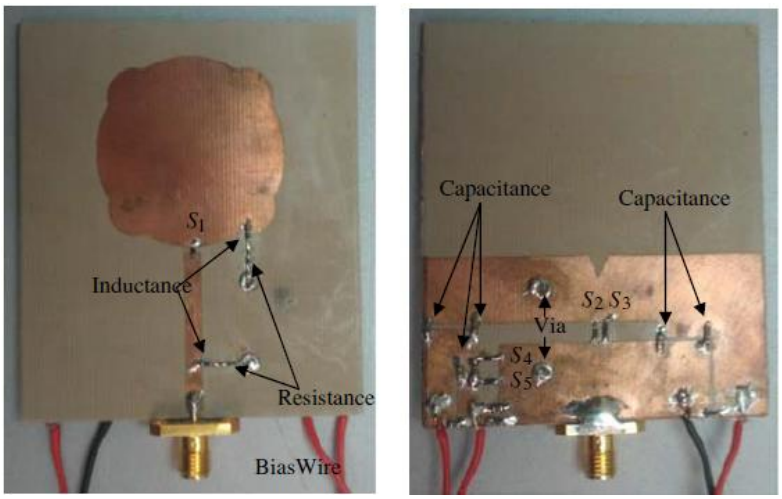

(b)

Figure 2.2- (a) Structure and Parameters of Antenna (b) Fabricated RA [50]

Note - Taconic RF35 substrate thickness, t = 1.52 mm, ε_r = 3.5, δ = 0.0018, size of the substrate 70 × 60 mm^2, d = 17 mm, a = 30 mm, b = 29 mm, c = 60 mm, e = 13.6 mm, g = 10 mm, h = 19.4 mm and k = 11.6 mm.

Dual reconfigurable disc antenna is presented by M. A. Al-alaa et al. [51] beginning from circular disc with modifications done to create three reconfigurable geometries. First is

reconfigurability in frequency at 1.85 GHz at ON configuration, while at 3.5 and 4.5 GHz at OFF position of PIN diodes and MEMS switches, second is reconfigurability in radiation pattern beam by rotating 60^0 angles with the help of PIN diode switches at resonating frequency of 5.73 GHz and third geometry provides dual reconfigurability that combines between radiation pattern and frequency changes.

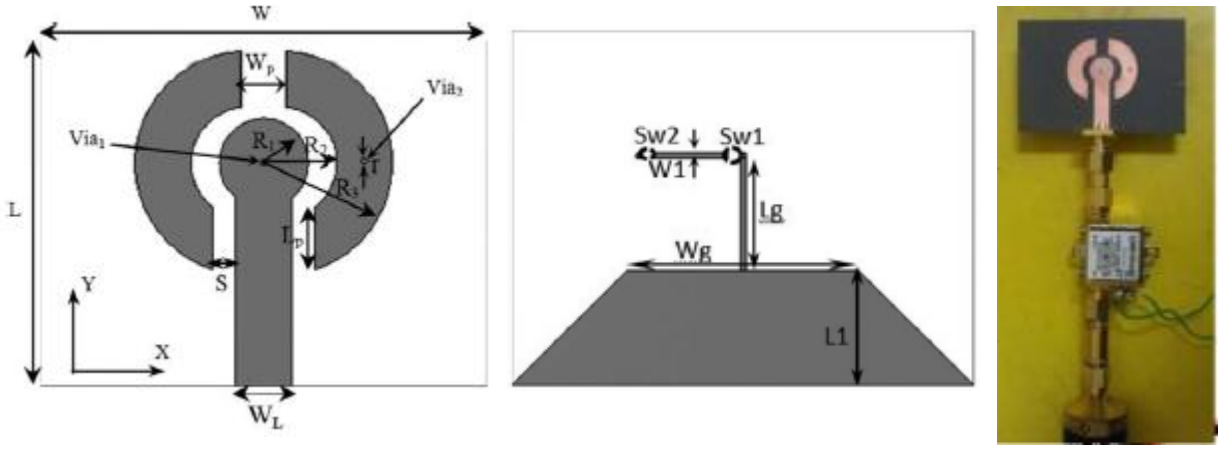

(a) **(b)** **(c)**

Figure 2.3- Frequency Reconfigurable Disc Antenna (a) Top side (Antenna Metal Patch) and (b) Ground Side (c) Fabricated Antenna under Testing [51]

Note - Rogers Duroid RT5870 = 31 × 40 mm^2, L = 31, W = 40, R_2 = 6.5, L_p = 5.54, W_L = 5, W_p = 4, R_3 = 11.5, W_g = 20, R_1 = 4, L_1 = 10, W_1 = 0.55, r = 0.55, S = 2. All dimensions are in mm.

Figure 2.3 shows the geometry of frequency reconfigurable slotted disc antenna. Two parasitic parts surround the circular disc and at the focal point of disc, there is a via1 attaching the ground plane and the disc. Second via2 is next to the right part to bond it to the bottom ground. Two RF switches are integrated on the ground plane over the L bent strip line. Further, in comparison results of antenna with either PIN diode or MEMS switches, its shows better performance of fabricated MEMS on MA. This is due to the excellent matching capability at higher frequencies on wider bandwidth range and lesser insertion loss.

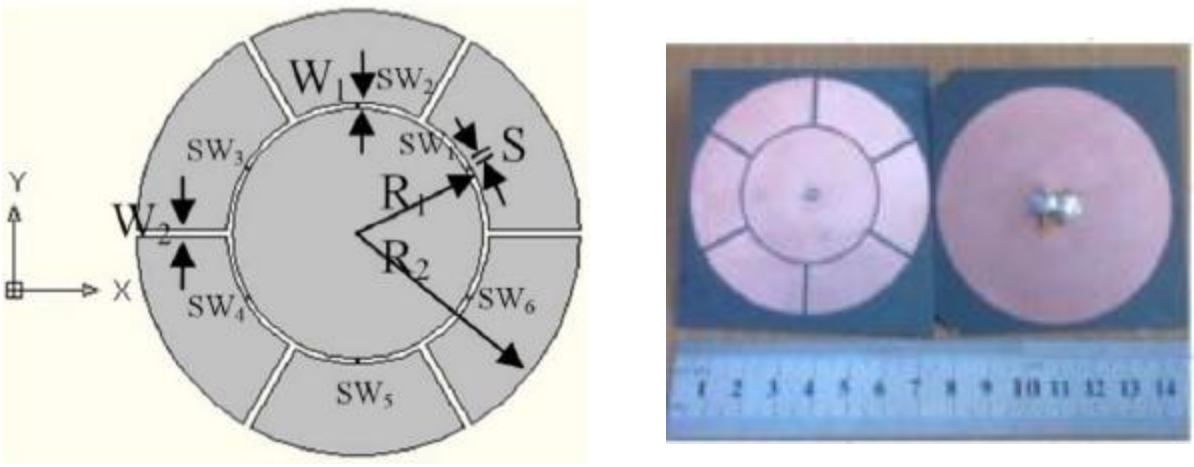

(a) **(b)**

Figure 2.4- (a) Reconfigurable Circular Disc Pattern Antenna Structure. (b) Fabricated Disc Antenna [51]

Note – R_1 (slot ring mean radius) = 19.75 mm, (disc antenna radius) R_2 = 35 mm, W_1 (width of slot) = 0.9 mm, W_2 (sector width gap) = 1 mm, S (width of switch) = 0.3 mm.

Circular disc structure of reconfigurable pattern antenna is shown in **figure 2.4** [51]. The presented antenna contains a circular patch having six sectored ring (fan type) adjacent parasitic patches surrounding the central circular disc and fed coaxially at central circular patch.

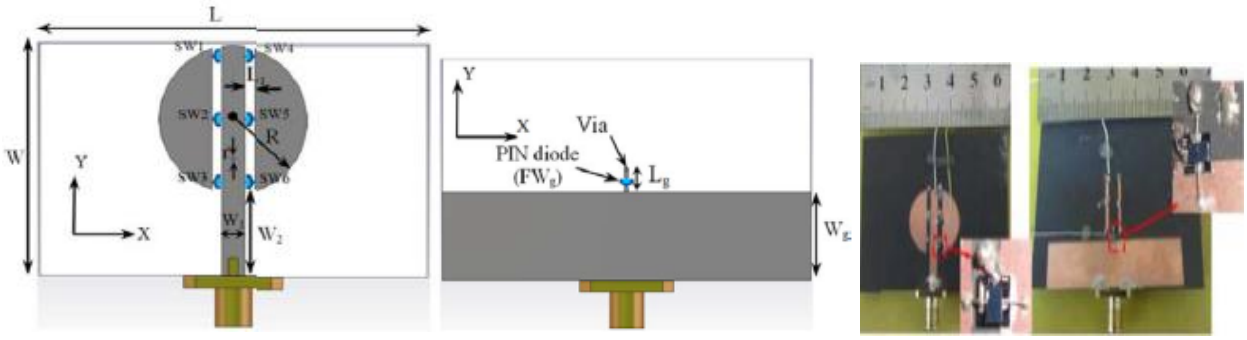

(a) **(b)** **(c)**

Figure 2.5- Dual Reconfigurable Disc Antenna Geometry (a) Top Side (Antenna Metal Patch) and (b) Ground Side (c) Fabricated Antenna [51]

Note - Rogers RT5870 substrate = 30 × 50 mm^2, L_1 = 1.24, L = 50, W_1 = 3.0, W = 30, W_2 = 10.73, L_g = 3.0, d = 5.12, W_g = 12.0, R (radius of disc) = 9.5, r (via hole radius) = 0.55. All dimensions are in mm.

Total seven RF switches have been integrated on antenna as shown in **figure 2.5**. There are six RF switches on patch plane to reconfigure the radiation beam direction at an angle of 180^0 and one switch in the ground plane in order to control the reconfigurability in frequency. The presented antennas are used in wireless applications like LTE, Wi-MAX, and WLAN bands of mobile handset transceiver.

Pattern and frequency reconfigurable Yagi patch antenna has been proposed by Majid et. al. in 2012 [52]. The reconfigurable antenna designed contains a reflector, a driver, two directors and five PIN diodes as shown in **figure 2.6**. By electrostatically directing the RF switches next to the reflector and directors, the patterns can be changed to either directional or almost omni-directional radiation pattern at 1250 MHz, 1850 MHz and 2450 MHz frequencies, respectively.

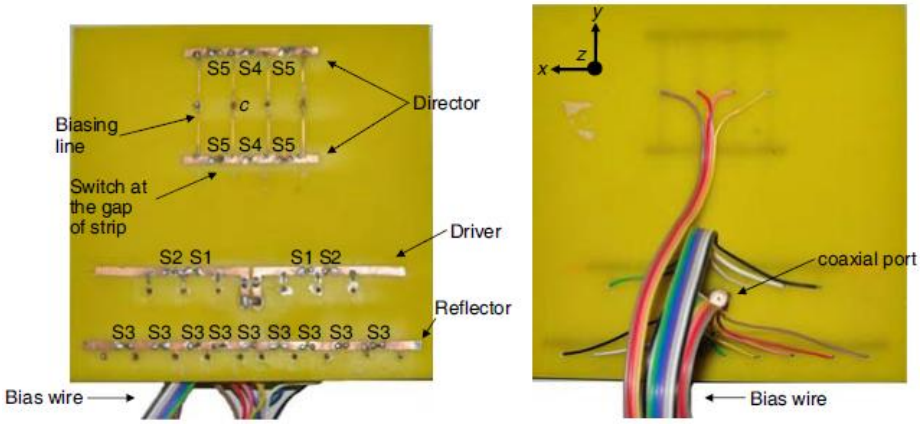

(a) **(b)**

Figure 2.6- Fabricated Reconfigurable Pattern and Frequency Yagi Patch Antenna (a) Forward-facing side and (b) Ground side [52]

By applying different biasing condition to PIN diodes on MA, reconfigurability in polarization is attained [53]. Linear or circular polarization of MA is achieved by controlling the circular corner truncated patch via four switches and its characteristic studied in time-domain.

MEMS switch based an electrically small frequency-reconfigurable microstrip antenna (FRMA) with a high frequency reconfigurable ratio of approximately seven i.e. 718 and 4960 MHz has been presented by Zohur et al. [54]. The schematic view of FRMA and physical dimensions are display in **figure 2.7** and **table 2.1**, respectively. Both operational modes are mutually enhanced, and further impedance and radiation pattern measurements are described.

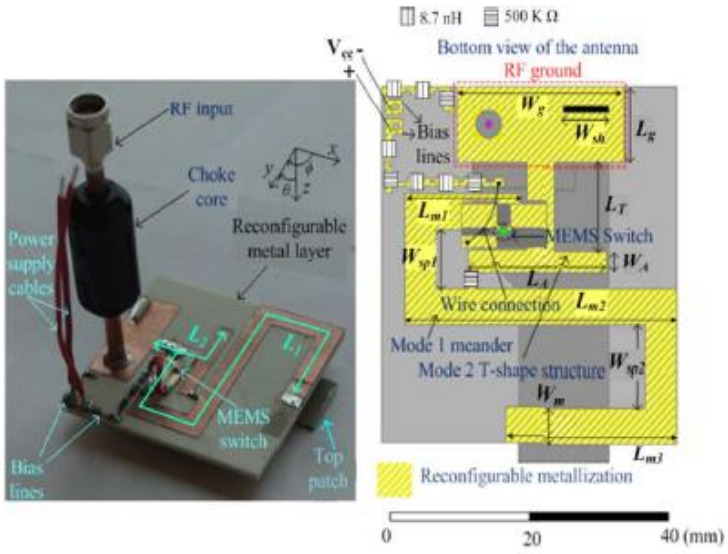

(a)

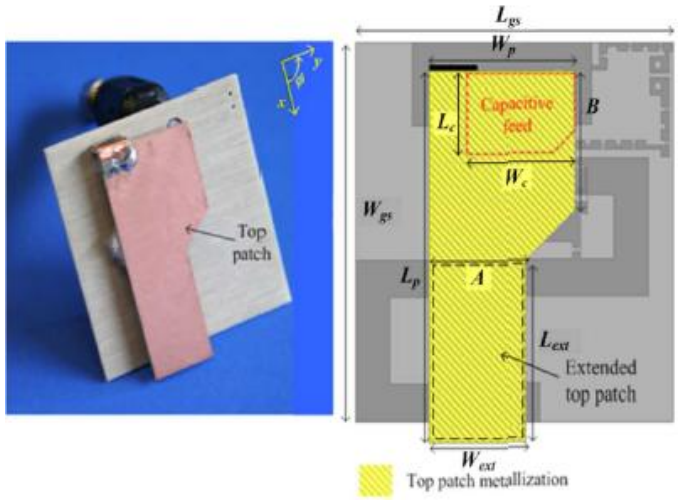

(b)

Figure 2.7- Photographs and Schematic views of RF MEMS based Integrated Antenna illustrating the Physical Parameters (a) Ground side and (b) Top side [54]

Table – 2.1: Physical Parameters of the RA (Measurements in mm) [54]

W_{gs}	45.0	W_{ext}	12.80	L_g	9.79	W_{sp1}	7.50
L_{gs}	41.7	A	12.80	L_T	11.0	W_{sp2}	10.30
W_p	19.2	B	16.50	W_A	3.90	W_m	4.50
L_p	44.0	L_c	9.60	L_A	18.50	W_{sh}	6.40
L_{ext}	21.60	W_c	14.40	L_1	104.0	L_2	19.0
W_g	23.50	L_{ml}	16.40	L_{m2}	38.60	L_{m3}	24.20

The key feature of this design approach is to jointly optimize both modes i.e. to keep the preferred performance characteristics of the FRMA in any one mode while enhancing the associated parameters of any other operational mode. The lateral values of antenna are $\lambda/10 \times \lambda/10$ at 718 MHz. In presented design, the meander shape (L_1) is used for mode-1 and T-shape (L_2) for mode-2 configurations joined by means of the upper patch and in this way act as radiating configurations. The width of the top patch is suitable in condition where a decent reflection/ matching coefficient for every single operational mode are desirable. A choke balun is introduced to compensate the small sized ground plane once attached through a coaxial t-line.

Further, it is concluded that PIN diode switch draws milli-ampere of currents while a MEMS switch draws current in μA/nA. Due to the negligible power consumption, high isolation as well low IL characteristics of MEMS, it is much superior as compared to FET or PIN diode switch. MEMS switch has also the benefit of being monolithically fabricated, which does not occur in case of other RF switches.

A compact size Pattern and frequency reconfigurable antenna has been proposed by Chen, Sun and Feng in 2007 [55]. Yang, Wang and Liu [56] presented a radiation pattern reconfigurable two element end-fire Yagi patch shaped antenna. Depending on odd-mode or even-mode frequency of operation of the MA, the radiation pattern plot is either a sum-pattern or a difference-pattern, respectively. Introduction of switched-EBG cells on MA, a new pattern reconfigurable antenna has been proposed. **Figure 2.8 (a)** shows the reconfigurable MA consisting of four parasitic elements and one driven element. The parameters of presented Yagi antenna and the etched EBG cell are composed of four rectangles and a narrow slot, shown in figure 2.8 (b-d). Three different states have been discussed, in which all switches in the cell are

either open or closed and these are referred as first and second stage. In third stage the two RF switches are closed and the middle switch is open as shown in fig. 2.8 (d).

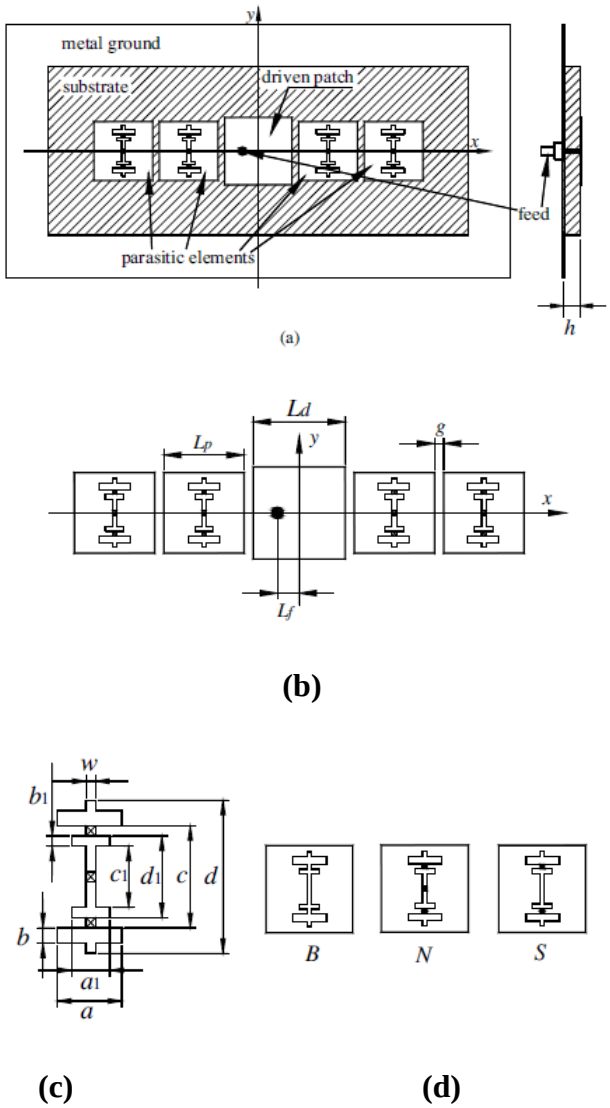

Figure 2.8- Reconfigurable Yagi patch Antenna (a) Scheme of the Antenna (b) Parameters of the Antenna Patches (c) Parameters of an EBG Cell (d) States of a Parasitic Patch [56]

A compact size (14×16×1 mm^3) coplanar asymmetric strip fed monopole RA that takes a corresponding reconfigurable performance by means of ability to work in the triple frequency WLAN bands and the dual band-stop ultra-wide band (UWB) with two notch bands lying between 3.3 to 4.2 GHz and other lying 5.0 to 6.0 GHz is presented by Parisa et al. [57]. The

rotational patch is controlled at different positions and thus antenna is reconfiguring to transmit/receive signals of cognitive radio.

A 3D reconfigurable directive pattern beam-steering antenna with a CPW in the ground plane is proposed by Lee et al. [58]. The different beam radiation patterns have been generated by designing two dipole arrangements with four RF artificial switches and a loop in the antenna structure. As shown in **figure 2.9**, the semi-circle structure of the CPW with ground is designed to increase the directivity of beam and for each selected state the poles are physically bent to increase angle of beam. It is mentioned by author that for obtaining exact locations of switches, distance between poles & loop, and pole dimensions & its shape are predicted by doing various parametric studies and simulation trials by keeping resonance frequency in desired band.

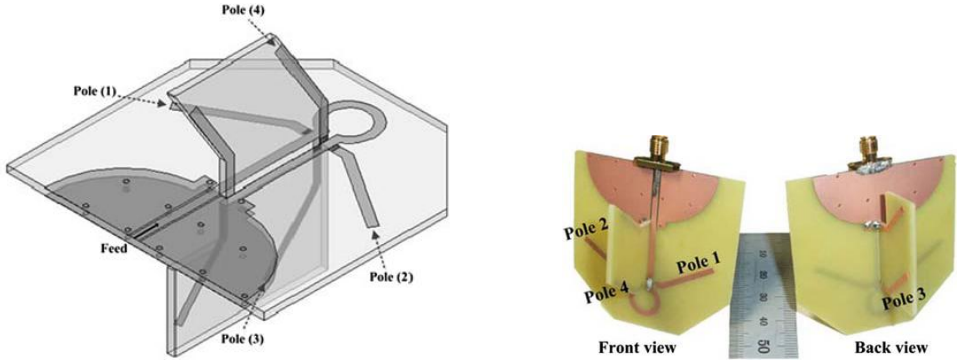

(a)

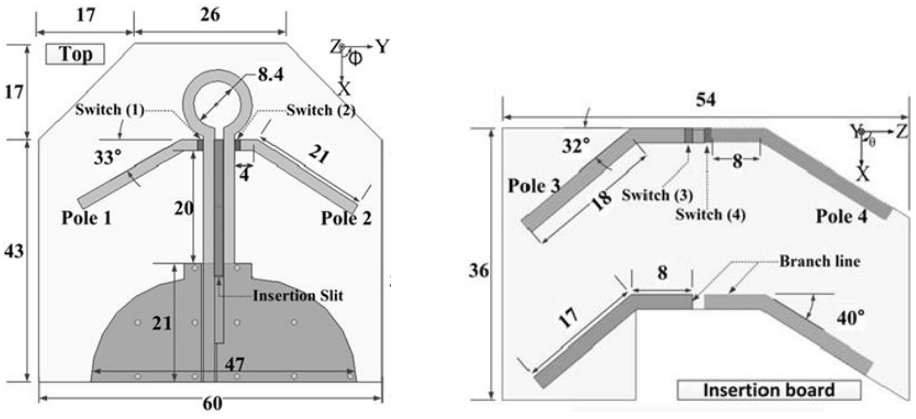

(b)

Figure 2.9- Geometry of the Reconfigurable Beam Directive Antenna (a) Fabricated Antenna Photograph (b) Structure of Antenna Parameters (units in mm) [58]

Anup and Satish [59] fabricated a slot printed antenna for Digital Television (DTV) ranging between 496 to 862 MHz and printed reconfigurable frequency loop antenna working at Long term Evolution bands having MIMO operation for wireless portable DTV multi-media players applications. The LTE covers two bands lying 1.71 to 1.88 GHz and 2.5 to 2.7 GHz.

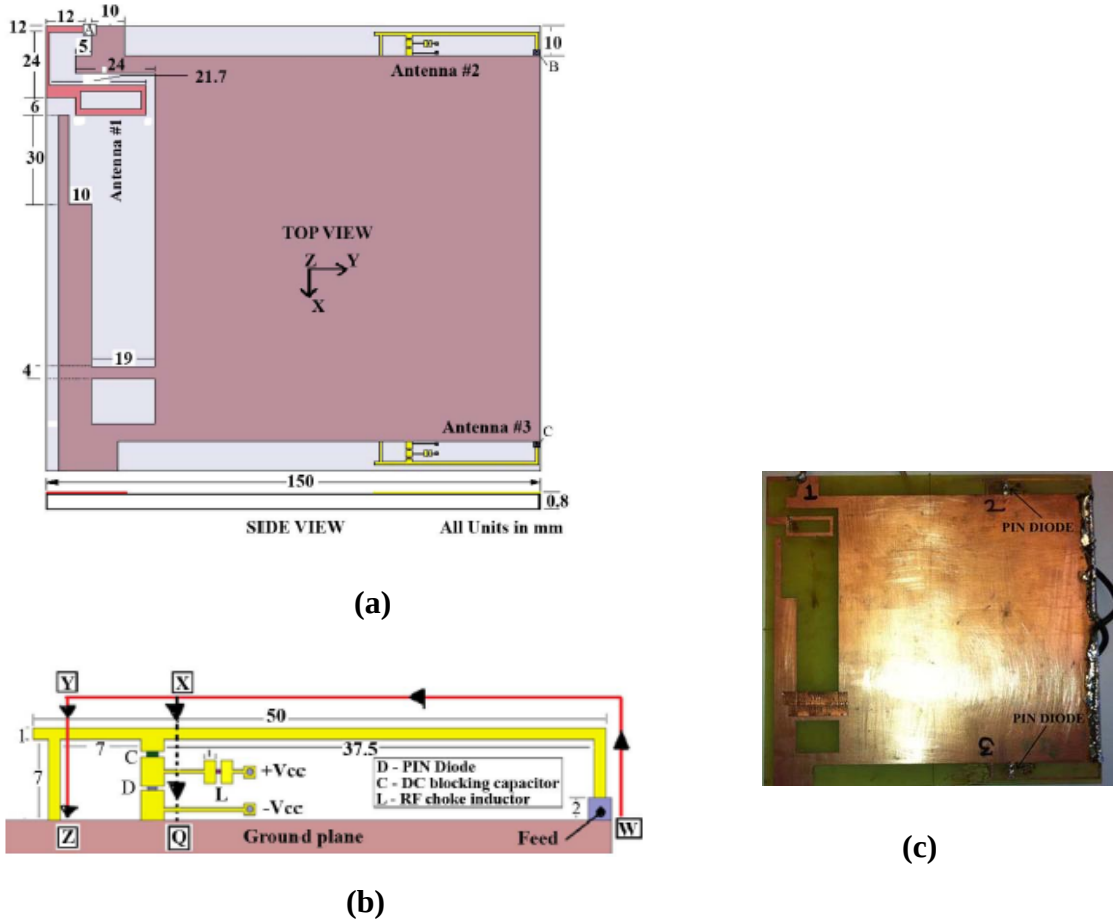

Figure 2.10- (a) Antenna Structure viewing the Three Antennas on a Ground Plane and (b) Reconfigurable Loop related with the Planar Antennas-2 and -3 (Zoom Version) (c) Fabricated Antenna [59]

On a single sided copper FR4 printed circuit board, a stair in the slot and a shorting track are introduced for matching at lower band of the Digital TV as shown in **figure 2.10**. An adapted L-shape microstrip transmission line is used for excitation. For reconfigurable frequency, PIN diodes (SMP 1340–040) is integrated on antenna along with 20 pF capacitor for blocking DC signal and a high magnitude inductor in series using a resistor having value of 47 ohm. **Figure 2.10 (b)** show the length of the loop separated into two resonate trail, either path W-X-Y-Z when

RF PIN diode is OFF or under ON position of same switch it follows path W-X-Q. So, accordingly resonates at 1800 MHz and 2600 MHz, respectively.

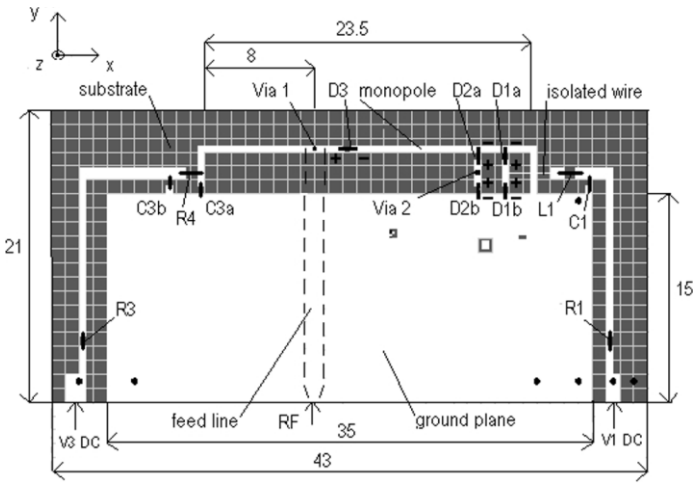

(a)

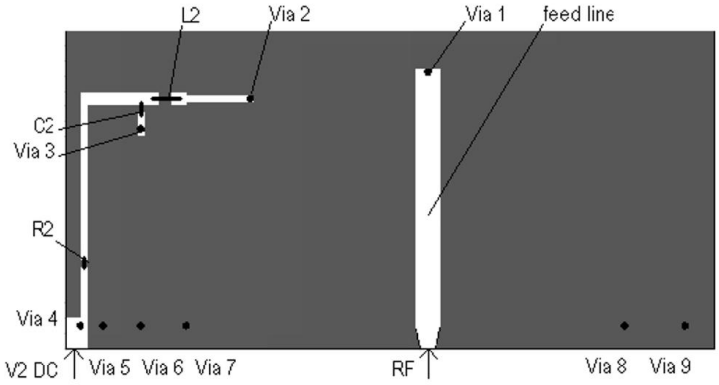

(b)

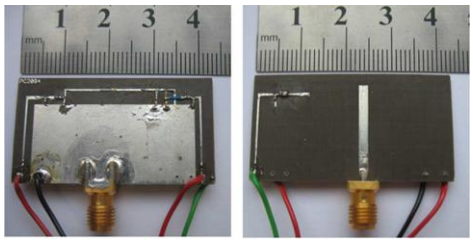

(c)

Figure 2.11- Simulated RA (depicted on a 1-mm Square Grid) (a) Front side (b) Back view (c) Fabricated Antenna Photograph [60]

In [60], the authors presented a vertical polarized, nearly omnidirectional and compact switchable reconfigurable multiband antenna by electronically controlling the five RF diode (PIN) switches on MA surface. Such antenna works at five next to frequency sub-bands, one frequency at a time, for the upper UWB (6.0–10.6 GHz) applications.

The arrangement of the RA is similar to that of a planar inverted-F antenna (PIFA) as shown in **figure 2.11**. But excluding the upper limb of the monopole antenna is just about a λ/2 long and also shorted to the ground plane at the preferred resonant frequency. In this way it works well as a slot, even though the amount of the metal along all sides is very less. Two pair of PIN diodes is joined in a shunt transversely the radiating slot and fifth switch is joined in series transversely by creating a thin gap in the extended support of the monopole.

A novel reconfigurable frequency planar antenna on a 1mm/0.01λ thickness of substrate is proposed by Ouyang et al. [61] for wideband antenna applications. The construction of antenna includes square patch and a coupling thin strip nearby the radiation edge. This represents an additive shunt joining resonance circuit. The six RF diodes at different location make the dissimilar *C* as well as *L* in the antenna structure. When the operational resonance frequency characteristic of antenna is near to the operational resonance frequency of circuit, the operational band should be altered while keeping up the radiation characteristics.

A slot array beam steering and reconfigurable antenna operating at different frequency is presented by Jamlos et al. in [62]. The combination of radial line slot array (RLSA) for high gain and aperture coupled geometry for achieving reconfigurability has been studied by authors for designing of antenna. Further in order to achieve reconfigurability, PIN diode RF switches are incorporated in the transmission line as an alternative for the coaxial to CPW and so feed the radial line slot array. The coupled slots are shaped in periodic spiral, to avoid congestion and touching of dissimilar arms at its middle area, as displayed in **figure 2.12**. They also calculate the quantity of coupling towards radiating surface as of the t-line of the antenna design.

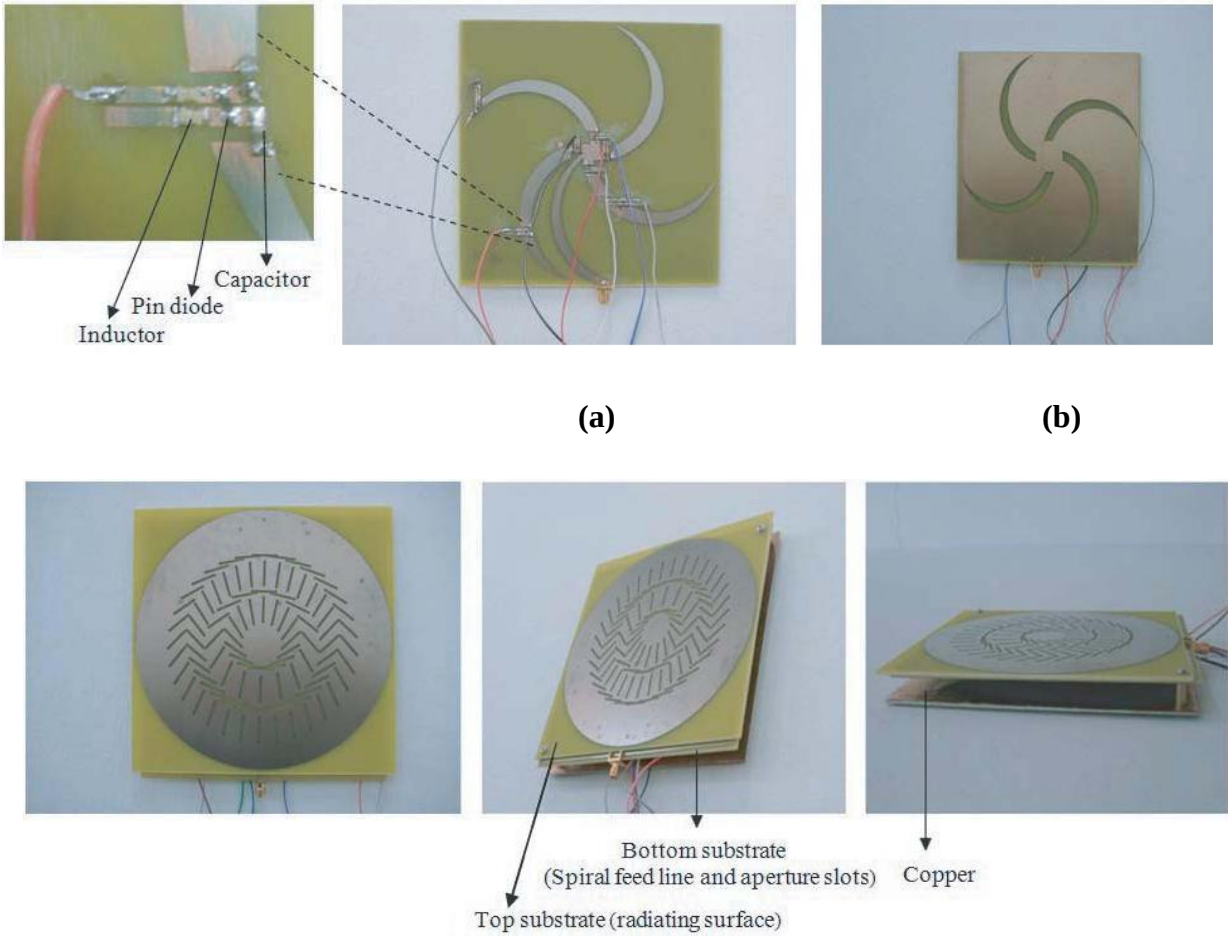

Figure 2.12- Snapshot of MA (a) Spiral-shape Feed Line (b) Aperture Coupled Slots (c) Top Substrate- Radiating Part (d) Complete Layout (e) Side plan [62]

The biasing circuit includes inductors and capacitors which are used to choke off the AC as well RF wave flowing into feed line and stop the DC simultaneously. Reconfigurable beam steering (RBS) and reconfigurable frequency switches (RFS) locations are displayed in **figure 2.13**.

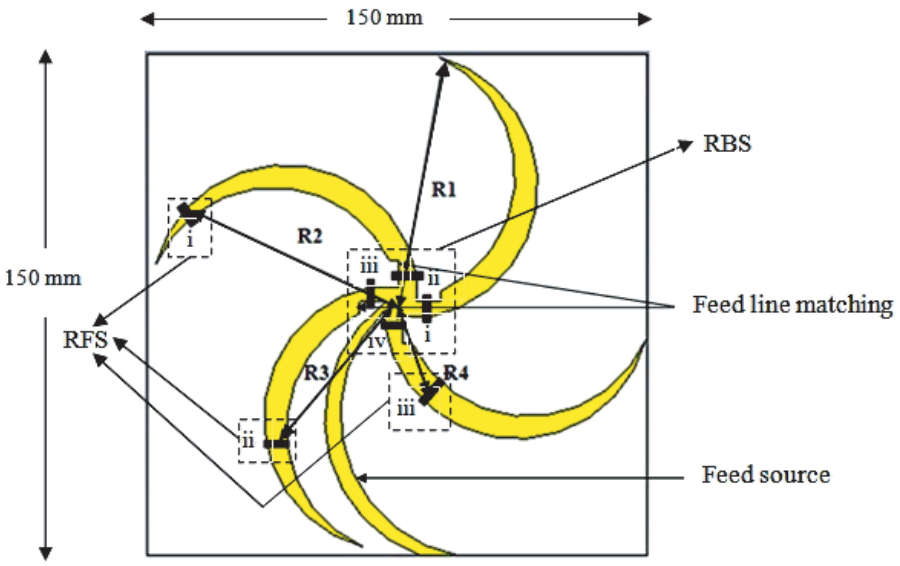

Figure 2.13- Spiral-shaped Feed Line contains Two Types of Switches- RBS and RFS [62]

The principle of achieving beam steering and change in operating frequency is explained by authors as follow -:

1. With the stimulation of the spiral structure of the feed line via certain ON/OFF position of RBS, beam steering is attainable. Steering is not possible if the feed line lengths are kept straight. At different RBS position, antenna steers on following angles 90, 180, 270 and 0/360 degree.

2. In order to shift the frequency bands, the radius length arms of the slot array varied with the help of RFS. For achieving higher frequency band a smaller radius length arms is required. Four resonating bands are 2.3 GHz, 2.6 GHz, 2.9 GHz and 3.3GHz.

A compact pattern-reconfigurable ultra-wideband monopole MA is presented by Clive Parini, Xiadong Chen et al. [63]. The directivity of antenna is changed by introducing two parasitic elements, four PIN diode RF switches. The antenna work well from 3 to 6 GHz frequency range and with effect of switches the radiation patterns are changing in either two opposite direction or in omni-directional. The antenna is designed for cognitive radio as it aids the pattern diversity in multipath surroundings and also enhances the flexibility of radio terminal [64].

Ding and Wang [65] proposed reconfigurable pattern antenna in which seven PIN diodes are integrated on a feeding network to achieve different radiation patterns for millimeter-wave

applications. The geometry of the reconfigurable antenna and the dimensions of the reconfigurable antenna $l_a \times w_a$ = 35.14 mm × 20.74 mm, and d_a = 3.38 mm has been shown in **figure 2.14**. The principle followed in this article is to put a metal reflection ground at the back side having a distance of ¼ working wavelength. This has been done to enhance the gain of the radiation. The undesired mutual interference between the radiation layer and feeding layer was eliminated by the provided common ground plane isolation. In conclusion statement three different reconfigurable radiation patterns (modes) towards the elevation axis by way of a gain variation < 0.6 dB have achieved.

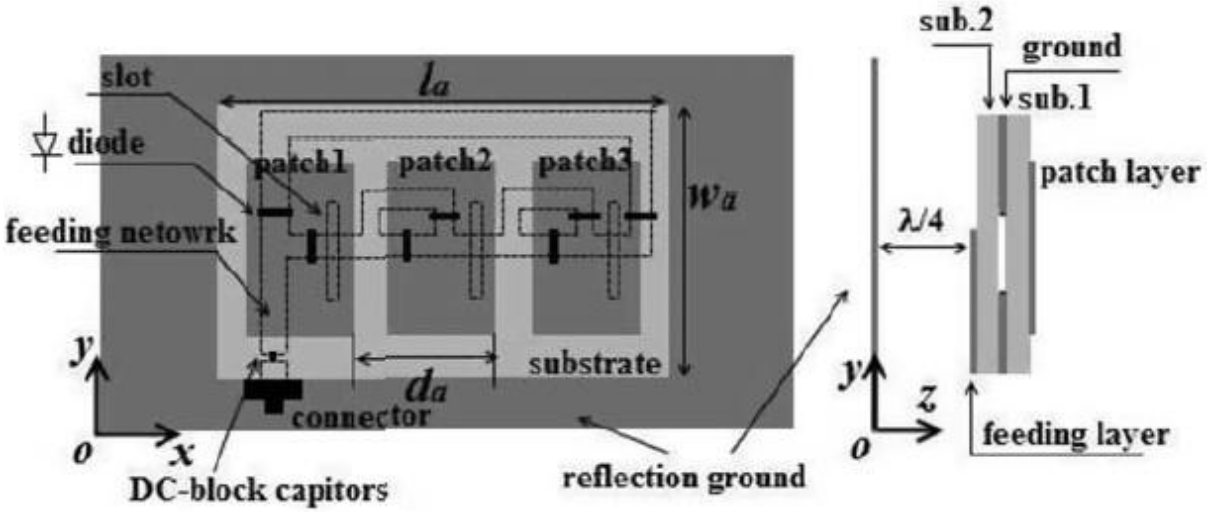

Figure 2.14- mm-Wave Reconfigurable Pattern Antenna with PIN Diode Feeding Configuration [65]

Xiadong Yang et al. [66] presented a UWB tapered slot antenna which can be used to reject the higher band allocated for WLAN and focusing on application ultra wideband wireless body area network. The UWB antenna construction involves an unequal arm which is H-shaped conductor.

A compact meta-material based pattern and frequency reconfigurable antenna is presented by Choi and Lim [67]. The electrical size of the antenna is reduced by means of 0^{th}-order resonance and reconfigurability in frequency as of 2.32 to 3.14 GHz is attained by introduction of PIN semiconductor diodes on the provided slots as shown in **figure 2.15**. The tunable physical slots are useful to achieve reconfigurability in the radiation pattern.

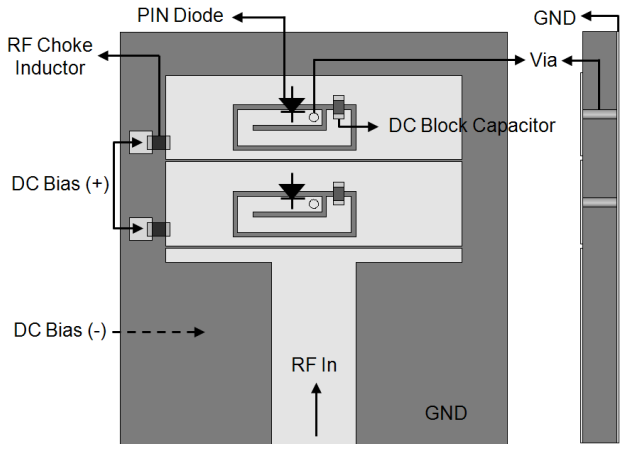

(a)

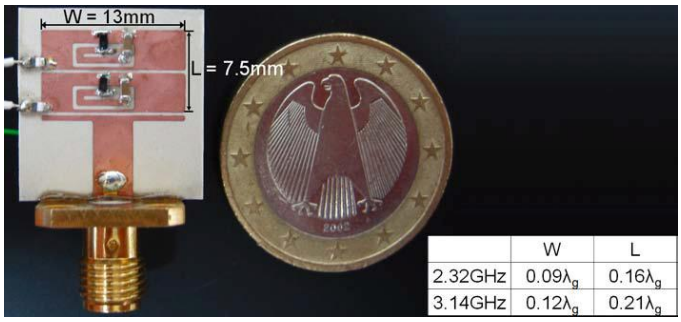

(b)

Figure 2.15- (a) Front schematic view of the Tunable Compact Resonant Antenna (b) Fabricated Planar Antenna with Electrical Size [67]

2.2 Summary of the Chapter

In early 1990's, telecommunication and RF device markets started witnessing exceptional growth fueled by an MEMS technology explosion and a microwave revolution, when the first MEMS RF switch is came into existence and it is introduced by Dr. L. Larson at Hughes research laboratory, USA. Afterward the researchers are emphasizing towards the advancement of MEMS RF switch in terms of minimizing the size, low power consumption, less IL, high isolation, less displacement time, compatibility with RF devices etc. While a great effort in late 90's has been focused, when the first functional MEMS switch based antenna is developed.

Various shapes of multiband antennas have been investigated which are suitable for designing the RAs and under this development fractal and array antennas are frequently discussed during the last 15 years. Recently, the numerous optimization techniques such as NN, GA, Quasi newton, PSO, pattern search etc. are being preferred extensively for optimizing the switch and antenna performance. These optimization methods not only decreases the computational time and also at the same stage act as efficient techniques. In the next chapter, designing and modeling of different MEMS RF switches for RAs, is taken up as a first research problem.

Chapter 3

RF MEMS Switches Design and Modeling

The prime objective of the present chapter is to study the design and modeling of various MEMS RF switches which include – DC metal-to-metal contact cantilever beam switches, Shunt capacitive switches, DC shunt MEMS switches and film bulk acoustic resonator (FBAR) cantilever resistive MEMS switches. All the RF switches proposed here are designed on common silicon (Si) substrate. The in-built transmission line on silicon substrate is either CPW or microstrip line.

This chapter is organized by first defining the basic principles and methods of operation of various RF MEMS switches. The construction and advantages of CPW and microstrip transmission line are discussed. The electrical, mechanical and electromagnetic characteristics of all four types of proposed MEMS switches as defined above are included next. The soul of this chapter includes the optimization of EM post-processing S-parameters with the help of generating equivalent circuit model of proposed switches. The RLC components and their equivalent relations with the physical dimensions of various parts of switch are also presented. The simulated results of proposed switches such as pull-in voltage, squeezed film damping, switching ON-OFF time, insertion loss, isolation, return loss are verified either mathematically or by numerical techniques. The comparisons of results of designed switches with previous work and their applications are included next. Finally, in the last sub-section the comprehensive fabrication modeling and designing steps of metal contact MEMS switch using PolyMUMPS foundry are presented.

3.1 Principles and Operation of MEMS RF Switches

MEMS switches are the combination of sensors, mechanical elements, electronics and actuators on a semiconductor wafer through surface and bulk micro-fabrication process. The micro-fabrication procedure generally comprises of a photo-lithography typed micromachining, bulk production basis fabrication, which usually offers benefits of lowest price while producing

enormous volume [68- 70]. From radio frequency circuit configuration, it can be parallel coupled or series joined by means of a t-line [71]. The physical connection can be either resistive i.e. conductor-to-conductor or capacitive i.e. conductor–insulator–conductor type. Each configuration of switch has many advantages in terms of manufacturability or working performance. The benefits of MEMS RF switches as compared to PIN diode, CMOS and FET RF switches are: almost zero power feeding, low insertion loss, high isolation intermodulation products, and linearity [72-75]. These miniaturized devices also have many advantages over electromagnetic relays in terms of size, and reliability [76-78]. MEMS RF switches air bridge, or a diaphragm, thin metal conducting cantilever can be considered from point of mechanical movement.

The mechanical movement is achieved with the help of force that can be produced using electrostatic, piezoelectric, thermal, and magneto-static actuation [29, 79]. These different types of actuation can be applied to study various multi-physics and electromagnetic properties of RF MEMS switches. The electrostatics actuation can be used to compute capacitance effects and charge distributions of the switch. The combination of electrostatics and mechanical (electro-mechanics) static actuation provides the solution of pull-in voltage and lift-off analysis of the beam. The electro-mechanics actuation in frequency domain can be useful to afford the harmonic analysis of the switch and therefore preferred to study the various modes of operation. Such solver deforms a switch to an equilibrium condition by a DC bias voltage, and then achieves a harmonic modal analysis, by applying an AC bias voltage, in that condition. The piezoelectric actuation applied to RF switch is subject to study the mechanical deformation of the beam and therefore to measure force, pressure, and acceleration applicable to piezoelectric layer, bottom as well as top electrode. The best suited example of this type of actuation is film bulk acoustic resonator (FBAR) cantilever based MEMS switch. Under the effect of thermal actuation, the transient behavior of the RF switch can be analyzed. The transient analysis includes ON-OFF time of the switch, electric power, contact forces between the lower contact pads and upper beam and effect of beam stiffness. In addition, because the MEMS RF switch is expected to be working in air, there are fluids forces as the upper electrode and bottom fixed beam are quickly squeezed together. This fluid action, frequently denoted to as squeezed-film gas damping effect, need also is considered within this analysis [29].

3.2 Design of Transmission Lines

CPW consists of a single-sided three number of conductors t-line. CPW has center conductor alongwith double grounds lying on same plane, reducing the effects of coupling and allowing for easy presence of shunt and series elements. Subsequently microwave based integrated circuits (ICs) are mostly coplanar in arrangement and therefore CPW lines are extensively used as circuit components and can be integrated lines. Next to millimeter (mm)-wave frequencies, CPW compromises the prospective of lower metal conductor in addition to radiation losses as related to microstrip t-lines. CPW has important advantage of varying magnitudes of the t-line without effecting the value of characteristic or matching impedance [71, 73, 80, 81].

An estimated formula [71], for the matching impedance of the CPW, assuming thickness of CPW (t) is negligible, $0 < p < 1$, in addition h >> w, is

$$Z_o = \frac{30\Pi^2}{\sqrt{(r+1)/2}}\left[\ln\left(2\frac{1+\sqrt{p}}{1-\sqrt{p}}\right)\right]^{-1} \text{ ohms} \tag{3.1}$$

$$p = \frac{w}{w+2s} \tag{3.2}$$

where 'h' is height of substrate, 'w' is center width strip, 's' is width of slot, and 'ε_{re}' is relative effective dielectric constant of the wafer.

An experimental equation for ε_{re} [71] is

$$_{re} = \frac{r+1}{2}\left[tanh\left(1.785\ log\left(\frac{h}{w}+1.75\right)+\frac{pw}{h}\left(0.04-0.7p+(1-0.1_r)\frac{(0.25+p)}{100}\right)\right)\right] \tag{3.3}$$

Further, microstrip transmission may be considered as a two wire line and is further viewed the most extensively used as a planar microstrip transmission line [74,75,82]. One side of the design is free to access for mounting on the hymite or other packaged devices and further geometrical construction lends itself well to printed circuit board patterning methods to define the complete circuit. Planar transmission line has been used extensively in microwave and milli-meter circuits and systems.

The structure is complex, due to which the mathematical expression of per unit length dimensions is difficult to calculate. Therefore, comparing the electrostatic force by the restoring mechanical force of the upper beam makes the computation easy and given as,

$$\frac{1}{2}\frac{_0 \times W \times w \times V^2}{g^2} = k(g_0 - g) \quad (3.4)$$

where, 'V' is actuation voltage between the electrode and beam, 'g' – separation between upper and bottom electrode and 'g_o' – relaxed gap, '$W \times w$' is area of electrode.

3.3 Types of RF MEMS Switches

The MEMS RF switches are broadly classified as either shunt or series configuration for radio frequency to milli-meter wave circuit applications [83]. In ideal shunt switch configuration, the switch beam is exactly placed in shunt between the ground and t-line. When electrostatic actuation voltage is introduced, the beam is located in up-position and it allows the signal passes through the t-line. Otherwise, when no actuation voltage is applied, the signal goes in to the ground and in this case the beam is located in down position [84,85]. The switch operation in series configuration is just opposite the shunt. The beam is in up-position when no actuation voltage is applied as here the beam makes no path for signal to flow. Further, as a result of applied votage, the series switch changes its position towards down and complete the path of signal from one RF port to the other. Under ideal condition, it is always desirable infinite isolation in off-position and zero IL in on-position [86,87].

The ideal series switch operates extensively for frequency lying between DC to 50 GHz applications. At RF and low microwave frequencies, the series switch offers isolation more than around 55 dB and low IL, nearby 0.05 to 0.20 dB [88]. Shunt capacitive MEMS switches are prefered for higher frequency range lying between 5.0 to 60 GHz applications. If the shunt capacitive switch is designed properly then low insertion, around ranging from 0.02 to 0.1 dB can be achieved. Although a acceptable isolation, around more than 20 dB can be successfully attained [90-91].

3.3.1 Capacitive Shunt MEMS Switches

The shunt configuration of capacitive MEMS switch with circuit model is shown in **figure 3.1**. The upper beam is held by two vertical post and makes a connection with the lower t-

line terminating the two post. In the OFF-position, the switch isolation is calculated by the effect of parasitic capacitance among the upper electrode and lower output t-line. The value of isolation ($S_{21\text{-off}}$) can be additional enhanced by adding a dielectric film of 1000 Å STO (strontium titanate oxide) or silicon nitride. It will also decrease the stiction problem between the transmission lines [91].

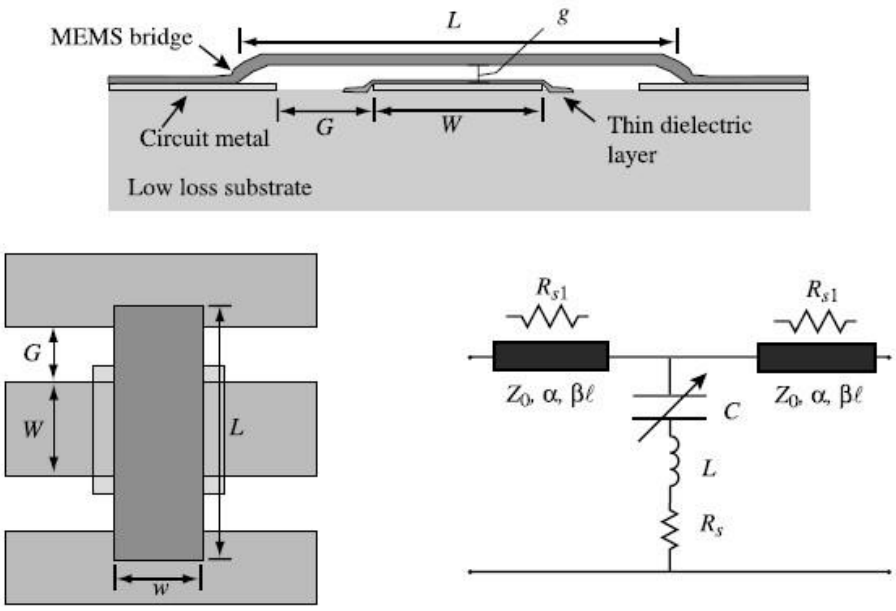

Figure 3.1- Demonstration of CPW Capacitive MEMS Shunt Switch (its Top as well as Side view) and its Equivalent Circuit Model [79]

3.3.2 DC Metal-to-Metal Contact Cantilever Beam Switches

The second type of switch is based on cantilever structure, named as metal contact cantiliver MEMS switch, which moves at one end in the downward direction and fixed at other end of the beam. The cantilever beam makes a metal contact with the transmission line as it moves in down direction in response of electrostatic actuation. When beam metal part connects the two ports of transmission line, switch is called in ON position, and when beam metal part disconnects the two ports of transmission line the switch is called in OFF position [87]. The presented MEMS resistive switches are different according to their beam shapes, and metal contact areas. The finite-element simulation solvers are used for the simulation, and analysis of switch performance. The advantage of choosing the thin micro-cantilever beam structure for

MEMS switch is its ease to calculate the pull-in voltage between top movable electrode and fixed bottom electrode. Its equivalent circuit model approximates as a parallel capacitor up in the air above a fixed bottom electrode by a perfect linear spring. Further in off/up-state condition of switch, the cantilever beam structure shows high impedance and avoids the requirement of continuous DC current. This ability makes it suitable candidate for low power dissipation microstrip RF circuit. The schematic and equivalent circuit of cantilever resistive MEMS switch is displayed in **figure 3.2**.

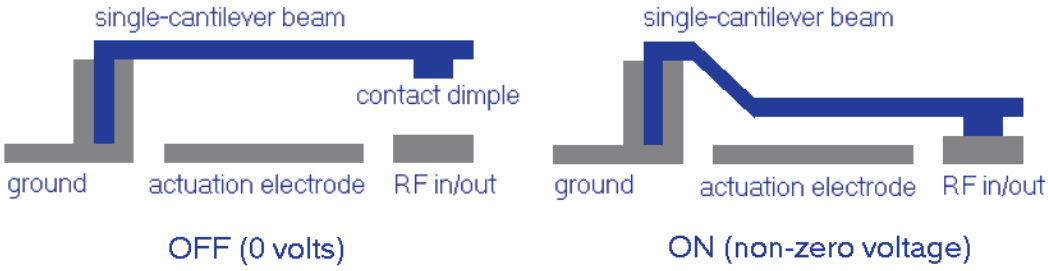

(a)

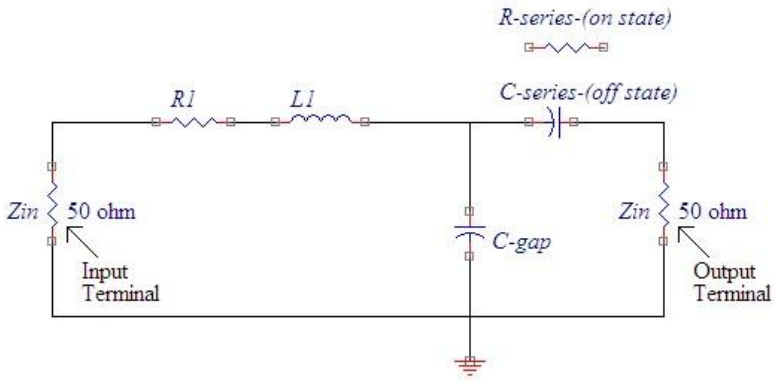

(b)

Figure 3.2- (a) Cantilever Beam MEMS Switch Schematic in Off- and On-positions (b) T-Equivalent Circuit Model

3.3.3 DC Shunt MEMS Switches

The third type of switch discussed here is DC metal contact shunt MEMS switch. The main difference between DC capacitive shunt and DC metal contact shunt switch is removal of nitride dielectric layer above the bottom pull-down electrode in case of later switch. So in down position of beam, there is a conductor-to-conductor contact between the ground plane and t-line [79]. It doesn't affect the electrostatic force on the RF MEMS. A distinct bottom electrode is

placed to pull down the upper bridge as shown in **figure 3.3**. The mathematical modeling and design construction of this switch in the up-configuration is similiar to capacitive MEMS switch, not including the dielectric thin layer uninvolved above the bottom elctrode with the help of borophosphosilicate glass (BPSG). In down position, it acts as a shunt R_sL equivalent circuit element with the t-line, wherever the notation R_s represents the addition of the bridge resistance and contact resistance.

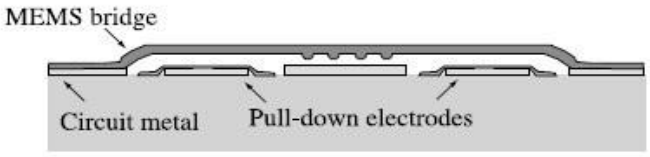

(a)

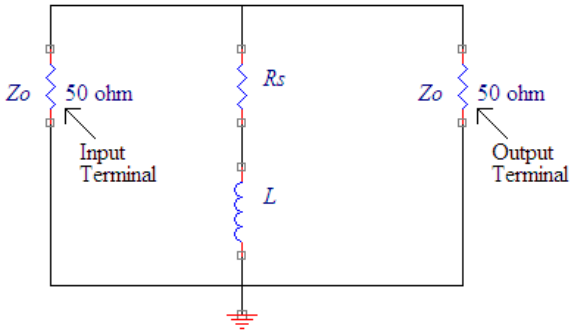

(b)

Figure 3.3- (a) DC Shunt Metal MEMS Switch Configuration with Pull-down Electrode (b) R_sL Shunt Equivalent Circuit

3.3.4 FBAR Cantilever Resistive Switches

The fourth type of switch is FBAR resistive cantilever beam based MEMS RF switch. The basic building block of such switch is FBAR, whose construction is shown in **figure 3.4 (a)**. These structures are initially opted to construct the filter circuits, which are configured to pass or reject some specific frequencies [92]. Later on, this technique is used to build as duplexer switch in wireless mobile communication to separate uplink and downlink frequency band [93]. An FBAR method is considered where strong resonance and narrow bandwidth is required. The construction includes a thin layer of piezoelectric i.e. aluminum nitride (AlN) wrapping an air gap opening designed on a silicon substrate. The principle of operation is defined by changing

the behavior of this piezoelectric layer. When RF signal is applied on device, it produces longitudinal mechanical vibrations and fundamental resonance is detected at condition that layer

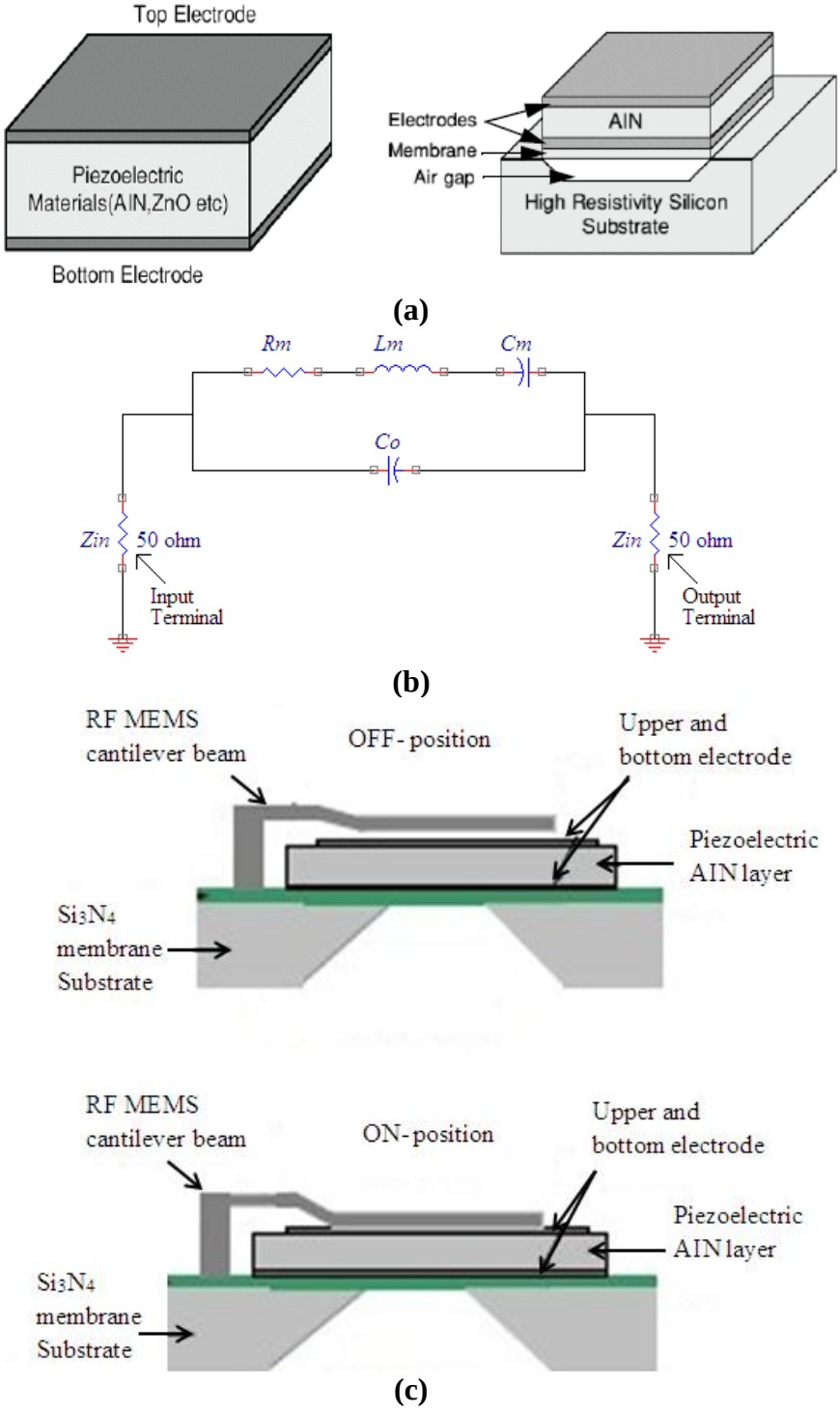

Figure 3.4- (a) Pictorial View of Piezoelectric FBAR Device (b) Butterworth-VanDyke Equivalent Circuit of FBAR (c) Cantilever FBAR Resistive Switch

thickness is $n\lambda/2$ of the signal. Here, 'n' is integral multiple constant and 'λ' is wavelength. At resonant frequency, there is severe alteration in electrical impedance and as a result the structure work as frequency selective filter [94,95].

The impedance equivalent circuit model of acoustic piezoelectric resonator can be characterized by circuit of Butterworth-VanDyke (BVD), as displayed in figure 3.4 (b). The different circuit components representing the FBAR have their usual meaning. The vibrating mass of the crystal is denoted by the motional inductance (L_m). The piezo-layer elastic properties are denoted by a motional capacitance (C_m), and the losses due to mechanical movement are denoted by a corresponding motional resistance (R_m). A static parallel plate capacitor is developed because of the surrounding electrodes on the surface of the piezo-layer and is represented stack capacitance (C_o) [95].

As aforementioned, by changing the thickness of the acoustic loading layer, the device can be operating at desired resonant frequency. Now the main challenge is to attain multi-band resonant frequency with the help of FBAR. It can be achieved by introducing the cascaded configuration of various FBAR structure in lattice or ladder form. For achieving dual band resonating structure the cantilever beam is introduced over basic FBAR design as shown in figure 3.4 (c). When the upper movable beam goes down, it will make a supplementary loading layer on the upper fixed conductor of the novel FBAR and in this way increases the total acoustic layer thickness. So, there is an additional layer of cantilever beam. In OFF-position, the acoustic layer thickness of the resonator is equal to the piezoelectric layer thickness in totaling to the thickness of the top and bottom electrodes. Therefore due to variation in thickness of layer in ON- and OFF- position, the RF MEMS switch operates at different resonant frequencies [92].

3.4 Modelling Action and Analysis of Various Proposed MEMS Switches

In next preceeding sections, five different MEMS switches structures are proposed. A thorough electrical and mechanical modeling as well as analysis of all five designed switches have been included based on multi-physics coventorware software. The extraction of switches main performance characteristics and the results are intuitionistic. This software is also used to know the association between material properties, actuated voltage and shape of the RF switch. Further, variation of displacement in switch i.e. from maximum z-direction to minimum z-

direction w.r.t. voltage is shown, when the switch is electrostatically actuated is also studied. The electromagnetic properties are studied by HFSS-Ansoft's software [30]. Further, the equivalent circuit model of proposed switches are generated and studied by means of Agilent based ADS software [31]. It also includes Momentum and 3D EM simulators which is based on both finite difference time domain (FDTD) and FEM solvers.

3.4.1 Analysis of Capacitive MEMS RF Switches

Under this section two different capacitive MEMS RF switches, named as, serpentine beam and fixed beam, are designed and mathematically analysed.

3.4.1.1 Serpentine Beam Capacitive MEMS Switch Analysis

The switch is designed on silicon (100) substrate of dimension 390 × 210 μm^2 having relative dielectric constant (ε_r) 11.9 and height of substrate is 1 mm which is covered with silicon nitrate of thickness 0.2 μm. The coplanar waveguide transmission line is made up of titanium (Ti) of thickness 0.5 μm. The trace width of CPW is 66.95 μm and the spacing between ground and centre conductor is 40 μm. By using equation 3.1 to 3.3, the characteristics impedance is calculated equal to 50 ohm and effective dielectric constant is 6.44. The complete 2-D and 3-D geometry with dimension and equivalent circuit in up and down state of switch is displayed in **figure 3.5 (a-d)**.

It is always desirable to use low spring constant of beam for low power consumption devices. There are numerous variants and shape of beams that can be prefered to bring down the value of actual spring constant (*k*) of RF MEMS switches. One of such shape is Serpentine flexure meander beam and its spring-constant calculation is given as [79]-

$$k \approx \frac{48\,GJ}{l_a^2\left(\frac{GJ}{EI_x}+l_b\right)n^3} \quad \text{for} \quad n \gg \frac{3l_b}{\frac{GJ}{EI_x}l_a+l_b} \tag{3.5}$$

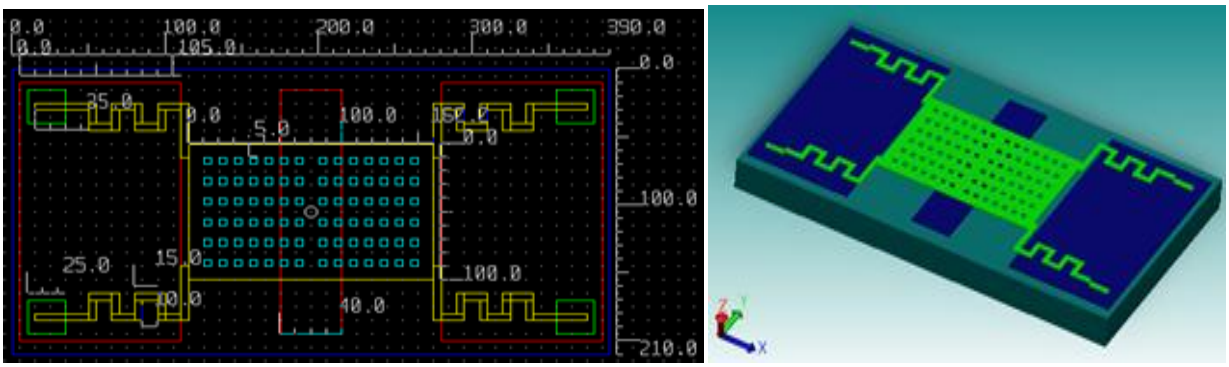

(a) **(b)**

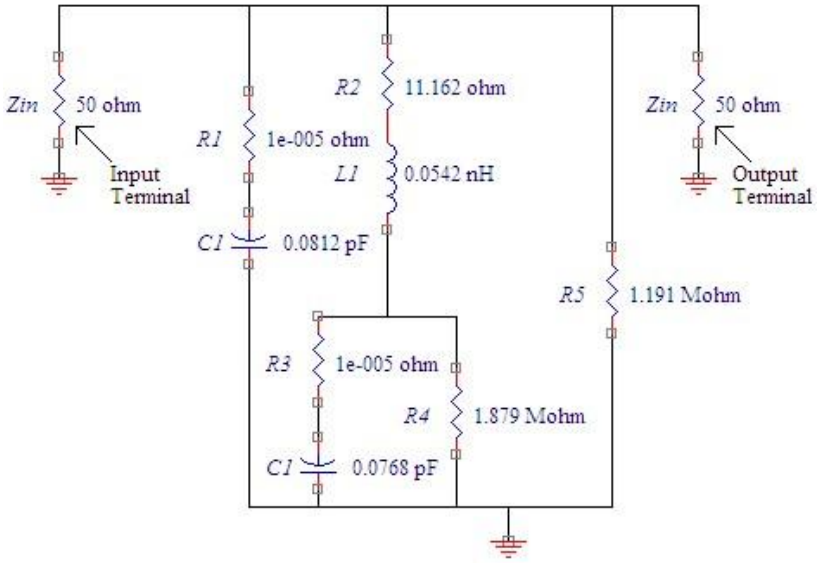

(c)

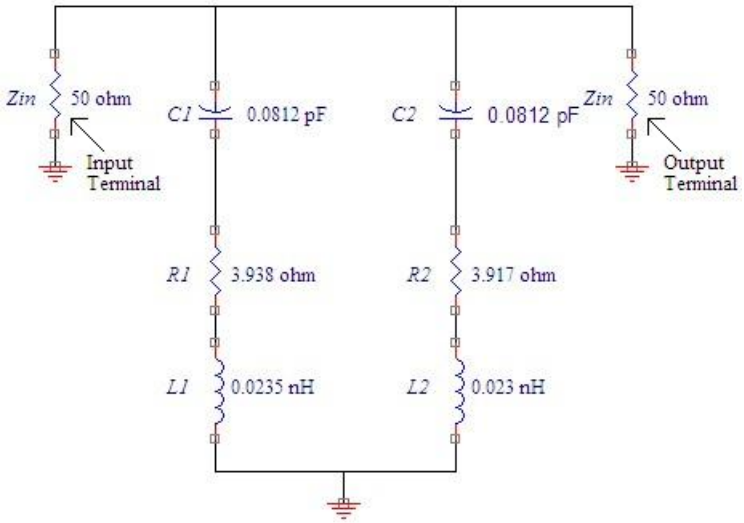

(d)

Figure 3.5- (a, b) 2D and 3D Layout of DC Shunt Capacitive MEMS Switch (c, d) Equivalent Circuit in Up- and Down-position

where '*n*' is amount of meanders used in the designed serpentine beam flexure, $G = {}^{E}/_{2(1+v)}$ reperesent torsion modulus, $I_x = {}^{wt^3}/_{12}$ denotes moment of inertia, l_a, l_b and w are primary length, secondary length and width of the meander, E is the elasticity, v belongs to Poisson's ratio and the torsion constant is specified by,

$$J = \frac{1}{3}t^3 w\left(1 - \frac{192}{\Pi^5}\frac{t}{w}\sum_{i=1,odd}^{\infty}\frac{1}{i^5}\,tanh\left(\frac{i\Pi w}{2t}\right)\right) \tag{3.6}$$

For the situation where $l_a \gg l_b$, the spring constant of the serpentine flexure turn out to be-

$$k \approx 4Ew\left({}^{t}/_{(nl_a)^3}\right) \tag{3.7}$$

The characteristics of various material are summarized in **table 3.1**.

Table 3.1: Material Properties [29]

Materials	**Young's Modulus E (GPa)**	**Poisson Ratio, ν**	**Electrical Conductivity (Sm^{-1})**
Gold (Au)	57	0.35	45.16×10^6
Copper (Cu)	128	0.36	59.6×10^6
Nickel (Ni)	180	0.31	14.4×10^6
Aluminum (Al)	77	0.30	37.8×10^6
Chromium (Cr)	140	0.30	7.75×10^6
Titanium (Ti)	110	0.33	2.56×10^6
Tungsten (T)	410	0.27	18.4×10^6

The aforementioned equations do not consider the effect of the residual stress. As low spring constant membrane has small restoring force, it becomes extremely delicate to stiction due

to contaminants and moisture. It is worth to note that residual stress plays a major role for estimating the low spring constant and is therefore the best analysed by multi-physics coventorware software. For proposed switch, the dimension and material properties are taken as l_a = 15 µm, l_b = 10 µm, w = 5 µm, t = 0.5 µm, n = 2, G = 57 GPa and v = 0.35 for calculation of k. By using equation (3.5) and (3.6), the spring constant of proposed switch for gold beam is calculated as 3.59 N/m. Small sized holes are introduced in the upper beam electrode to improve the switching mechanism, reduce the squeeze film damping and lowering the mass of beam. The electrostatic actuation or corresponding pull-in voltage may be decreased by declining the k of beam, minimizing the air gap, and increasing the actuation area.

When the external electrostatic voltage is applied on the actuation pad, an electrostatic resultant force is generated on the switch beam. The reaction force (F) balance the generated electrostatic force produced in beam structure. At two-third air gap, the switch beam becomes unstable and breakdown the lower transmission line in down-state position [80, 89, 96]. The pull-in voltage is influenced by the value of spring constant of beam shape; gap and electrode area. The requirement for low pull-in voltage in MEMS RF switches has frequently caused too much design and fabrication complexity and also rise in the dimensions of the product. The pull-in or pull-down voltage is defined as [80]-

$$V_{pull-down} = V_{p-in} = V\left(\frac{2g_0}{3}\right) = \sqrt{\frac{8k}{27_0 Ww}g_o^3} = \sqrt{\frac{8k}{27_0 A}g_o^3} \qquad (3.8)$$

where W is denoted width of upper beam, A is the electrode area, g_0 is the air gap and ε_0 = 8.854×10^{-12} Fm^{-1} is defined permittivity of the free space. The pull-in voltage calculated at g_0 = 0.32 µm and A = 100 × 66.95 μm^2 is 0.69 V. **Figure 3.6** presents the simulated results of minimum displacement of upper beam electrode in z-direction i.e. towards the fixed lower electrode. The pull-in voltage measured at 0.67 V, which is very close to mathematically analysed voltage. The magnitude of total displacement covered by upper electrode is 0.164 µm from ideal up-position to touching down-position. The 1 V voltage is applied on beam with respect to ground and charge value noticed at this voltage is 0.311 pC. The development of multilayer design and accumulation of a conducting layer keen on the process movement permitted a excessive rise of the RF switch on- position capacitances. Further, the **table 3.2** shows the capacitance matrix between various part of switch.

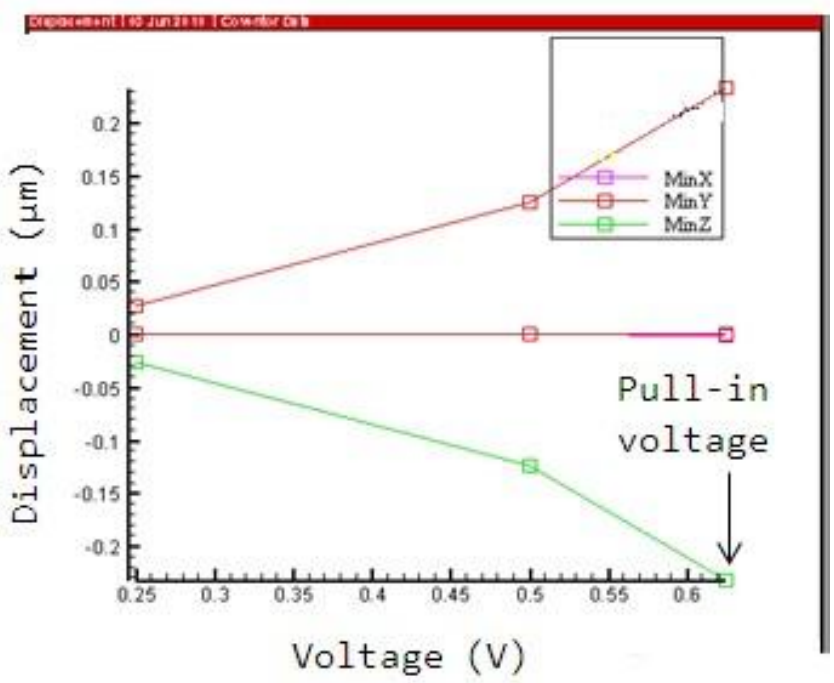

Figure 3.6- Simulated Results of Normalized Gap Height/ Displacement (in z-direction) versus Applied Voltage (Pull-in Voltage Characteristics)

Table-3.2: Capacitance Matrix (pF) of Proposed Serpentine Beam MEMS RF Switch

	Ground	**Beam**	**Wgnd1**	**Wgnd2**	**Conductor**
Ground	1.979	-7.739×10^{-2}	-8.110×10^{-1}	-8.109×10^{-1}	-2.801×10^{-1}
Beam	-7.739×10^{-2}	3.110×10^{-1}	-9.949×10^{-2}	-1.017×10^{-1}	-3.233×10^{-2}
Wgnd1	-8.110×10^{-1}	9.949×10^{-2}	9.106×10^{-1}	-8.968×10^{-5}	-2.933×10^{-5}
Wgnd2	-8.109×10^{-1}	-1.017×10^{-1}	-8.968×10^{-5}	9.128×10^{-1}	-2.931×10^{-5}
Conductor	-2.801×10^{-1}	-3.233×10^{-2}	-2.933×10^{-5}	-2.931×10^{-5}	3.125×10^{-1}

The reaction forces that developed at the fixed ends is a result of pressure load exerted in downward direction. **Table 3.3** shows the vector components in x-, y-, and z- directions of force on four anchors.

Table-3.3: Vector Components of Force (in N/m^2) on Four Anchors of Designed Switch

	F_x	F_y	F_z
Anchor 1	-2.556×10^1	5.611	4.337
Anchor 2	-2.556×10^1	-5.611	4.337
Anchor 3	2.556×10^1	5.611	4.337
Anchor 4	2.556×10^1	-5.611	4.337

The occurrence of natural vibration at some specific frequencies results in the existence of modal shapes. Such vibrating response assumes the properties of physical system. At equilibrium, the resonant frequencies of MEMS upper electrode is calculated. The different mode shapes (as shown in **figure 3.7**) and their concern frequencies very much resemble the characteristics of under-damped response.

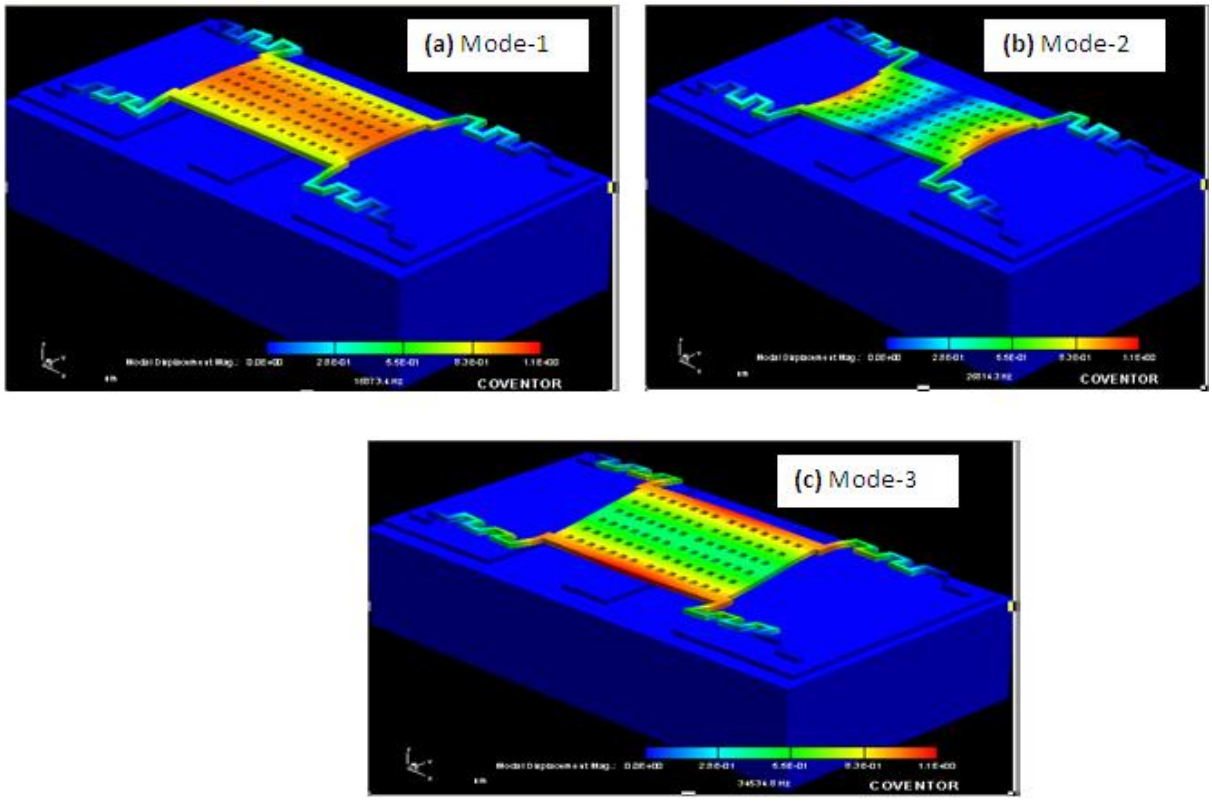

Figure 3.7- Vibrational Modes (1 to 3) Generated in Coventorware Software

3.4.1.2 Fixed Beam Capacitive MEMS Switch Analysis

Table 3.4 demonstrates the processing steps of fixed beam capacitive MEMS RF switch. The MEMS switch is considered on silicon material (100) of dimension 280 × 150 μm^2, relative dielectric constant 11.9, and thickness is equal to 10.0 µm which is enclosed with silicon nitrate of thickness 0.2 µm. The microstrip t-line are made up of titanium (Ti) of thickness 0.5µm and complete geometry of switch with dimension and lumped equivalent circuit (in down state) is shown in **figures 3.8 (a-d)**. The spring constant is calculated from mathematical equation given in [79] and is equal to 6.14 N/m. The value of k is calculated by taking thickness of beam (t) is equal to 0.5 µm, width of beam (w) is 85 µm, length of the beam (l) is 260 µm, elasticity of gold beam (E) is 57 GPa, Poisson ratio (v) of gold beam is 0.35, and residual stress (σ) is 10 MPa.

Table 3.4: Processing Steps of Fixed Beam Capacitive MEMS Switch

Sr. No.	Step Name	Layer Name	Material Name	Thickness (µm)	Mask Name	Photoresist
1.	Substrate	Substrate	Silicon (100)	10	Ground	
2.	Stack Material	Nitride	Silicon Nitride (SIN)	0.2		
3.	Planar Fill	Waveguide	Titanium	0.5		
4.	Straight Cut				Wave-guide	+
5.	Planar Fill	Sacrifical	BPSG	1.0		
6.	Straight Cut				Anchor	-
7.	Conformal Shell	Beam	Gold	0.5		
8.	Straight Cut				Beam	+
9.	Straight Cut				Holes	-
10.	Sacrifice		BPSG			

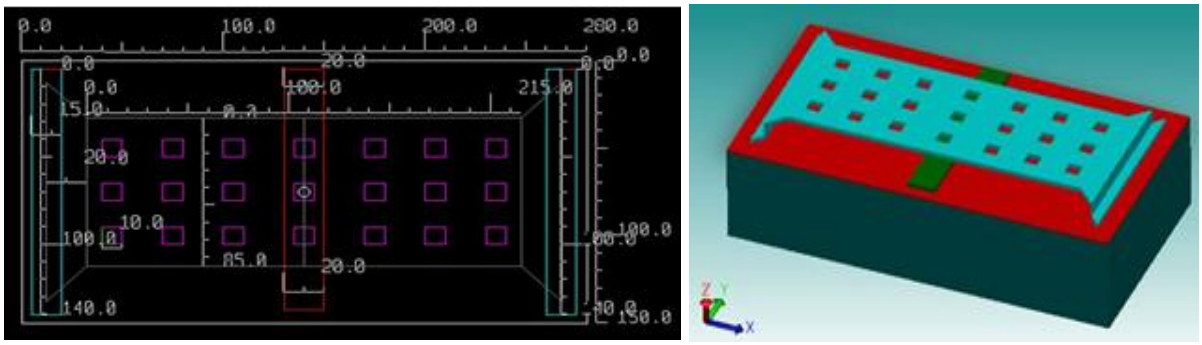

(a) **(b)**

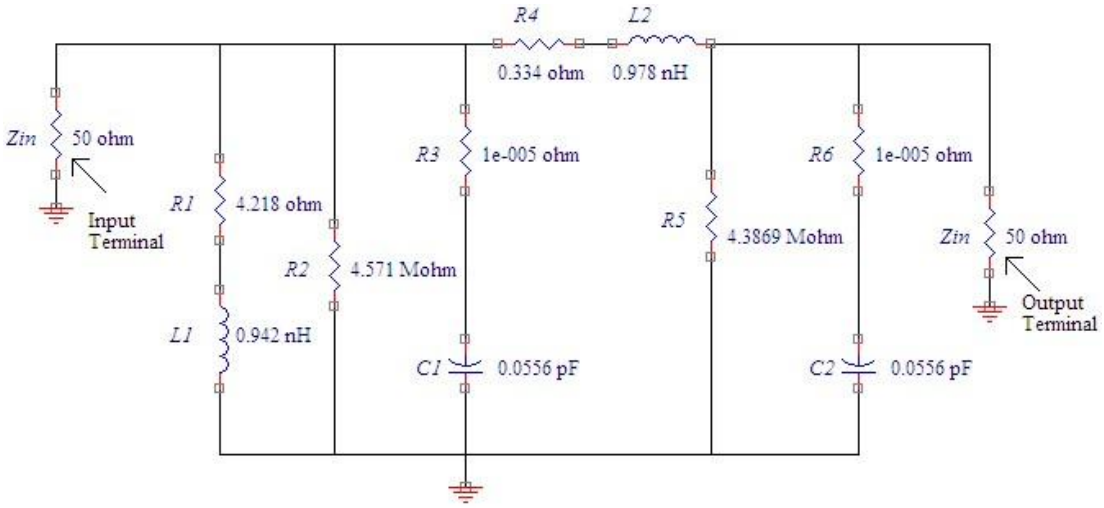

(c)

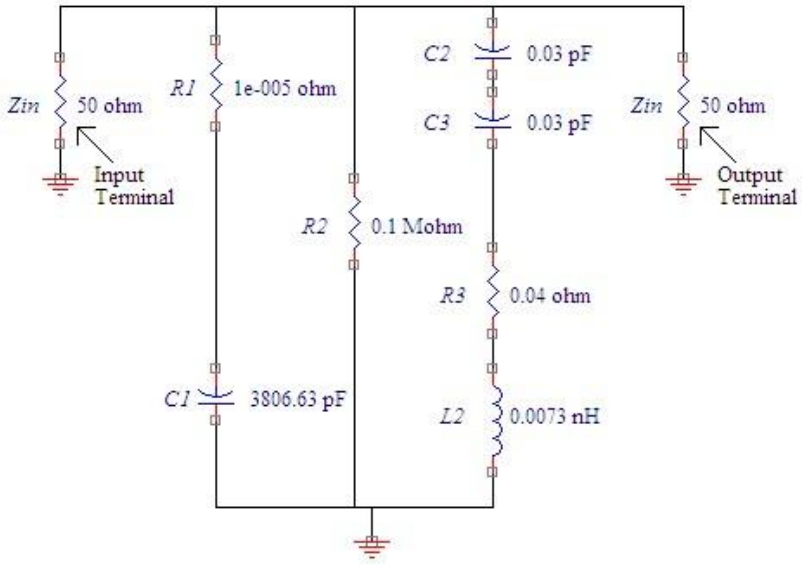

(d)

Figure 3.8- (a) 2-D layout with Dimension (b) 3-D layout of Fixed Beam Capacitive Switch and its Equivalent Circuit in (c) Up- and (d) Down- state

Table 3.5: Capacitance Matrix (pF) of Fixed Beam MEMS RF Switch

	Ground	CPW	Beam
Ground	2.933×10^{-1}	-1.226×10^{-1}	-1.707×10^{-1}
CPW	-1.226×10^{-1}	1.373×10^{-1}	-1.466×10^{-2}
Beam	-1.707×10^{-1}	-1.466×10^{-2}	1.853×10^{-1}

Table-3.6: Vector Components of Force (in N/m^2) on Two Anchors of Fixed Beam Switch

	F_x	F_y	F_z
Anchor 1	2.219×10^{-1}	2.585×10^{-1}	9.358
Anchor 2	-2.219×10^{2}	-2.590×10^{-1}	9.363

Table 3.5 and **Table 3.6** illustrate the capacitance matrix between various part of switch and vector components of force in x-, y-, and z- directions on two anchors. The six different mode shapes (as shown in **figure 3.9**) and their related frequencies are considerably be like the characteristics of under-damped response. The pull-in voltage analysed using coventorware simulator for fixed beam MEMS switch is found to be 3.22 V, as made known in figure **3.10,** which represents the minimum displacement of the upper electrode in z-direction i.e. in the direction of the fixed lower electrode.

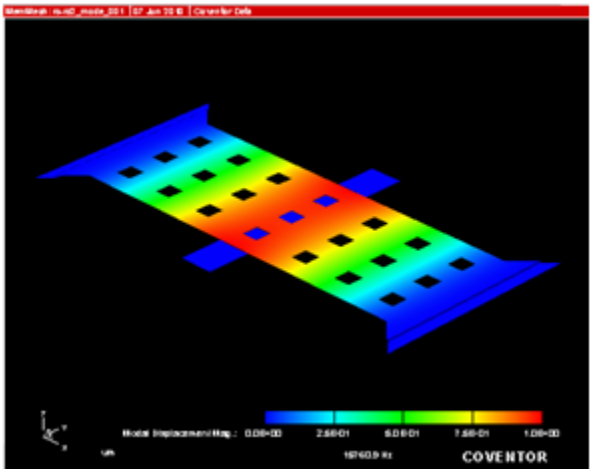

(a)

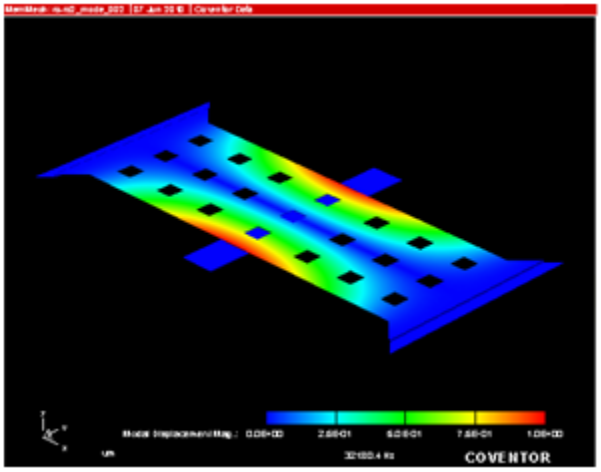

(b)

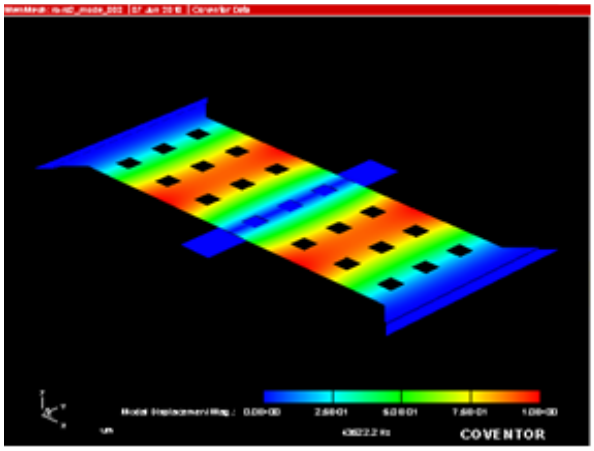

(c)

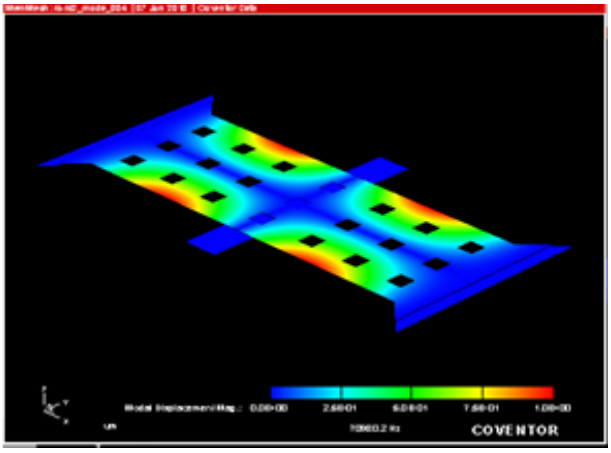

(d)

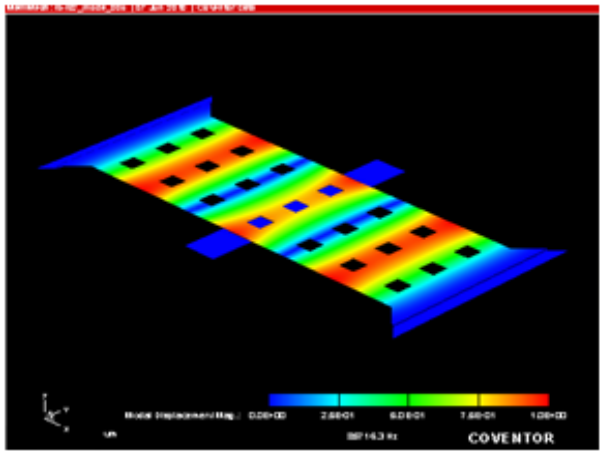

(e)

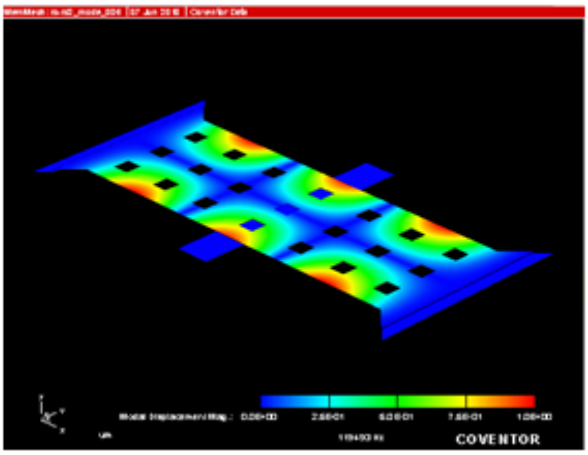

(f)

Figure 3.9- Harmonic Generation of Fixed Beam MEMS RF Switch (a) - (f) Demonstrations of Operational Six Modes

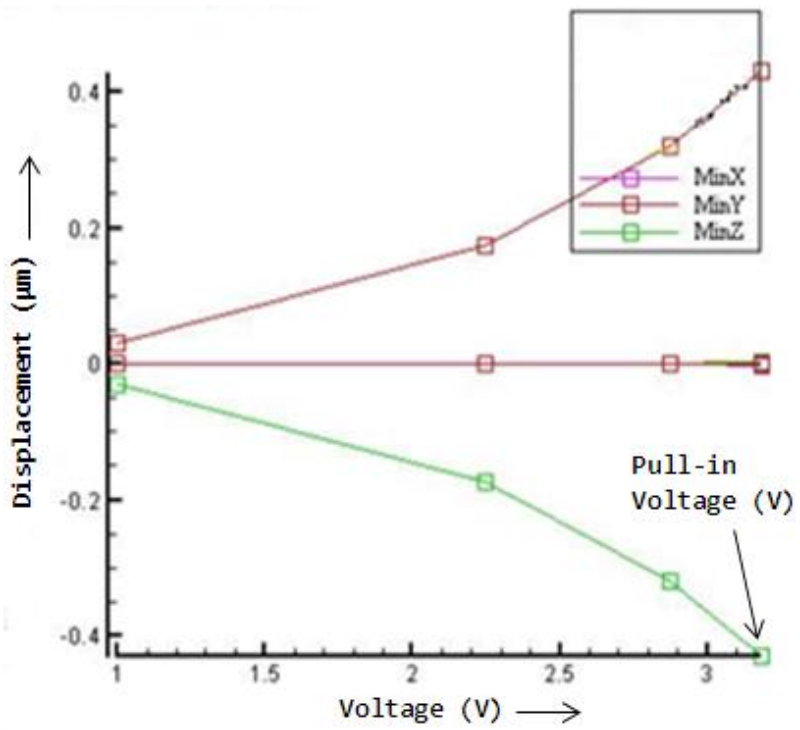

Figure 3.10- Displacement (in z-direction)/Normalized Gap Height versus Applied Voltage (Pull-in Voltage Characteristics) of Fixed Beam Switch

3.4.1.2.1 Equivalent Circuit Analysis and its Effect on S-parameters

The circuit model of MEMS switch is used to extract the *C*, *R* and *L* parameters, where *C* is the capacitance of bridge in up and down state, *R* is the beam resistance and *L* is the inductance. Here the actual equivalent circuit of proposed design structure of **figure 3.5 (a, b)** and **figure 3.8 (a, b)** is generated by using HSPICE model file. The HSPICE file from HFSS is exported to ADS software to validate the results through equivalent circuit and layout approach. The bridge is represented by the two short segments of transmission line as well as a lumped LCR circuit of the designed bridge having a different up- also down-position capacitance value [97]. The bridge capacitance in down state is due to the bridge-dielectric and transmission line active overlapping area. Further, up-state is due to the active overlapping area between the beam and the conductor. The up-state capacitance (C_{up}) is always less than the down-position capacitance (C_{down}). This effect is owing to the collapse of MEMS upper electrode/bridge on the dielectric surface, while an electrostatic actuation is introduced between the transmission line and the switch bridge. The equivalent generated electrostatic force causes large increase in the

switch beam capacitance. The LCR model of shunt capacitive MEMS switch behaves as an inductor above the series resonant frequency, as a capacitor below the resonant frequency and behaves as a series resistance at resonance. Further, in up-position of switch, the inductance plays no role and only shunt capacitance has a major role to define/model the MEMS bridge. Further, it is observed in down-position of the MEMS bridge, the inductance plays a significant role.

For the proposed fixed beam MEMS switch, the resonant frequency occurs at 22 GHz for C_{up} = 0.0556 pF and L_{up} = 0.942 nH, when it is in on-position. For C_{down} = 3806.63 pF and L_{down} = 0.0073 nH, the switch resonate at 1 GHz frequency when the MEMS bridge is in down or off position. According to these circuit values in on-condition, the IL measured is 0.34 dB at 4 GHz and 0.98 dB at 8 GHz. The values of isolation are 67.6 dB at 4.0 GHz and 73.6 dB at 8 GHz in off-condition. The EM parameters are optimized by varying the shunt inductance and capacitance values. Except the characteristics impedance (Z_0 = 50 ohm), other circuit values are permitted to vary the isolation and IL results calculations. It has been observed that by decreasing the C_{up} from 0.0556 pF to 55.6 fF and by increasing L_{up} from 0.942 nH to 58.84 nH, the insertion loss improves to 0.22 dB at 4 GHz and 0.61 dB at 8 GHz, respectively. The effect on insertion loss by varying up-state shunt inductor at fix value of series inductor and capacitor is displayed in **figure 3.11**. Further, the effect on IL and RL by keeping both inductor constant and by varying both capacitor is shown in **figure 3.12**. The best EM results are noticed at C1 = C2 = 55.6 fF. Additionally, by varying the series inductance and by keeping other lumped values constant, the optimized EM outcomes are observed at L2 = 97.8 pH, as shown in **figure 3.13**.

Similarly, in down position the optimized isolation of 87.68 dB at 4 GHz and 93.59 dB at 8 GHz has been achieved, by increasing L_{down} from 0.0073 nH to 73 pH and at the same time by increasing C_{down} from 3806.63 pF to 38.06 nF. By changing the shunt capacitance and by keeping other lumped values constant, the optimized isolation and RL are observed at C1 = 380 nF, as shown in **figure 3.14**. For these optimized circuit elements, the switch resonates at 3.94 GHz and 0.95 GHz in on- and off-condition, respectively.

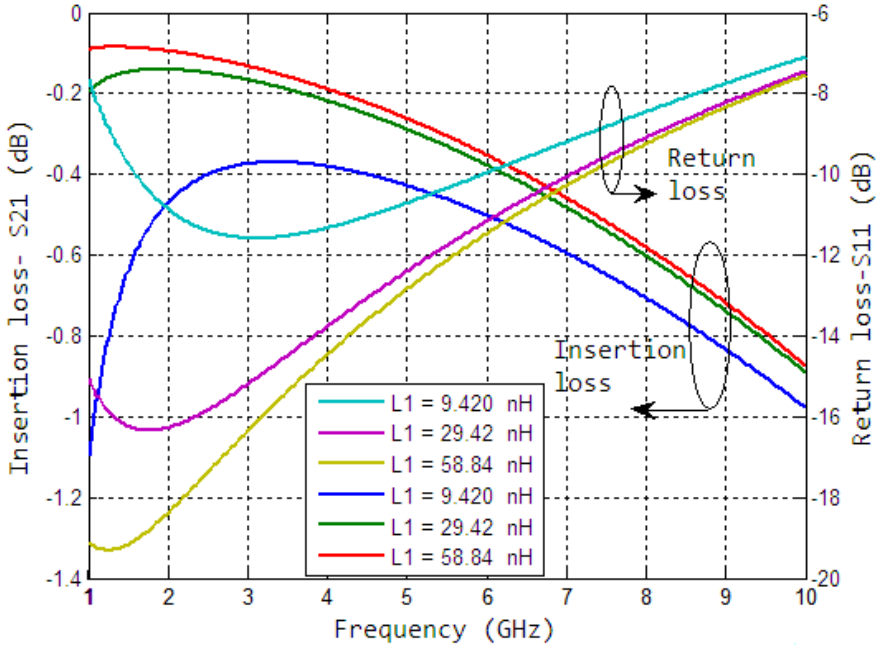

Figure 3.11- Simulation Outcomes of *S*-parameters using Different Shunt Inductance *L1* at the ON-position of the Proposed Switch (*L2* = 0.978 nH, *C1* = *C2* = 55.6 fF)

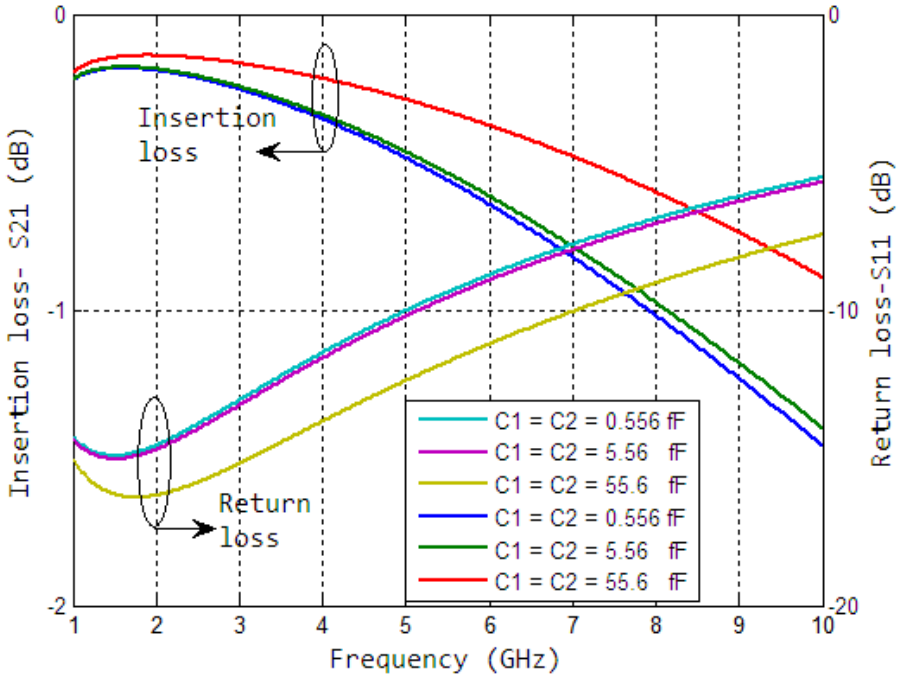

Figure 3.12- *S*-parameters Results with Various Shunt Capacitances *C1* and *C2* at the ON-position of the Proposed Switch (*L1* = 29.42 nH, *L2* = 0.978 nH)

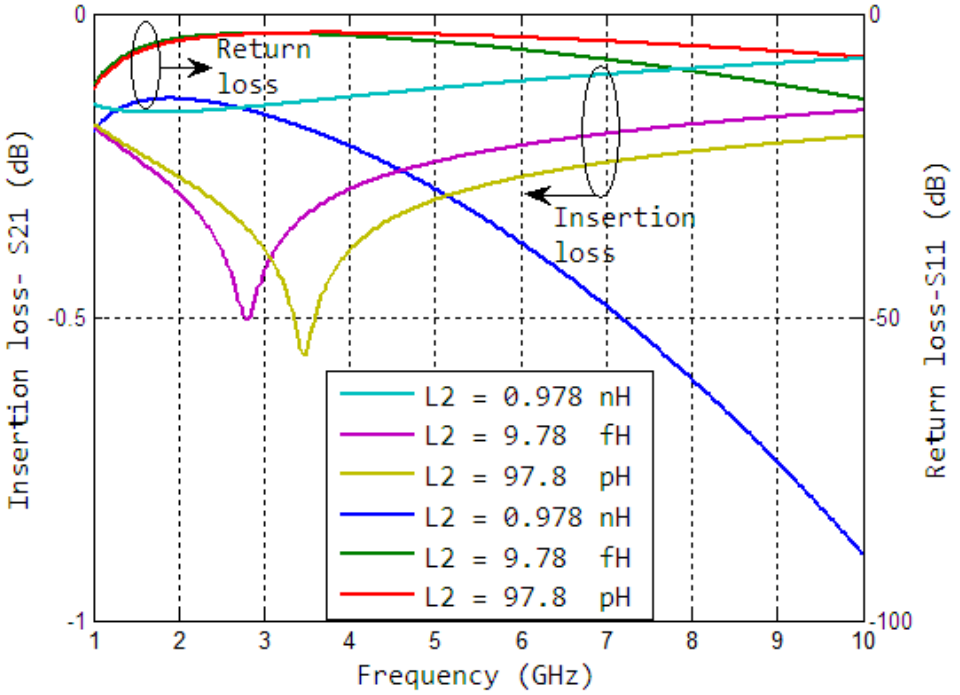

Figure 3.13- *S*-parameters Results with Various Series Inductances *L2* at the ON-position of the Proposed Switch (*L1* = 29.42 nH, *C1* = *C2* = 55.6 fF)

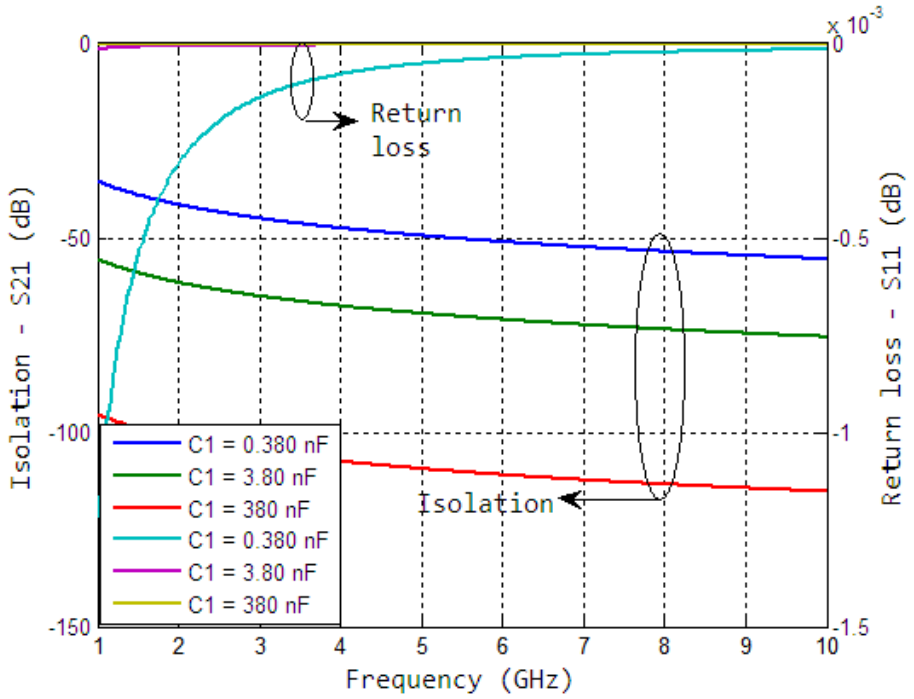

Figure 3.14- *S*-parameters Results with Various Shunt Capactiances *C1* at the OFF-position of the Proposed Switch (*L2* = 0.73 pH)

Further, the simulated up state capacitance and isolation results are verified from the following equations [80],

$$|S_{11}|^2 \cong \frac{w^2 C_{up}^2 Z_o^2}{4} \tag{3.9}$$

and

$$|S_{21}|^2 \cong \begin{cases} \left(\frac{2R_s}{Z_o}\right)^2 & for\ wL \ll R_s \\ \left(\frac{2\sqrt{2}R_s}{Z_o}\right)^2 & for\ wL = R_s \\ \left(\frac{2wL}{Z_o}\right)^2 & for\ wL \gg R_s \end{cases} \tag{3.10}$$

Here, w- Angular resonating frequency, Z_o- Charateristics impedance, C_{up}- Up state capactiance.

3.4.2 Analysis of Shunt MEMS RF Switch

The shunt MEMS switch is designed on silicon (100) substrate of dimension 336 × 192 μm^2 having relative dielectric constant 11.9 and height of substrate is 1.0 mm which is covered with silicon nitrate of thickness 0.2 μm. The coplanar waveguide transmission line are made up of titanium (Ti) of thickness 0.5 μm. The trace width of CPW is 66.95 μm and the spacing between ground and centre conductor is 40 μm. By using equation 3.1 to 3.3, the characteristics impedance is calculated and equals to 50 ohm and effective dielectric constant is 6.44. The complete 2-D and 3-D geometry with dimension and equivalent circuit in up and down state of switch is displayed in **figure 3.15 (a-d)**.

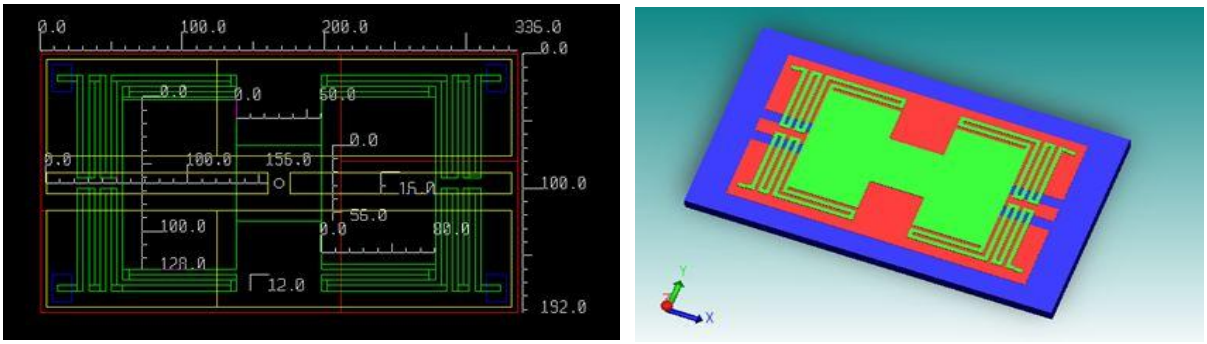

(a) **(b)**

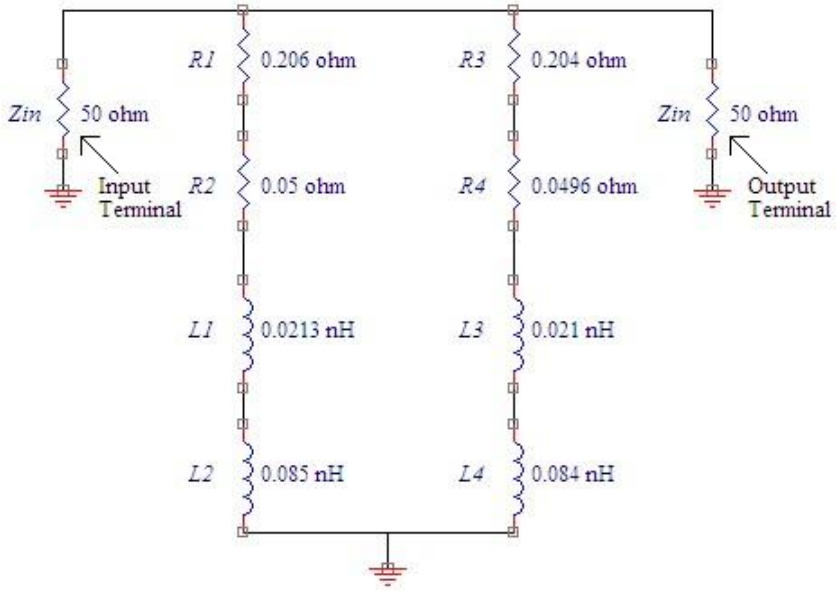

(c)

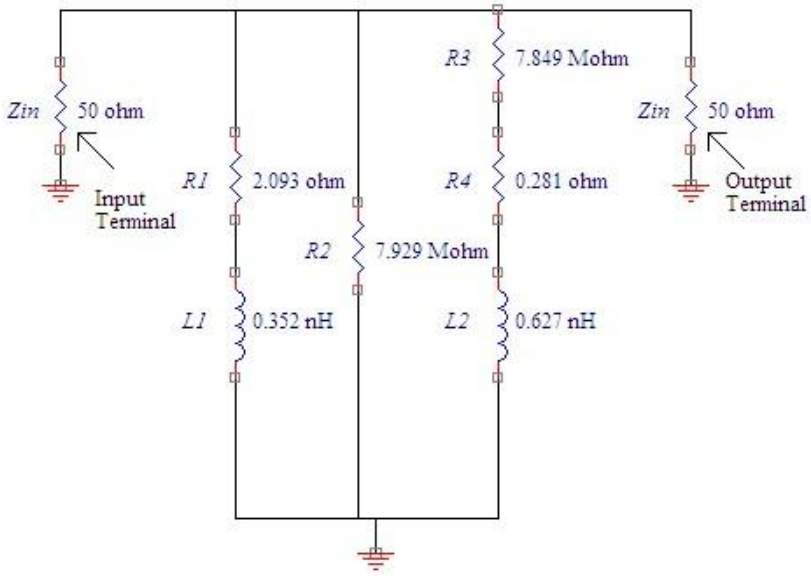

(d)

Figure 3.15- (a, b) 2D and 3D Layout of DC Shunt MEMS Switch (c, d) Equivalent Circuit in Down- and Up- position

Table-3.7: Capacitance Matrix (pF) of MEMS Shunt Switch

	Ground	Wgnd1	Wcon1	Wgnd2	Wcon2	Beam
Ground	2.265	-1.015	-9.926×10^{-2}	-1.014×10^{-1}	-9.925×10^{-1}	-3.705×10^{-2}
Wgnd1	-1.015	1.161	-6.908×10^{-5}	-2.707×10^{-5}	-9.193×10^{-5}	-1.457×10^{-1}
Wcon1	-9.926×10^{-2}	-6.908×10^{-5}	1.126×10^{-1}	-1.076×10^{-4}	-4.404×10^{-7}	-1.319×10^{-2}
Wgnd2	-1.014×10^{-1}	-2.707×10^{-5}	-1.076×10^{-4}	1.160	-9.458×10^{-5}	-1.456×10^{-1}
Wcon2	-9.925×10^{-1}	-9.193×10^{-5}	-4.404×10^{-7}	-8.458×10^{-5}	1.126×10^{-1}	-1.319×10^{-2}
Beam	3.705×10^{-2}	-1.457×10^{-1}	-1.319×10^{-2}	-1.456×10^{-1}	-1.319×10^{-2}	3.547×10^{-1}

For the proposed switch, the dimension and material properties are taken as l_a = 12 µm, l_b = 80 µm, t = 0.5 µm, w = 5 µm, n = 4, G = 57 GPa and v = 0.35 for calculation of k. Torsion modulus and torsion constant are computed from aforementioned equations and their values are 21.1 GPa and 20.14×10^{-26}, respectively. By using equation (3.5) and (3.6), the spring constant of proposed switch for gold beam is calculated as 0.228 N/m. The pull-in voltage calculated at g_0 = 3.15 µm and A = 40 × 28 µm^2 is 22.48 V. **Figure 3.16** represents the simulated results of minimum displacement of upper beam electrode in z-direction i.e. towards the fixed lower electrode. The pull-in voltage measured is 22.86 V, which is very close to mathematically analysed voltage. The voltage on beam applied is 1 V with respect to ground and charge value noticed at this voltage is 0.311 pC. The up-state capacitance calculaled is equal to the 13.19 fF. Further, the **table 3.7** and **table 3.8** shows the capacitance matrix between various part of switch and vector components of force in x-, y-, and z- directions on four anchor.

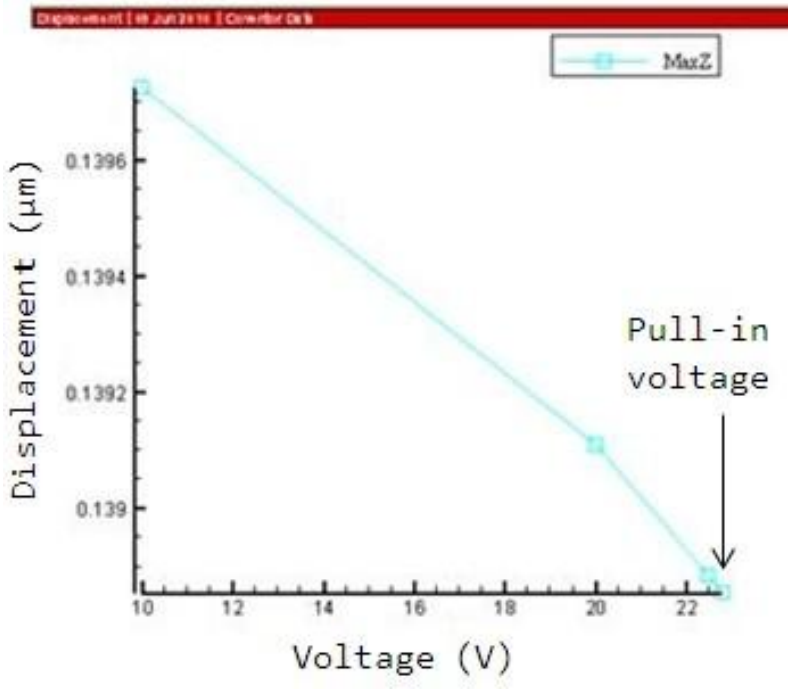

Figure 3.16- Simulated Results of Displacement (in z-direction) versus Applied Voltage (Pull-in Voltage Characteristics)

Table-3.8: Vector Components of Force (in N/m^2) on Four Anchors of MEMS Shunt Switch

	F_x	F_y	F_z
Anchor 1	5.567	2.225	7.668
Anchor 2	5.567	-2.225	7.668
Anchor 3	-5.567	2.225	7.668
Anchor 4	-5.567	-2.225	7.668

3.4.2.1 Circuit Model Analysis of Shunt Switch and its Electromagnetic Study

The DC-contact MEMS shunt switch designing steps are the same in up-position as that of capactive shunt MEMS except that the silicon nitride film is removed below the metal bridge. The CPW transmission line sepration is provided. As a result, there is a contact of metal to metal layer among the transmission line and the ground surface. In the down-position of these two DC

contact shunt MEMS switches result in an $R_{Sh}L_{down}$ equivalent circuit in parallel using the transmission line. Shunt resistance (R_{Sh}) is the addition of the metal bridge resistance as well as the contact resistance. The RLC parameters extraction of both switches monitors the same method as per capacitive shunt MEMS switch. The isolation value in the down-state of shunt MEMS switch can be optimized up to 45.9 dB at 4 GHz and 45.8 dB at 8 GHz by decreasing the shunt inductance from 0.0123 nH to 12.3 pH, as shown in **figure 3.17**. Additionally, up-position results show that by increasing inductance from 0.352nH to 3.5 nH, the IL 0.378 dB at 4 GHz also 0.10 dB at 8 GHz can be achieved, as shown in **figure 3.18**.

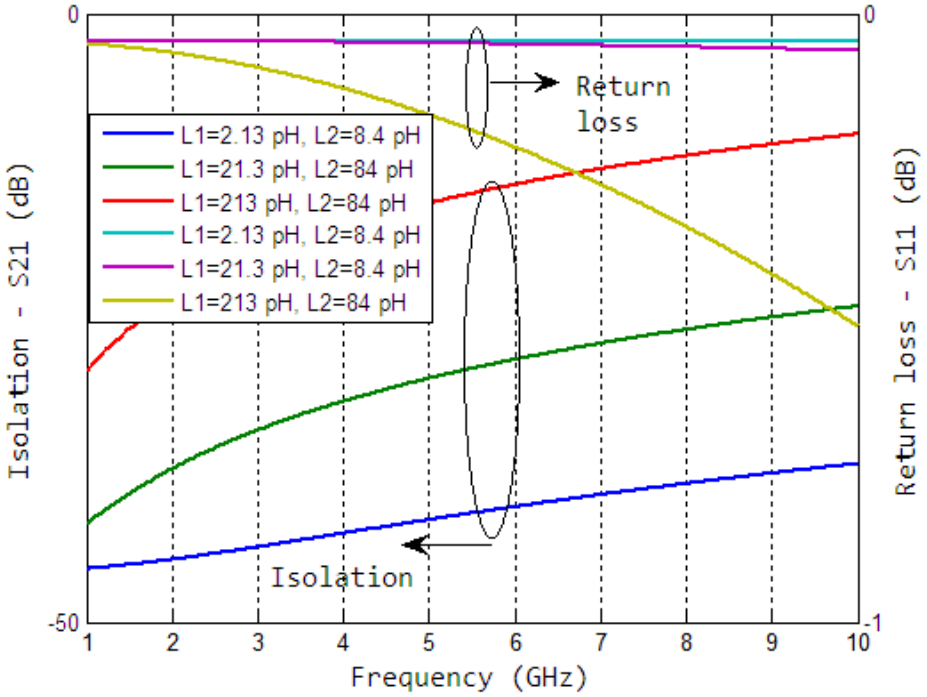

Figure 3.17- Simulation Outcomes of *S*-parameters using Different Shunt Inductance *L1* at the OFF-position of the Proposed Switch

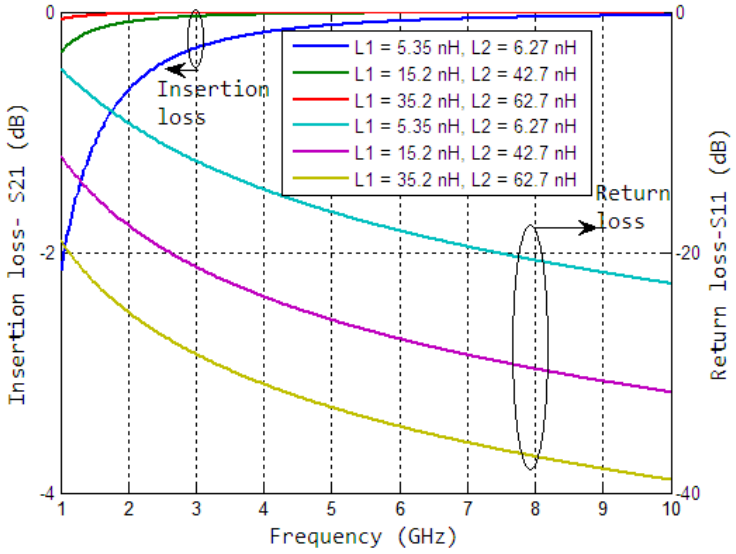

Figure 3.18- Simulation Outcomes of *S*-parameters using Different Shunt Inductances *L1* and *L2* at the ON-position of the Desgined Switch

3.4.3 Analysis of Series Cantilever MEMS RF Switches

Figure 3.19 shows 3-D view of the metal-contact RF MEMS switch implemented on silicon substrate of area 272 × 118 μm^2 and thickness 48 μm. The cantilever beam is made of gold and silicon nitrate of thickness 0.2 μm. A 0.5 μm thick dimple is used to make metal to metal contact, and to separate the cantilever beam from actuation pad in down-position. The spring constant calculated from [79] for gold beam is given as 5.0 N/m.

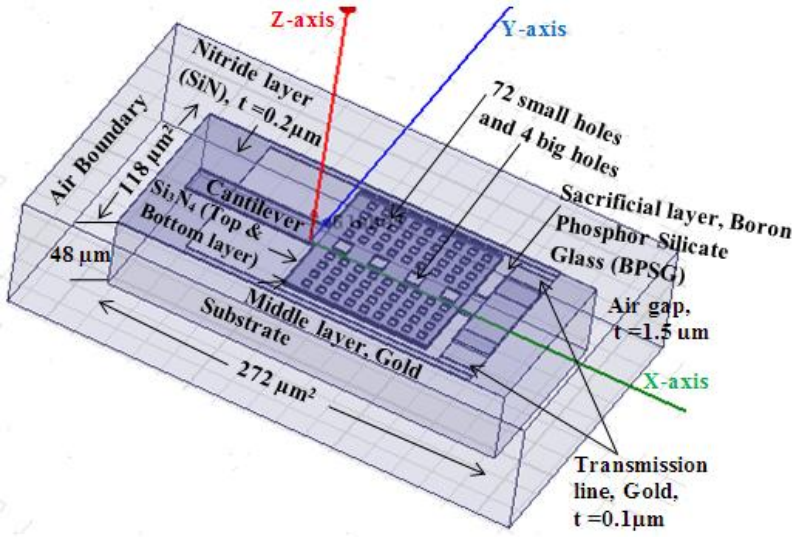

Figure 3.19- 3-D Layout of Metal-contact MEMS Switch (in Coventorware Software)

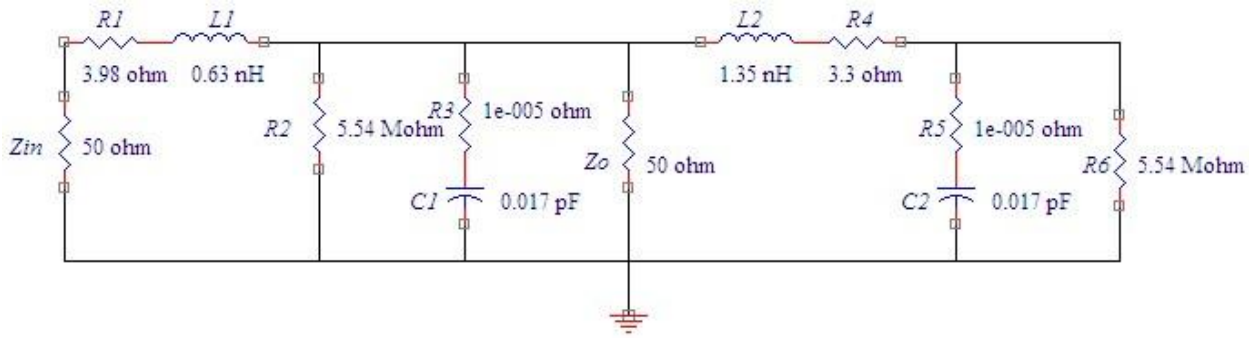

(a)

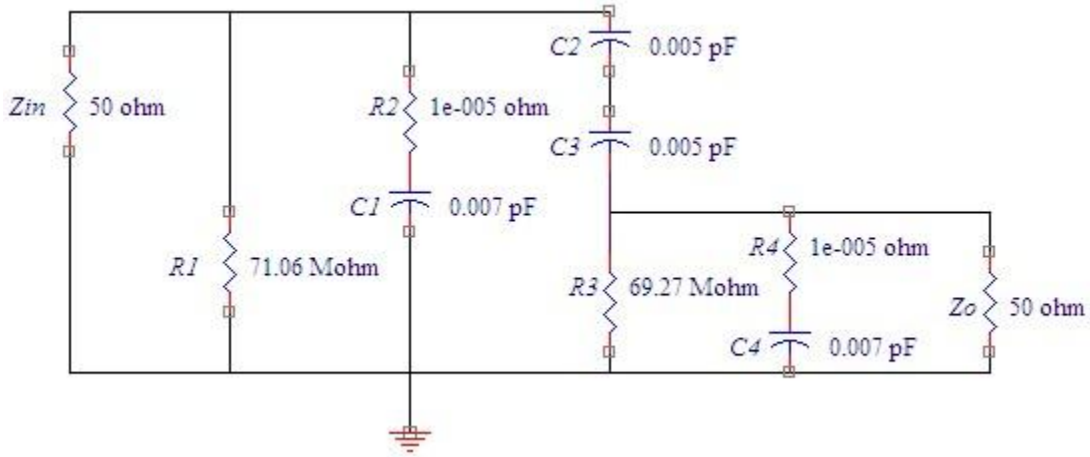

(b)

Figure 3.20- Equivalent R-L-C Circuit of Metal-contact MEMS Switch in (a) On-position (b) Off-position

There are a number of circuit elements which represent the physical part of the proposed cantilever beam MEMS switch [12], **figure 3.20**. Here in **figure 3.20 (a)**, *R1* = 3.98 ohm, represent a value of line resistor; *L1* = 0.63 nH, a value of line inductor of the cantilever beam. Further, *R4* = 3.3 ohm, contact resistance value; *L2* = 1.35 nH, contact inductance value; and *C1* = *C2* = 0.017 pF, the shunt coupling capacitance value. The rest of the shunt resistors (*R2* = 5.54 ohm, *R3* = 1e-005 ohm, *R6* = 5.54 ohm and *R5* = 1e-005 ohm), represent the losses effect due to the holes, at higher frequencies. In off-state position of the switch (as shown in **figure 3.20 (b)**), *C4* = 0.007 pF, represents a series switch capacitance value. After solving equivalent circuit with the help of matlab software, at a given solution frequency, the impedance in ON position is equal to $Z_{eq} = R_{sw} + iwL_s$ =3.98 + 2.52i and in OFF position the capacitance value calculated is C_c = 2.74 fF. The generated lumped LCR model of switch in ADS was simulated again by setting Z_{in}

= Z_{out} = 50 ohm impedance at the input and output terminal for verification of post-electromagnetics parameters and further comparison show similar results as generated by HFSS.

According to aforementioned generated equivalent model, the S_{21} can be defined as [99],

$$S_{21} = \frac{2}{2+\left(\frac{Z_0+Z_1+Z_2}{Z_3}\right)+\left(Z_1+Z_2+\frac{Z_1Z_2}{Z_3}\right)/Z_0} \quad (3.11)$$

where $Z_1 = R_1 + jwL_1$ (3.11.a)

$$Z_2 = \begin{cases} \frac{1}{jwC_s} & at\ the\ down\ position \\ R_c & at\ the\ up\ position \end{cases} \quad (3.11.b)$$

$$Z_3 = \frac{1}{jwC_g} \quad (3.11.c)$$

w represents the angular signal frequency i.e. $w = 2\pi f$, *f* is linear signal frequency and C_g denotes a coupling shunt capacitor.

At the up-position of the cantilever beam MEMS RF switch, the series capacitance (C_s) plays a major role to define the isolation ($S_{21\text{-off}}$) of the RF switch. For two conditions –

$$S_{21} << -10\ dB \text{ and } wC_sZ_0\left[2 - w^2C_gL_1 + \frac{C_g}{C_s} + \frac{R_1}{Z_0}\left(1 + \frac{C_g}{C_s}\right)\right] << 1$$

The $S_{21\text{-off}}$ of RF switch can be approximated as –

$$S_{21} \approx j2wC_sZ_0 \quad (3.12)$$

In this way, the capacitance of the up-position switch can be taken out for measuring the isolation ($S_{21\text{-off}}$) by using mathematical equation (3.12). The switch is simulated for various values of the capacitance to define the isolation (dB) of the MEMS RF switch at different frequencies. From the result shown in **figure 3.21**, it can be concluded that at up-position of the RF switch, the isolation (dB) improves with the increase in capacitance value from 0.005 fF to 5.0 fF. The equivalent off-state capacitance of proposed metal contact MEMS switches is 2 – 10 fF ranging for frequency between 1.0 to 10.0 GHz.

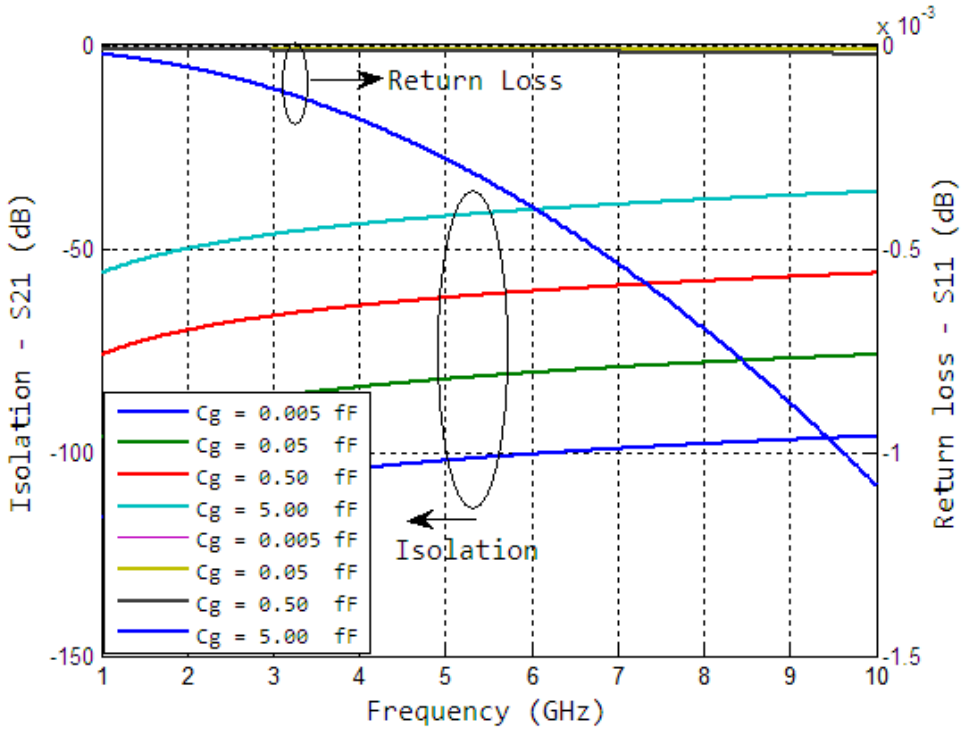

Figure 3.21- S-parameters Simulation Results with Various Shunt Capacitances C_g at Off-position of the Designed Switch

At the down-position of the MEMS RF switch, the RL (S_{11}) and the IL ($S_{21\text{-}ON}$) can be defined as,

$$S_{11} = \frac{A_1 + j.A_3}{2 + A_1 + j.A_2} \tag{3.13.a}$$

$$S_{21} = \frac{2}{2 + A_1 + j.A_2} \tag{3.13.b}$$

where

$$A_1 = \frac{R_1 + R_c}{Z_o} - w^2 C_g L \left(1 + \frac{R_c}{Z_o}\right) \tag{3.13.c}$$

$$A_2 = w \left[C_g \left(R_1 + R_c + Z_o + \frac{R_1 R_c}{Z_o}\right) + \frac{L}{Z_o}\right] \tag{3.13.d}$$

$$A_2 = w \left[C_g \left(R_1 - R_c - Z_o + \frac{R_1 R_c}{Z_o}\right) + \frac{L}{Z_o}\right] \tag{3.13.e}$$

At lower frequency range, when $2 + A_1 >> 0$ and $A_2 << 2 + (R_1 + R_c)/Z_o$, the RL and IL of the RF MEMS can be written as-:

$$S_{11} \approx (R_1 + R_c)/[2Z_o + (R_1 + R_c)] \quad (3.14.a)$$

$$S_{21} \approx {}^{2}/_{[2 + (R_1 + R_c)/Z_o]} \quad (3.14.b)$$

Figure 3.22 and **figure 3.23** show the simulation results of IL ($S_{21\text{-}ON}$) and the RL (S_{11}) of the MEMS RF switch at the down-positions with numerous values of input line and series resistance. RF switch performances at the down-positions get worse by the rise in resistance. As soon as the resistance sum ($R1 + R4$) is less than 2.0 ohm, the IL is < 0.2 dB times up to 10 GHz. While ($R1 + R4$) rises to 10.0 ohm, the IL is greater than 1.2 dB around 10.0 GHz. The RL is degraded by increase of ($R1 + R4$) value. Therefore, for attainment of optimized results i.e. high RL and low IL, a small value of sum resistance ($R1 + R4$) is desirable. **Table 3.9** shows the effect on IL by varying the input line and series resistance at some selected frequency bands of proposed MEMS series cantilever switch. Further, in down position, by varying the input line inductance ($L1$) from small value of nH to small value of pH, the IL less than 0.35 dB can be achieved up to 10.0 GHz, as shown in **figure 3.24**. For same variation in inductance the RL results also improves as demonstrated in **figure 3.25**. At $L1$ equal to 0.63 pH, IL is almost constant i.e. 0.32 dB for frequency range 1.0 to 10 GHz and RL is in the range of -25 to -30 dB throughout the frequency range. These results are obtained by keeping the ($R1 + R4$) values constant. Another important observation is noticed that by varying the series capacitance and keeping the line inductance and resistance constant, IL is optimized at 47.0 fF and is in the range of 0.2 to 0.4 dB for up to 10 GHz frequency, as shown in **figure 3.26**. The best RL is also observed at mentioned series capacitance value.

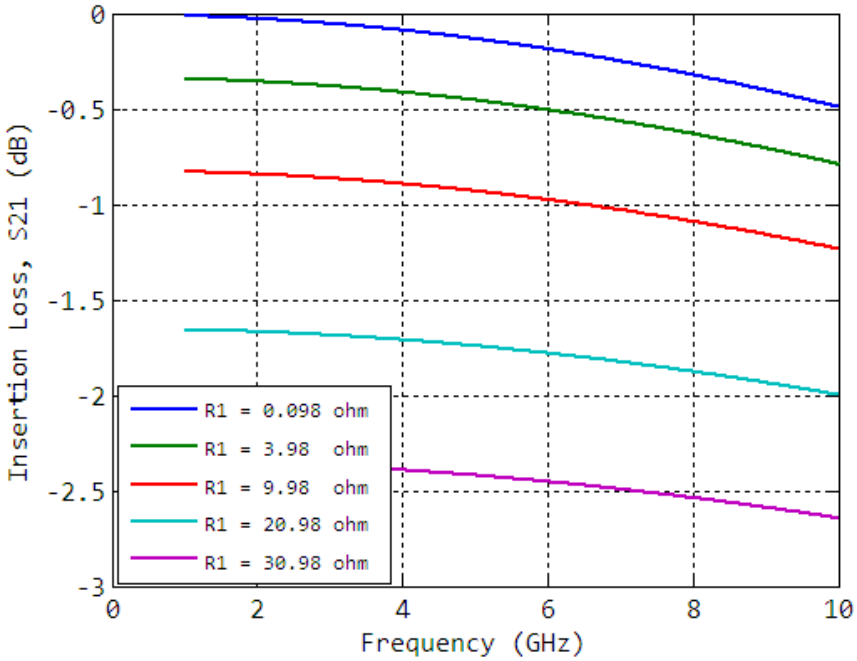

Figure 3.22- ILwith Various Series Resistance *R1* at the ON-position of the Designed Switch (*L1* = 0.63 nH)

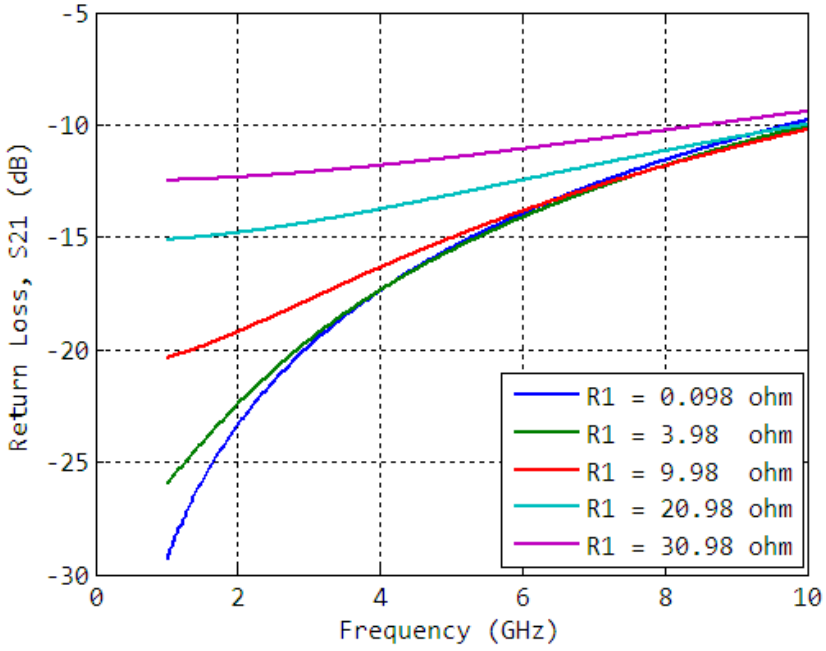

Figure 3.23- RL with Various Series Line Resistances *R1* at the ON-position of the Designed Switch (*L1* = 0.63 nH)

Table-3.9: IL by Varying Series Line Resistance at Selected Frequencies MEMS Series Cantilever Switch

Series line resistance (R1 + R4) in ohm ↓	Freq. (GHz) →	Insertion loss-S_{21} (dB) at selected frequencies									
		1.5	1.8	2.1	2.4	2.6	3.0	3.5	5.4	5.75	6.5
0.098		0.037	0.039	0.042	0.045	0.047	0.052	0.058	0.093	0.101	0.120
3.98		0.187	0.190	0.194	0.197	0.199	0.204	0.211	0.245	0.253	0.270
9.98		0.359	0.376	0.390	0.401	0.407	0.418	0.429	0.471	0.479	0.498
20.98		0.485	0.541	0.590	0.632	0.656	0.697	0.738	0.837	0.851	0.878
30.98		0.504	0.529	0.651	0.717	0.758	0.831	0.908	1.098	1.122	1.168

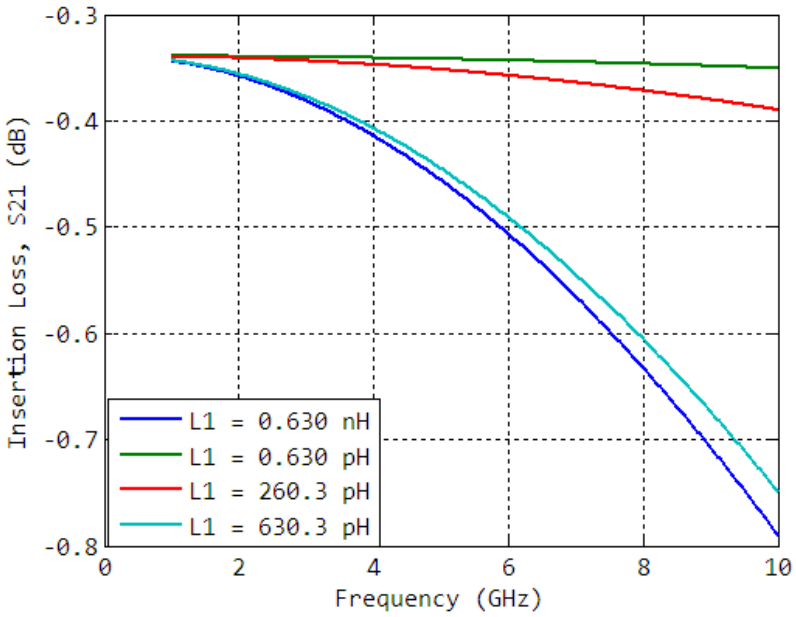

Figure 3.24- IL Simulation Results with Various Series Inductances *L1* at the ON-position of the Designed Switch (*R1* = 3.98 ohm)

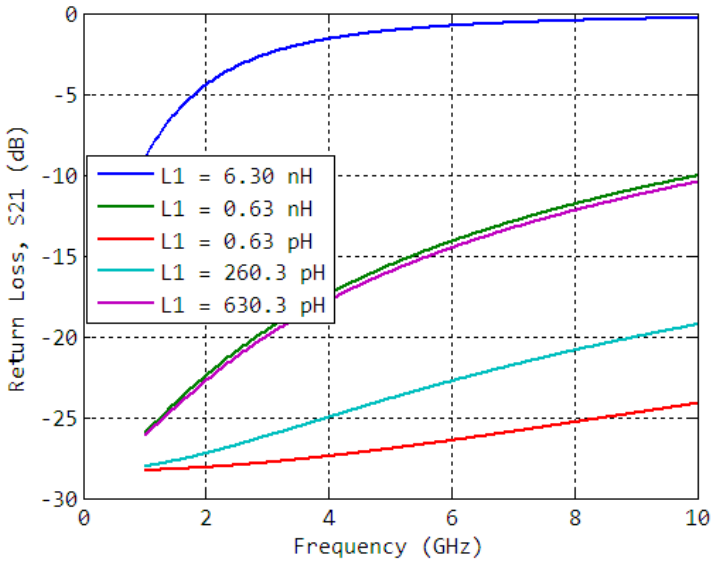

Figure 3.25- Simulation Outcomes of RL with Various Series Inductances *L1* at the ON-position of the Designed Switch (*R1* = 3.98 ohm)

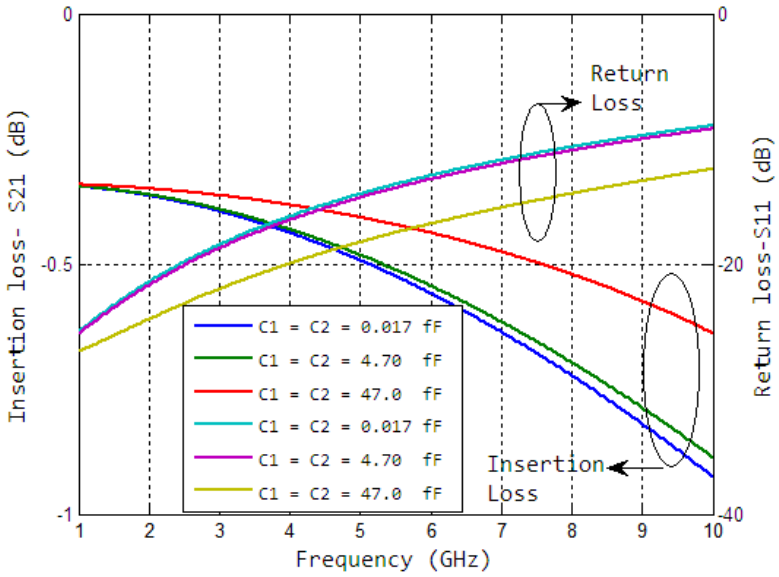

Figure 3.26- S-parameters Simulation Results with Various Series Capacitances *C1* and *C2* at the On-position of the Designed Switch (*R1* = 3.98 Ω, *L1* = 0.63 nH)

3.4.4 Analysis of FBAR MEMS RF Switches

The desired resonating frequency band of FBAR MEMS switch involves not only the proper selection of piezoelectric and electrode material but also the appropriate thickness of these materials. In the recent development of FBAR MEMS switches, the most widely used material for piezoelectric layer are Zinc Oxide (ZnO), Lead Zirconate Titanate (PZT), as well as Aluminum Nitride (AlN). The AlN is dominating material out of all, as it is more compatible with integrated circuit (IC) fabrication processes. The PZT material has significantly higher coupling coefficient than either ZnO or AlN, a large zero bias permittivity, both piezoelectric and ferroelectric properties are exhibited, and very dense film thicknesses are viable. Many electrode materials like Tungsten, Molybdenum and Aluminum have been used because of their relatively high acoustic stiffness. If the device needs low resistance and does not require exceptional coupling coefficient, Aluminum is a good choice. Higher acoustic impedance metals (i.e. Tungsten, Molybdenum and Platinum) provide higher coupling coefficient. Platinum has higher electrical resistance than other metal which is undesirable for FBAR switch performance [92-95].

In this section, the FBAR switch is designed for Long Term Evolution (LTE)/4G applications. The thickness of upper electrode of FBAR resonator is increased or decreased with the help of cantilever beam in such a manner that the switch either resonates at 3.5 GHz or 3.15 GHz. Accordingly the calculation of various design parameters of electrode and piezoelectric layer can be as follow :-

Properties of piezo-electric layer (*AlN)* are [29]:-

Density (ρ) = 3450.5 kg/m^3, piezoelectric constant (e) = 1.55 C/m^2, Relative dielectric permittivity (ε_{r33}) = 9.66, stiffness (c_{33}) = 3.95 × 10^{11} N/m^2, coupling coefficient (k_t^2) = 0.065, Acoustic velocity (v_p) = 11361.9 m/s.

Properties of upper and bottom electrode (Tungsten) are:-

Density (ρ) = 19350 kg/m^3, Acoustic velocity (v_e) = 5210 m/s Young's modulus (E) = 411 GPa, Poisson ratio (σ) = 0.28.

Resonance frequency condition:

$$\frac{1}{\tan\theta_e} \times \left(\frac{1}{\tan\theta_p} - \frac{k_t^2}{\theta_p}\right) = Z_e / Z_p \quad (3.15.a)$$

Anti-resonance frequency condition:

$$\frac{Z_p}{Z_e} = \tan\theta_e \tan\theta_p \quad (3.15.b)$$

z_e is the impedance of the electrode, which can be calculated as $z_e = \rho v_e$ and impedance of piezoelectric material can be calculated as $z_p = \rho v_p$.

The fabrication steps of FBAR designing are given in **table 3.10**.

Table-3.10: Fabrication Process of Proposed FBAR

Sr. No.	Step Name	Layer Name	Material Name	Thickness (µm)	Mask Name	Photo-resist	Depth (µm)
1.	Definition N-type (100) Silicon 1-2 Ωcm	Substrate	Silicon	10	Ground		
2.	Stack Material	Nitride bottom	SiN	0.25			
3.	Straight Cut				Nitride	-	
4.	Stack Material	Silicon	Silicon (100)	20			
5.	Straight Cut				KOH-etch	-	
6.	Stack Material	Membrane	SiN	0.25			
7.	Straight Cut				KOH-etch	-	
8.	Stack Material	Electrode bottom	Tungsten	0.08			
9.	Straight Cut				Electrode bottom	+	20.9
10.	Stack Material	PZE	AlN	0.793			
11.	Straight Cut				PZE	+	
12.	Stack Material	Electrode top	Tungsten	0.08			
13.	Straight Cut				Electrode top	+	

Now for anti-resonance frequency at 3.6 GHz, let electrode thickness (t_e) is 80 nm.

$$k_e = \frac{2\pi f_a}{v_a} = 9.345e6\ m^{-1} \quad (3.16.a)$$

$$\theta_e = k_e t_e = 0.3738\ \text{radian} \quad (3.16.b)$$

Calculation of piezoelectric material thickness

$$k_p = \frac{\omega_a}{v_p} = 6.82 \times 10^5\ m^{-1} \quad (3.17.a)$$

$$\theta_p = k_p t_p / 2 \quad (3.17.b)$$

$$\frac{Z_p}{Z_e} = \tan\theta_e \tan\theta_p \quad (3.17.c)$$

$$t_p = 0.351 \times 10^{-6}\ m$$

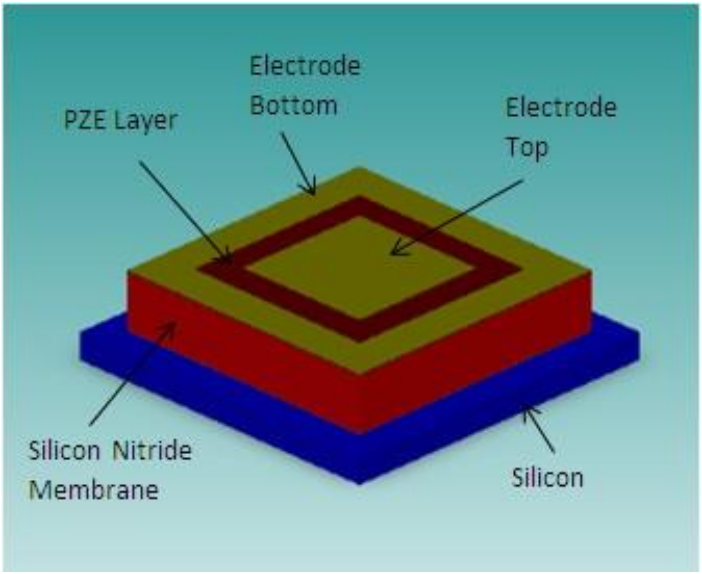

Figure 3.27- 3D-geometry of Designed FBAR (in Coventorware Software)

The 3D structure of presented FBAR in coventorware simulator is displayed in **figure 3.27**. The characteristic impedance magnitude and phase angle plots simulated in coventorware software are shown in **figure 3.28 (a)** and **3.28 (b)**, respectively. Further, when the top electrode thickness is increased from 80 nm to 0.612 µm, at the same time keeping the bottom electrode thickness to 80 nm and piezoelectric layer thickness to 0.793 µm, the resonance frequency band decreases from 3.52-3.6 GHz to 3.15-3.26 GHz, as shown with the help of magnitude and phase angle plots in **figure 3.29 (a)** and **3.29 (b)**, respectively.

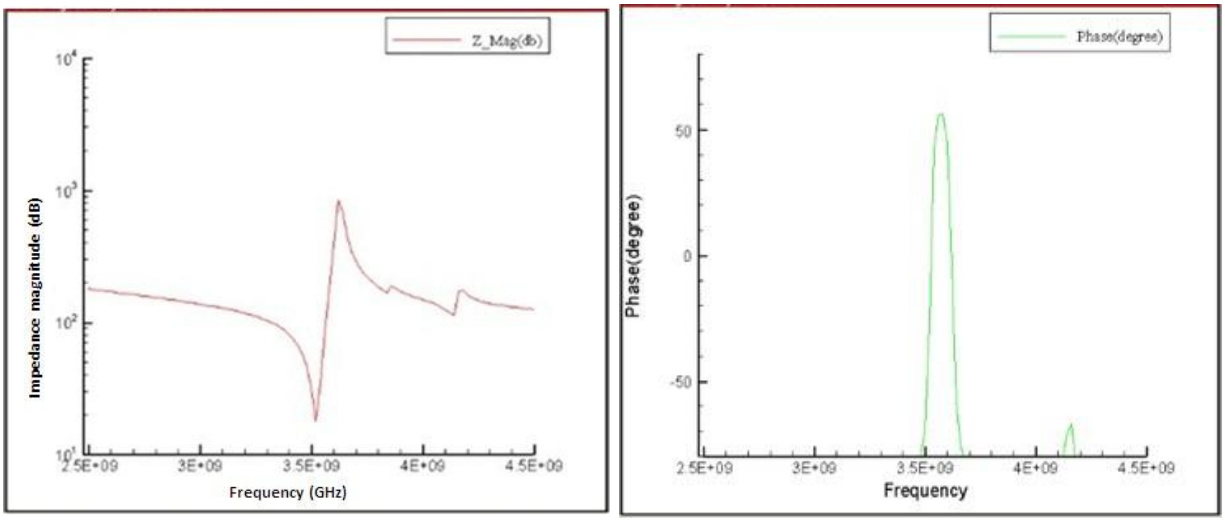

(a) **(b)**

Figure 3.28- (a) Impedance Characteristics Magnitude (dB) and (b) Phase (degree) of FBAR Filter at 3.52-3.6 GHz

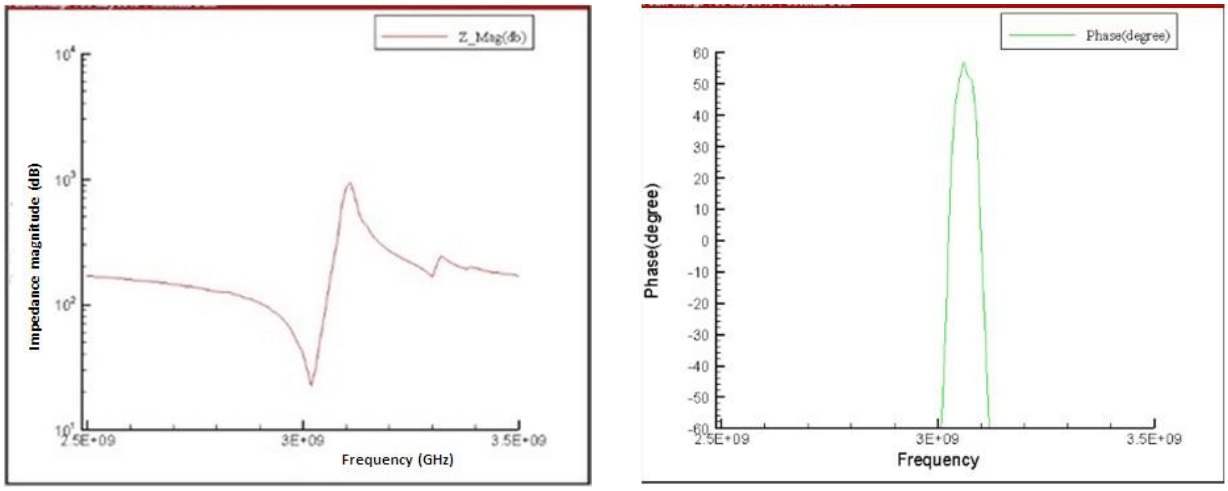

(a) **(b)**

Figure 3.29- (a) Impedance Characteristics Magnitude (dB) and (b) Phase (degree) of FBAR Filter at 3.15-3.26 GHz

In order to obtain both resonating bands (3.5 GHz or 3.15 GHz), a cantilever beam is introduced over the top electrode of FBAR having the same length and breadth as the top electrode but different thickness, which is equal to 0.532 µm (i.e. 80 nm – 0.612 µm) as shown

in **figure 3.30**. When the cantilever is in air, the FBAR MEMS switch operates at 3.5 GHz and when it touches the top electrode, the switch resonates at 3.15 GHz.

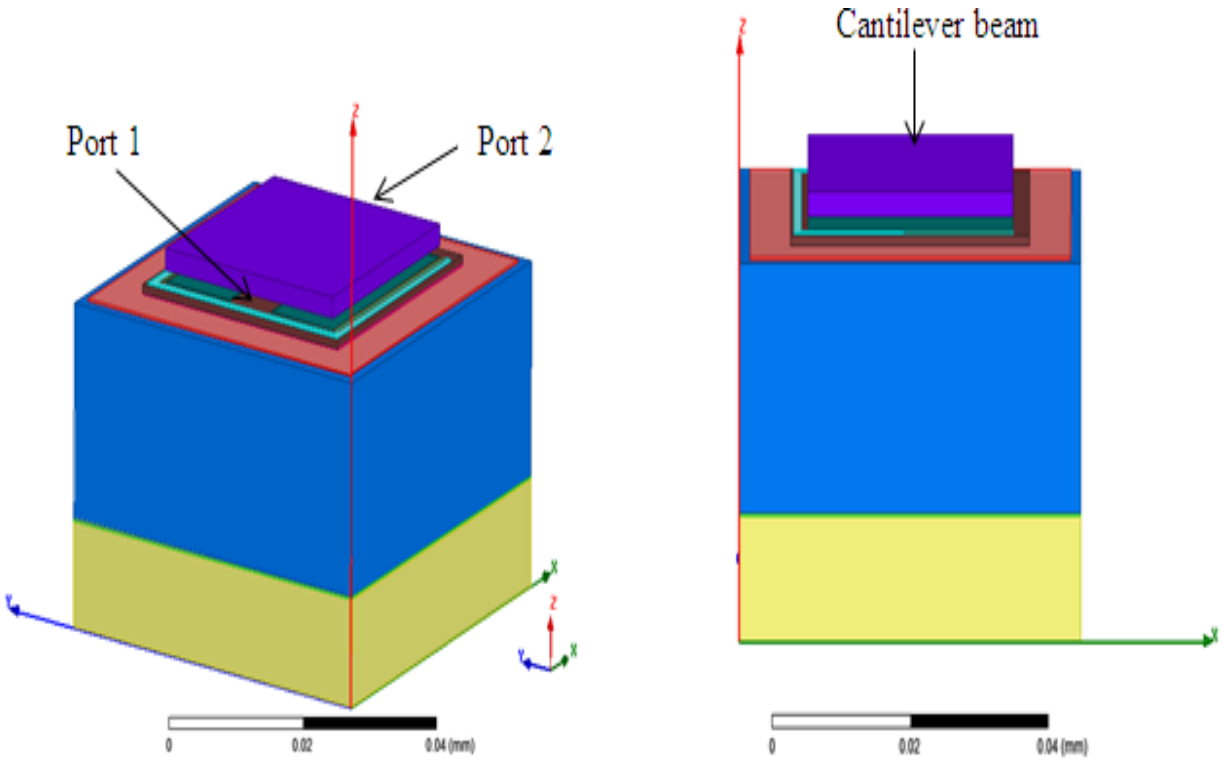

Figure 3.30- 3D-side Views of Cantilever FBAR MEMS Switch

A gold plated cantilever beam has higher value of spring constant and found to be 21.36 N/m from equation given in [79]. The S-parameters are calculated for 1 to 6 GHz frequency range in HFSS software by treating it inline RF switch, as in port1 and port 2 is shown in **figure 3.30**. While the RF switch is in off-position, the isolation is nearby 29 dB and in on-position; the IL measured is nearly 1.9 dB, as shown in **figures 3.31 (a)** and **figure 3.32 (a)**. By using computational techniques and optimization method, which are discussed in upcoming chapter, these results can be improved.

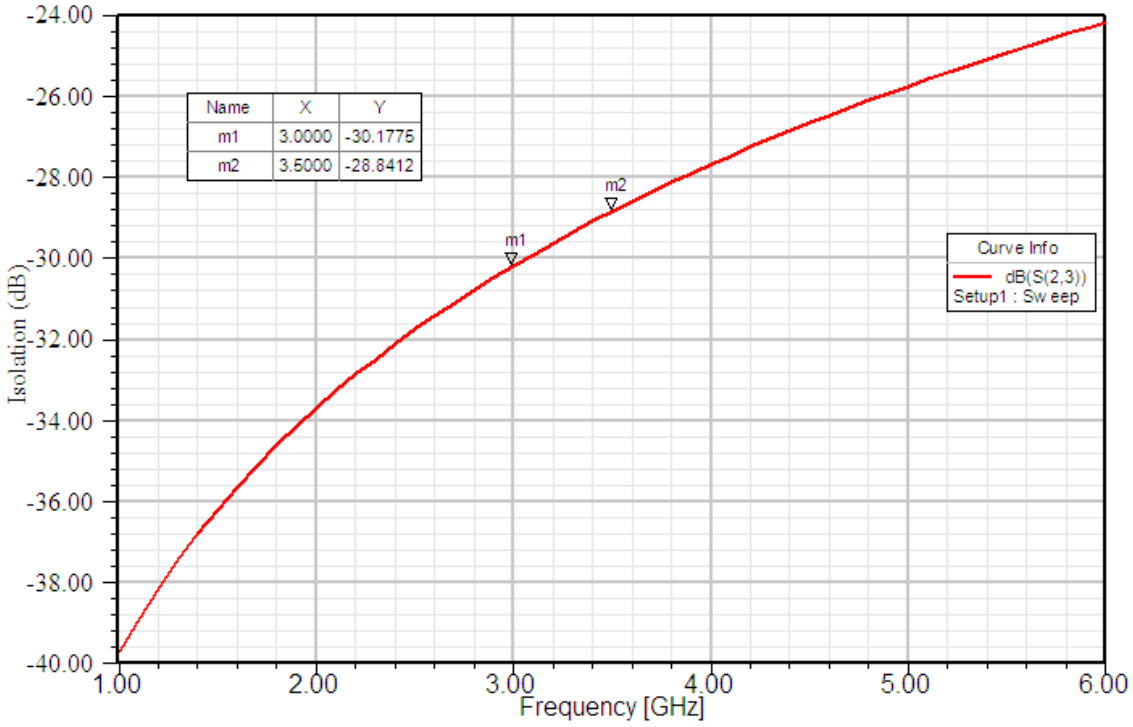

(a)

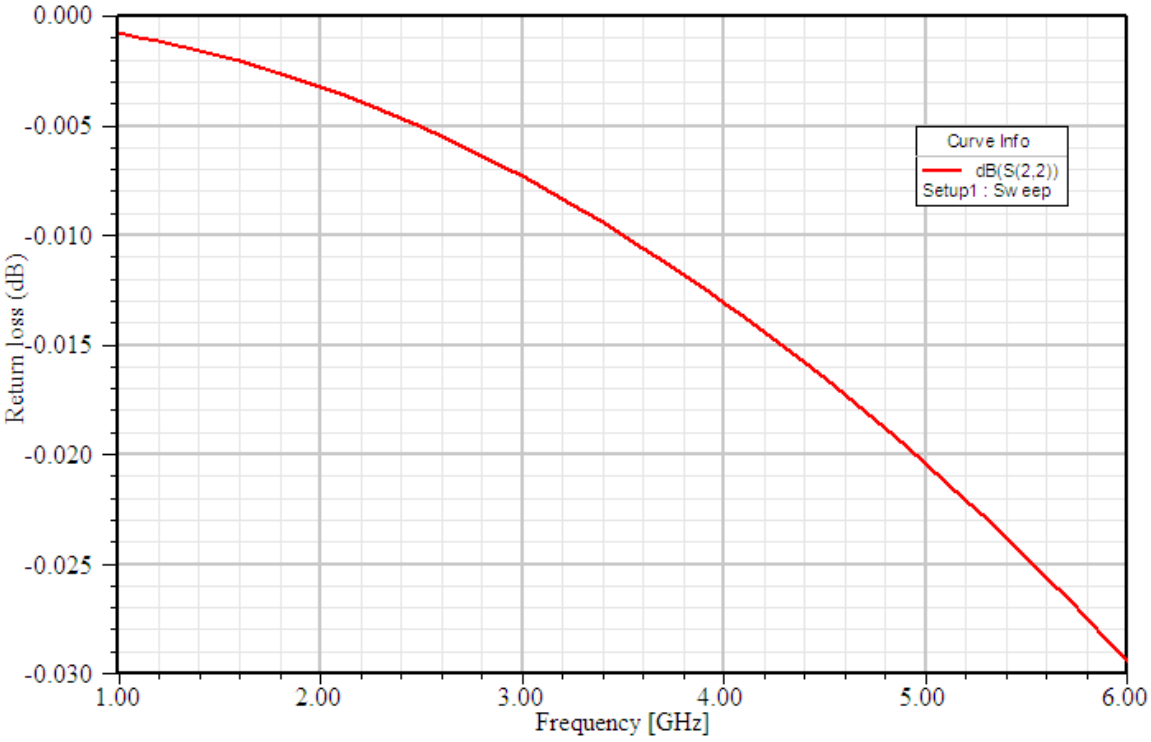

(b)

Figure 3.31- (a) Simulated Isolation and (b) RL Results of FBAR MEMS Switch in OFF-condition

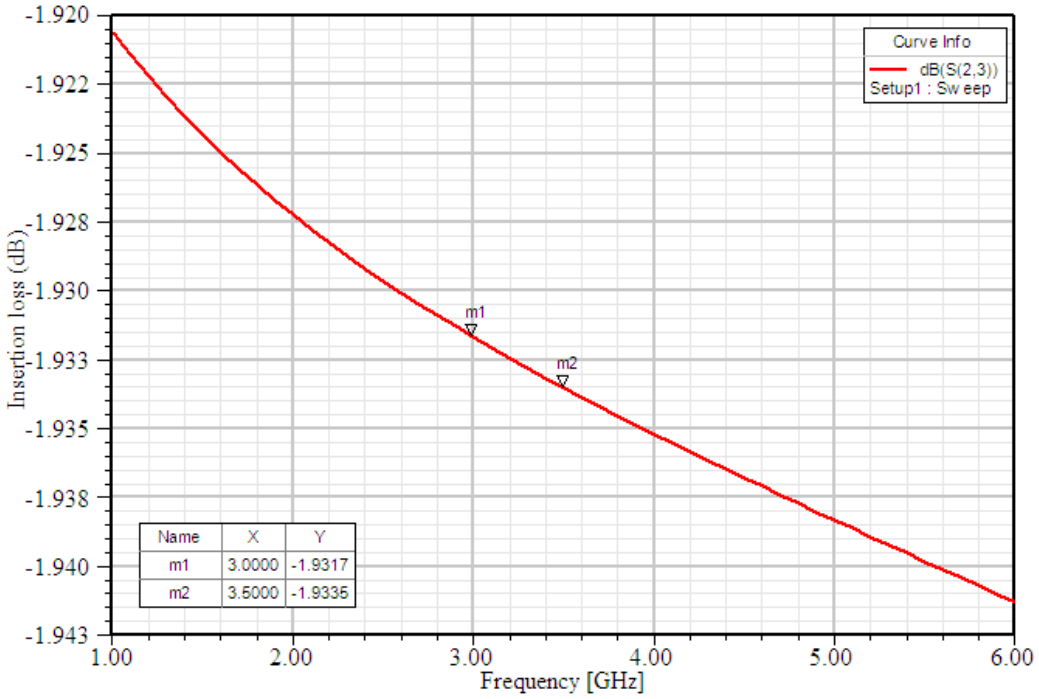

(a)

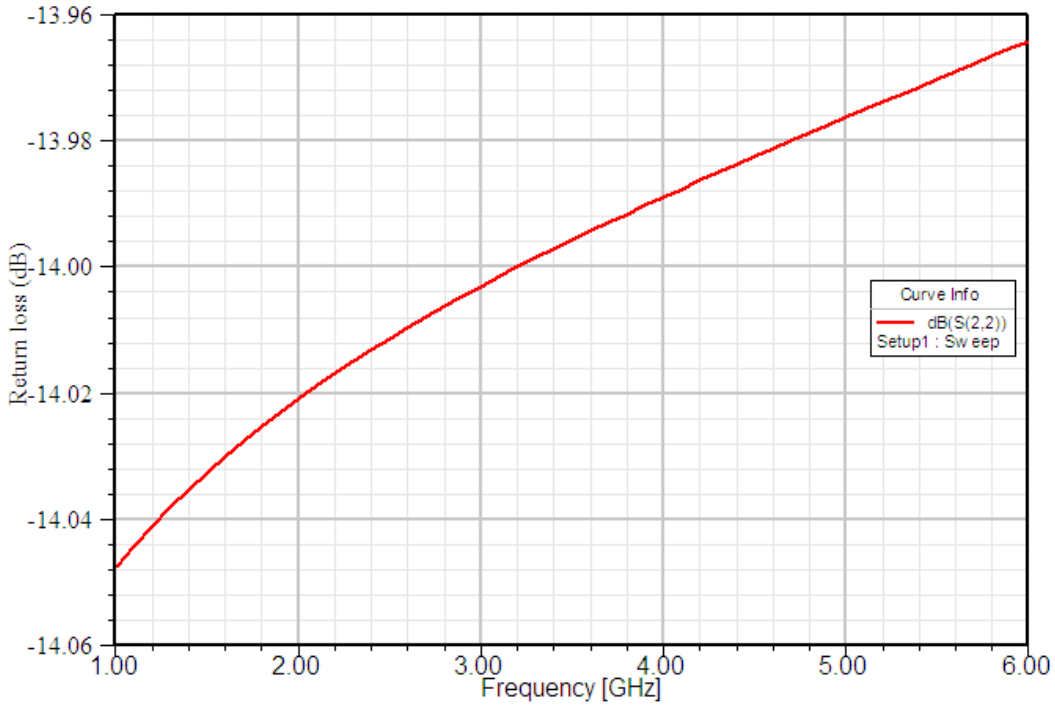

(b)

Figure 3.32- (a) Simulated IL and (b) RL results of FBAR MEMS Switch in ON-condition

Further, FBAR can be used for filter design by cascading individual FBAR into series and parallel combinations. The RF filter is designed here by associating three FBARs in ladder

topology working for LTE application and the frequency range lies between 3.52 - 3.6 GHz. The series and shunt resonator design parameters are given in **table 3.11**. These design parameters are calculated by using equation 3.15 to 3.17.

Table-3.11: Designing Parameters of FBAR RF Filter

Parameters	Series Resonator	Shunt Resonator
Area (μm^2)	180 × 180	250 × 250
Lower resonance frequency	3.56 GHz	3.52 GHz
Upper resonance frequency	3.6 GHz	3.55 GHz
Piezoelectric thickness	0.797 µm	0.816 µm
Electrode thickness	80 nm	80 nm
Capacitance (C_o)	3.778×10^{-12} F	7.119×10^{-12} F

The equivalent circuit of proposed FBAR filter is shown in **figure 3.33**. The simulations for S-parameters are done using ADS software and results are shown in **figure 3.34**.

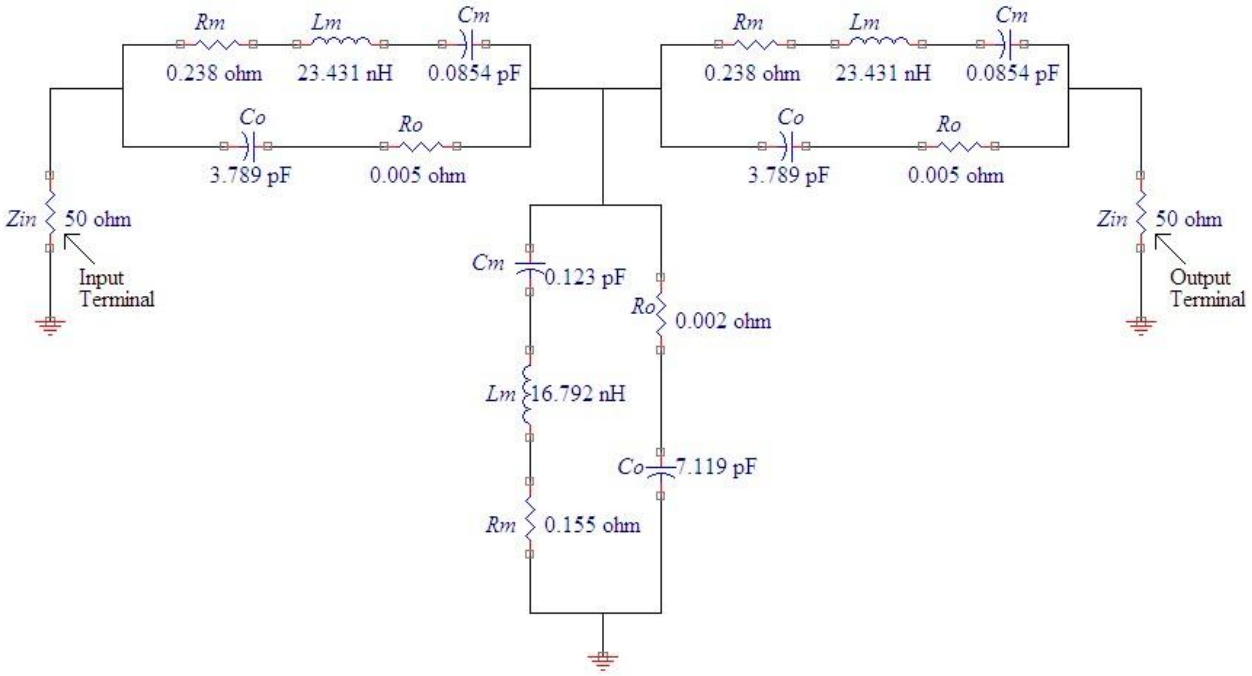

Figure 3.33- Equivalent Structure of Ladder FBAR MEMS Filter

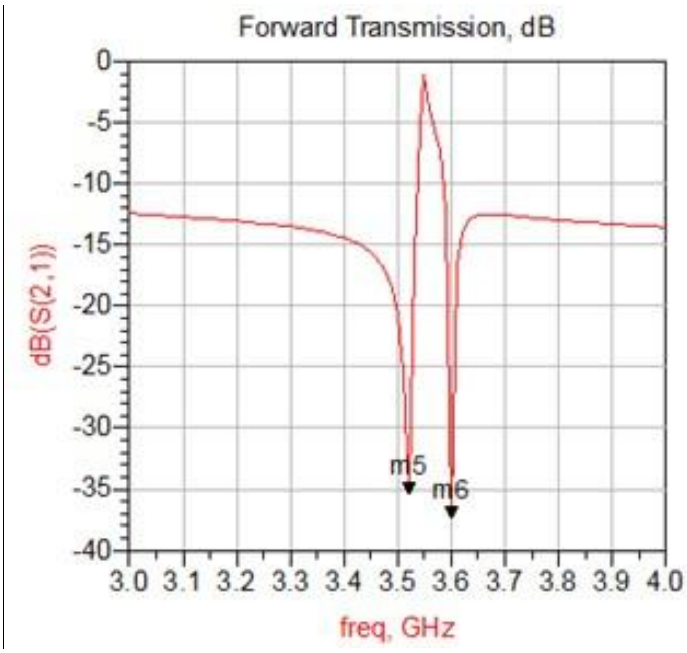

(a)

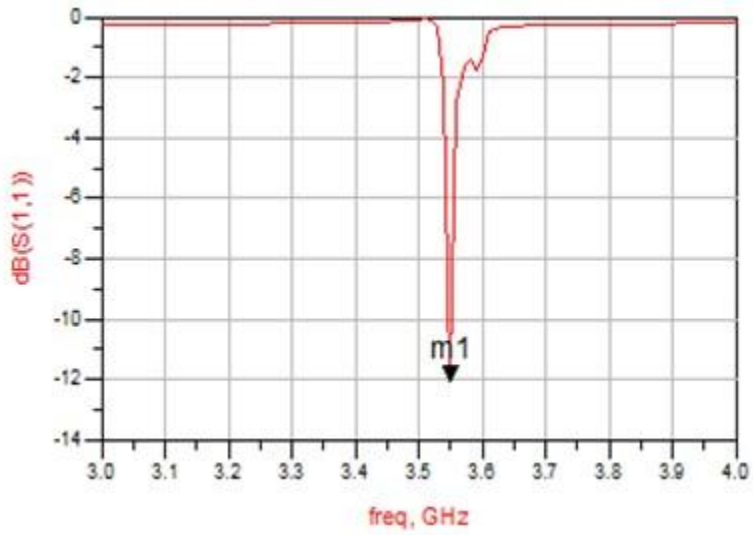

(b)

Figure 3.34- (a) ADS Simulated Forward Transmission Response and (b) RL of Ladder FBAR MEMS Filter

It has been noticed that by adding inductance and capacitance in ladder FBAR filter the bandwidth can be changed. Adding the series inductance of specific value in shunt resonator to the ladder filter will lead to an increase in the bandwidth. After performing number of simulations for different value of series inductance, the best results are found when adding series

inductances (1-2 nH) to the shunt resonators, as shown in **figure 3.35**. Also, it is noticed in **figure 3.36**, the return loss is improved as compared to without series inductance. The introduction of series inductance is preferred for those applications where larger bandwidth is desirable, but at the same time it is observed that these inductors are described by a minor quality factor (5 to 10) w.r.t. the FBAR (400 to 1000), and therefore they occupy a comparatively huge size. Thus, inserting inductors bring some improvements, but their presence creates specific undesirable effects also. The effect of adding the series capacitors to the shunt resonators, as shown in **figure 3.37**, are also studied. Addition of capacitors having quality factor ranging from 20 to 50 with regards to the capacitance size doesn't degrade the FBAR circuitry performance. By controlling the series and parallel capacitance ratio will enable us to control the electromechanical coefficient, and as a consequence the filter bandwidth. For converting narrow band FBAR to wide bandwidth circuitry the series capacitors are added to the shunt resonators. Also, it is noticed from **figure 3.38** that the return loss is better than -13 dB.

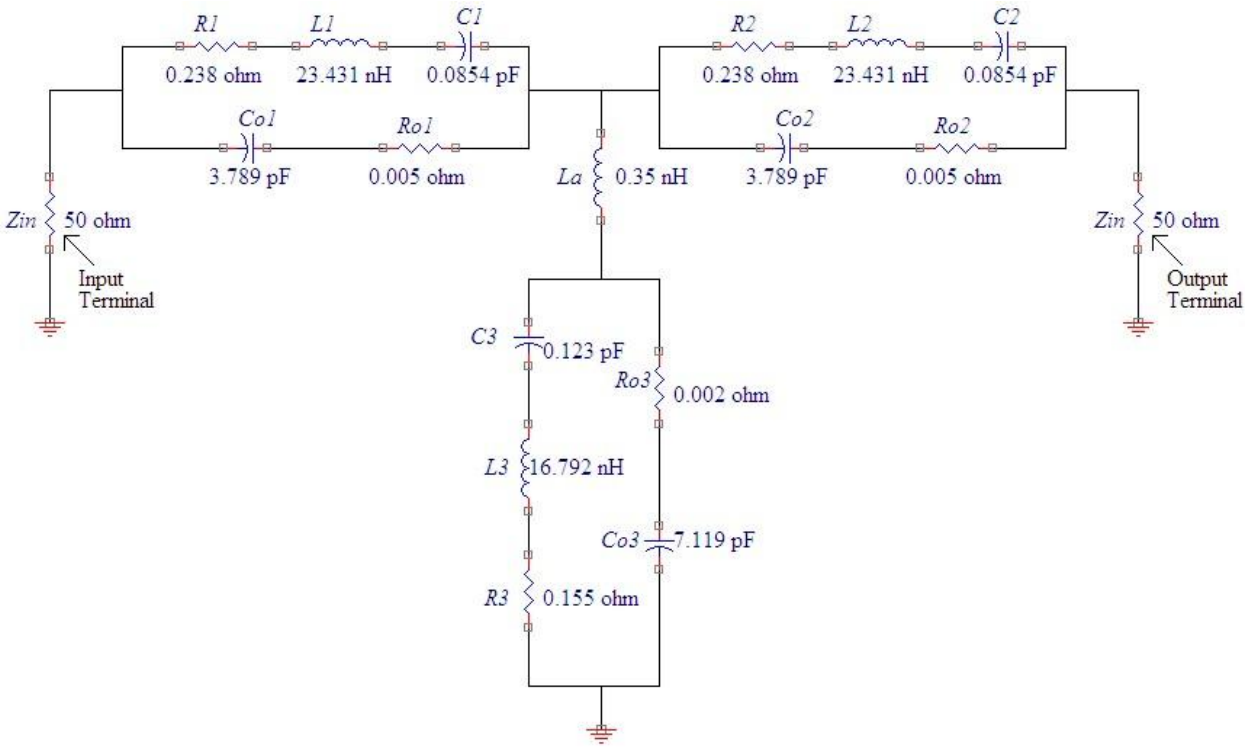

Figure 3.35- Addition of Shunt Inductance in Equivalent Structure of Ladder FBAR MEMS Filter

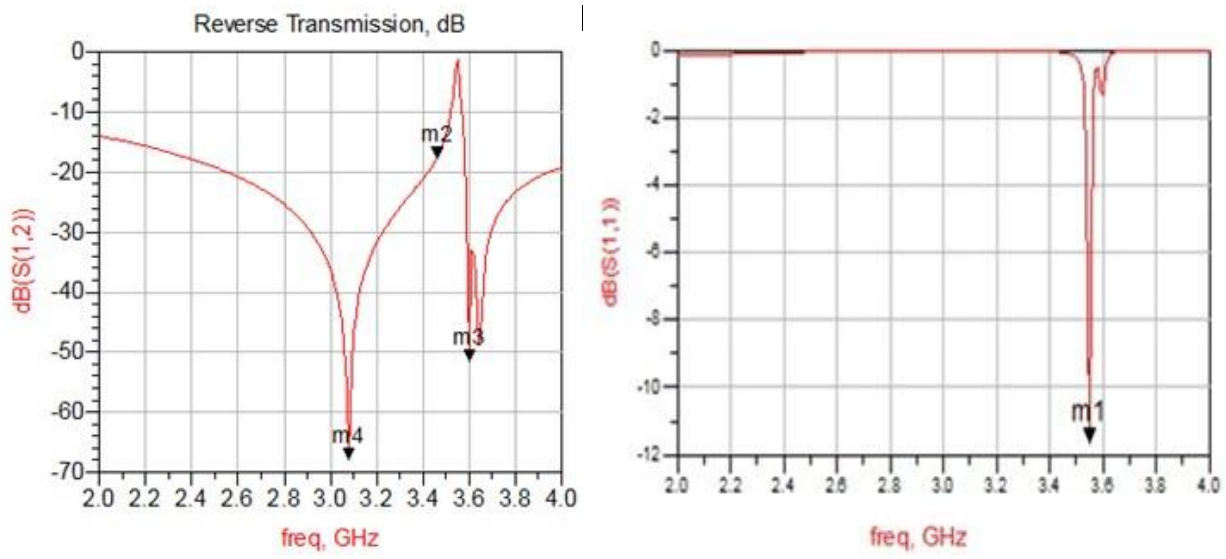

(a) **(b)**

Figure 3.36- Effect of Addition of the Shunt Inductance on (a) ADS Simulated Reverse Transmission Response and (b) RL of Ladder FBAR MEMS Filter

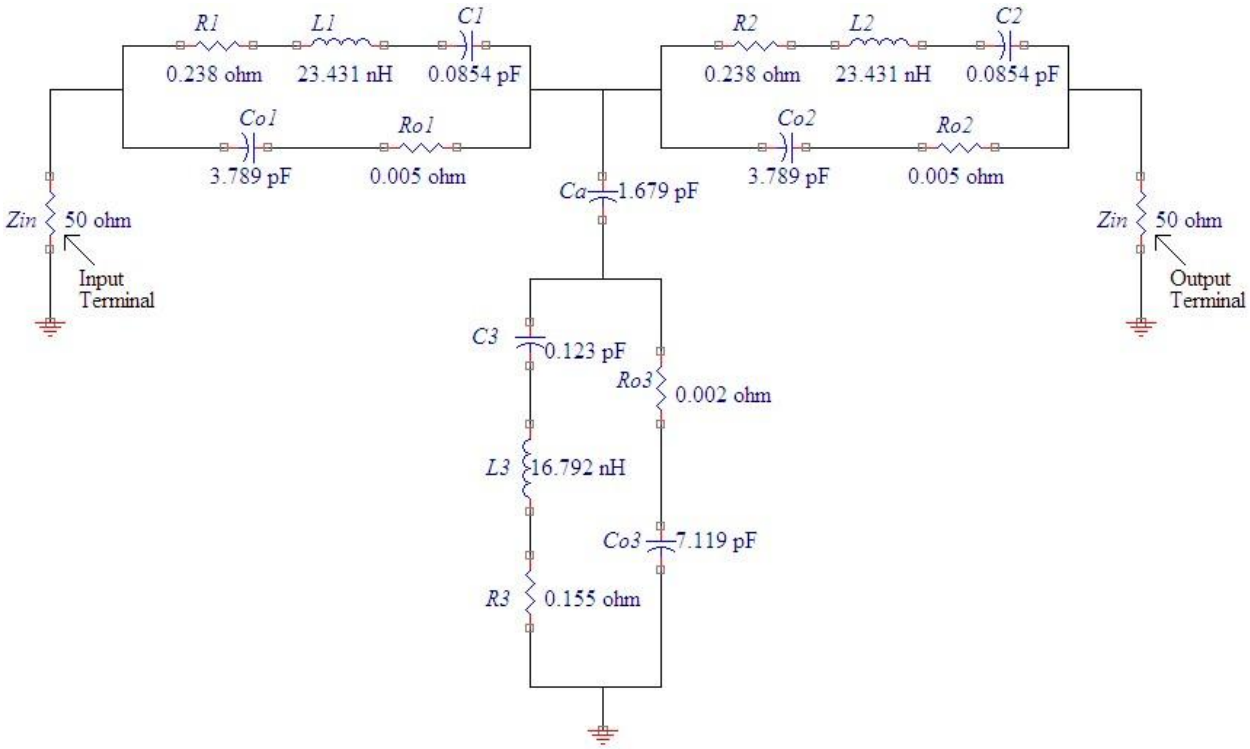

Figure 3.37- Addition of Shunt Capacitance in Equivalent Structure of Ladder FBAR MEMS Filter

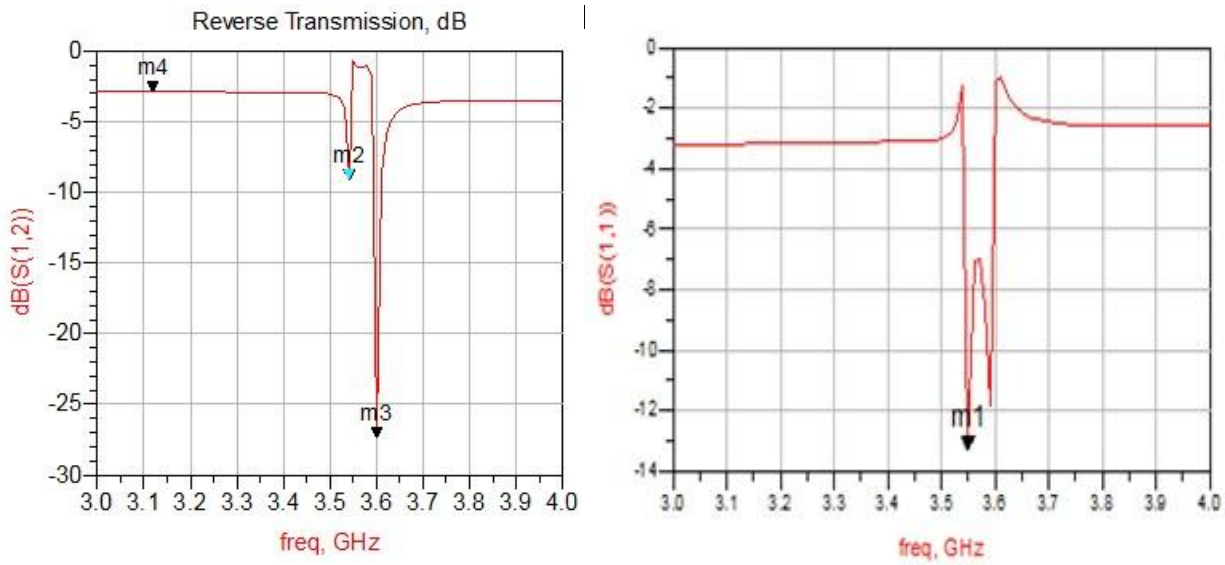

(a) **(b)**

Figure 3.38- Effect of Addition of the Shunt Capacitance on (a) ADS Simulated Reverse Transmission Response and (b) RL of Ladder FBAR MEMS Filter

3.5 Fabrication Standard Process of Cantilever Switch throug PolyMUMPs

The fabrication of the RF MEMS switches is complicated and involves multi-layered processes. Each step requires a lot of care to avoid deterioration in the device performance. The most important and critical steps can be deposition of patch material, electroplating, the patterning step of thin film of dielectric aimed at the MEMS RF switches, dc bias line pad patterning, and fabrication and release step of the switch membrane. PolyMUMPs has followed the idea of standard process steps approach as a much clear path to device functionality and volume production [99]. For larger scale systems, PolyMUMPs chips act as a standard building unit, where the microelectromechanical chip is only single piece of the overall building block. PolyMUMPs technology is also used as a benchmarking tool for statistical studies and software models, where experimented and measured data from actually fabricated chips are validated with theories [29,99]. Following are the steps, as display in **table 3.12**, involved in designing of MEMS switch using PolyMUMPs technology -:

Table-3.12: Fabrication Steps of Designed Cantilever MEMS Switch through PolyMUMPs Foundry

Sr. No.	Step Name	Layer Name	Material Name	Thickness (µm)	Mask Name	Photo-resist	Depth (µm)
1.	Definition N-type (100) Silicon 1-2 Ωcm	Substrate	Silicon	20	Ground		
2.	LPCVD Deposition 600 nm Si_xN_y	Nitride	Si_xN_y_ PolyMUMPs	0.6			
3.	LPCVD Deposition 500 nm PolySi	Poly0	PolySilicon0_ PolyMUMPs	0.5			
4.	Etch RIE 500 nm Poly0				Poly0	+	
5.	Etch RIE 500 nm Poly0				Hole0	-	
6.	LPCVD Deposition PhosphoSilicate 2000 nm	Oxide1	PSG	2.0			
7.	Etch RIE 750 nm PSG				Dimple	-	0.75
8.	Etch RIE 2000 nm PSG				Anchor1	-	
9.	Etch RIE 2000 nm PSG				Anchor2	-	
10.	LPCVD Deposition 2000 nm Poly1	Poly1	PolySilicon1_ PolyMUMPs	2.0			
11.	Etch RIE 2000 nm Poly1				Poly1	-	
12.	Etch RIE 2000 nm Poly1				Hole1	-	
13.	Etch RIE 2000 nm Poly1				Anchor2	-	
14.	LPCVD Deposition	Oxide2	PSG	0.75			

	PhosphoSilicate 750 nm						
15.	Etch RIE 200 nm				Poly1 Poly2Via	-	
16.	Etch RIE 200 nm				Anchor2	-	
17.	LPCVD Deposition 1500 nm Poly2	Poly2	PolySilicon2_ PolyMUMPs	1.5			
18.	Etch RIE 1500 nm Poly2				Poly2	+	
19.	Stack Material	Actuation Pad	Gold	1.0			
20.	Straight Cut				Actuation Pad	+	
21.	Stack Material	Layer2	PSG	0.35			
22.	Stack Material	Beam1_ Bottom Layer	Si_3N_4	0.5			
23.	Straight Cut				Beam1_ Bottom Layer	+	1.0
24.	Planar Fill	Beam2_ middle layer	Gold	1.0			
25.	Straight Cut				Beam2_ middle layer	+	
26.	Planar Fill	Beam3_ Top layer	Si_3N_4	0.5			
27.	Straight Cut				Beam3_ Top layer	+	
28.	Straight Cut				Holem	-	2.0
29.	HF (49%) Release Etch		PSG				

The complete layer by layer fabrication process through POLYMUMPs technology of proposed cantilever MEMS switch is given in **Appendix A**.

3.6 Results and Discussions

Five proposed MEMS switches (two alike and three different configurations) are chosen for comparison, as shown in **table 3.13**. All switches have either series/shunt configurations, micron-meter range dimensions and are simulated for the study of the electromagnetic as well as electromechanical characteristics, with different beams structures. Typical dimensions of all designed switch beam lengths are ranging from 50 to 300 μm and thickness ranging from 0.5 to 1.5 μm. The "serpentine beam" switch shows a significant improvement over the rest of four designed switches in terms of pull-in voltage i.e. given as 0.63 V. It has been observed that in DC shunt MEMS switch, as the number of meanders are increased as compared to serpentine beam structure, the spring constant can be reduced and the value obtained is equal to 0.228 N/m. In all the proposed switches except FBAR MEMS switch, small diameter holes of 5.0 μm are introduced on beam which lower the mass, release some amount of residual stress and reduce Young's modulus. The lower mass in turn yields an upper resonant frequency which is shown in generated harmonic modes.

Furthermore, switches electromagnetic performance comparison has been done in the range of operational frequency bands lying from 1.0 to 8.0 GHz. IL minimum values achieved in case of serpentine beam switch is equal to 0.05 dB at 4.0 GHz and 0.10 dB at 8.0 GHz for DC shunt switch, respectively. High isolation value is examined in case of fixed beam switch i.e. 87.7 dB at 4.0 GHz and 73.6 dB at 8.0 GHz, respectively.

3.7 Summary of the Chapter

In this chapter, five different MEMS RF switches are designed, analyzed and compared. The relations of Young's modulus, actuated voltage and the material composition, C_{on}/C_{off} and electrostatic-forces of series and shunt switches have been analysed with the help of coventor software. The effect of varying the lumped equivalent element of the presented switches on IL and isolation has also been studied. One of the main emphasis of this work is to lower down the pull-in or actuation voltage, that is desirable in those circuits which require less power consumption such as RF MEMS based mobile front-end section. Further, the effect of beam thickness on pull-in voltage has also studied. The thickness of beam has direct relationship with pull-in voltage, i.e. as the thickness of beam increases, the pull-in voltage also increases. Hence

in this chapter five new improved RF MEMS on/off switches for reconfigurable planar antenna have been proposed and optimization of these switches are the subject of the next chapter.

Table-3.13: Comparison of Five Different Proposed MEMS RF Switches

Switch Type → / **Parameter ↓**	**DC shunt capacitive MEMS switches**		**DC shunt MEMS switch**	**Metal-contact MEMS switch**	**Cantilever FBAR MEMS switch**
	Serpentine Beam	**Fixed Beam**			
Substrate Size (μm^2)	390 × 210	280 × 150	272 × 118	336 × 192	50 × 50
Spring Constant- *k* (N/m)	3.59	6.14	0.228	5.0	21.36
Pull-in voltage (V)	0.63-0.75	3.19-3.50	22.8-23.1	9.08-9.12	15.63-15.91
RL (dB) in ON-position	20.30 @ 4 GHz 14.40 @ 8 GHz	13.80 @ 4 GHz 9.09 @ 8 GHz	11.40 @ 4 GHz 17.10 @ 8 GHz	19.95 @ 4 GHz 25.54 @ 8 GHz	13.99 @ 4 GHz 13.92 @ 8 GHz
IL (dB)	0.05 @ 4 GHz 0.19 @ 8 GHz	0.22 @ 4 GHz 0.61 @ 8 GHz	0.38 @ 4 GHz 0.10 @ 8 GHz	0.25 @ 4 GHz 0.41 @ 8 GHz	1.93 @ 4 GHz 1.97 @ 8 GHz
RL (dB) in OFF-position	0.675 @ 4 GHz 0.659 @ 8 GHz	0.003 @ 4 GHz 0.005 @ 8 GHz	0.004 @ 4 GHz 0.004 @ 8 GHz	0.53 @ 4 GHz 2.10 @ 8 GHz	0.014 @ 4 GHz 0.034 @ 8 GHz
Isolation (dB)	23.1 @ 4 GHz 23.4 @ 8 GHz	87.7 dB @ 4 GHz 73.6 dB @ 8 GHz	45.9 @ 4 GHz 45.8 @ 8 GHz	45.4 @ 4 GHz 38.6 @ 8 GHz	27.8 @ 4 GHz 22.4 @ 8 GHz

Chapter 4

Parametric Analysis and Optimization of MEMS Switches and Fractal Antenna

This chapter deals with the role of various optimization algorithms used for tackling the EM problems. Now-a-days, most of these optimization tools are compatible with simulated softwares available in the market. Optimization is the procedure of detecting the smallest of an operator defined cost function (CF). Optimizers modify the variable calculations until the lowest gets hold of it with adequate precision. The optimizers are distinguished by either search methods (SM) or error function (EF) formulations.

- The SM regulates the optimizer to reach at different parameter values. When optimizers perform their search method, they support different parameter values to consequence a decrease in the calculated value of error function.
- The EF formulation procedures the transformation between the desired and computed reactions. Lesser the significant value of the EF, the more thoroughly the reactions happen together.

Most advanced optimizers in case are local optimizers. Simulated Annealing (SA) and Genetic algorithm (GA) are global optimizers and further Random Optimizer has the ability to novelty the global optimal explanations.

To offer a wide choice of competence, HFSS software incorporates the subsequent kinds of numerical optimizers:

- Pattern Search (PS)
- ANN (matlab software compatible)
- Quasi Newton
- Sequential Mixed Integer Non-linear Programming (SMINLP)
- GA
- Sequential Non-linear Programming (SNLP)

The aforementioned optimizers take up the minimal problem which is to be analyzing and providing freedom of defining a specific problem formulation region, to describe an extreme limit of iterations, to state the linear association among the entered constraint and selected variables, and therefore help to reach the nearby optimal solution.

In this chapter ANN and PS optimization methods have been studied to enhance the performance of proposed MA and MEMS switches designed. MEMS switches configurations are similar as discussed in chapter 3 but different beam shape have been considered.

ANN is a unique widely held smart procedure in explaining engineering and mathematical problems. An ANN consists of neurons which are organized into different layers. These neurons are simple and several in number, contain non-linear type of functional blocks and they are mutually connected by very much similar synaptic weights. During the learning process, these synaptic weights could be weakened or strengthened and therefore helping the data to be kept in the ANN [80,100]. The benefits, feasibility and flexibility of ANN is that no formula is necessary to design planar antenna owing to its realistic nature, founded on the statement of physical occurrence, less computational time as compared with other optimization method, and its compatibility with commercial electromagnetic software [80, 100-102]. Neural networks can be used for the applications of wireless communications. In research domain of microwave devices, a NN has been preferred to construct rectangular planar antenna. Similarly, ANN has been preferred for the construction of circular MA [101], calculating various parameters for example resonant frequency, input impedance and return loss of circular MA.

The grid-based PS optimization is performed using simplex search, which makes use of tetrahedral in 3D and triangles in 2D space. The simplex represents the Euclidean symmetrical spatial element with least quantity of boundary defining points, for example tetrahedron in 3-D space, a trio in 2-D space, and line segment in 1D space. The optimization algorithm calculates the cost value at various vertices of the simplex geometric elements. The optimization process copies the simplex at one face and searches for new simplex for better results according to mathematical guidelines. If this process does not produce better result than pattern continues the next face in search used for mirroring. If no progress in results takes place, grid is refined. If progress in result comes about, the step/value is recognized and the fresh generated simplex replaces the original one.

4.1 Artificial Neural Network Introduction

An ANN consists of neurons which are organized into different layers. These neurons are simple, many, contain non-linear type of functional blocks and they are mutually connected to very much similar synaptic weights. During the learning process, these synaptic weights could be weakened or strengthened and therefore helping the data to be kept in the ANN [80, 100]. Neural networks can be used for the applications of wireless communications.

4.1.1 Neuro-computational Modeling for Design of Swastika Fractal Antenna

In this section, an ANN based easy method for the design of a swastika/gammadion geometry fractal antenna (SFA) as forward side and analysis as reverse side of problem has been proposed. SFA is simulated up to 2nd iteration by means of HFSS software, as geometry of antennas is shown in **figure 4.1**. The main benefit of using ANN technique is that a well-trained NN completely avoids the complex iterative procedure for the construction and analysis of this microstrip antenna.

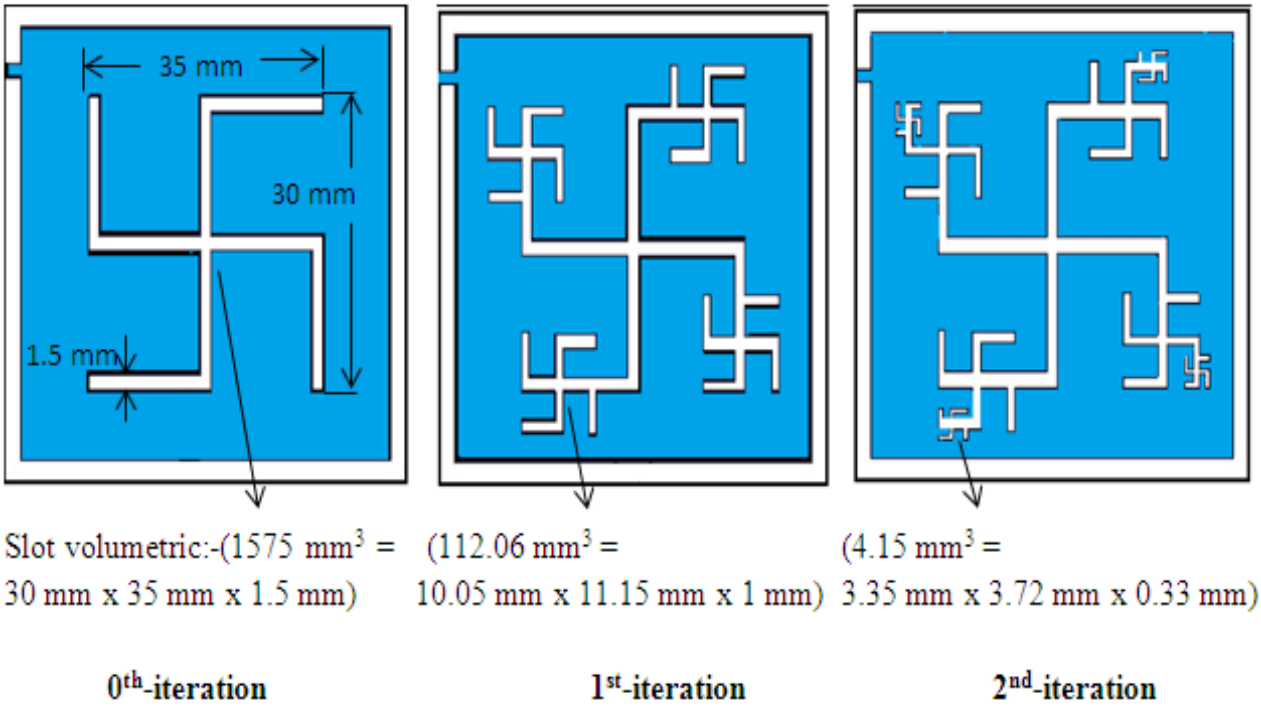

Figure 4.1- SFA Structures from 0th- to 2nd- iteration with Dimensions

Neuro-computational model for design of SFA is as shown in **figure 4.2**, indicates that proposed Feed Forward Back Propagation (FFBP)–ANN method having six inputs (resonant frequencies G_1 to G_5, thickness of substrate 't', dielectric constant of substrate 'ε_r' and number of iteration 'I' and slot volumetric of antenna (V), two outputs. NN trained on information dictionary make sure been useful to estimate the slot volumetric of SFA, i.e., 'V' and number of iterations 'I' for given values of resonant frequencies 'G', thickness of board 't' as well as dielectric constant of board 'ε_r'. The proposed ANN model contains the tan sigmoidal neurons in the form of one hidden layer having activation function is equal to 'f_1'. The input information is given to the first level and subsequently that output is set as input data for the final output level. The intermediate hidden level output is transmitted in the form of neurons to the final output level, containing two neurons and as a final point calculates the network output. In this case, the activation function is considered as 'f_2'.

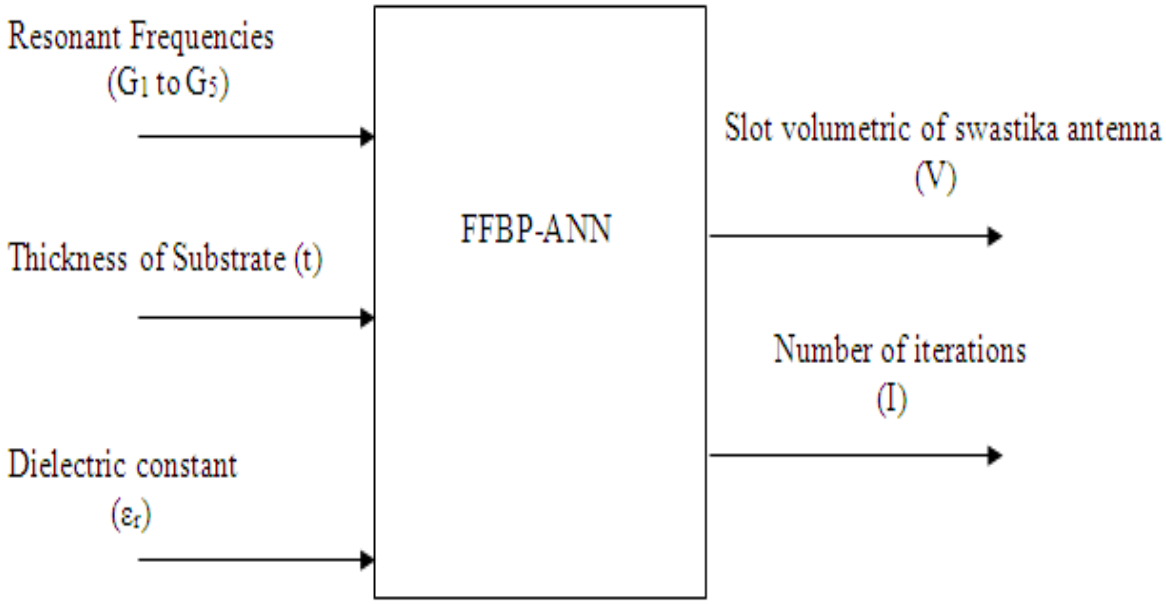

Figure 4.2- Neuro-computational Model for Design of Swastika-fractal Antenna

The output of presented ANN is calculated as-

$$X = f_2([OW](f_1([FW][Y] + [FB]) + [OB]) \quad (4.1)$$

$$Y = \begin{bmatrix} G_1 \\ G_2 \\ G_3 \\ G_4 \\ G_5 \\ t_i \\ r_i \end{bmatrix} \quad (4.2)$$

$$X = \begin{bmatrix} V_i \\ I_i \end{bmatrix} \quad (4.3)$$

$$FW = \begin{bmatrix} fw_{1,1} & \cdots & fw_{1,7} \\ \vdots & \ddots & \vdots \\ fw_{35,1} & \cdots & fw_{35,7} \end{bmatrix} \quad (4.4)$$

$$FB = \begin{bmatrix} fb_1 \\ \vdots \\ \vdots \\ \vdots \\ fb_{15} \end{bmatrix} \quad (4.5)$$

$$OB = \begin{bmatrix} ob_1 \\ ob_2 \end{bmatrix} \quad (4.6)$$

$$[OW] = \begin{bmatrix} ow_{11} & ow_{12} & \cdots & ow_{1,35} \\ ow_{21} & ow_{22} & \cdots & ow_{2,35} \end{bmatrix} \quad (4.7)$$

The performance term i.e. mean square error (MSE) is known by-

$$MSE = \frac{1}{n}\sum_{i=1}^{n}[y_i - F_{ANN}(x_i)]^2 \quad (4.8)$$

The proposed model has been trained with Levenberg Marquardt algorithm and structure 7-35-2 as depicted in **figure 4.3** is found best fit structure for estimation of dimensions of SFA. This ANN structure has an input layer with seven input neurons. A hidden layer with 35 hidden neurons and output layer have two output neurons.

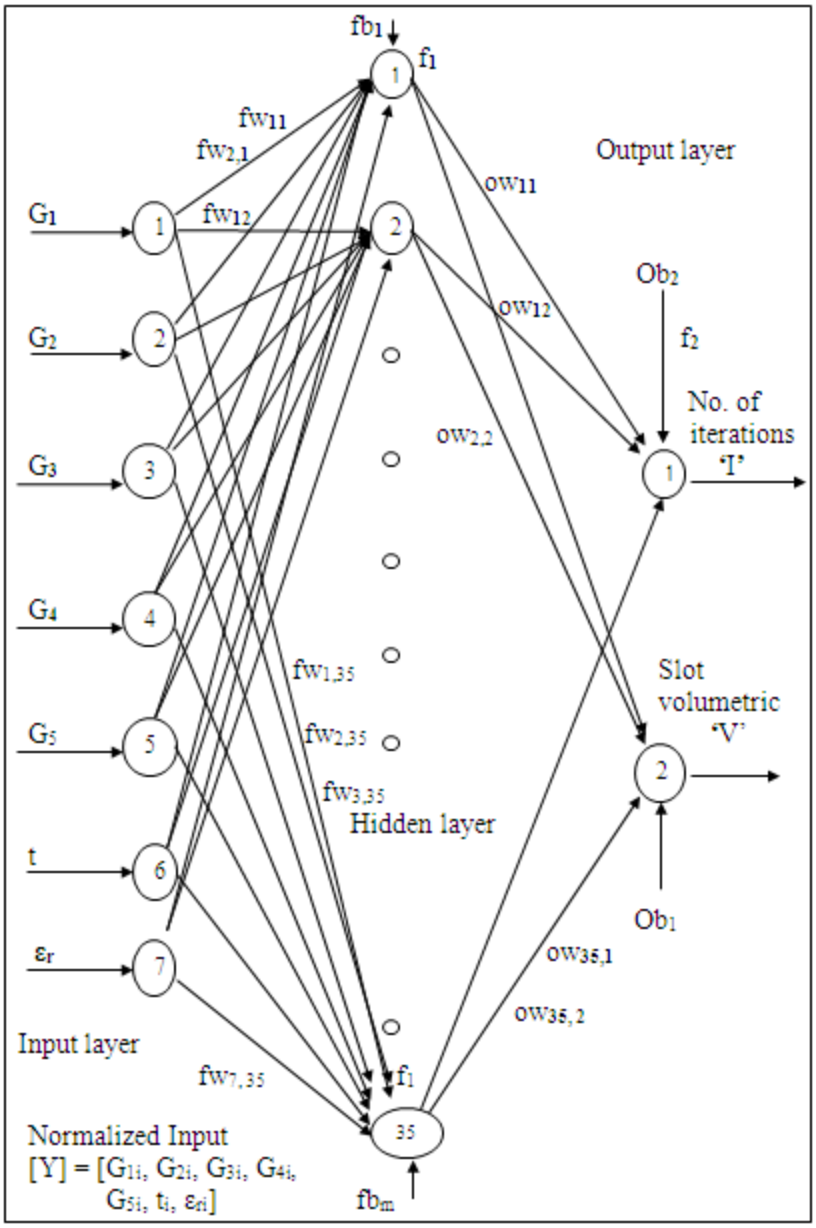

Figure 4.3- FFBP-ANN Constructed Neuro-computational aimed at Design of SFA

4.1.2 Neuro-computational Modeling for Analysis of SFA

For analysis of SFA reverse process is done. Thickness of substrate (t), dielectric constant (ε_r), slot volumetric of SFA (V) and number of iterations (I) are taken as input. Resonant frequencies, G_1 to G_5 are taken as output. Neuro-computational model for the analysis of gammadion fractal planar antenna is shown in **figure 4.4**. In the above example for analysis of SFA for zero iteration, we took input V, t, ε_r, I = 1575, 0.762, 3.48, 0 and G_1, G_2, G_3, G_4, G_5 =

2.32, 2.58, 0, 0, 6.43 as output. For first iteration, we took input V, t, ε_r, I= 112.07, 0.762, 3.48, 1 and G_1, G_2, G_3, G_4, G_5 = 2.1, 2.98, 0, 4.08, 6.02 as output. For 2nd iteration, we took input V, t, ε_r, I = 8.369, 0.762, 3.48, 2 and G_1, G_2, G_3, G_4, G_5 = 2.14, 2.86, 3.93, 4.14, 5.89 as output.

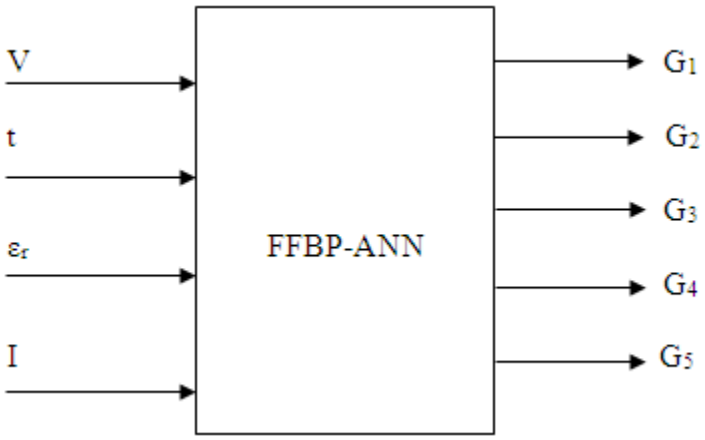

Figure 4.4- Neuro-computational for Computing the Resonance Frequency of SFA

For analysis of SFA, the presented model has been trained using Levenberg Marquardt algorithm and structure 4-35-5 as shown in **figure 4.5** is bring into being finest fit structure. NN expert on statistics dictionary make sure useful to estimate the resonant frequencies of SFA i.e., G_1 to G_5, for set value of slot volumetric 'V' and number of iterations 'I', thickness of board 't' and dielectric constant of board 'ε_r'. Further, the implemented neural model comprised of similar model as followed for training purpose.

The first layer with four neurons accepts input information and its output value is known as input to hidden layer with 35 neurons. The output value on or after neurons of hidden in between layer is conveyed to the final layer of five neurons, which to end with calculates the output of network. The output of presented ANN is calculated as-

$$X = f_2([OW](f_1([FW][Y] + [FB]) + [OB]) \quad (4.9)$$

$$Y = \begin{bmatrix} V_i \\ t_i \\ r_i \\ I_i \end{bmatrix} \quad (4.10)$$

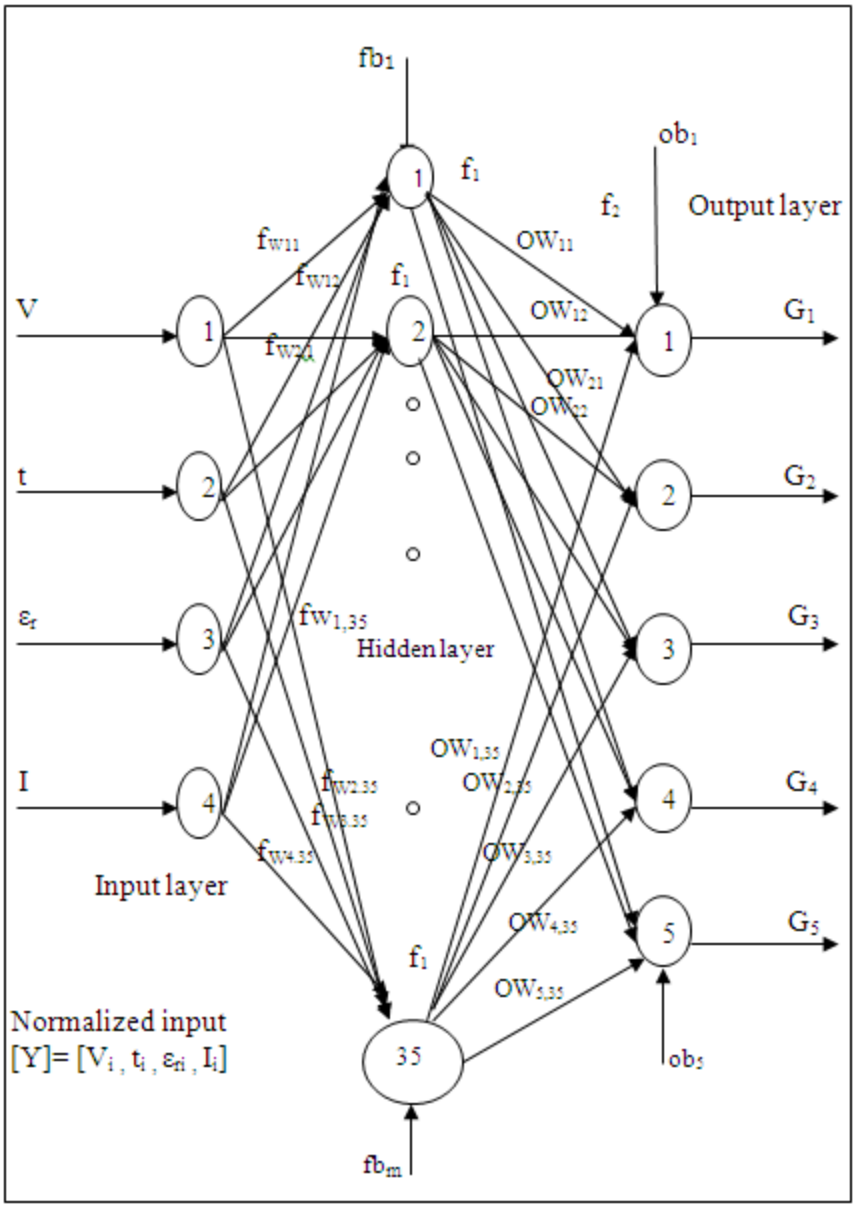

Figure 4.5- Proposed FFBP-ANN based Neuro-computational for Approximating Resonance Frequency of SFA

$$X = \begin{bmatrix} G_1 \\ G_2 \\ G_3 \\ G_4 \\ G_5 \end{bmatrix} \quad (4.11)$$

$$\text{FW} = \begin{bmatrix} fw_{1,1} & \cdots & fw_{1,4} \\ \vdots & \ddots & \vdots \\ fw_{35,1} & \cdots & fw_{35,4} \end{bmatrix} \quad (4.12)$$

$$[\text{FB}] = \begin{bmatrix} fb_1 \\ \vdots \\ \vdots \\ \vdots \\ fb_{35} \end{bmatrix} \quad (4.13)$$

$$[\text{OB}] = \begin{bmatrix} ob_1 \\ ob_2 \\ ob_3 \\ ob_4 \\ ob_5 \end{bmatrix} \quad (4.14)$$

$$[\text{OW}] = \begin{bmatrix} ow_{1,1} & \cdots & ow_{1,35} \\ \vdots & \ddots & \vdots \\ ow_{5,1} & \cdots & ow_{5,35} \end{bmatrix} \quad (4.15)$$

4.1.3 Results of Trained ANN

With the aim of calculating the performance results of presented FFBP-neural network created model for the SFA design, results of simulation are obtained using HFSS software for correct determination of dimensions of this antenna. ANN is trained using 75 inputs as well outputs training configurations. The training data obtained above is meant for training the presented 7-35-2 NN structure for design and 4-35-5 for analysis of SFA. Result in relations of performance analysis parameters for instance number of epochs in use aimed at training, performance goal MSE, maximum valued absolute error in addition to percentage error for design and analysis are shown in **table 4.1** and **table 4.2**, respectively. It is worth noting that detected total number of 292 epochs are desired to decrease level of MSE to a small value 9.89e-007 for design and 380 epochs are desired to decrease MSE level to a small value 9.87e -006 for analysis of SFA. Attainment of aforementioned low MSE value of performance target specifies that trained NN is a precise model for designing and analysis of SFA. Absolute error as well as % error at every value of slot volumetric and number of iterations for design and resonant frequencies for analysis as a consequence of learning with Levenberg Marquardt algorithm is

shown in **table 4.1** and **4.2**, respectively. The maximum error for estimating the slot volumetric and number of iterations is 0.0074 and 7.19e -004, respectively. Further, percentage error for estimating the slot volumetric and number of iterations of gammadion antenna are 0.39 and 0.035, respectively. Small value of this error indicates that neural model is an exact model for the design. Similarly, the maximum errors for estimating the resonant frequencies of SFA are 0.011, 0.007, 0.027, 0.005 and 0.004, respectively.

Table-4.1: Results of FFBP-NN Created Model for the Estimation of Slot Volumetric and Stage Number of SFA for Training Data

Training algorithm	Number of neurons in hidden layer	Epochs	MSE	Absolute error for estimation of		%age error for estimation of	
Levenberg Marquardt algorithm	35	292	9.89e-007	Slot volumetric 'V'	Iteration Number 'I'	Slot volumetric 'V'	Iteration Number 'I'
				0.0074	7.19e-004	0.39	0.035

Table-4.2: Results of FFBP-ANN based Model for the Estimation Resonant Frequencies of SFA for Training Data

Training algorithm	Number of neurons in hidden layer	Epochs	MSE	Absolute error for estimation of					%age error for estimation of				
Levenberg Marquardt algorithm	35	380	9.87e-007	G_1	G_2	G_3	G_4	G_5	G_1	G_2	G_3	G_4	G_5
				0.011	0.007	0.027	0.005	0.004	0.18	0.083	0.471	0.472	0.034

4.1.4 Validity Results of SFA Design

To test the results meant for SFA design we generated 45 inputs–output patterns for testing proposed trained 7-35-2 ANN structure for design and 4-35-5 ANN structure for study of aforementioned antenna. Absolute error as well as error (percentage FS) at every value of slot volumetric, number of iterations for design and resonant frequency for analysis of this antenna as proof of concept are shown in **table 4.3** and **table 4.4**, respectively. Attainment of such small

value of errors further indicates that the neural network is a perfect model used for the fractal antenna design and analysis.

Table-4.3: **Comparison of Error Obtained for Finding the Slot Volumetric and Stage Number of SFA using FFBP-ANN 6-35-2 Structure for Validation of Data**

	Absolute error for estimation of		**%age error for estimation of**	
Parameters	Slot volumetric 'V'	Iteration Number 'I'	Slot volumetric 'V'	Iteration Number 'I'
	0.060	0.032	2.899	1.601

Table-4.4: Comparison of Error Obtained for Finding the Resonant Frequencies of Fractal Antenna using FFBP-ANN 4-35-5 Structure for Validation of Data

	Absolute error for estimation of					**%age error for estimation of**				
Parameters	G_1	G_2	G_3	G_4	G_5	G_1	G_2	G_3	G_4	G_5
	0.017	0.035	0.123	0.089	0.068	0.291	1.200	0.386	2.211	2.171

4.1.5 SFA ANN Optimization Conclusion

In aforementioned particular sections, ANN based computation is proposed for developing high performance system to reduce development cycle which otherwise requires lengthy procedures and design cycles by conventional methods. The SFA described here used FFBP – NN using hidden layer as an estimated model for design and analysis. The results of the proposed methods are quite promising. From the analysis, it has been detected that the presented modeling procedure is very appropriate to model ANN for predicting the design parameters under specified conditions and applications of neural networks. By given modeling techniques the proposed design of antenna seems a simple inexpensive and correct method. The results obtained by discussed methods compared very well with simulated results.

4.2 Parametric Analysis on MEMS RF Switch

This section gives the parametric study of MEMS RF switch at small DC frequencies capable of 8 GHz which cater RA devices. The optimize post processing S-parameter results of MEMS

switch be influenced by the physical dimensions, dielectric constant as well other material properties of wafer, air gap and beam. During the construction of MEMS RF switches, the beam are prepared of gold, nickel, aluminum, copper, tungsten, chromium besides titanium [80] so far been presented in previous research. The change in dimensions like thickness, length and width, changes the '*k'*. As an outcome of this, S-parameter results can be optimized. The MEMS switch on which parametric optimization is performed displays outstanding RF features in terms of power consumption, current capability and also low pull-in voltage lying between 1.913 - 2.124 V. A FFBP algorithm of NN is as well considered for the justification of changing the arm upper beam width, length of anchor, and dielectric of MEMS RF switch. The NN collects novel data samples during training from FEM based electromagnetic solver tool HFSS. Analysis results of the NN are compared with the electromagnetic generated solver. These physical magnitudes are varied and then the switch is optimized to achieve best of S-parameters results. The established algorithm permits the optimization of the given structure to be passed out by substituting repeated simulations and furthermore offers smaller processing times although still retaining an exceptional accuracy as related with FEM modeling. The optimized IL and isolation outcomes are in decent settlement equal to 99.4% as compared with the theoretical results.

4.2.1 Optimization of Thickness and Cantilever Dimensions of MEMS Switch using NN and Parametric Analysis

The shunt MEMS switch is dealt by increasing the meander arm's length and thus also growing the overlapping area, as shown in **figure 4.6**. In the present work, CPW is designed using gold having center conductor width of 102 µm besides gap of 58 µm to form the 50Ω characteristic impedance. The thickness of CPW is 0.8 µm. The dielectric layer of 0.2 µm thick silicon nitride is coated on the center conductor. The ε_r of the film is 7.5. The anchors with 2.2 µm height were attached to the CPW ground surface and the beam is connected to these anchors using four square-arms of width 10 µm. It consists of 1 µm thick aluminum. The detailed physical dimensions are ($a \times b \times t \times w \times g_o =$ 14 µm × 68 µm × 0.8 µm × 5 µm × 2.5 µm). The torsion length is taken as 55 µm.

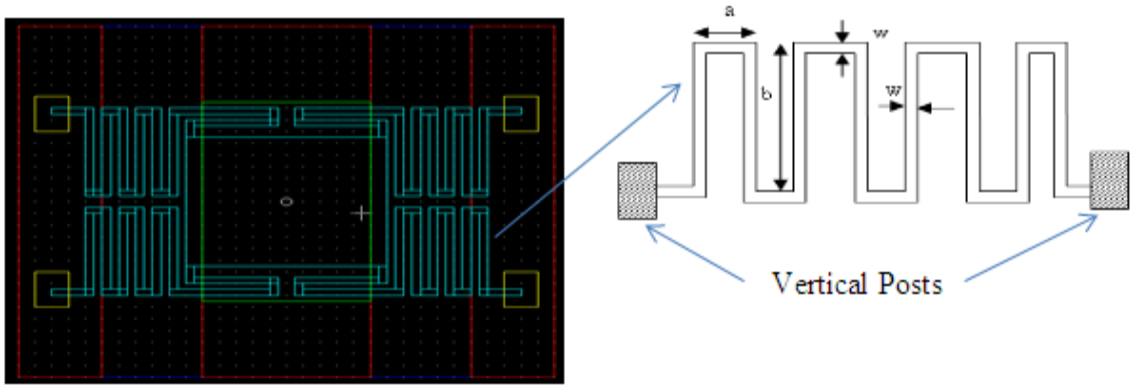

Figure 4.6- Extended Meander-shaped MEMS Shunt Switch for Parametric Optimization

For aluminum beam, the '*k*' of the RF switch is originated as 0.098 N/m to be calculated from equation 3.5. With gap g_0 = 2.5 µm between center conductor and electrode beam, the simulated pull-in voltage (V_{pi}) of the RF switch is 2.1 V and verified from equation 3.8. In up-configurations, the MEMS switch showed RL of 22 dB to 56 dB at *C*, *X* and *L* band frequencies. The IL of 0.05 dB at 6 GHz and 0.12 dB at 12 GHz is measured. In down-configurations, the MEMS switch displayed RL less than 1.5 dB at *C*, *X* and *L* band frequencies and isolation of the switch is 23 dB at 12 GHz. With C_{up} = 51.3 fF and C_d = 4.9 pF and L = 17 pH, the resonance comes about at 170 GHz and 17.5 GHz. The cut-off frequency of the MEMS for switch resistance R_s = 0.55 Ω and C_{up} = 51.3 fF is 5.6 THz.

4.2.2 Generation of Input Samples

The NN collects novel input data for the purpose of training from HFSS. The deviations in S-parameter results due to change in physical magnitudes are displayed in **figure 4.7** to **figure 4.11** in view of the MEMS switch in on- as well as off- position.

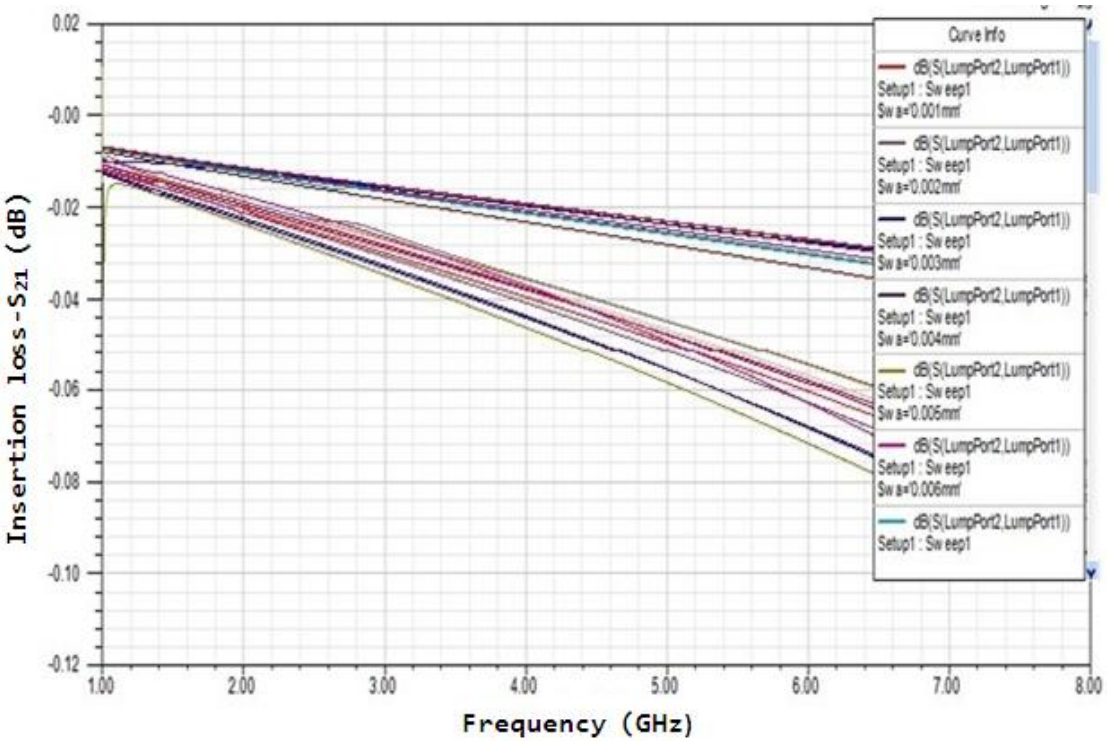

Figure 4.7- Effect of Varying the Anchor Arm Width at ON- position of MEMS Switch

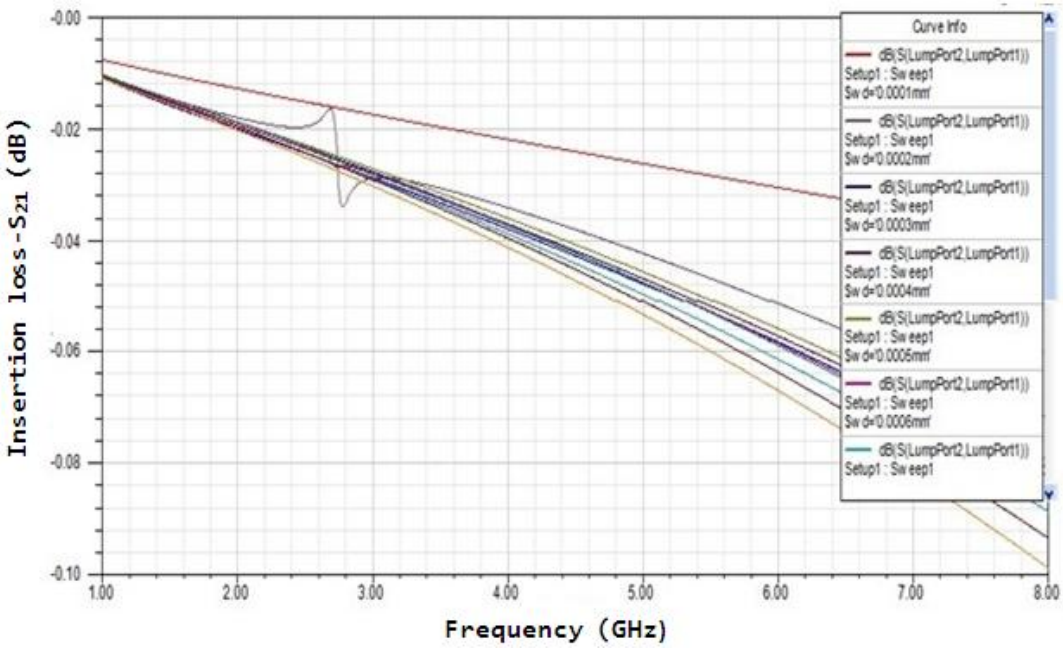

Figure 4.8- Effect of Varying the Dielectric at ON-position of MEMS Switch

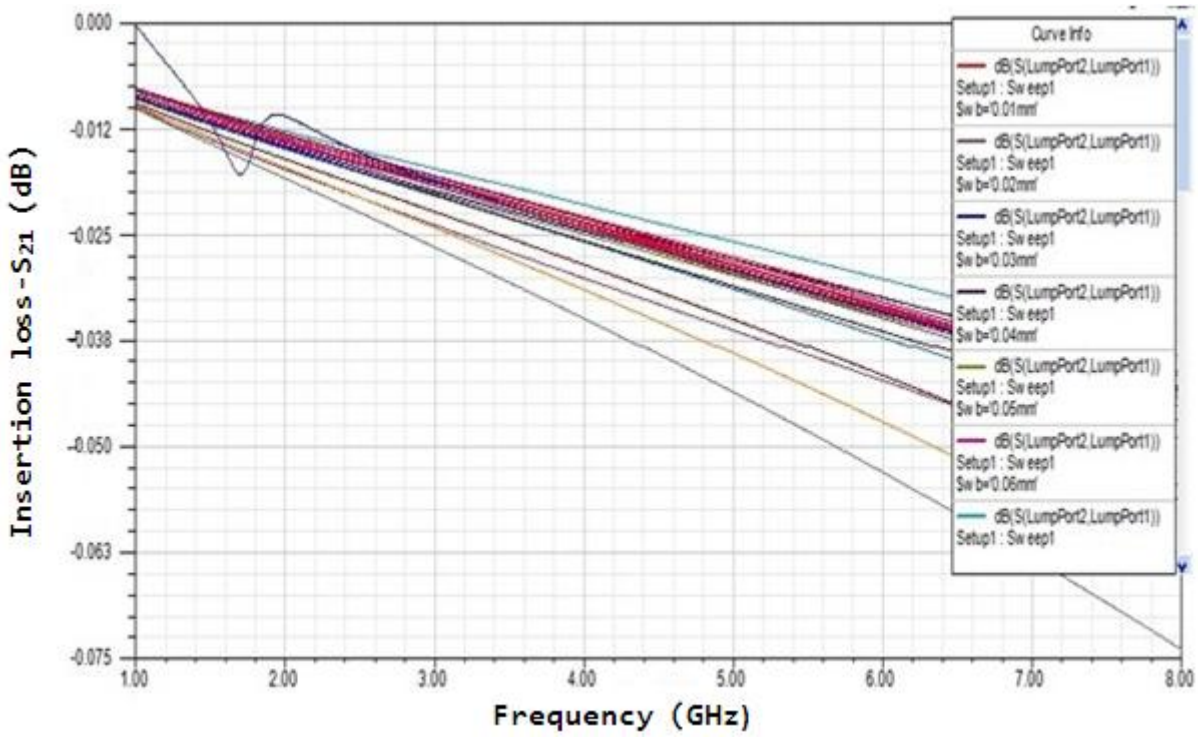

Figure 4.9- Effect of Varying the Top Beam Width at ON-position of MEMS Switch

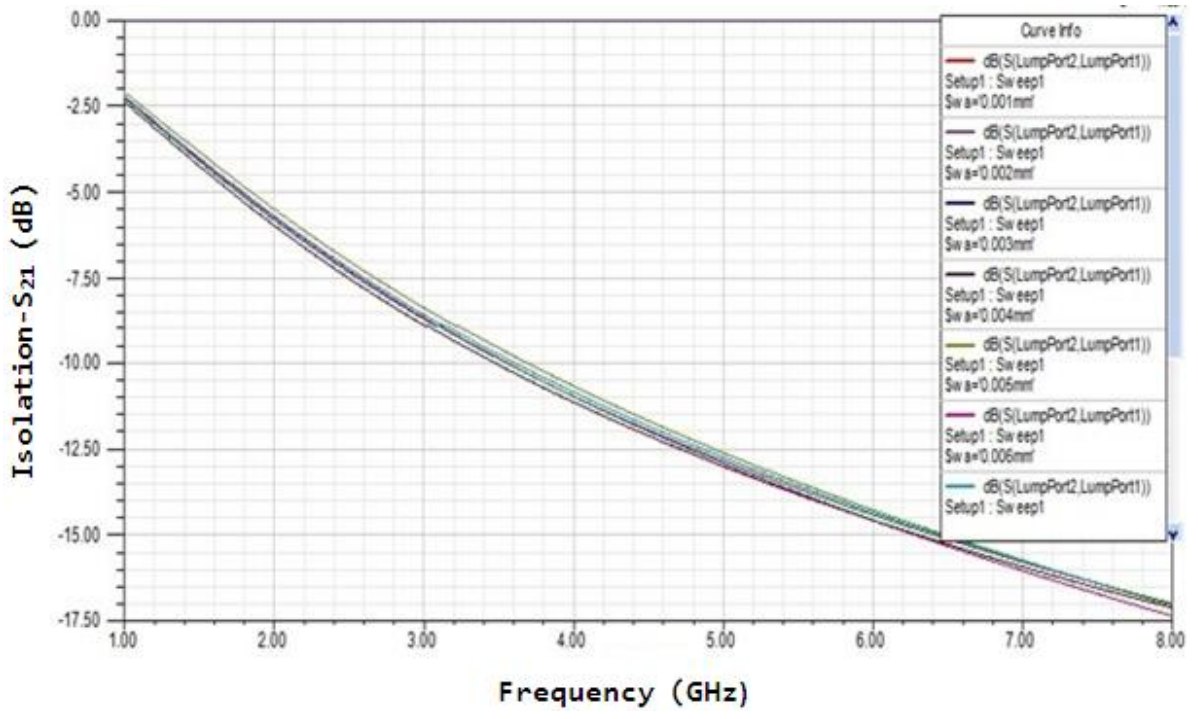

Figure 4.10- Effect of Varying the Arm Width of Anchor at OFF-position of MEMS Switch

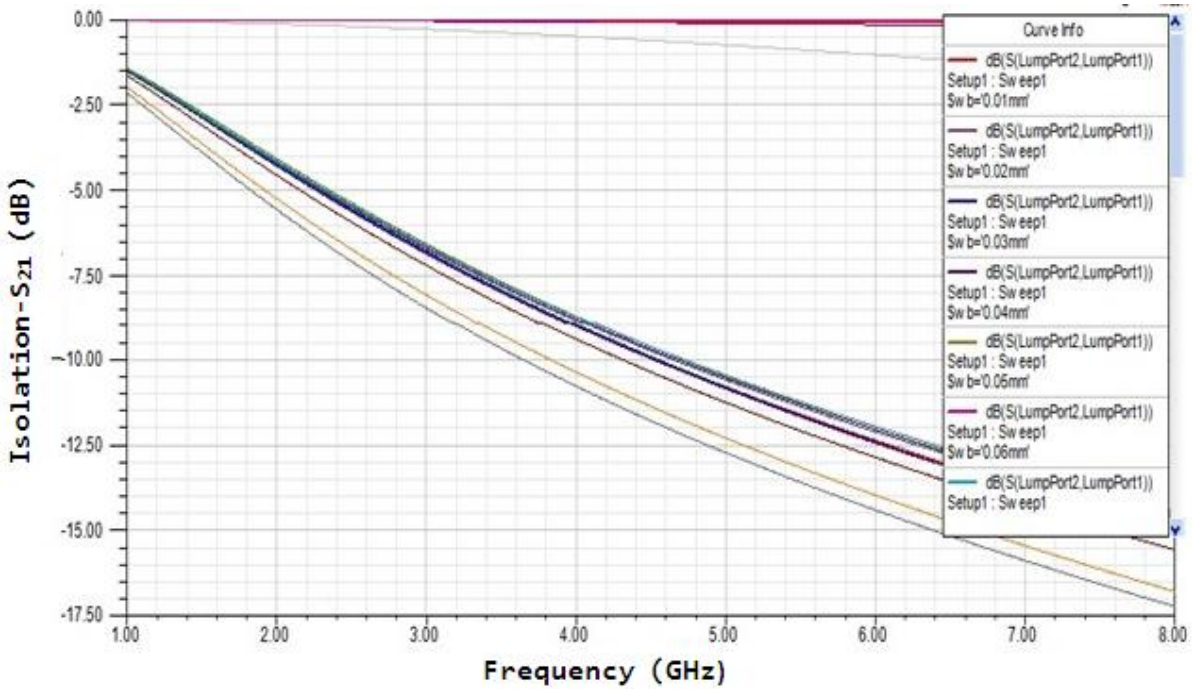

Figure 4.11- Effect of Varying the Top Beam Width at OFF-position of MEMS Switch

4.2.3 NN Analysis and Comparative Study

An NN is followed by a multi-layered perceptron procedure here for the justification of altering the dielectric, arm length of anchor, top beam width of MEMS switch. The 1000 data values are produced as of HFSS software and 160 input samples data have been taken for NN. The produced data is preferred for training, validating and testing of FFBP-NN procedure. The procedure involves the input level, three hidden levels and output level. The first level has 35 neurons. The data produced by changing magnitudes is first analyzed and calculated in HFSS solver. After further observations, finest results are computed by keeping rest of the two physical magnitudes constant. Considering both (up- as well down-) configurations, the finest result are recorded when the arm width is taken as 0.006 mm, dielectric is 0.0007 mm and beam width is 0.0l mm. The parameter called learning rate for the training purpose of the NN is considered to be 0.00l. Best validation results of the NN are recorded to be 0.0148 at epoch value 9, as displayed in **figure 4.12**.

In the course of training the NN spontaneously corrects its threshold and weight values so that the inaccuracy between sampled and predicted outputs is reduced. “Trainlm” training algorithm is used. The transfer functions (TF) favored is Purelin and Tansig in the design. The

FFBP-NN architecture followed here is analyzing the post-processing result of MEMS switch design with high accuracy and efficiency. The training and testing results are shown in **table 4.5** and **table 4.6**.

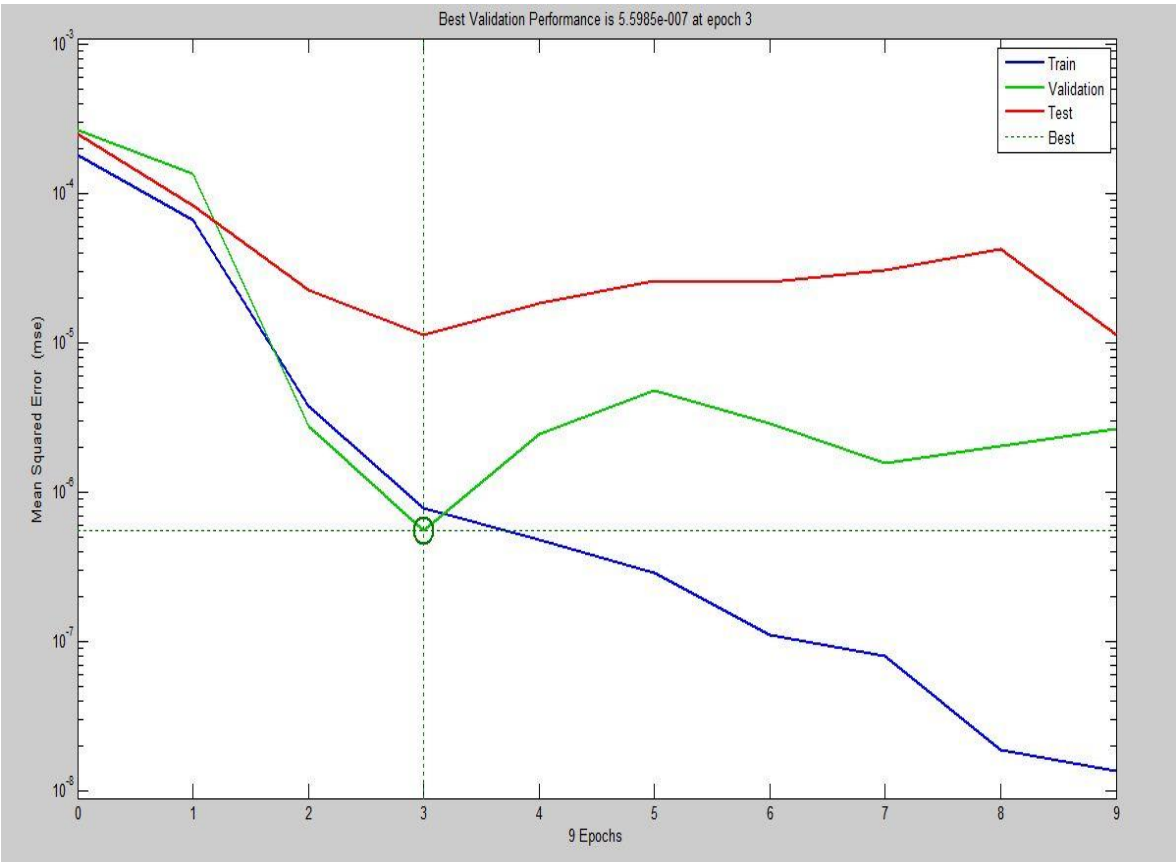

Figure 4.12- Performance Analysis of FFBP-NN Technique Established for Model the MEMS Switch

Table-4.5: Error Difference between Tested and Training Data of S-parameter Results at ON-position of Switch

Sr. No.	Target and Training IL-S_{21} at optimized arm width generated by HFSS	Target and Training IL-S_{21} at optimized dielectric thickness generated by HFSS	Target and Training IL-S_{21} at optimized beam width generated by HFSS	Tested data of ANN S_{21} arm width	Tested data of ANN S_{21} dielectric	Tested data of ANN S_{21} beam width	Average difference between target and tested data
1	-0.0067	-0.007691	-0.00793	-0.012091	-0.01046	-0.01325	0.00532
2	-0.0089	-0.010145	-0.010172	-0.0088734	-0.010145	-0.012626	0.0024539
3	-0.0109	-0.012445	-0.012349	-0.010369	-0.012445	-0.014619	0.0022705
4	-0.0129	-0.014678	-0.014506	-0.013303	-0.014678	-0.014633	0.0001274
5	-0.0147	-0.016808	-0.016546	-0.014728	-0.017925	-0.016753	0.00020652
6	-0.0165	-0.018952	-0.018519	-0.017455	-0.018952	-0.018727	0.00020771
7	-0.0183	-0.020996	-0.020477	-0.018685	-0.019129	-0.015447	-0.00503
8	-0.0201	-0.023044	-0.022566	-0.020527	-0.019839	-0.021606	-0.00096
9	-0.0219	-0.025044	-0.024567	-0.023028	-0.025044	-0.028112	0.0035454
10	-0.0237	-0.02706	-0.026597	-0.024185	-0.02706	-0.026448	-0.0002
11	-0.0256	-0.029069	-0.028651	-0.024061	-0.029069	-0.028859	0.00020766
12	-0.0274	-0.031044	-0.030708	-0.025356	-0.031044	-0.031156	0.00044826
13	-0.0293	-0.033049	-0.032835	0.029946	-0.033049	-0.032698	-0.0002
14	-0.0313	-0.035056	-0.035001	-0.032608	-0.035056	-0.036341	0.0013403
15	-0.0333	-0.037038	-0.03717	-0.032781	-0.035061	-0.037418	0.00024773
16	-0.0345	-0.039057	-0.039402	-0.032776	-0.035332	-0.037431	-0.0019711

Table-4.6: Error Difference between Tested and Training Data of S-parameter Results at OFF-position of Switch

Sr. No.	Target and Training isolation-S_{21} at optimized arm width generated by HFSS (0.006 mm)	Target and Training isolation-S_{21} at optimized dielectric thickness generated by HFSS (0.0002)	Target and Training isolation-S_{21} at optimized beam width generated by HFSS (0.11 mm)	Tested data of ANN S_{21} arm width	Tested data of ANN S_{21} dielectric	Tested data of ANN S_{21} beam width	Average difference between target and tested data
1	-6.1763	-5.0094	-5.0006	-5.2087	-5.1032	-6.1086	-0.3234
2	-6.7654	-6.1517	-6.3878	-6.2086	-6.3645	-6.4321	0.0164
3	-7.6743	-7.1706	-7.5489	-7.0986	-7.6438	-7.5463	0.0203
4	-8.7674	-8.4710	-8.44249	-8.5497	-8.5216	-8.6542	-0.1682
5	-9.145	-9.0815	-9.3073	-9.1564	-9.4530	-9.275	-0.0089
6	-9.6626	-10.0391	-10.068	-10.1654	-10.0316	-9.748	-0.0061
7	-10.7070	-11.1754	-10.7277	-11.0897	-10.6021	-10.8065	0.4949
8	-11.6590	-12.1975	-11.4058	-12.0876	-11.5012	-11.5479	-0.0057
9	-12.5187	-13.1138	-11.8287	-13.0768	-11.7021	-12.6584	-0.4295
10	-13.3214	-14.0122	-12.2499	-14.1265	-12.2499	-13.4327	-0.4455
11	-14.0635	-15.1079	-13.0752	-15.0976	-13.1093	-14.0764	-0.4759
12	-14.7437	-15.811	-14.8159	-15.7654	-14.7864	-14.0423	-0.5402
13	-15.3894	-16.0508	-15.4220	-16.1546	-15.653	-15.4753	-0.6136
14	-15.9955	-16.4898	-15.8662	-16.3476	-15.7539	-15.9852	-0.7122
15	-16.5586	-16.9997	-16.3175	-16.9437	-16.4092	-16.6036	-0.8491
16	-17.0996	-17.4211	-17.2093	-17.8765	-17.1032	-17.0960	0.1450

4.3 Optimization of Isolation and IL using Pattern Search Method

The PS algorithm is a non-random technique for examining minima of a fitness function which is not essentially stochastic, continuous, or even differentiable without needing the gradient knowledge. For this reason, it can be exploited capably in explaining optimization problems. As contrasting to more old-style optimization techniques that use knowledge about the higher derivatives or gradient to look for an optimum point, a PS method explorations set-points nearby the current point [45], aiming at a unique solution, where the experimental value of the CF is lesser as compared to value at the existing point. The insertion, isolation and RL of presented MEMS switch in on-off condition are optimized using PS method. These parameters were improved by varying the physical dimensions (width and length) of transmission lines as shown in **figure 4.13** and **figure 4.14**. The substrate thickness and cantilever dimensions are already optimized during the designing process of the RF switch. Here the problem statement and objective function is given by varying dimensions of transmission line of RF MEMS switch to find the maximum transmission from Wave Port 1 to Wave Port 2 (S21=>1), define the CF to be –mag (S (WavePort2,WavePort1)) at some specific frequency. The physical dimensions for optimization purpose must be limited so as to avoid the overlarge size as compared with the substrate area, so the restrict limits are set as (20 μm ≤ (L = length) ≤ 45 μm) and (5 μm ≤ (W = width) ≤ 25 μm), respectively. During optimization analysis, the target is set to identify maximum condition to achieve aforementioned CF in both on and off position.

Table 4.7 summarizes the optimized S-parameters of metal-contact switch at 5 GHz. The PS optimization takes six and eight iterations in on and off-positions to optimize the S-parameters with simulation time of 39 and 38 minutes, respectively. The minimum CF is achieved in fourth iteration in on position and sixth iteration in off position. The optimized value of length and width in on-position are 45 μm and 25 μm, and in off-position of switch are 20 μm and 5 μm. It has been observed from optimized results there is a that major improvement in isolation, reasonable improvement in RL and minor improvement in IL of the optimized switch as compared to unoptimized switch. This is because that PS algorithm follows the designing equations for antenna analysis and not includes the transmission-line effect. As a result they are simply beneficial for comparison through simulated data in controlled conditions.

Table-4.7: S-parameters of MEMS Switch at 5 GHz

S-parameters	Without optimization (dB)	With PS optimization (dB)
Insertion loss	-0.32	-0.28
RL in down-state	-17.59	-20.25
Isolation	-41.95	-60.90
RL in up-state	-0.0008	-0.0001

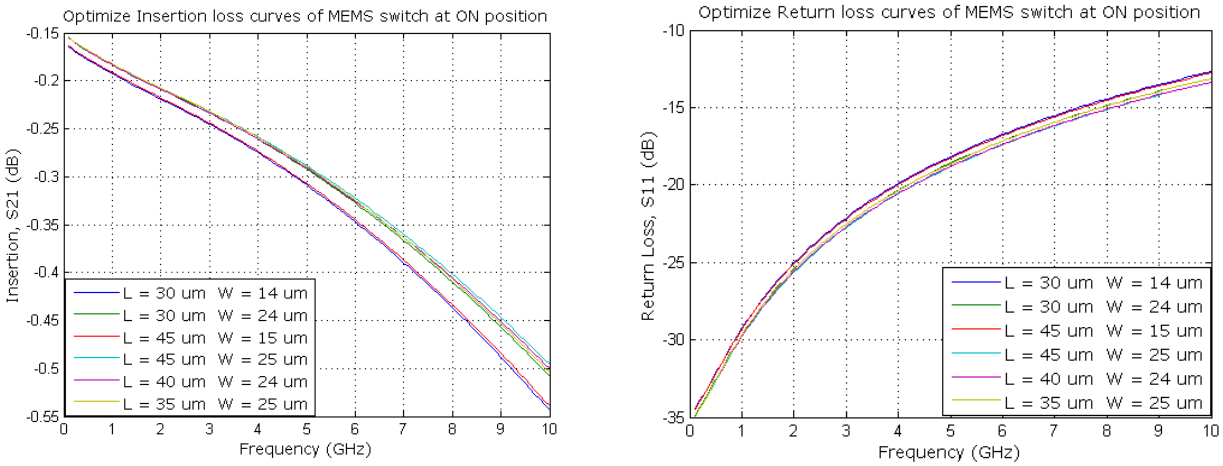

(a) **(b)**

Figure 4.13- Optimized Results at ON-position of Switch (a) Insertion (b) RL

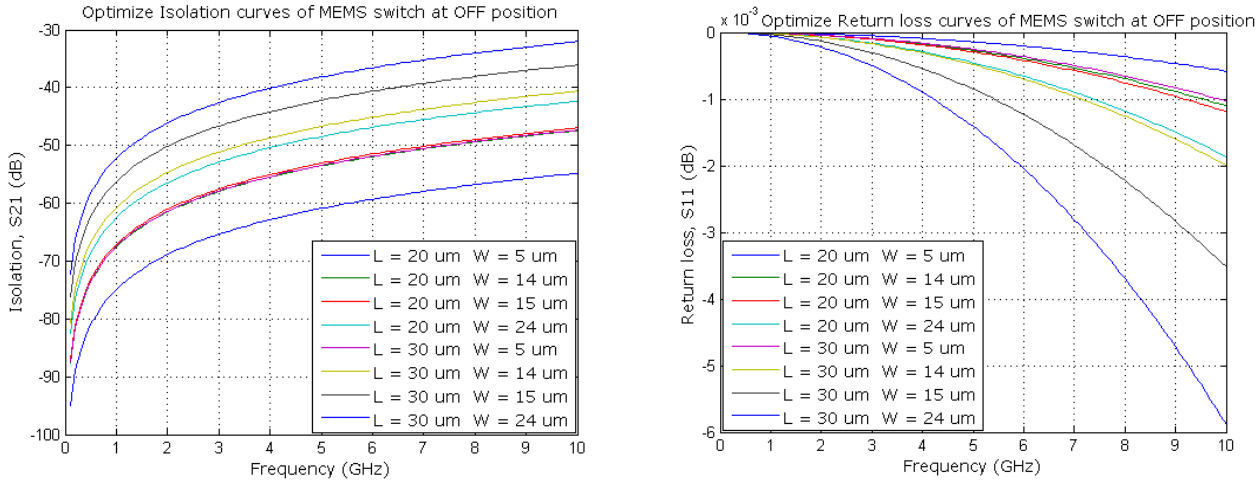

(a) **(b)**

Figure 4.14- Optimized Results at OFF-position of Switch (a) Isolation (b) RL

4.4 Summary of the Chapter

In this chapter optimized RF MEMS switches and fractal antenna are proposed. The effects of varying different geometrical parameters of presented designs on S-parameters are analyzed by using HFSS. It has been examined that there is always a tradeoff in design performance, when the parametric analysis has performed. Some of the post-parameter results are optimized at the cost of other results and thus providing the option to the user to choose the best outcomes depending on the application of the device. In next chapter, the optimized switches are act as prefect switching elements and used to reconfigure the frequency of the proposed optimized as well as other antennas.

Chapter 5

Multiband and Reconfigurable Antennas

5.1 Reconfigurable Antennas Analysis

A RMA is made of antenna patch elements, which are trained independently to reconfigure their physical configuration through RF switches and thus modifying the frequency and polarization characteristics of the MA. However, reconfiguring one property of the MA affects the rest, i.e. alteration in frequency response results in change of radiation pattern and vice versa. This relation is one of the principal challenges in the growth of RMA.

The structure diversity of RMA involves variable-geometry arrangements, which should be specifically controlled via good quality of RF switches. Here, from good quality of RF switches means good switching characteristics, which includes inherent low IL, high isolation, and linearity as well as minimum power consumption. Furthermore, using few of these RF switches for reconfiguration purpose of an MA is adequate; nevertheless when they are used in big numbers the degradation of the MA characteristics is noticed. In this chapter, three different configurations of MA have been presented to alter their physical structure through MEMS RF switches. MEMS switches deal greater RF characteristics and therefore they can get combined in great quantities surrounded by the antenna geometry. In addition, they can be organized by means of high resistance bias electric lines over an actuating pad; consequently the bias network of MEMS RF switches can be widespread in big antennas arrays without affecting any degradation and interference to the MA patterns. The bias DC network also consumes less power, which is an essential aspect when huge numbers of RF switches are used, especially for wireless mobile or aero-space applications. Their micro-scaled size and capability to become integrated monolithically surrounded by the antenna structures on high efficiency microwave substrate make the MEMS RF switches the perfect solution for RMA structures. Point toward this goal a novel, modest, consistent and easy to deal with MEMS RF switch has been proposed in **chapter-3**.

Due to the multi-level designing procedure of RMA, the numerical computational modeling method poses high scale challenges. ANN optimization method, which has already

been proposed comprehensively in **chapter-4** for designing of the gammadion geometry multiband MA, can handle non-differentiable, multi-dimensional, and discontinuous cost functions using numerous potential local maxima despite the fact converge quickly to the optimum end result. Considering the proposed optimized MEMS switches in chapter 3 as a switching elements for MAs, three RMAs are analyzed and discussed next.

5.1.1 Gammadion-shaped Multiband Antenna

In this section the theory of fractal (i.e. self-similar properties) has been implemented on the structure of square patch MA to achieve multi-band operating frequencies. The unique self-similar geometry particularly used here for designing of conducting patch, called as "swastika (gammadion geometry)", is displayed in **figure 5.1**.

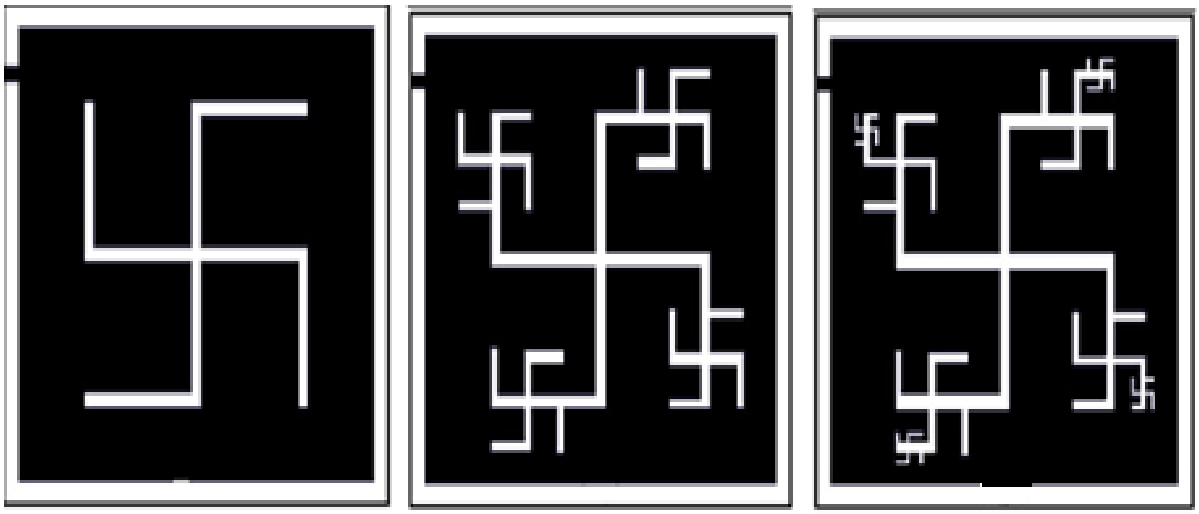

Stage 0 Stage 1 Stage 2

Figure 5.1- Gammadion-shaped Fractal Slot Antenna upto of 2nd Iteration

The 2nd iteration gammadion antenna has been converted into RMA by combining with MEMS RF switches.

Design of microstrip antenna requires resonant frequency, dielectric constant and substrate thickness. For designing SFA, to begin with, patch dimensions of (30 mm x 35 mm x 1.5 mm) with slot volumetric (V), 1575 mm^3; substrate material Roger RO4350 printed circuit board (PCB) having 't' is equal to 0.762 mm, and 'ε_r' is 3.48 have been taken to get 0th iteration

structure as illustrated in **figure 5.1 (a)**. The antenna is simulated by means of HFSS simulator. RL versus frequency plot is shown in **figure 5.2**. As shown in **figure 5.2**, it is clear that the RL is less than -10 dB at three different frequencies of 2.31 GHz, 2.57 GHz and 6.44 GHz. Further, the sizes of length (l), breadth (b) & width (w) of slots are equal to 1/3rd of 0th iteration sizes i.e. 10.05 mm x 11.15 mm x 1 mm are dropped from this geometry to get 1st iteration structure which is illustrated in **figure 5.1 (b)**. The geometry is simulated over again and a plot of RL versus frequency is as shown in **figure 5.3**. From this plot, it is understandable that RL is less than -10 dB at four different frequencies of 2.10 GHz, 2.97 GHz, 4.08 GHz, and 6.01 GHz. Subsequently the sizes of slot volumetric are dropped 1/9th times the sizes of 0th iteration structure i.e. 112.07 mm^3 from 1st iteration structure to get 2nd iteration structure which is shown in **figure 5.1 (c)**. The slot volumetric is now equal to 4.15 mm^3. This structure is again simulated by means of HFSS simulator and RL versus frequency plot as illustrated in **figure 5.4**. Commencing this figure, it is understandable that RL is less than -10 dB at five different frequencies of 2.15 GHz, 2.86 GHz, 3.93 GHz, 4.14 GHz and 5.90 GHz, respectively.

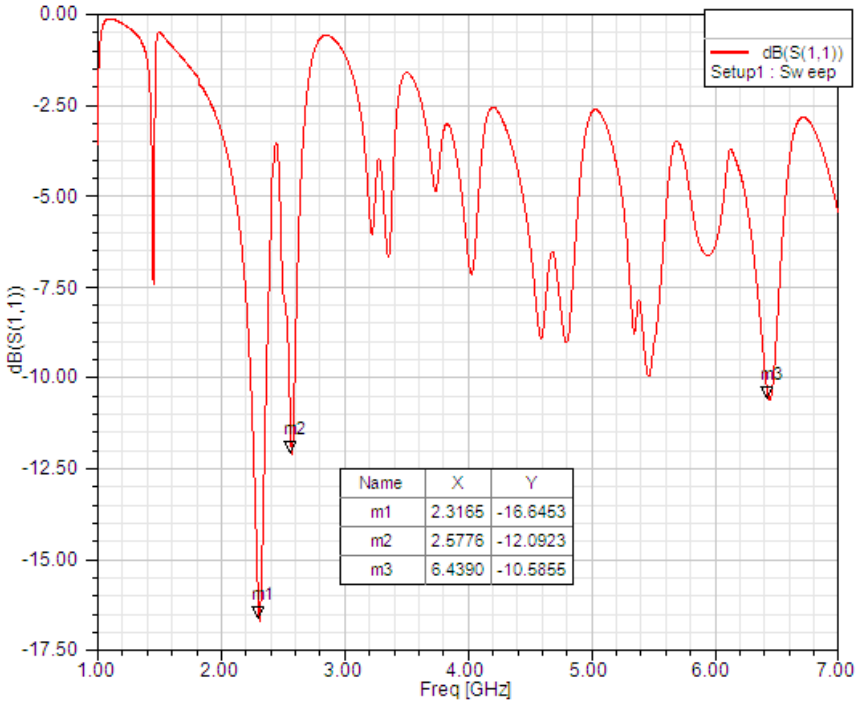

Figure 5.2- RL versus Frequency Plot of SFA aimed at 0th Iteration

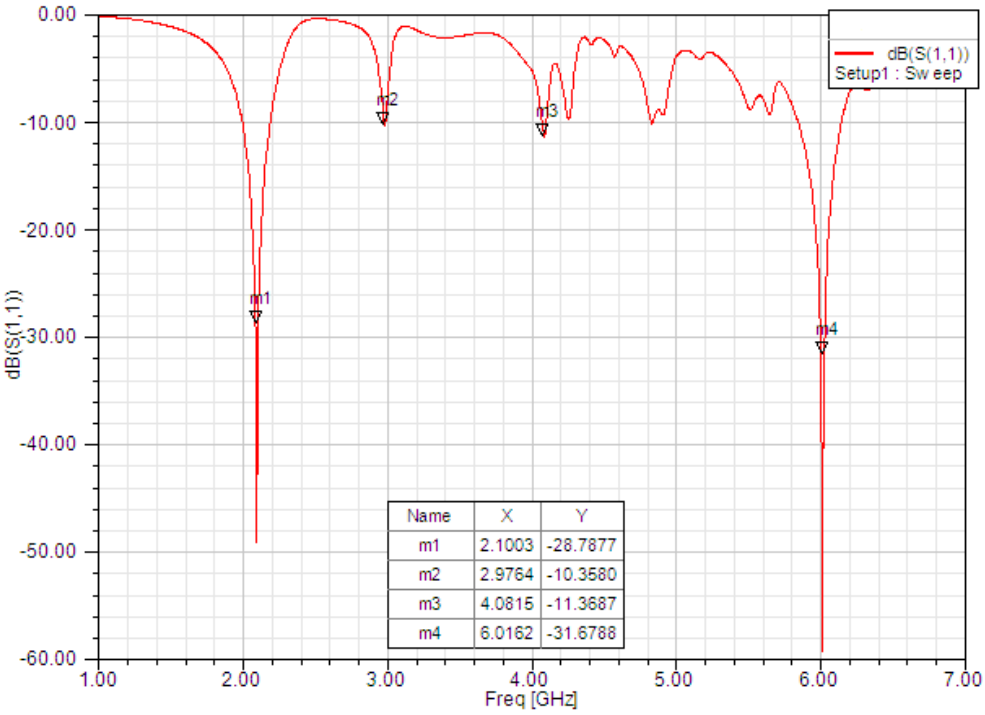

Figure 5.3- RL versus Frequency Plot of SFA aimed at 1st Iteration

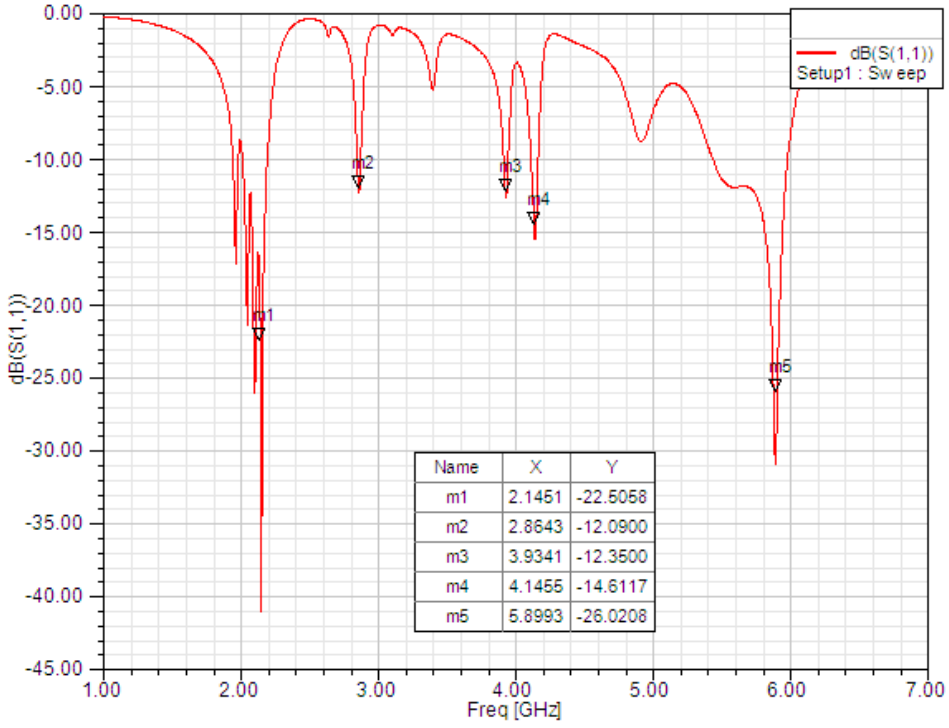

Figure 5.4- RL versus Frequency Plot of SFA aimed at 2nd Iteration

5.1.1.1 Gammadion RA Designing and Testing Arrangement

In this specific section the proposed 2nd iteration SFA is transformed into RA by applying RF switches. The schematic and dimensions (in mm) of proposed RA along with location of RF switches, is shown in **figure 5.5**. Initially, the minimum gap of RF switch size was provided between each individual gammadion shaped slot. As of the simulation perspective, the series cantilever MEMS RF switch selected for gammadion RA is same as that of described in **section 3.4.3**. When the MEMS switch is in on-position, its equivalent lumped component values are mentioned as, R_{sw} = 3.98 ohm and L_s = 2.52 Henry. Whereas in case of off-position the MEMS RF switch indicate the value of the C_c = 2.74 fF. These aforementioned RLC lumped values act as the equivalent switching elements and located at the appropriate slot i.e. in between the patch on the microstrip antenna. So, according to structure of RA, a total of eight switching RLC elements are employed as exhibited in figure 5.5. The simulation of the RA along with MEMS RF switches is done using HFSS simulator. There are total 256 (=2^8) switching configuration (i.e. on- and off-) can be generated by using eight switches and in effect of this RA is alter its response at different resonance frequencies. The S-parameter results confirm that RA worked well between 1.8 to 6.4 GHz at particular operating frequency band.

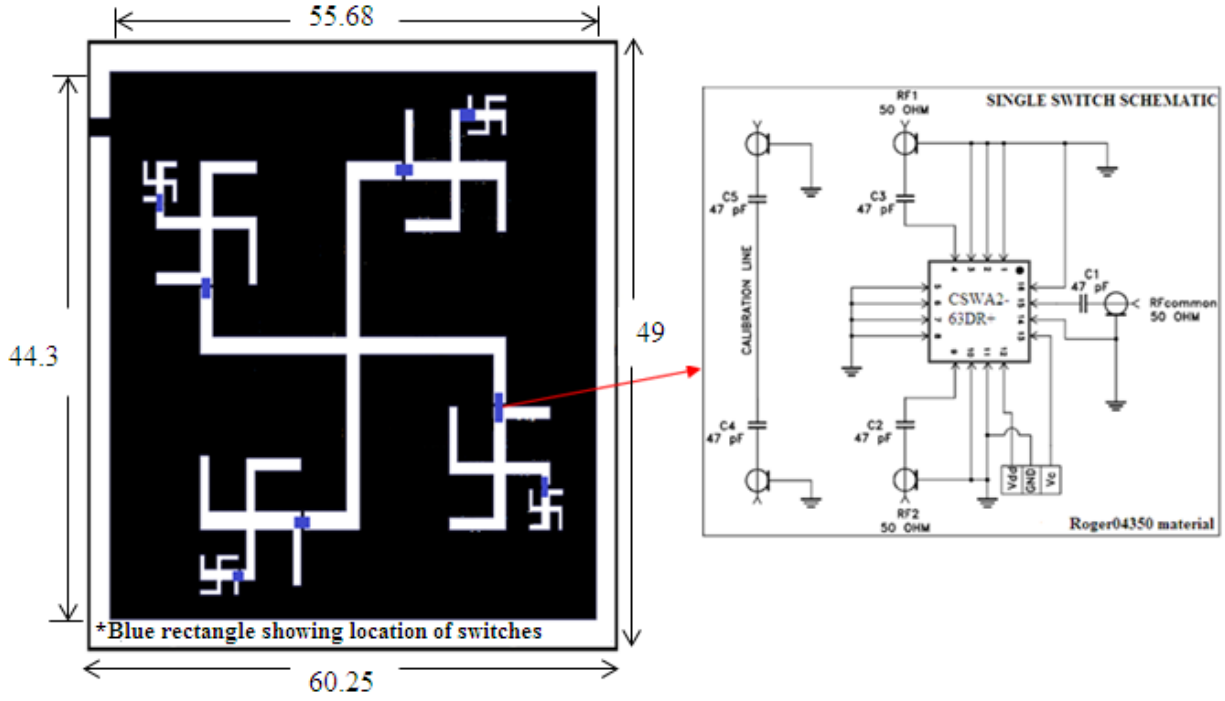

Figure 5.5- Reconfigurable SFA Dimensions and Switch DC Biasing Schematic

The normalized radiation pattern explanation for the RA at extreme switching configuration (all-on and all-off) is incorporated afterward. At specified resonant frequency, the deviation of current distribution on the patch surface by means of different switching configurations is the reason for the generation of different patterns. Normalized power radiation patterns, i.e., YZ-, XZ- and XY- cut patterns are displayed in **figures 5.6 (a) – 5.6 (d)** at specified frequency 4 GHz are attained. The collective magnitude of the E- field components in the preferred polarization are shown next in **figures 5.6 (e) – 5.6 (f)**. A figure of eight pattern in XY-plane (as displayed in **figure 5.6 (b)** indicates a dipole shape of radiation pattern. RA as estimated realizing fairly normalized omni directional radiation patterns. As of 3D pattern plot, it has been noticed that the microstrip antenna behave non-directional in the azimuth plane and steering in the elevation plane. Additionally, the RA is presenting well-behaved linearly polarized performance as because of axial ratio (E_y/E_x) is greater than one at theta is equal to zero.

For testing purpose, the anticipated RA with RF switches fabrication and electromagnetic measurement setup are majorly divided into five subdivisions - gammadion planar antenna, SPDT RF switches (CSWA2-63DR+) PCB including DC biasing pad and tracks, variable DC regulated power supply to change the desired configuration (on/off) of RF switches, Agilent Technologies E5071C Vector Network Analyser (VNA) and last the anechoic chamber. For the proof of the concept equivalent absorptive ceramic SPDT RF switch having almost similar isolation, IL and characteristics impedance equal to 50 ohm as related to proposed series cantilever switch is considered. The aforementioned RF switch consumes very less power (in micro-watt) and the supply current value is around 18 micro-amperes. It is a hermetic package, small in size (4 mm x 4 mm x 1.2 mm), low profile, and also having an internal driver circuit.

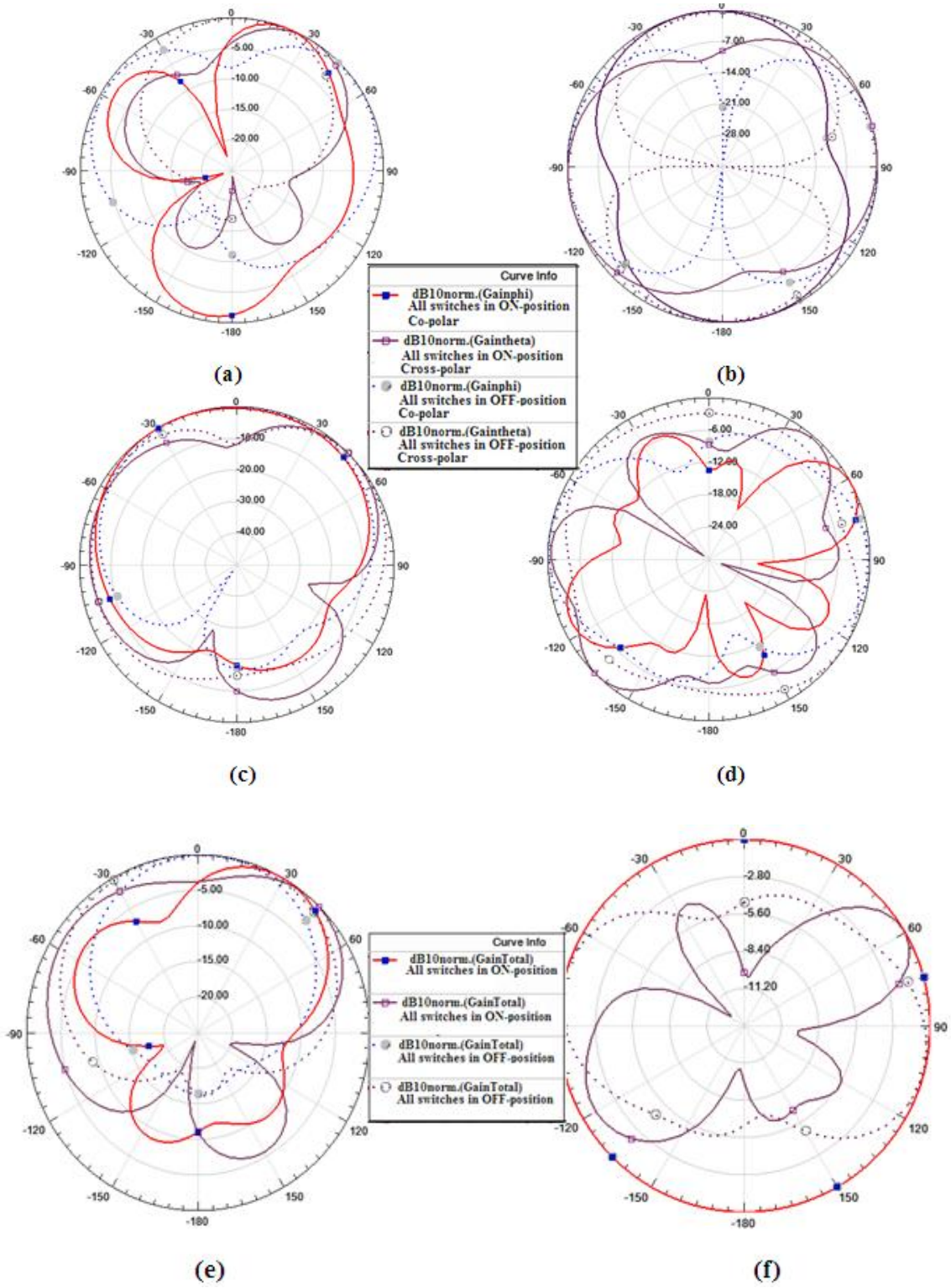

Figure 5.6- Normalized Total Gain Patterns, Co- and Cross-polar in E- and H-plane for the RA at Extreme Switching Configurations (a) XZ-(Ø = 0), (b) XY-(Θ=0), (c)YZ-(Ø = 90), (d) Gainphi and Gaintheta (Θ = 90), (e) Gaintotal (Ø = 0, Ø = 90), (f) Gain total (Θ = 0, Θ = 90)

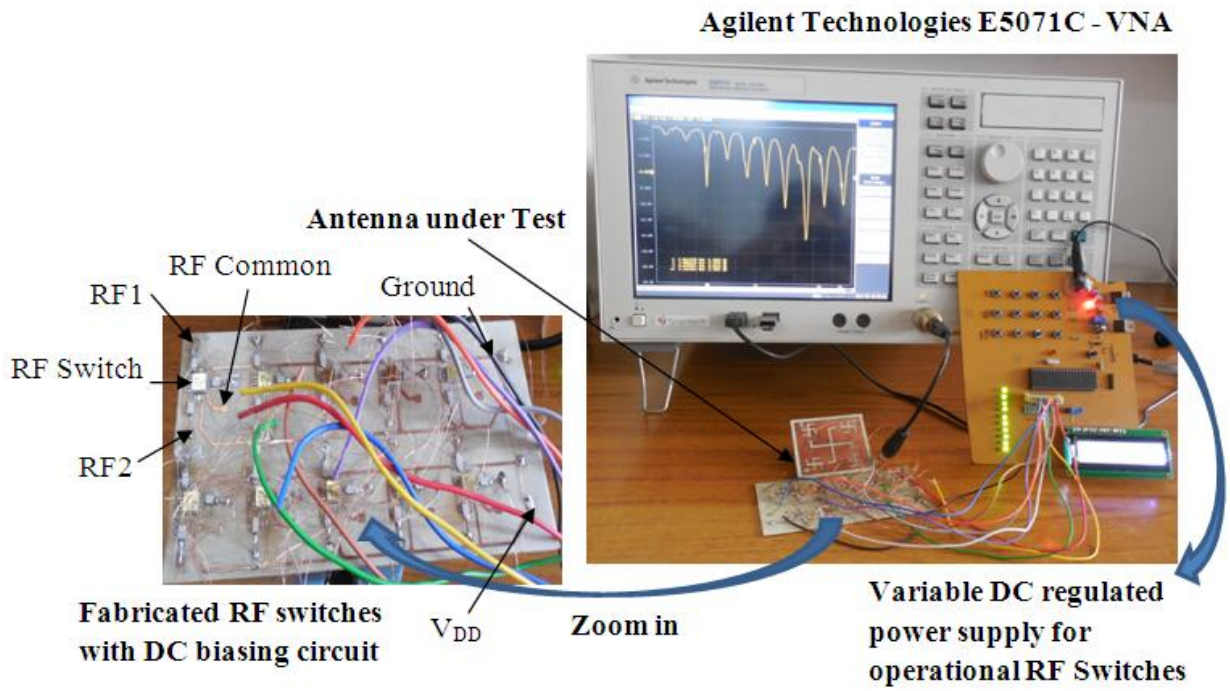

Figure 5.7- Reconfigurable SFA Measurement Setup for RL Characterization

The extensive bandwidth lies from 0.5 to 6.5 GHz, proves that this switch is appropriate for proposed RA design. An isolated sheet of Roger RO4350 substrate having identical 't' and 'ε_r' as that of planar gammadion antenna is used to integrates the RF switches. To block the DC components, the highly stable on-chip capacitor dielectrics C0G (NP0) ceramics of 47 pF value is preferred. The regulated power supply varies from 1.28 to 4.89 V is designed to operate RF switches. The RF common, RF1, and RF2 pads (as displayed in figure 5.5 and figure 5.7) from incorporated switches are directly attached to SFA through excellent quality of thin copper wires having thickness 0.025 mm. The complete set up of testing the RA with switches is shown in **figure 5.7**. The S-parameter comparison results are displayed in **table 5.1**.

Table-5.1: Evaluation of Simulated and Measured S-parameter of Proposed Antennas with and without RF Switches

Antenna configuration (Switching/non-switching state)	Resonating freq. (GHz)		RL (S_{11}) in dB		Bandwidth (MHz)		Applications of proposed antennas
	Simulated	Measured	Simulated	Measured	Simulated	Measured	Typical uses
SFA for 0th iteration.	2.32 2.58 6.44	2.41 2.52 6.38	-16.65 -12.09 -10.59	-14.32 -11.97 -11.08	122.60 44.80 108.9	118.40 46.34 106.36	Bluetooth/UMTS 4GWiMAX/IEEE 802.16 Personal communication
SFA for 1st iteration.	2.11 2.98 4.08 6.02	2.10 3.02 4.03 6.11	-28.79 -10.36 -11.37 -31.68	-26.46 -11.24 -11.02 -29.12	185.8 22.34 24.14 293.1	178.68 24.56 26.32 288.64	GSM/CDMA 4GWiMAX/IEEE 802.16 Personal communication Personal communication
SFA for 2nd iteration (without switches).	2.14 2.86 3.93 4.15 5.89	2.12 2.96 3.98 4.08 5.81	-22.51 -12.09 -12.35 -14.62 -26.02	-20.54 -11.98 -11.85 -14.20 -24.86	174.6 30.54 32.12 46.26 531.8	172.42 28.86 34.86 48.84 526.64	GSM/CDMA 4GWiMAX/IEEE802.16 Personal communication Personal communication WLAN/IEEE 802.11a
Reconfigurable SFA for 2nd iteration (all switches in on position).	2.40 2.52 4.33 5.37 6.27	2.40 2.53 4.29 5.40 6.31	-17.69 -19.76 -12.43 -10.16 -20.90	-16.97 -18.14 -11.33 -10.88 -19.87	64.10 80.10 52.10 22.18 258.28	66.42 82.26 54.68 28.42 252.46	Bluetooth/UMTS/Wi-Fi 4G/LTE Personal communication WirelessLAN/IEEE802.11a Personal communication
Reconfigurable SFA for 2nd iteration (all switches in off position).	2.35 2.59 4.37 5.41 6.32	2.31 2.52 4.29 5.40 6.36	-18.56 -20.04 -12.71 -10.19 -20.80	-16.77 -18.84 -12.45 -10.37 -19.24	66.10 90.10 54.10 20.15 252.30	68.48 92.72 56.28 24.25 250.64	Wi-Fi /IEEE802.11 4G/LTE Personal communication WirelessLAN/IEEE802.11a Personal communication

5.1.2 Hexagonal Fractal Antenna Design-IFS Approach

In this section, the hexagon geometry having identical sides (r) is designed as a fractal patch microstrip antenna element. The IFS method is implemented on the hexagon geometry. The self-similarity approach on the presented design is preferred to attain multiple resonances, moreover known as multiband frequency support. The total number of scale factor and the iterations for presented structure is three and two, respectively. Punete *et al.*, 1996 [103] used scale factor of two to realize multiband performance. To begin with, two hexagonal structures are located in such a way that their corner vertices do not touch each other, without providing any conducting path among them. The presented structure of hexagonal fractal patch antenna can be expressed in matrix arrangement. The best IFS transformation coefficients [104] suitable for the design of the hexagonal shaped fractal can be specified as:

$$w\_r\begin{bmatrix}x\\y\end{bmatrix} = \begin{bmatrix}a\_11 & a\_12\\a\_21 & a\_22\end{bmatrix}\begin{bmatrix}x\\y\end{bmatrix} + \begin{bmatrix}b\_11\\b\_21\end{bmatrix} \quad (5.1)$$

Where

w_r: affine transformation

*a*_11, *a*_22: controls scaling

*a*_12, *a*_21: controls rotation

*b*_11, *b*_22: control linear translation.

Different iteration geometries of the hexagonal fractal patch antennas are displayed in **figure 5.8**. Here out of all proposed iterative designs the second iteration of the hexagonal patch antenna is aimed at multiband operation.

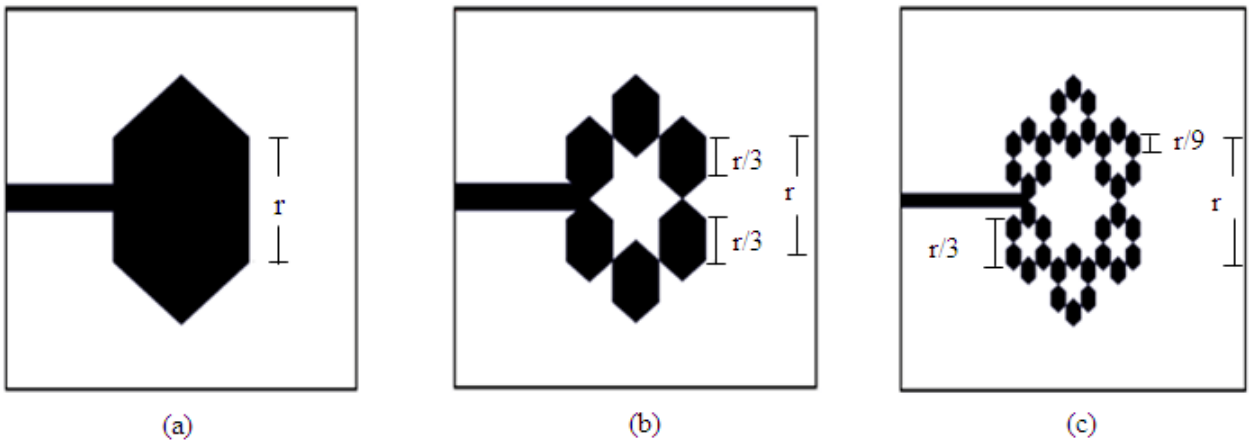

Figure 5.8- Hexagonal Patch Geometry (a) 0th Iteration (b) 1st Iteration (c) 2nd Iteration

The fairly accurate frequency resonance expression is well thought-out for the hexagonal fractal patch MA, with 'r' as side length of patch, 'ε_r' is the relative permittivity, loss tangent i.e. tanδ = 0.019, and 'd' is the thickness of the substrate [105]. The side length 'r' is given by –

$$r = \frac{F}{\sqrt{\left[1+\frac{2d}{\pi\varepsilon_r F}\left[\ln\left(\frac{\pi F}{2d}\right)+1.7726\right]\right]}} \tag{5.2}$$

where

$$F = \frac{8.791 * 10^9}{f_r \sqrt{\varepsilon_r}} \tag{5.3}$$

Another expression of fractal hexagonal antenna which relates resonant frequency to scale factor (δ) are given by (Tang & Wahid, 2004) [105] as -

$$f_r = \frac{0.468 * c}{[r * \delta^{r-2}]} \qquad 2 \leq R \leq k+1 \tag{5.4}$$

where ‘c’ is designated as light velocity, ‘R’ is the resonance and ‘k’ is the iteration factor.

Further, the gap comparable to the element of MEMS RF switch is provided among the consecutive vertices of the hexagons. Due to the occurrence of MEMS switches, such anticipated microstrip line fed hexagonal MA demonstrates the reconfigurablity in operating frequency. It is noticed that the distribution of current on the hexagon patches vary as switches transform their position, where the switches are connected by means of DC biasing wires.

The hexagonal patch MA is first simulated without RF switches and the electromagnetic results are compared with the fabricated and tested results on VNA as shown in **figure 5.9**. The magnitude of current distribution on patch is presented in the same figure. The recommended MA is employed on three frequency bands 2.90 GHz, 5.96 GHz and 7.14 GHz, respectively. Both fabricated and simulated RL results indicate significant degree of agreement. Additionally, to increase the bandwidth as well as gain and suppression of side lobes an energy band gap structure (EBG) is brought together in the geometry. The holes diameter size, number of holes, location of introduced RF switches and complete geometry shape of hexagonal MA with EBG are displayed in **figure 5.10**.

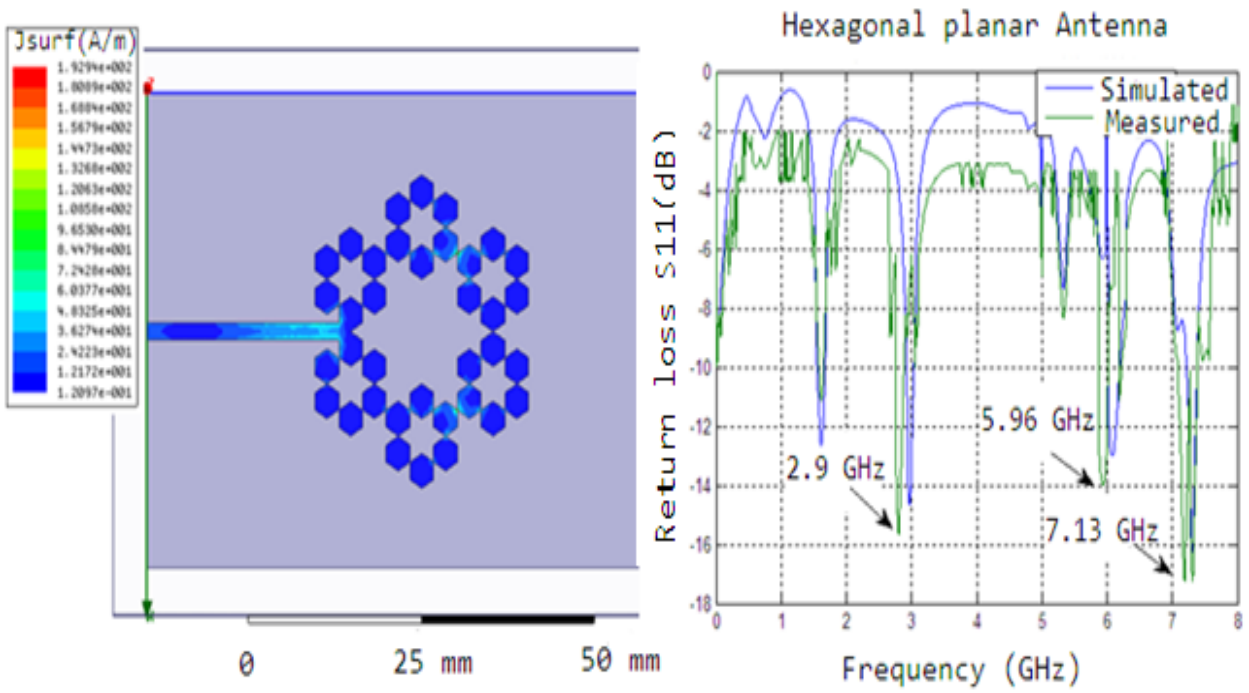

Figure 5.9- Simulated and Measured RL S_{11}(dB) of the Hexagonal MA

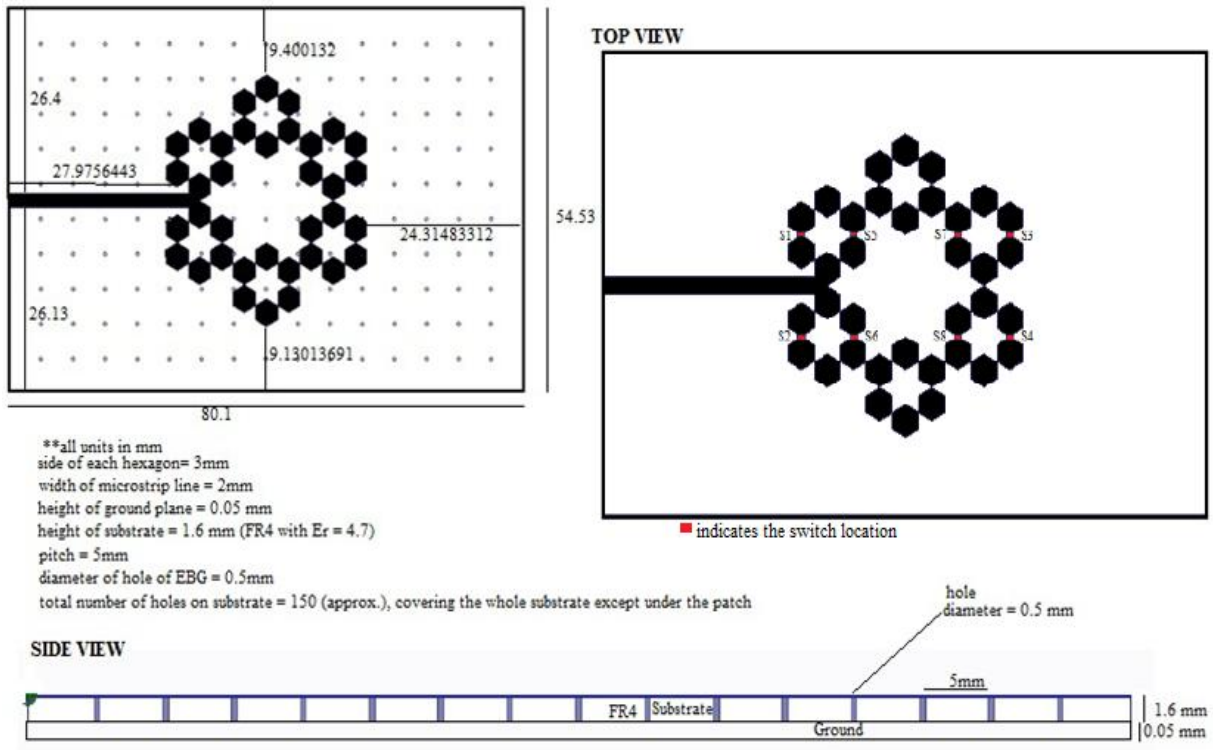

Figure 5.10- Location of MEMS Switches on Patch Hexagonal MA with EBG

The hexagonal planar antenna with EBG results is also simulated using HFSS software at solution frequency of 5.95 GHz as displayed in **figure 5.11**. A significant increase (by 12%) in bandwidth and 14.7% in peak realized gain as compared to without EBG is noticed. The surface waves and harmonics are also supressed due to introduction of EBG.

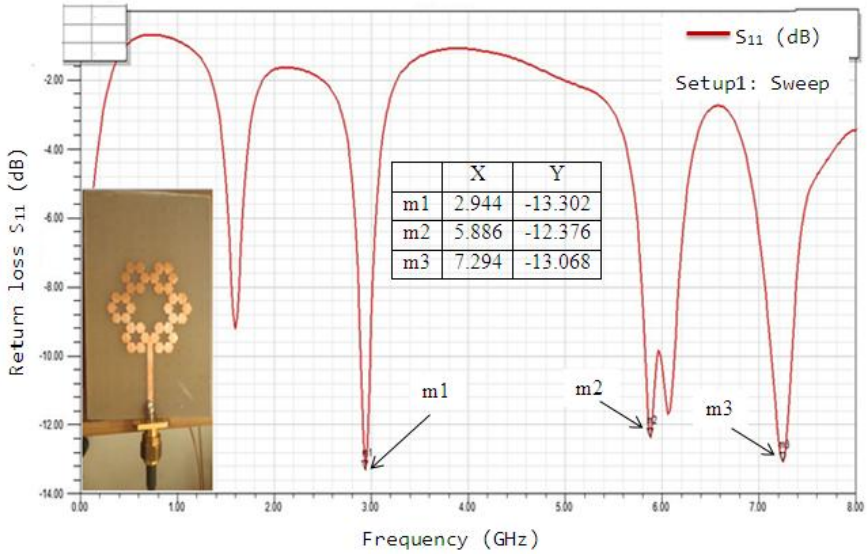

Figure 5.11- Simulated RL of the Hexagonal MA with EBG

It is worthwhile to notice that the EBG holes on the PCB of MA modify the amount of current distribution on the patch, and consequently the presented antenna gain is increased. The complete effect of introduction of EBG on proposed MA is displayed in **table 5.2**.

Table-5.2: The Effect of EBG on the Patch Hexagonal MA Performance

Type of hexagonal MA	Maximum power density per unit solid angle (W/Sr)	Peak Realized Gain	Peak Gain	Peak Directivity	Radiated Power (W)	Accepted Power (W)	Radiation Efficiency
without PBG	0.020	0.257	0.314	0.944	0.273	0.819	0.333
with PBG	0.024	0.301	0.349	0.981	0.306	0.863	0.355

Radiation patterns - The pattern analyses for both type of patch hexagonal MAs (without and with EBG) conferred above are incorporated next. The simulated normalized power radiation patterns, i.e., Y-Z and X-Y cut patterns are shown in **figures 5.12 (a)–5.12 (b)** at 5.95 GHz acquired from the HFSS simulator. The left side of **figure 5.12 (a) & 5.12 (b)** are displayed in elevation plane i.e. E-theta component, which match up to co-polarization (y-z plane, phi=90) and cross polarization (x-z plane, phi=0) cut planes and the right side of **figure 5.12 (a) & 5.12 (b)** are displayed in azimuth plane i.e. H-phi component in co polarization (x-y plane, theta=0) cut planes. A pattern of figure-eight in xy-plane indicates a dipole shape. Both MAs as expected realizing a fairly omni-directional and normalized relative patterns are maintained through the simulated three dimensional recognized gain patterns (**figure 5.13**) which display the quality of pattern is almost omni-directional as determined. Further, both MAs have well-behaved linearly polarized as axial ratio (E_y/E_x) is greater than one at theta value equal to zero.

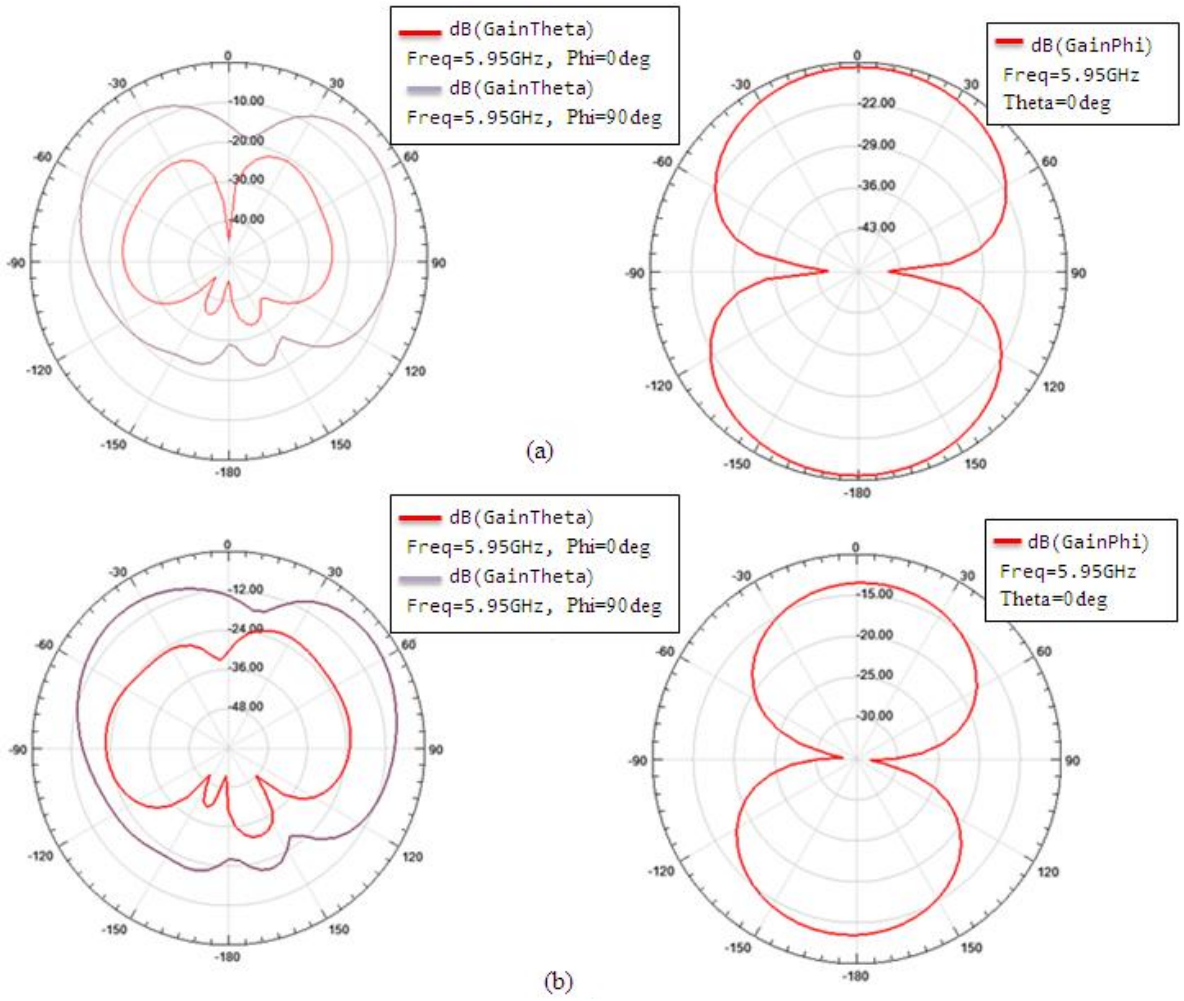

Figure 5.12- Co- and Cross-polar Patterns of Hexagonal MA at 5.95 GHz in E- (Y-Z plane, phi = 0, phi = 90) and H- (X-Y plane, theta = 0) Plane (a) Without EBG (b) With EBG

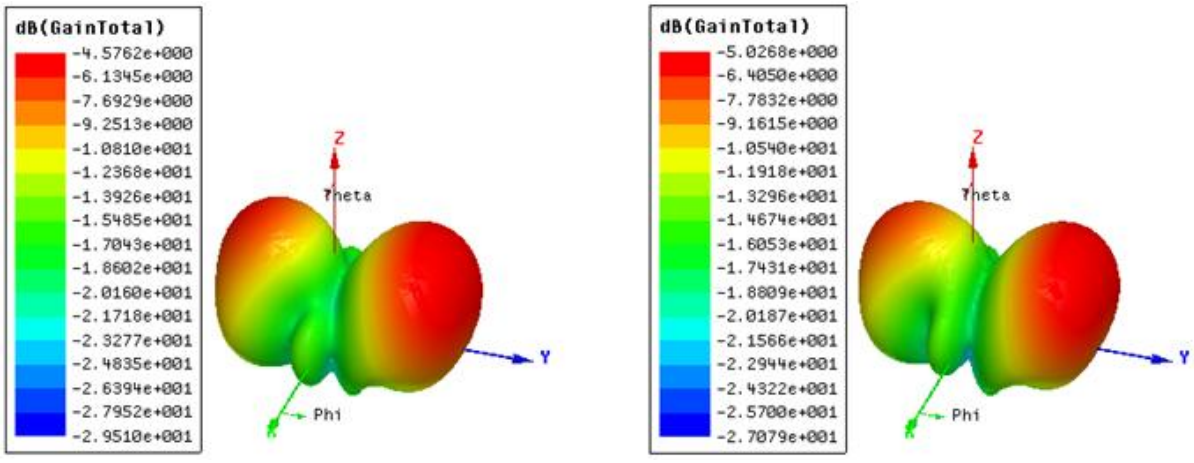

Figure 5.13- 3D-polar Plot of Hexagonal Antenna (a) Without EBG (b) With EBG

5.1.2.1 Hexagonal RA Designing and Testing with RF Switches

As of the simulation viewpoint, the capacitive MEMS RF switch carefully chosen for hexagonal patch RA is identical as that of demonstrated in **section 3.4.1.2**. While the capacitive MEMS switch is in on-position, its equivalent lumped numerical values are stated as, L_{up} = 0.942 nH and C_{up} = 0.0556 pF. However in off-position, the equivalent capacitive MEMS RF switch the numerical values are specified as, L_{down} = 0.0073 nH and C_{down} = 3806.63 pF. These aforementioned RLC lumped numerical values work as the ideal equivalent rectangular switching elements and positioned at the suitable place on the MA. The Quasi-Newton (QN) optimization approach is used to find the best location of RF switches.

The presented hexagonal RA designing and measurement testing setup comprise mostly five sections- hexagonal MA, RF switches, power supply circuit to control switches, VNA and anechoic chamber. For proof of concept equivalent absorptive ceramic SPDT RF switch (CSWA2-63DR+) having almost similar IL, isolation and 50 ohm matching is considered. The electronic switches are integrated on power supply PCB which further activates the desired RF switches through 40 pin Atmel microcontroller. The PCB layout of complete power supply section and C-language programing code of Atmel microcontroller to control the RF switches on the antenna is specified at **Appendix-B**. The measurements of RA electromagnetic characteristics were done with the help of Agilent Technologies E5071C VNA in an anechoic chamber. Although small variation in results are noticed in ON-position of switches at antenna, as compared to simulated results, because of different insertion loss value of tested switch. The complete set up of measurement is shown in **figure 5.14**. Left side of the **figure 5.14** shows the laminate sheet consists of ten RF switches and here in this work only eight switches (*S1-S8*) are used.

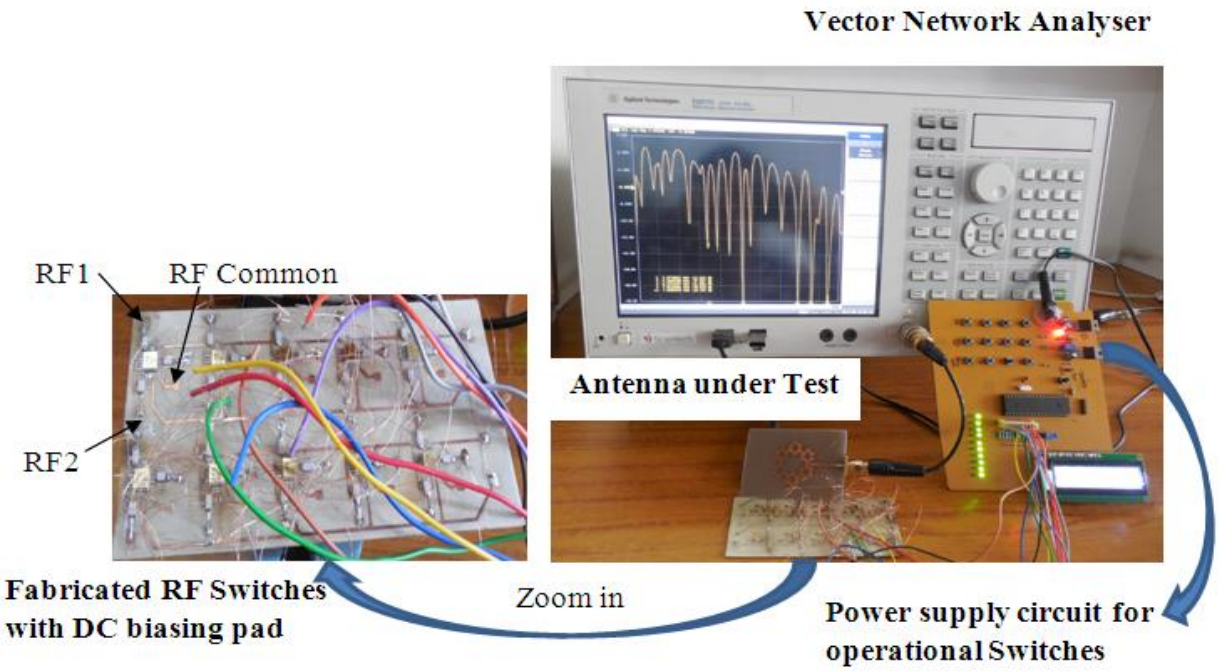

Figure 5.14- Hexagonal RA Testing Setup for RL Characterization

Out of 256 (=2^8) different combination of RF switches, total 64 selected cases of reconfigurable antenna were simulated. These configurations cover almost all present as well as future mobile and wireless communication bands lying between 1.5 to 7.5 GHz as shown in **figure 5.15**.

Further, the total gain pattern in elevation plane i.e. E-theta component at phi=90 degree of reconfigurable antenna with RF MEMS switches has been considered in **figure 5.16**. For illustration the effect of switches on antenna at two extreme cases i.e. when all switches are in ON and OFF position are considered. The radiation pattern result include the dielectric losses, mismatch loss and ohmic losses connected with antenna and RF MEMS switches. The effects of DC biasing and connection pads are not considered in this study, which may affect the characteristics of radiation pattern.

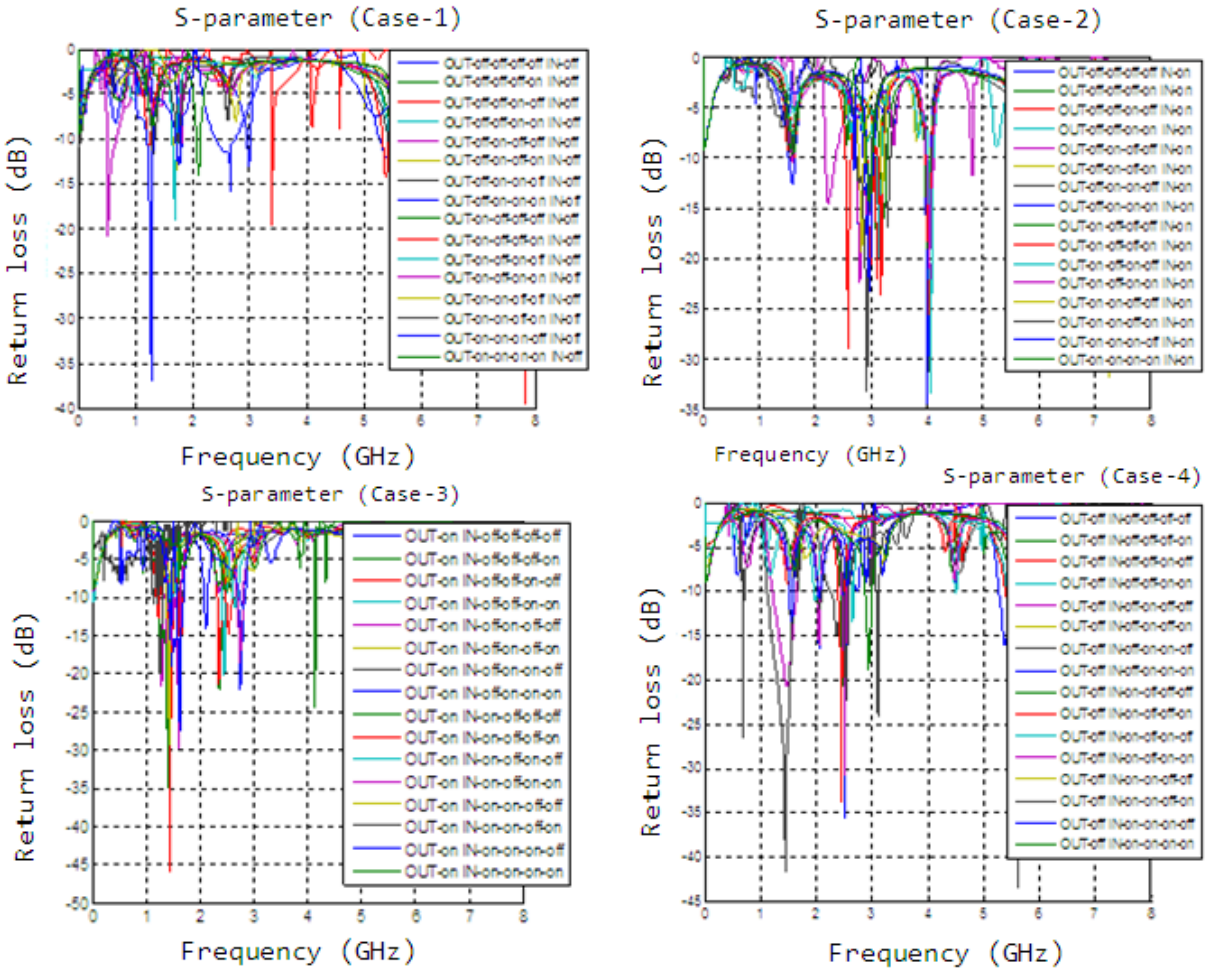

Figure 5.15- Simulated RL of Hexagonal RA (16 × 4=64 Selected Cases)

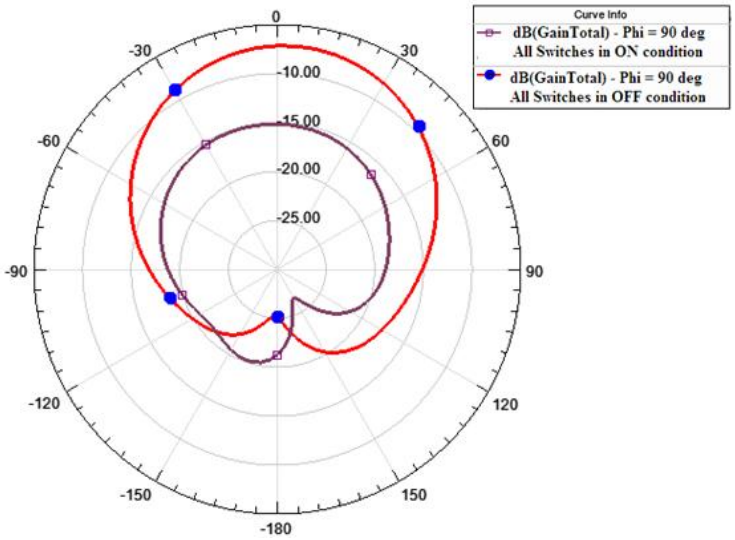

Figure 5.16- Radiation Pattern of RA with RF MEMS Switches when all Switches in ON and OFF Condition

5.1.2.2 Conclusions of Hexagonal RA

An innovative fractal multiband hexagonal patch MA is designed by using IFS method. The EBG method applied on the PCB exhibited a significant decline in side lobe level and increase in power density. Further, a novel frequency RA using a fractal hexagonal shaped structure using capacitive RF switches is designed, fabricated and tested. QN optimization approach is preferred to find out the position of MEMS RF switches. For all possible RF switching configurations, during designing and testing of anticipated multiband RA structure needs to be well-suited at all measured frequencies band lying between 1.5 to 7.5 GHz. As of industrial application point of view, the proposed compact RA with RF switches is considered in mobile RF front end terminal which include all existing as well as upcoming wireless and mobile communication bands.

5.1.3 Spiral-shaped Reconfigurable antenna

The structure of the presented spiral MA is displayed in **figure 5.17**. It comprises of rectangular shaped spiral patch combined with resistive MEMS switches. It is designed on the FR4 Poly-tetra-fluoro-ethylene (PTFE) material (ε_r = 4.4, h = 1.588 mm, tan δ = 0.002). The measurement of the laminate as well as the ground plane is 50.0 mm x 50.0 mm. At the central position of the FR4 laminate on which the patch is designed, a feed line (i.e. a coaxial cable) is introduced via inserting hole and can produce the circular polarization. The width of spiral arm is calculated to be 0.50 mm and increasing in right hand direction by way of every single arm length varies from 10.0 mm to 40.0 mm. The resistive MEMS switches are positioned in such a manner depend upon the RL of the spiral MA at the preferred choice of resonance frequencies. The slots are cut for placing MEMS switches that extending from 0.001 to 0.3 mm. After applying optimization technique, each slot dimensions are settled at 0.2 mm. Initially, operational band is from 1.0 to 6.5 GHz which is later on extended up to 11.0 GHz after using optimization. In this regime of frequency band operation, RA is well suited for mobile RF front end section of mobile and some other useful PC applications.

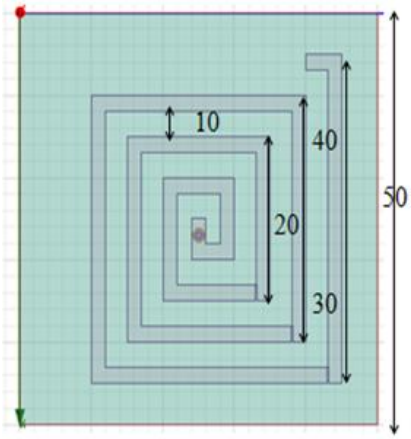

Figure 5.17- Stacked Patch Representation Designed in HFSS Simulator (Dimensions are in mm)

5.1.3.1 Spiral Antenna with MEMS RF Switches- Results and Discussions

The positions of the three resistive MEMS RF switches at spiral-shape MA is demonstrated in **figure 5.18**. Three MEMS switches S1, S2 and S3 are employed at the edge corner of each spiral arm end respectively, as spiral arm increases from the starting point. Initially, for placing these switches, the 0.2 mm slots size is cut on spiral patch. By means of three MEMS switches, total nine switching (on-/off-) permutations can be recognised.

Each combination of MEMS switches on spiral RA is useful to attain the desired performance and also a criterion of selecting final bandwidth, over the microstrip operational frequency bands. The RL (S_{11}) results of spiral RA at different position of MEMS RF switches are displayed in **table 5.3**.

Almost all simulated different configurations of RA demonstrate VSWR, which is found to be inside the vicinity of the acceptable limit of two and RL is less than -10.0 dB. The total eight bands are attained i.e. 2.5, 3.5, 4.5, 6.0, 7.0, 8.0, 9.0 and 9.5 GHz with acceptable RL and operational bandwidth. The EM result lies in the middle of 1.0 to 6.5 GHz and total six bands are attained which is displayed in **table 5.4**. The effect of spiral MA without RF switches is also measured and shown in **table 5.5**.The rest of the post-processing EM results of spiral RA such as directivity; peak realized gain and other important results are shown in **table 5.6**. The peak gain and average peak directivity for all the switching configurations stays at around 0.92 and 2.73, respectively.

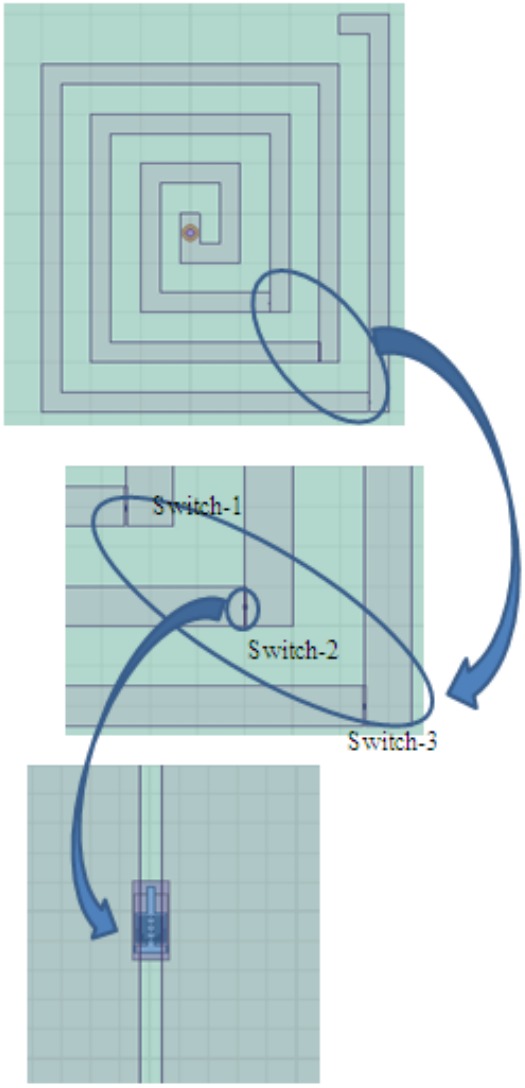

Figure 5.18- Initial RA Design with MEMS RF Switches Connections

In view of two cases out of all nine cases, in the first case S1-on/S2-off/S3-off arrangement bandwidth of 611 MHz (3.08-3.69 GHz), 200 MHz (4.40-4.60 GHz), 1.44 GHz (5.54-6.98 GHz), 1.65 GHz (7.74-9.39 GHz) is achieved. In the second case S1-on/S2-on/S3-off configuration bandwidth of 657 MHz (3.11 to 3.77 GHz), 300 MHz (4.34 to 4.64 GHz), 1.60 GHz (5.56 to 7.16 GHz), 1.54 GHz (7.86 to 9.39 GHz) is achieved. At all switching configurations, the RL of the spiral MA is displayed in **figure 5.19**. These outcomes also defend the circumstances if proposed antenna is integrated on mobile RF front end section, it retain the impedance bandwidth in excess of 300 MHz. At higher operational frequency band more bandwidth is essential for mobile TV and video applications.

Table-5.3: Spiral RA RL Results using All Configurations of MEMS Switches

Switch-1 (S1)	Switch-2 (S2)	Switch-3 (S3)	Resonance frequency (f_r in GHz)	RL (in dB)	Resonance frequency (f_r in GHz)	RL (in dB)
			Simulated	Simulated	Measured	Measured
ON	ON	ON				
			4.50	-11.10	4.46	-11.48
			6.00	-19.54	5.82	-18.54
			9.00	-20.31	8.72	-19.02
ON	ON	OFF				
			3.50	-14.07	3.52	-14.56
			4.50	-11.65	4.54	-10.34
			6.00	-21.01	5.76	-22.42
			9.00	-18.48	8.78	-17.78
ON	OFF	ON				
			7.00	-26.69	6.86	-25.32
			9.50	-12.51	9.42	-11.38
ON	OFF	OFF				
			3.50	-12.87	3.50	-13.02
			4.50	-11.71	4.46	-10.92
			6.00	-26.08	5.80	-24.38
			9.00	-18.73	8.92	-17.42
OFF	ON	ON				
			2.50	-12.50	2.48	-13.06
			3.00	-16.54	3.02	-17.34
			3.50	-20.40	3.51	-21.72
			4.00	-22.20	4.14	-20.64
OFF	ON	OFF				
			4.50	-10.62	4.52	-10.96
			6.00	-21.38	5.9	-20.54
			9.00	-14.84	8.94	-13.62
OFF	OFF	ON				
			3.50	-16.80	3.52	-17.04
			4.50	-12.74	4.54	-12.82
			6.50	-20.56	6.42	-22.64
			8.00	-17.47	7.90	-16.04
			9.00	-21.73	8.86	-19.06
OFF	OFF	OFF				
			3.50	-11.61	3.50	-12.42
			6.00	-23.43	5.80	-22.06
			9.00	-14.68	8.88	-13.48

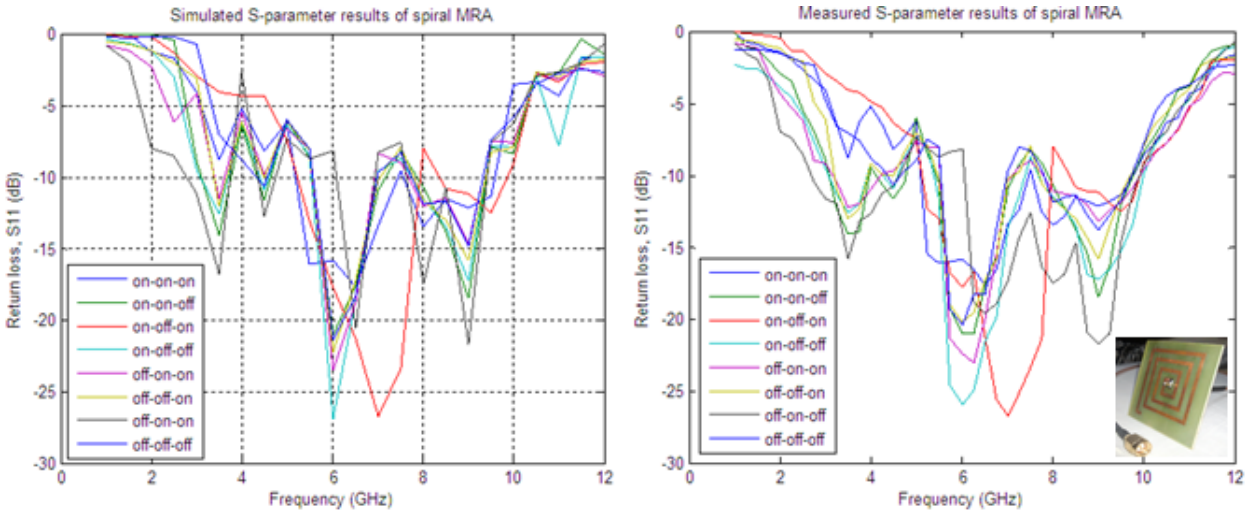

Figure 5.19- RL versus Frequency Plot for All Combination of RF Switching

Table-5.4: Spiral MA RL Result without MEMS RF Switches

Resonant frequency (GHz)	RL (dB)
1.4	-12.11
2.27	-12.30
3.08	-16.99
3.62	-20.20
4.3	-24.20
6.12	-30.51

Table-5.5: Spiral MA RL Result using Three Equal Slot Lengths (0.2 mm)

Resonant frequency (GHz)	Return loss (dB)
5.0	-13.36
6.0	-16.15

The proposed new RA shows circular polarization (RHCP and LHCP). Usually, the polarization of the radiating wave is specified with the polarization of locally generated uniform wave and as well the polarization of incident wave is called the polarization of plane wave, which is having the flux density which results in maximum power at the MA output terminals. Polarization mismatch is the cause of loss of power at the output. One can measure this loss of EM power by measuring the polarization loss factor (PLF). If PLF = 1, then antenna is perfectly matched, there will be no loss of EM power and if PLF = 0 then antenna becomes a loss storage

device. For achieving the frequency of interest, axial ratio and gain, the locations of RF MEMS switches should be chosen carefully. Here the theoretical value of axial ratio (E_y/E_x) is 0dB for circular polarization. The E-field and polarization plot is shown in **figure 5.20.**

Table-5.6: Post-processing Results of Spiral RA

Sr. No.	Quantity	Simulated results
1.	Max U	0.072 W/Sr
2.	Peak Directivity	2.723
3.	Peak Gain	0.920
4.	Peak Realized Gain	0.910
5.	Radiated Power	0.334 W
6.	Accepted Power	0.989 W
7.	Incident Power	1.00 W
8.	Radiation Efficiency	0.438

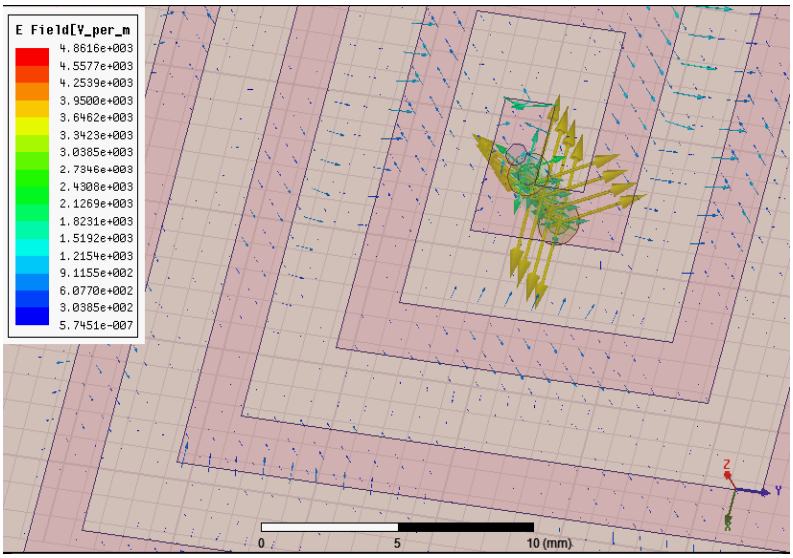

Figure 5.20- Polarization and E-field of Spiral Antenna

Radiation patterns performances – The normalized radiation patterns for the reconfigurable spiral antenna (RSA) at eight possible cases (either on or off) of RF MEMS switching position are described next. The power patterns, i.e., XY-, XZ- and YZ- cut patterns

are shown in **figures 5.21 (a) –5.21 (c)** at center frequency 5 GHz. The total gain magnitude of the electric field components in the desired polarization are plotted next in **figure 5.21 (d)**. As shown in **figure 5.21 (a)**, a pattern named figure-eight in the XY-plane denotes a dipole shape of radiation pattern. According to 3-D radiation pattern figure (not shown here), it has been observed that the RSA behave non-steering in the azimuth plane and directional in the elevation plane, therefore achieving fairly omni-directional patterns.

5.1.3.2 Conclusions of Spiral RA

From QN method optimization results of MRA, it is concluded that as the slot size reduces it more approaches towards lower band. Also using optimization techniques, it is concluded that as numbers of switches increase more operating bands can be achieved but the problem of leakage current from DC biasing pad, electromagnetic losses and more consumption of power has been observed. The novelty of the proposed reconfigurable antenna can be installed in future mobile RF front end transceiver to cover 4G WiMAX (3.0 and 3.5 GHz)/IEEE 802.16, wireless personal communication and WLAN (5.8 GHz)/IEEE 802.11a (outdoor) mobile communications while at the same period holding a practical integrity with very good bandwidth characteristics, has been reported.

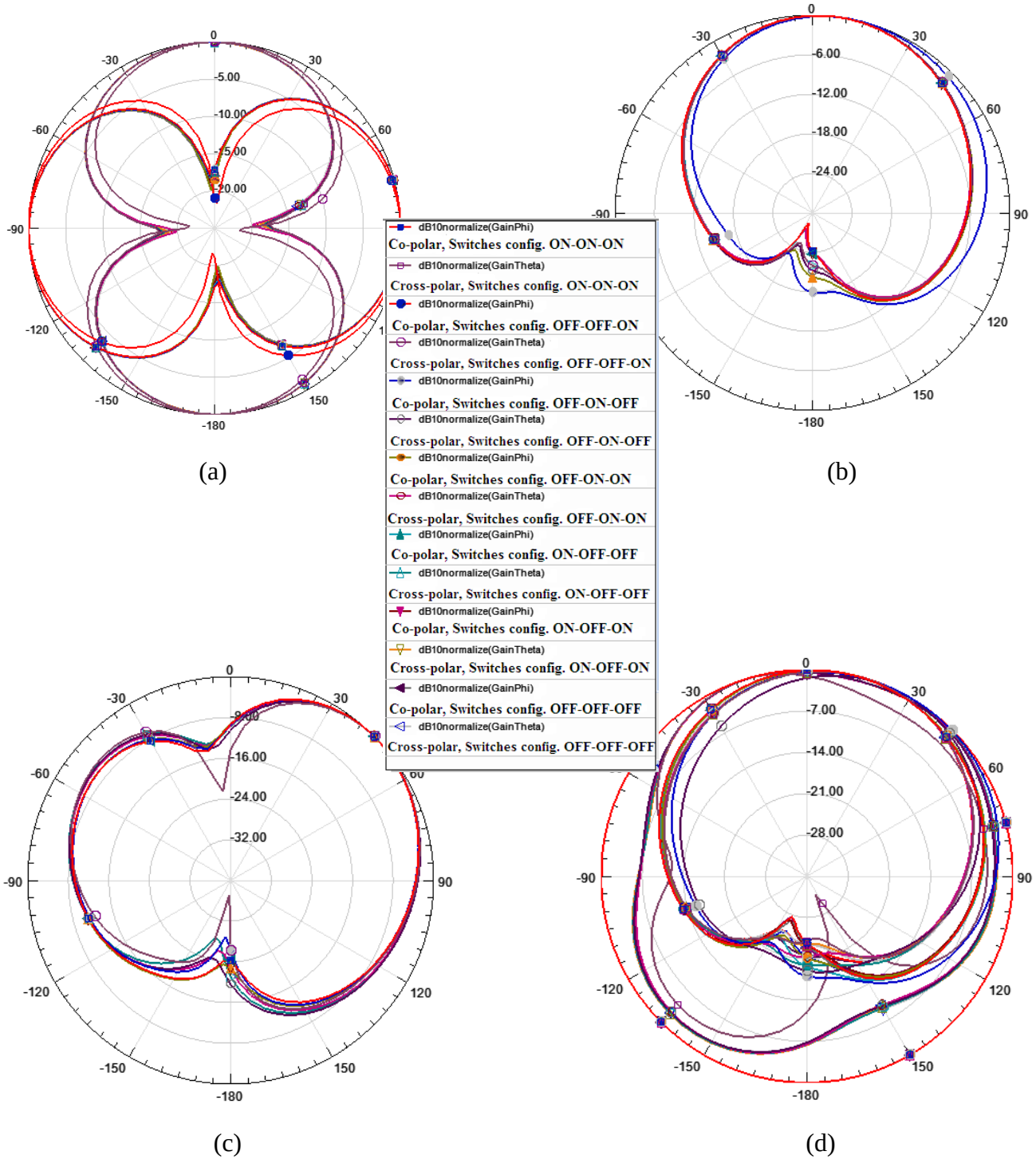

Figure 5.21- Normalized Co-, Cross-polar and Total Gain Patterns in E- also H-plane for the RSA at Different Switching Configuration (a) XY-plane(Θ=0), (b) XZ-plane(Ø=0), (c) YZ-plane(Ø=90), (d) Gain total(Ø=0, Ø=90) and Gain total(Θ=0, Θ=90)

Chapter 6

Conclusion and Future Scope of Work

6.1 Conclusions

The design of RF MEMS based reconfigurable antenna is a challenging task. The MEMS switch should be frequency agile over wide range of frequencies. The reconfigurable antenna should be able to extract the diversity.

6.1.1 RF MEMS switches conclusion statements

Different MEMS switches have been proposed to be developed through this thesis (research work), are mainly divided into four categories, as explained in **chapter-3**. The proposed important research recommendations regarding MEMS RF switches are summarized as follows:-

- DC metal-to-metal contact cantilever beam switch
  - A metal-contact MEMS switch for slotted-RA has been presented, simulated and optimized.
  - For optimization of S-parameters of switch, PS algorithm has been used.
  - After PS optimization, the switch shows improvements in IL (0.15 to 0.49 dB) and isolation (94.91 to 54.80 dB) at 0.1-10 GHz performances.
  - It has been concluded that metal contact cantilever switch perform better in the frequency range lying between DC to 7.0 GHz.
- Shunt capacitive switch
  - Advantage of designing shunt MEMS switch is to find the relations of actuated voltage, Young's modulus, material composition, C_{on}/C_{off} and electrostatic-forces with the help of coventor software.
  - By introducing small size holes in the upper electrode of switch reduces the spring constant and as a result pull-in voltage decreases. The low voltage is always desirable for devices where less power consumption is the main requirement.

- Serpentine-shape meander beam structure for MEMS switch help to reduce the spring constant.
- The V_{pi} is mainly affected by the '*k*' of beam shape; gap between upper and bottom electrode, and area of contact electrode. The need for low $V_{p\text{-}in}$ has often produced extreme designing and fabrication complication in addition to rise in the dimensions of the MEMS switches.
- The RLC equivalent circuit of shunt MEMS capacitive switch shows that the switch behaves as an *L* beyond the series resonant frequency, as a *C* under this frequency and reduces as a series *R* at resonance. Further, in up-configuration, the *L* role is negligible and only shunt *C* has main role to describe the characteristic of MEMS switch. Although, it is invstigated in down-configuration, the *L* act as important parameter.

❖ DC shunt MEMS switch

- The DC metal contact shunt switch is similar to DC capacitive shunt switch except that the absence of dielectric Si_xN_y layer beyond the bottom pull-down electrode, as in case of earlier switch.
- In down configuration, the switch plays as a shunt R_sL corresponding circuit element with the t-line and in up-configuration work similar as of shunt capacitive switch. The only difference is the metal contact when the upper beam is in down-state.

❖ FBAR cantilever resistive MEMS switch

- Aluminum is preferred over other electrode material for designing FBAR because it provides small resistance and does not need excellent coupling coefficient property. For piezoelectric layer, AlN is observed as a good choice.
- The single FBAR resonator can be resonate on dual frequency, if a cantilever is introduced over upper electrode. In this way it act as FBAR switch and resonate at two different frequencies that depend upon the ON-/OFF- configuration.
- By introducing the series *L* in shunt resonator of the ladder filter increases the bandwidth but has disadvantage to occupy enormous space. Further, it has been concluded that by adding series *C* in resonating arm also increases the bandwidth and at the same time maintains the good performance of FBAR filter.

6.1.2 Optimization conclusion statements

In **chapter-4** various optimization algorithm methods are discussed and applied to optimize the performance of MEMS switches and antenna. Following are the conclusion statements about optimization techniques presented hereby-

- It has been concluded that numerous optimization tools are available which include- PS, ANN, QN, SMINLP, GA, and SNLP for optimizing the EM properties.
- The main advantage and flexibility of using ANN as optimizer tool is that no formulation is essential to design RF circuits. It can be preferred over other optimization techniques because of its empirical behavior, based upon the statement of physical phenomenon and ability to provide output in small amount of time.
- The PS algorithm tackles the electromagnetic optimization problem by searching the set-points around the existing point to find out the optimal solution.

6.1.3 RAs conclusion statements

Three different shapes of RAs have been presented in this research work in **chapter-5** mainly to cover the standard mobile communication bands and to satisfy various other useful electromagnetic applications. The proposed RAs main conclusion points are discussed and summarized next-:

- Hexagonal fractal shape
  - An innovative multiband hexagonal antenna has designed using IFS method.
  - By introducing holes on the hexagonal antenna substrate and therefore creating PBG structure exhibited increase in maximum power density and a significant decline in level of side lobes.
  - QN optimization method has been used to find the exact location of MEMS switches on antenna substrate.
  - The proposed self-similar hexagonal fractal shape RA has been designed to cover all existing as well as upcoming wireless and portable communication bands as frequencies lying between 1.5 to 7.5 GHz.

- Gammadion geometry
  - In order to design gammadion-shaped MA, ANN based mathematical model is presented for emerging high performance procedures to decrease advance cycle, unless we need lengthy events and design cycles by conservative approaches.
  - The gammadion-shaped MA proposed in this work used FFBP ANN procedure with hidden layer as an estimated typical technique for study and analysis.
  - From the outcome analysis, it has been investigated that the presented ANN modeling procedure is suitable for predicting the design parameters of gammadion geometry antenna under stated circumstances and applications.
  - Further, the second iteration microstrip gammadion-shaped antenna has been transformed into RA by integrating eight MEMS switches on aforementioned substrate.
  - For completely probable RF switching positions, the outcomes of presented RA functioned well for frequency range lying in the middle of 1.5 to 7.5 GHz.
  - From telecommunication industry point of interpretation, the presented small sized gammadion geometry RA can be suitable in mobile terminal RF front end section. It covers standard communication bands like IEEE 802.16/4G WiMAX, IEEE 802.11a (outdoor) wireless communications /WLAN (5.8 GHz), and UMTS (IMT-2000) while alike time holding a functional reliability in its sensible bandwidth appearances has been reported.
- Spiral shape
  - The spiral-shaped MA has been converted into RA by introducing MEMS switches. Initially, three new metal-contact cantilever electrode MEMS switches are designed at mm and μm frequencies up to 10 GHz. Out of all proposed switches, the best results of squeeze film damping response and pull-in voltage has been noted to be 2 ms and 3.5 V, respectively. Similarly, the optimized isolation and IL value has been calculated to be 47.77 dB and 0.218 dB at 4 GHz, respectively.
  - The electromagnetic and multi-physics results of presented MEMS switches for RA display tremendous performance as relate to semiconductor RF switches.

- Furthermore, the QN optimization technique has been applied on planar spiral antenna and it has been concluded that as the slot- size of the antenna decreases, the S-parameter results more approaches near to lower frequency band.
- Also by using QN optimization method, it has been observed that as quantities of MEMS switches increase more resonant frequency bands are attained. However, difficulty of handling the outflow current through DC biasing circuit, electromagnetic RF losses and feeding of more power has been noted.
- The originality of the presented RA can be mounted in future mobile terminal transceiver to include wireless personal communication (WPC) bands, IEEE 802.16/4G-LTE/ WiMAX (3.0 and 3.5 GHz), and IEEE 802.11a (outdoor propagation) mobile communications/WLAN (5.8 GHz) standards.

6.2 Future Scope of Research Work

- Need perfection in designing to avoid failure in MEMS switches

In this research work, the low pull-in voltage conductor to conductor contact in capacitive MEMS switches has been presented with reasonable switching speeds. But the metal to metal contacts worsen and collapse the MEMS switches performance due to high current flow which causes the failure mechanism of the switch. Therefore, in future, there is need to improve design of metal to metal contact switch so that it does not fail in on state.

- Improvement in wafer level packaging and RF feed through mode

The wafer packaging procedures and RF feed through modes are chief concerns (attenuation occurs) for the practical use of RF MEMS switches. But the question relating to improvement of such wafer packaging technique and feed through mode used for the MEMS RF switches is not considered in this work which affects the loss, size, cost, weight, functional and performance of MEMS RF switches.

- Monolithic integration of MEMS switch and MA

The subsequent step in the field direction to carry on this investigation would be to monolithically fabricate the MEMS RF switches, DC biasing pad and biasing wires along with

the antenna. In addition, RF wave loss there due to the mismatch between the high permittivity substrates of the MEMS switch and the low profile planar antenna PCB. This is due to the variation in the electrical characteristics of their substrates.

- ❖ Reconfigurable mobile RF front-end terminal

Researchers from many countries all over the world are already working in the field of reconfigurable RF front end of mobile terminal using RF MEMS for next-generation communication applications. However, not much work is reported in the field of implementation of multiband RF front end configuration that contains antenna, duplexer, and power amplifier (PA) reconfigured using RF MEMS switches. Moreover, not much work is reported on low noise amplifier (LNA), U/C (Up Converters), D/C (Down Converters) and filters integrated onto 1-chip transceiver. Till now the research work is only extended up to repeatability of components depending upon the number of different resonant frequency bands. Further, the telecommunication industry is looking for a solution for integrating the next generation technologies on to one transceiver. In this regard there is lot of research is going on by combining the CMOS and MEMS technology. With existing ASIC technology it is very much conceivable to club CMOS-MEMS on a same platform.

- ❖ Meta-material based RA

The reconfigurable MEMS antennas presented in this research efficiently operate in standard mobile communication bands. The hazardous effects of such antennas on human body especially, on brain are not considered in this thesis. In extension of the current work, the next step can be the study and introduction of meta-material based RA for the welfare of public health care.

Appendix - A

i. Consider n-type (100) silicon as a substrate. By means of dopant source $POCl_3$, it is comprehensively doped in a diffusion furnace.

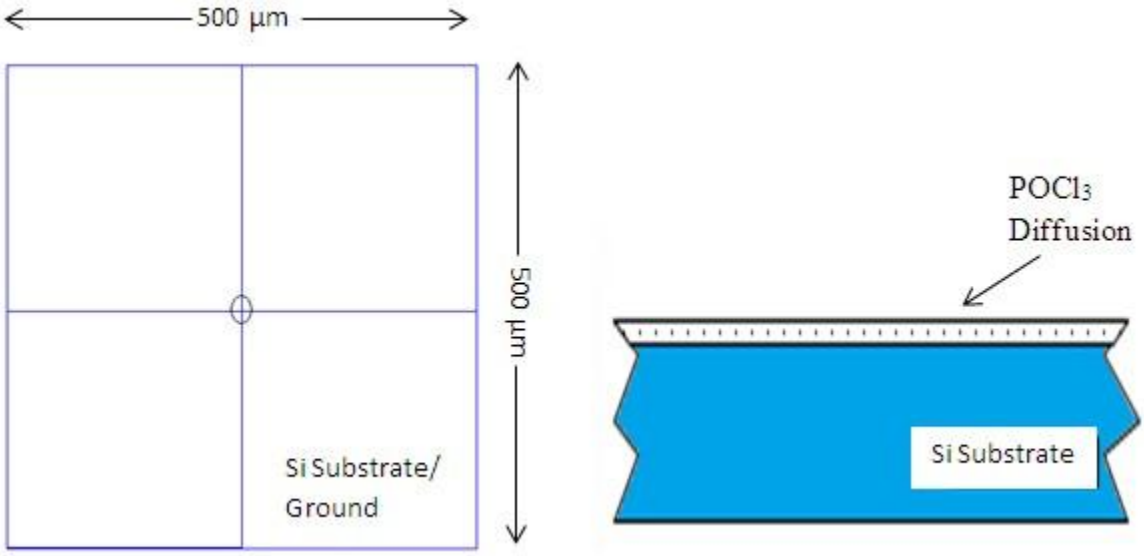

ii. A 600 nm extensive coating of low tension silicon nitride (SiN) is set down.

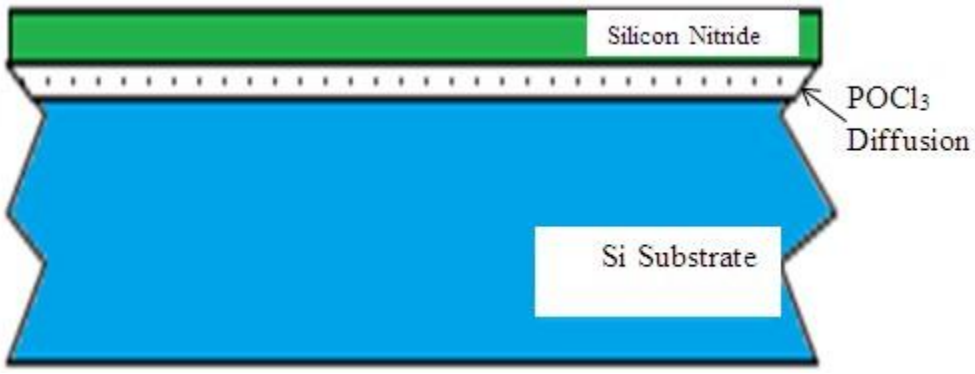

iii. It follows an extensive coating of poly-silicon (Poly0) having 500 nm depth. The substrate is then layered by way of ultraviolet (UV) penetrating photoresist (PR).

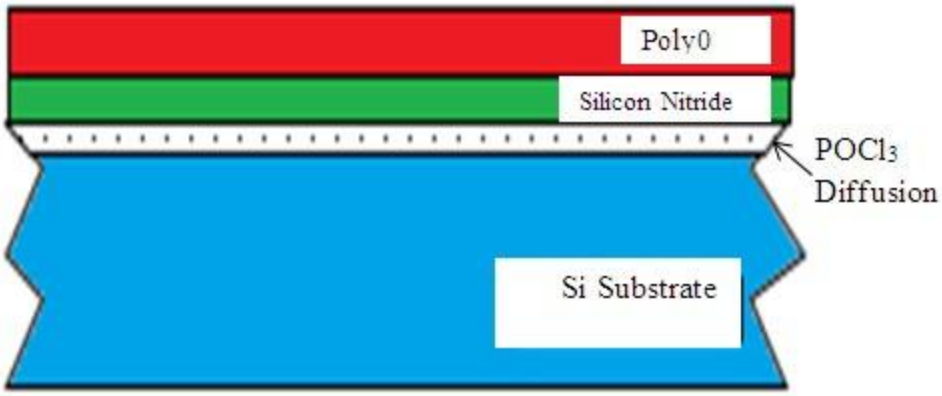

iv. The PR is then lithographically patterned using uncovering it to ultraviolet light over the first mask (POLY0) in addition to then emerging it. A patterned photo-resist level mask for etching is used and exposed areas are removed. RIE is then preferred to take out the undesirable poly-silicon. Once the etching is complete, the PR is chemically exposed in an immersion. This technique of designing the substrate using PR, etching in addition to strip off the left over PR is used over and over again in the MEMS-MUMPs procedure.

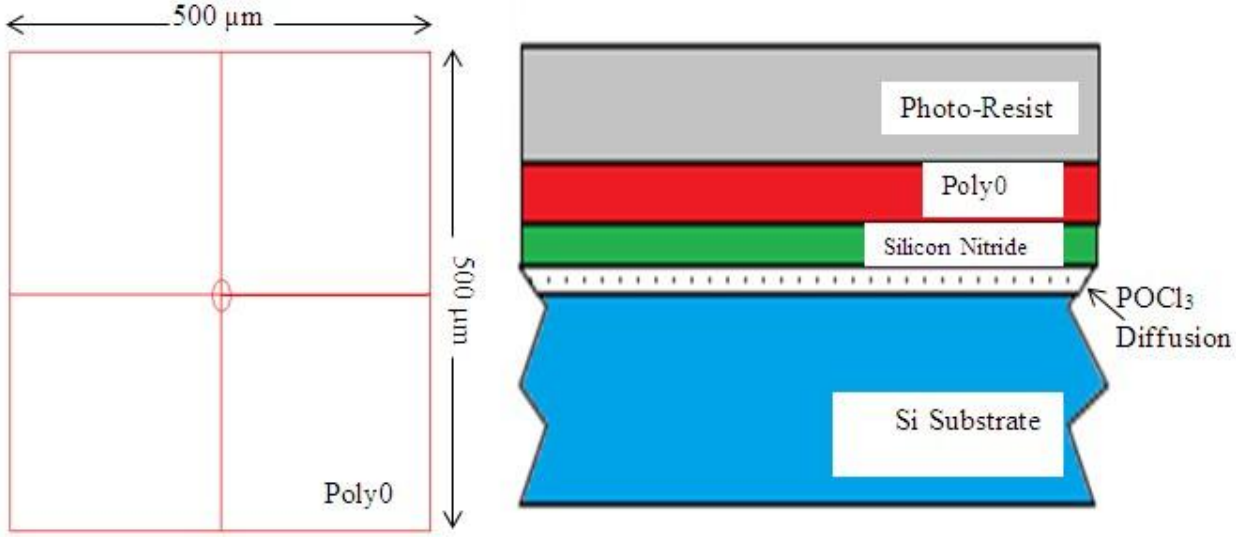

v. RIE is then preferred to take out the undesirable poly-silicon.

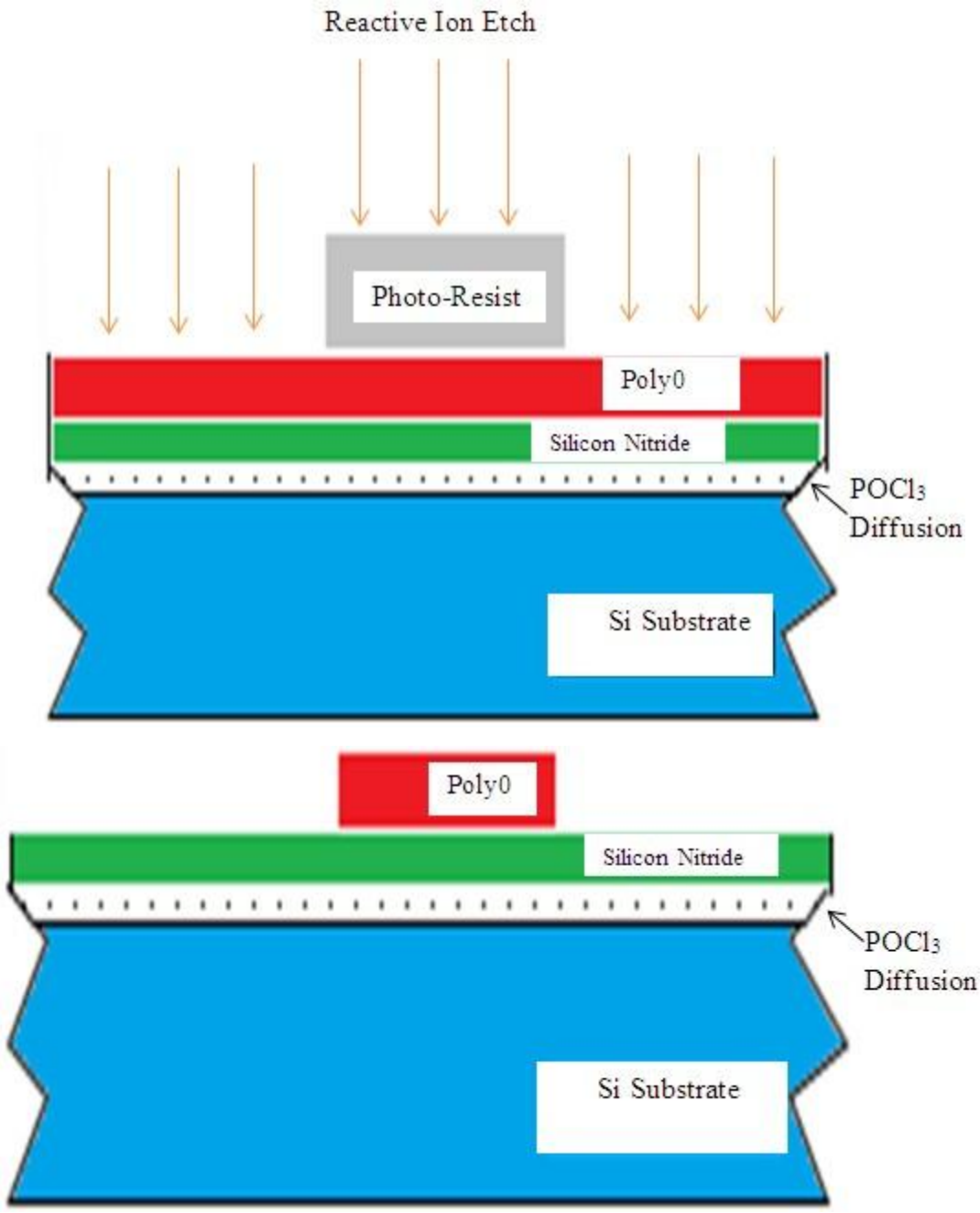

vi. In general, the hole coatings (HOLE0 to HOLEM) aimed at POLY0 to METAL, correspondingly, is displayed as distinct levels so as to create layout easier. One purpose of HOLE0 is to deliver a way to "remove" holes on or after a bright field level. Here mask Hole0 is used to etch the shape of the transmission line.

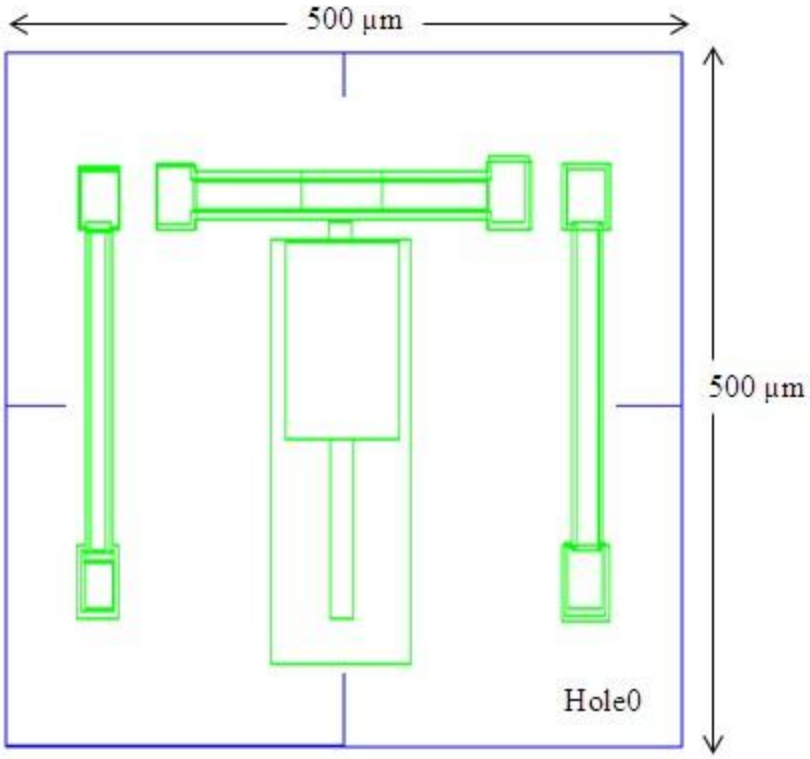

vii. After that a 2.0 µm coating of PSG remains set down on the substrate through low pressure CVD. Furthermore, this is designated as first sacrificial coating.

viii. The substrate are coated using PR besides the subsequent level, named as DIMPLE, is patterned by lithography process. The depth of 750 nm dimples is RIE keen on the oxide first coating. After the etching, PR is exposed.

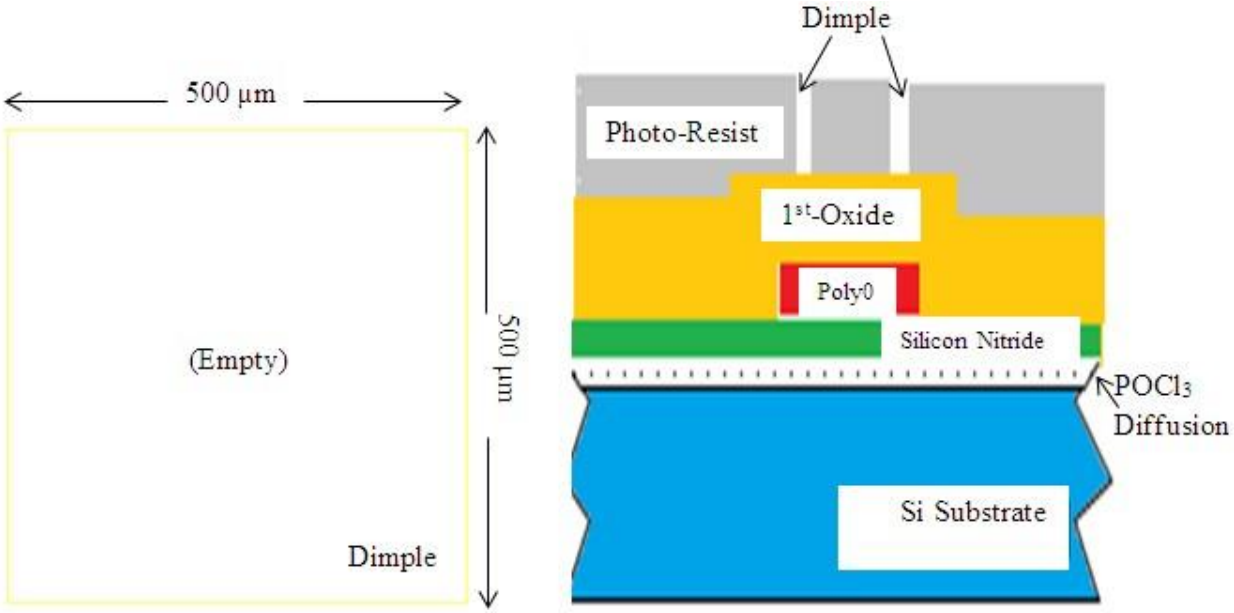

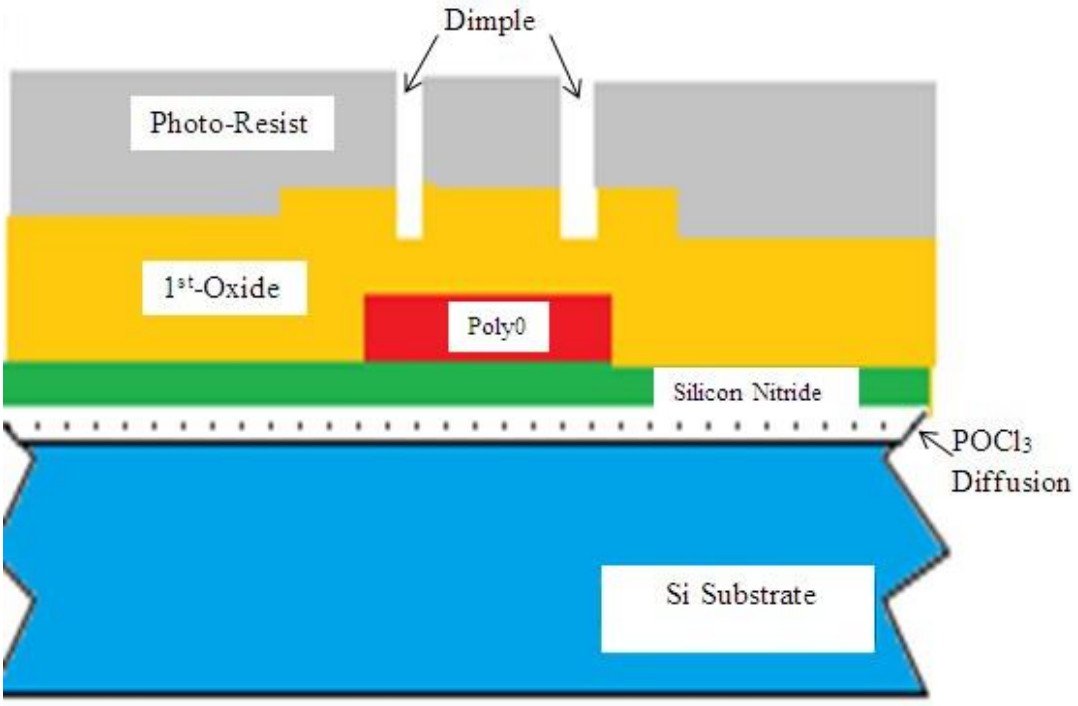

ix. In the next step, substrate is re-coated using PR then the next 3rd level, named as ANCHOR1, is patterned by lithography process. The undesirable oxide is distant in an RIE etch besides the PR is uncovered.

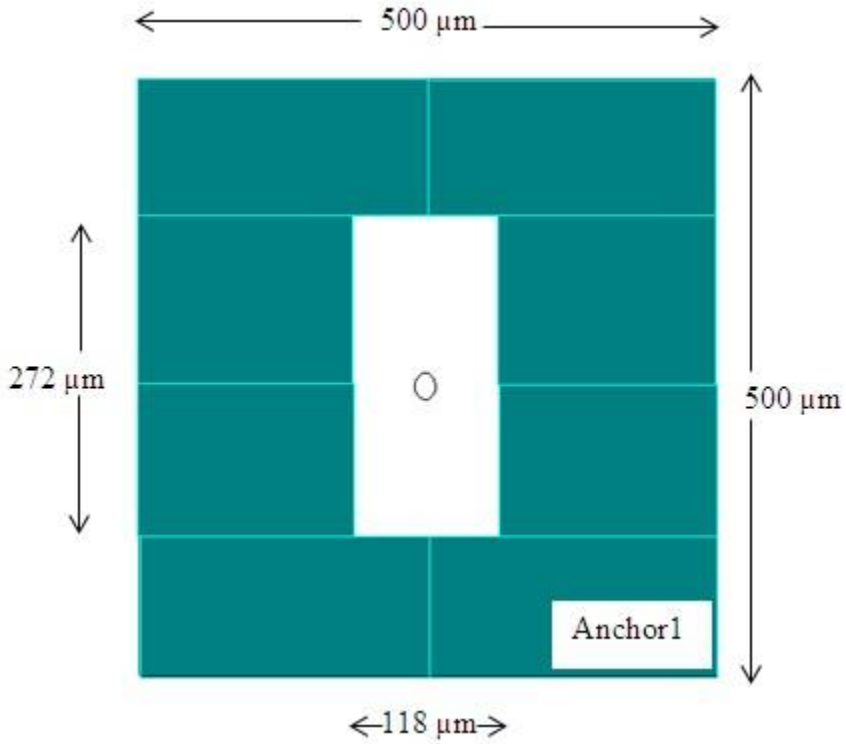

x. The substrate is re-coated using PR and the third level (in this case ANCHOR2) is patterned lithographically. The undesirable oxide is distant in an RIE etch also the PR is exposed.

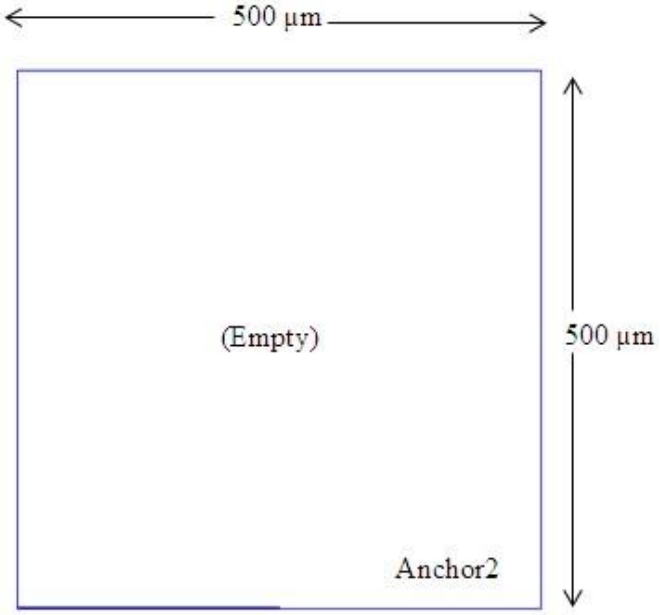

xi. An extensive 2.0 µm coating of pure poly-silicon is set down through LPCVD tracked by the removal of 200 nm deep PSG in addition a 1060°C/hour anneal. These annealing works for both decreases it's left over stress also fix the poly-silicon.

xii. The substrate is layered using PR then the 4th level, named as POLY1, is patterned by lithography process. In the next step, PSG is 1st etched to make a firm mask in addition Poly 1 is RIE. After completion of etching process, the PR as well as PSG firm mask is uninvolved.

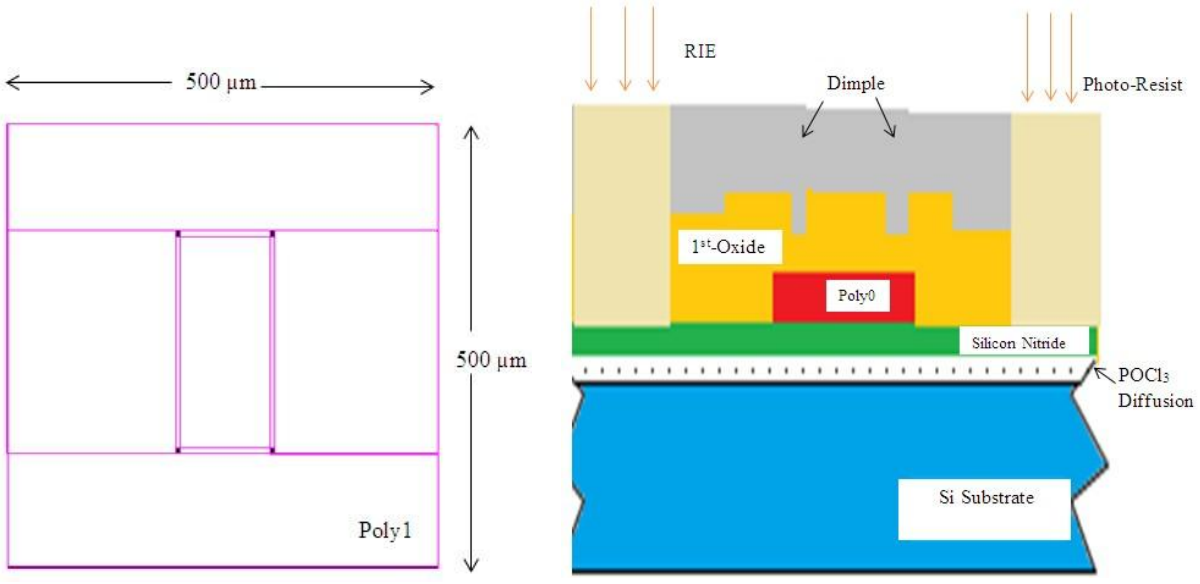

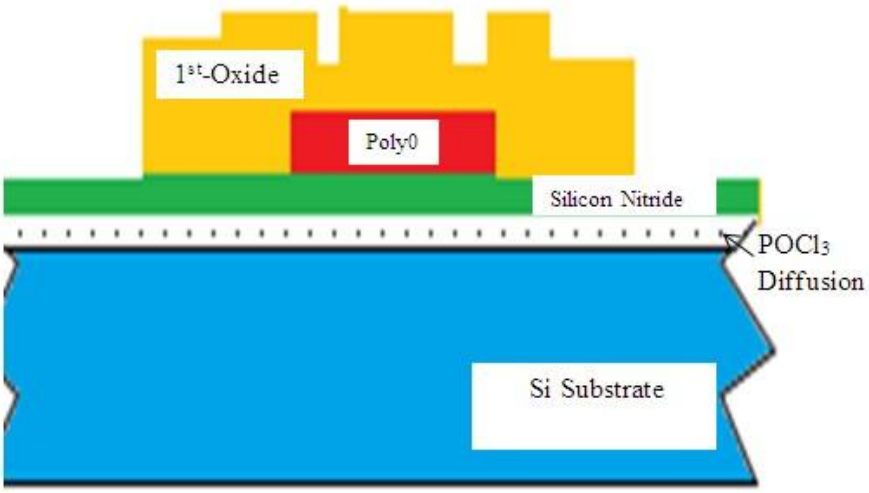

xiii. In general, the determination of HOLE1 is to arrange for smaller discharge etch paths below enormous polysilicon structures. The secondary determination is to offer a way to "remove" holes after a bright field level.

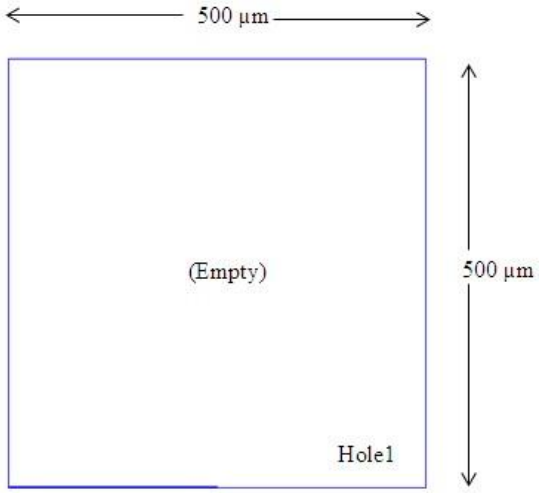

xiv. Another ANCHOR2 level offers beginnings for Poly2 (to be deposited later) to dealings through Nitride or Poly 0.

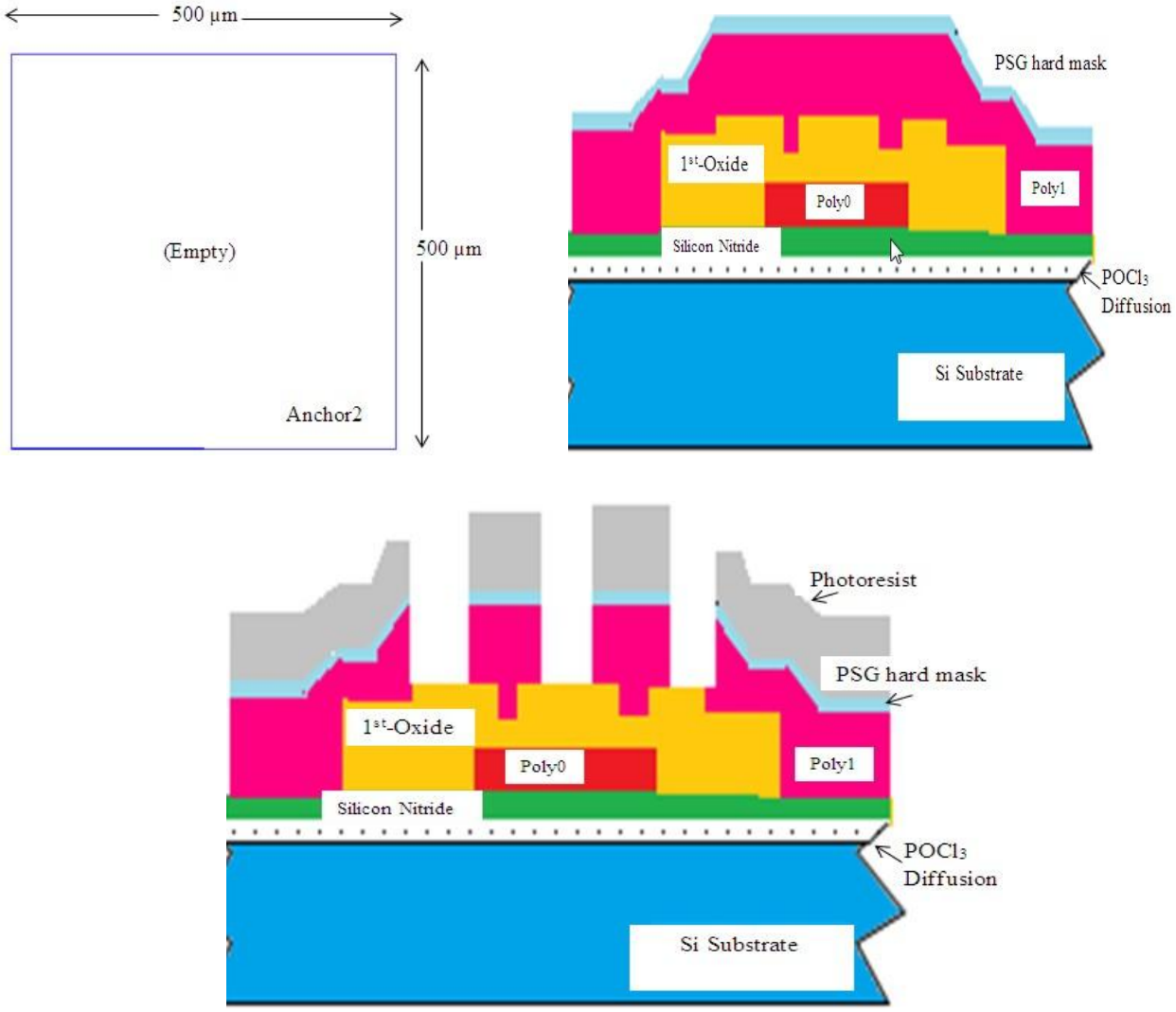

xv. In the next step, 2nd oxide coating having PSG depth of 0.75 µm, is placed on the substrate. This coating is twice patterned to permit interaction together Poly1 as well as wafer layers.

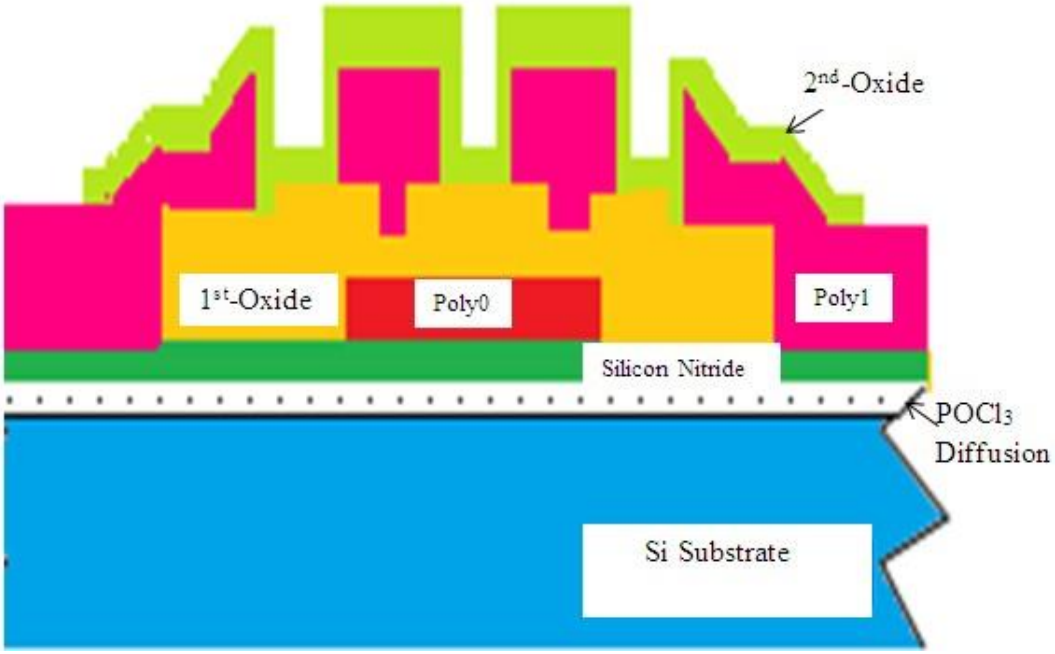

xvi. The substrate is covered by PR and the 5th level, named as POLY1_POLY2_VIA, is patterned by lithography process. The undesirable 2nd oxide is RIE, preventing on Poly1, also the PR is uncovered.

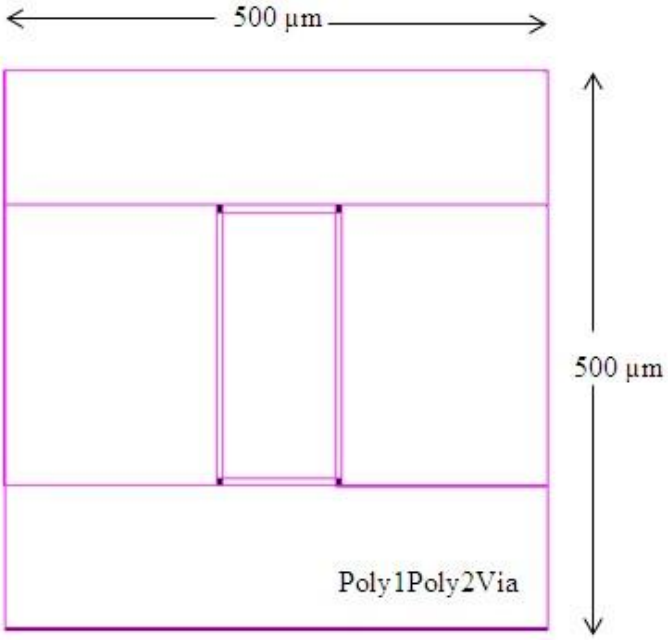

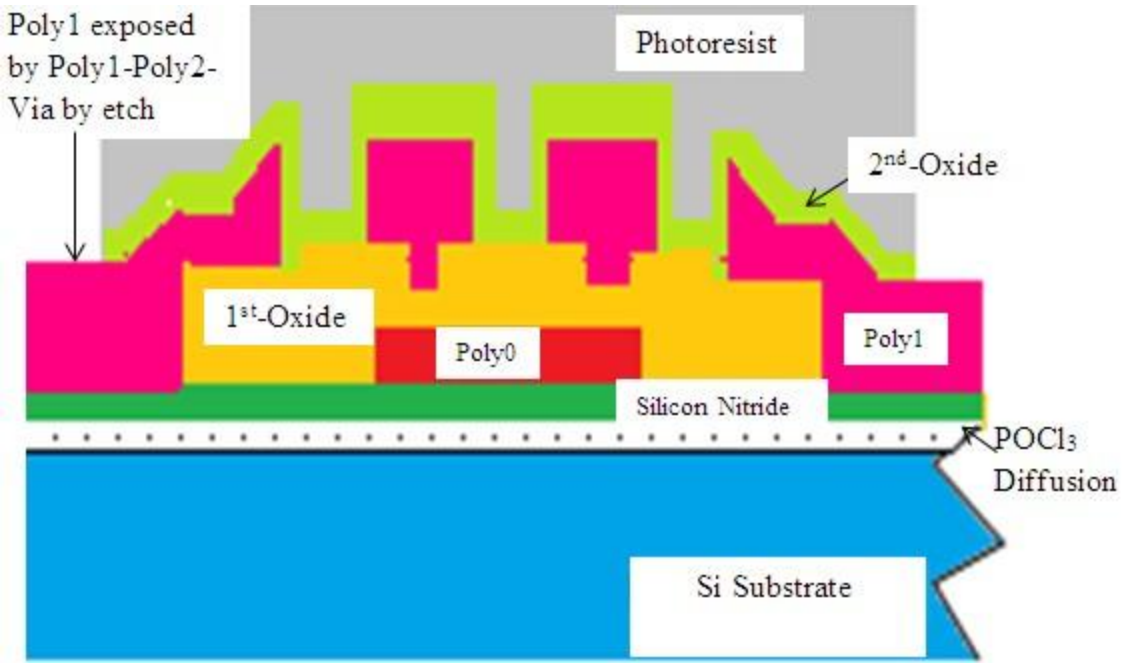

xvii. The substrate is re-layered through PR in addition to 6th level, named as; ANCHOR2 is patterned by lithography process. The 2nd and 1st oxides are etched by RIE, preventing on either Poly0 or Nitride, then the PR is uncovered. Next ANCHOR2 level delivers beginnings for Poly2 to dealings using Poly0 or Nitride.

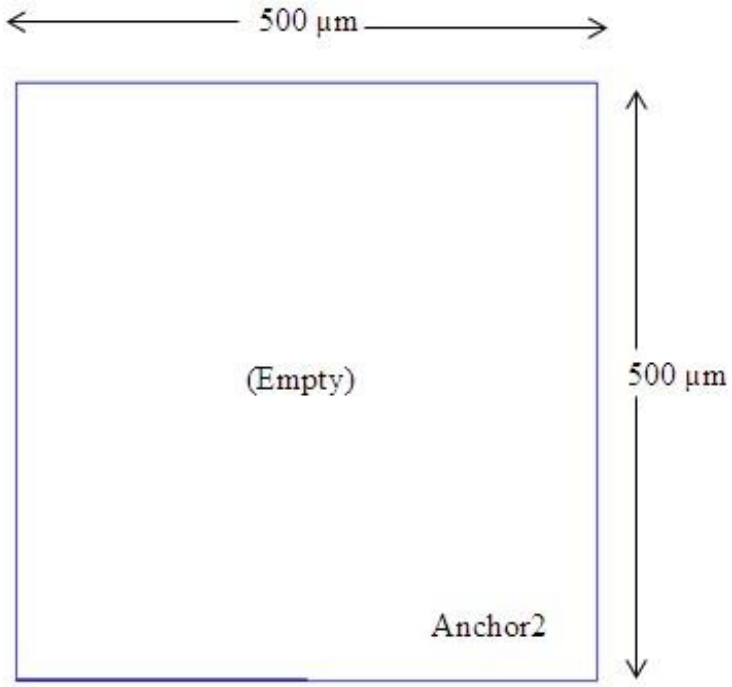

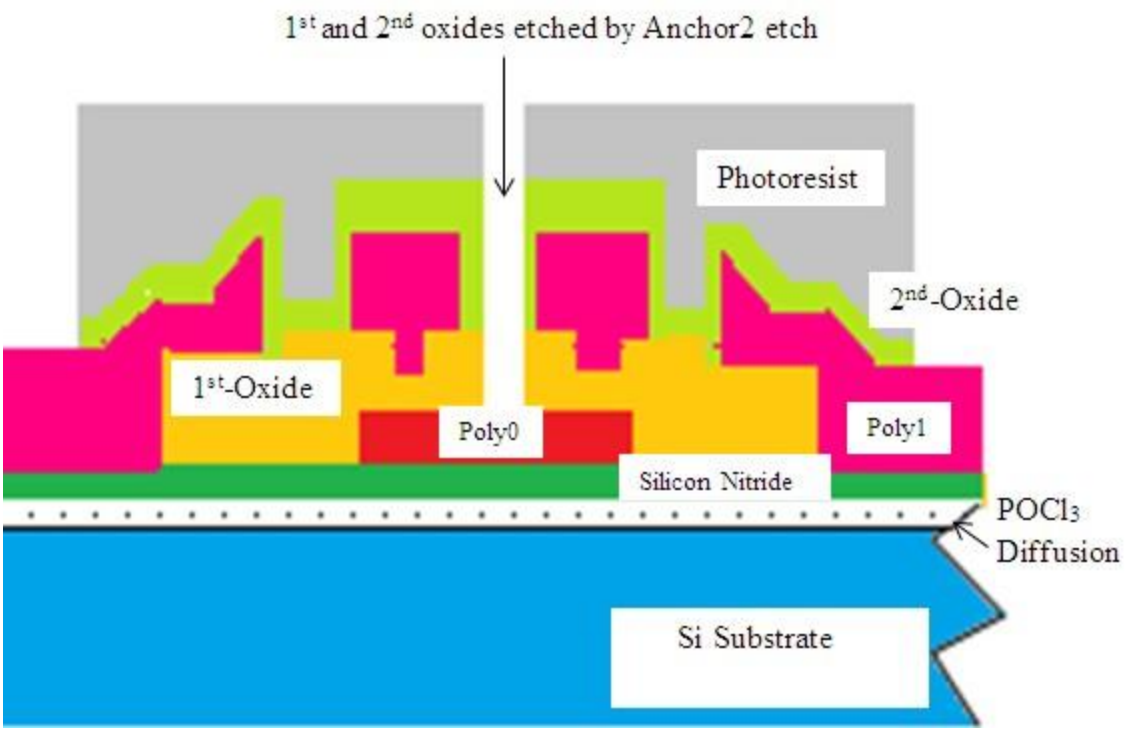

xviii. A depth of 1.5 µm pure poly-silicon coating is set down tracked via a depth of 200 nm PSG firm mask layer. The substrate is annealed at 1060°C/ hour to impure the poly-silicon also decrease residual stress.

xix. The substrate is layered using PR and the 7th level, named as POLY2, is patterned by lithography process. The PSG firm masks as well as Poly2 coatings are etched through RIE and then PR as well firm mask are uninvolved.

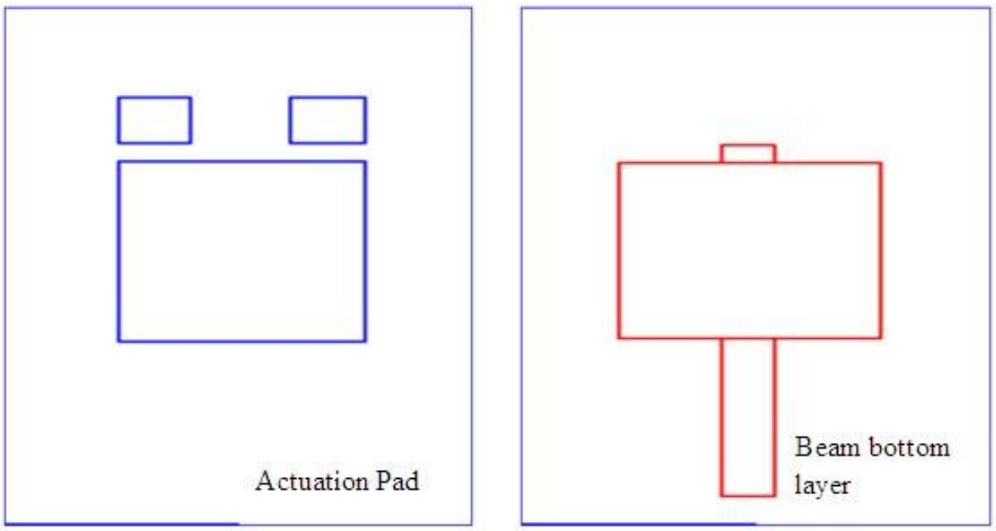

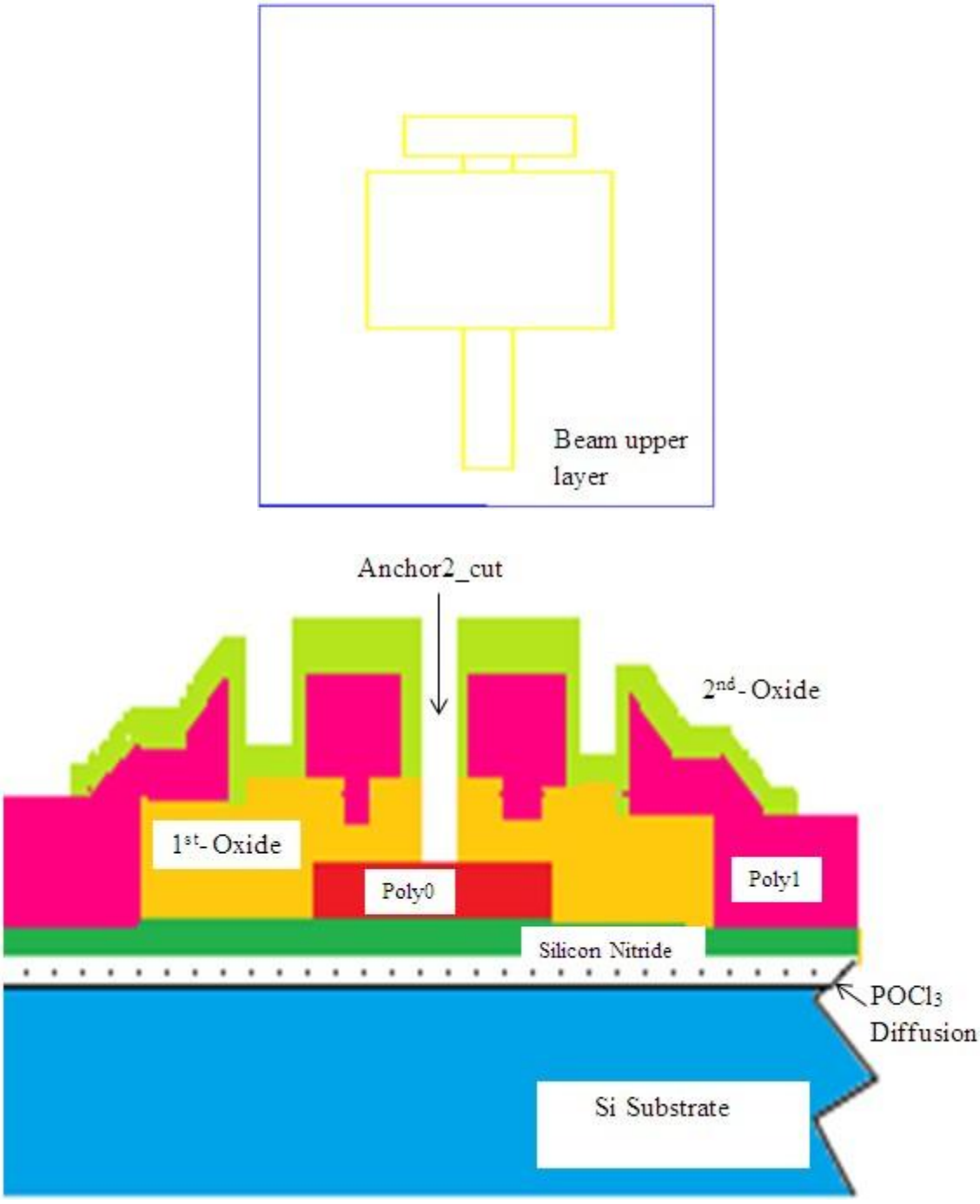

xx. The principle purpose of HOLE2 is to offer smaller discharge etch paths below enormous poly-silicon structures. The secondary determination is to deliver a way to "remove" holes after a bright field level. All mechanical configurations have at this moment been fabricated. The left over processes are adding the metal coating and eliminate the oxides sacrificial layer.

xxi. The wafer is located in a vacuum chamber at normal room temperature through a crucible covering the physical material to be put down. A source of heating at high temperature is preferred for crucible initiating the measurable to evaporate as well as condense taking place at all open cool planes of the wafer and vacuum chamber. The procedure is usually accomplished on single side surface of the wafer on a time. Usual heating sources are: resistive heating, E-beam, Inductive RF heating. In particular arrangements the wafer can be excited throughout deposition to modify the structure/stress of the set down material.

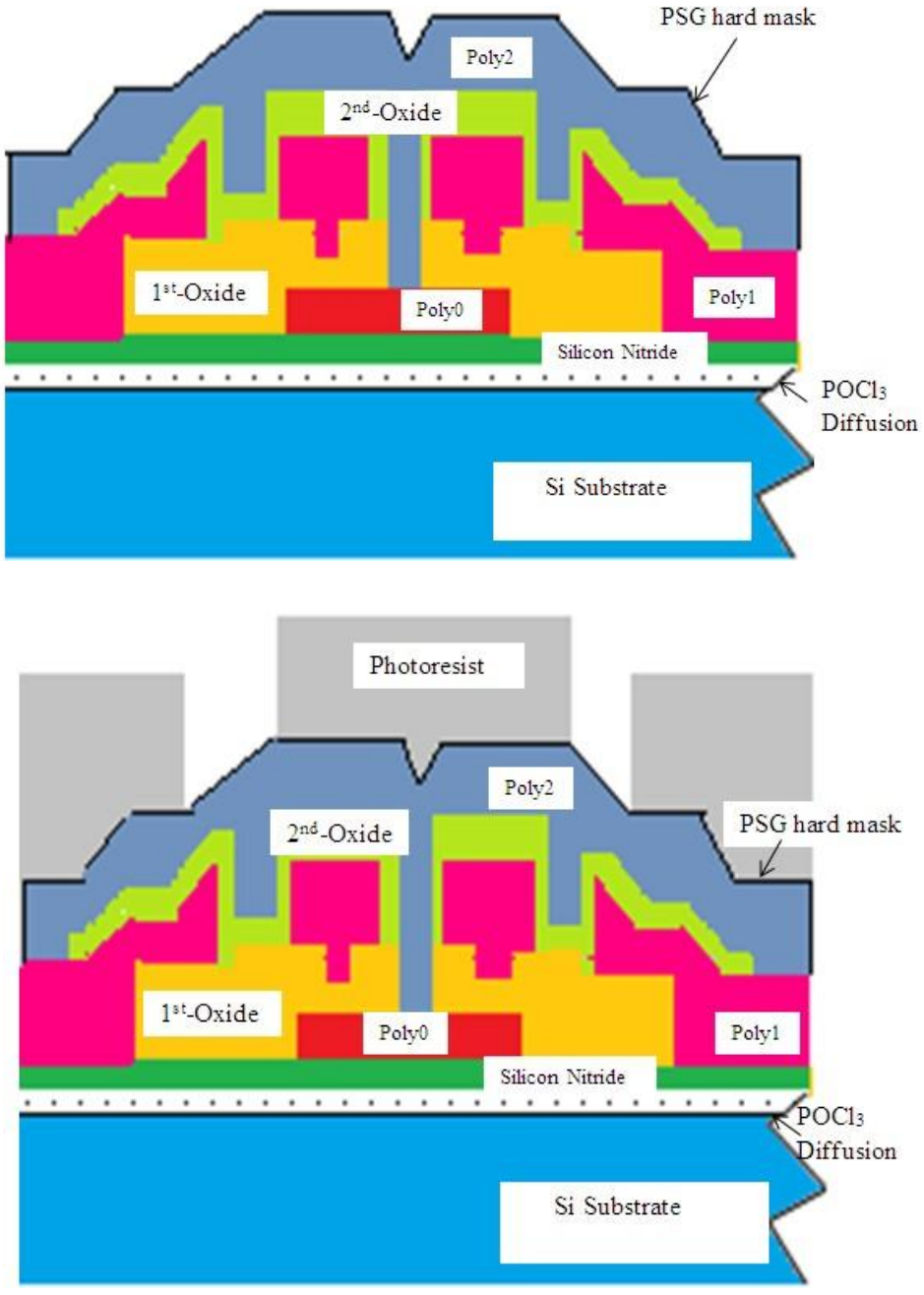

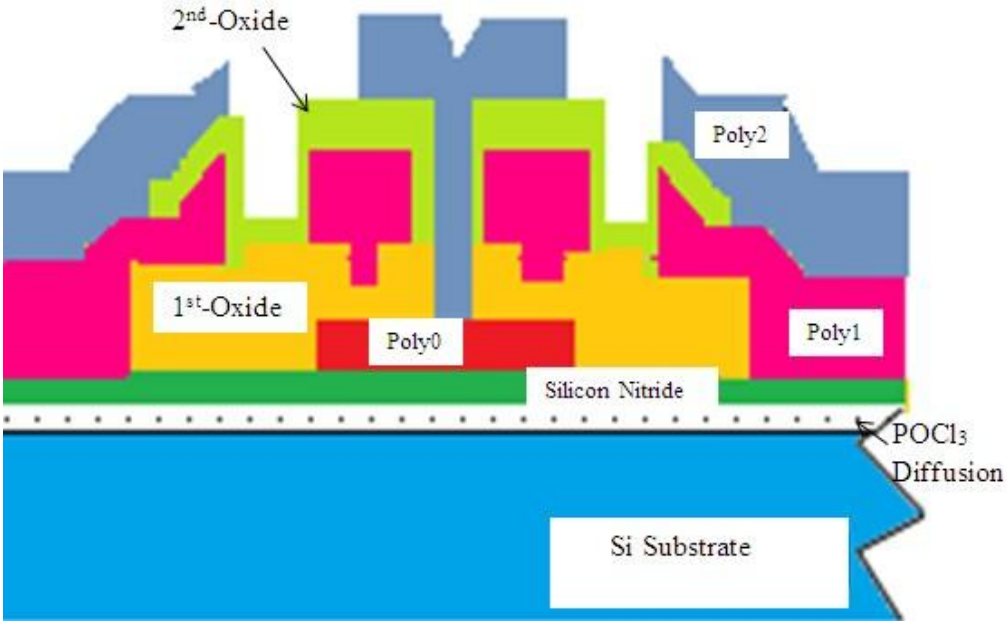

xxii. The lateral wall of the PR is slanted at a reentrant position, which permits the metal layer to be set down on the exteriors of the substrate then the PR, but offers discontinuities the metal layer in excess of the reentrant PR step. The PR and undesirable metal (an upper the PR) are then uninvolved in a flush bath.

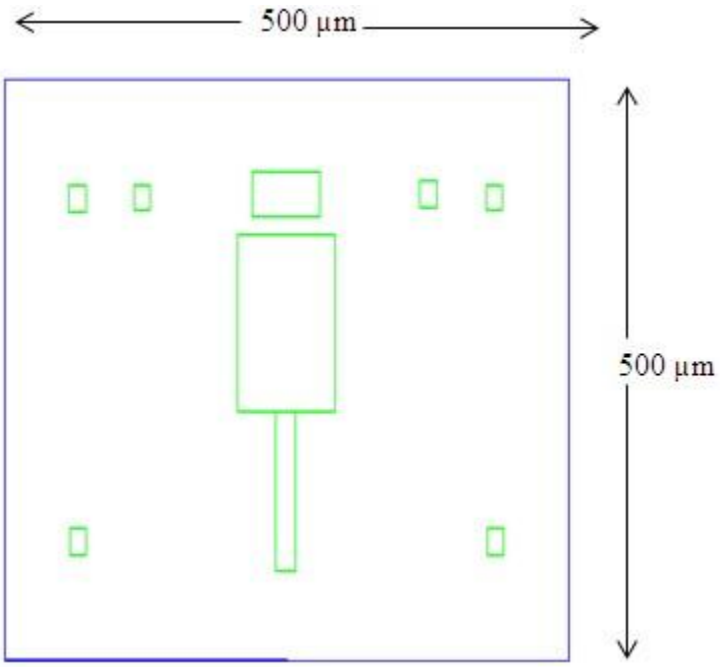

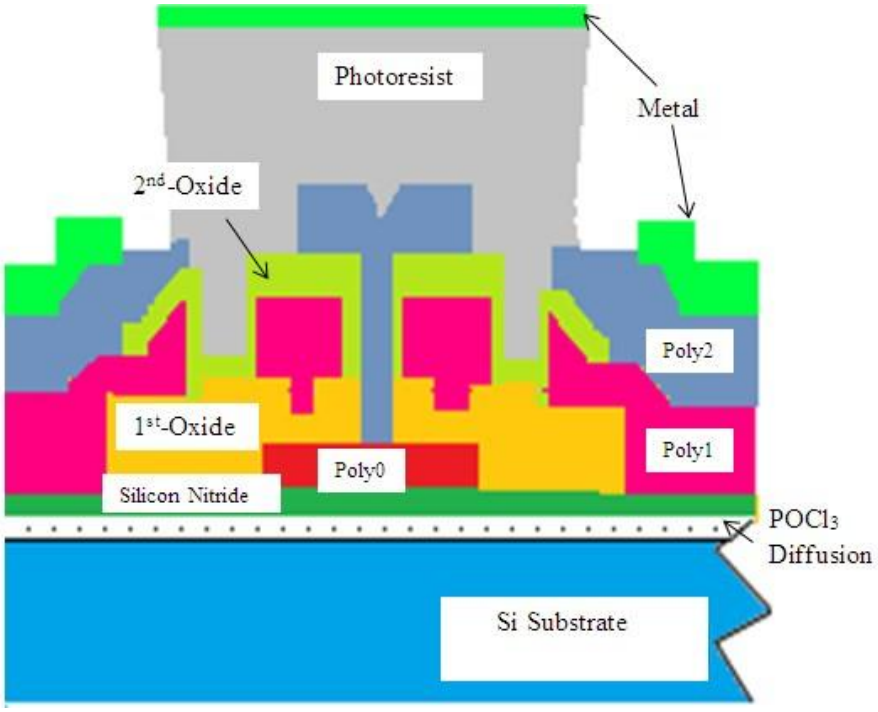

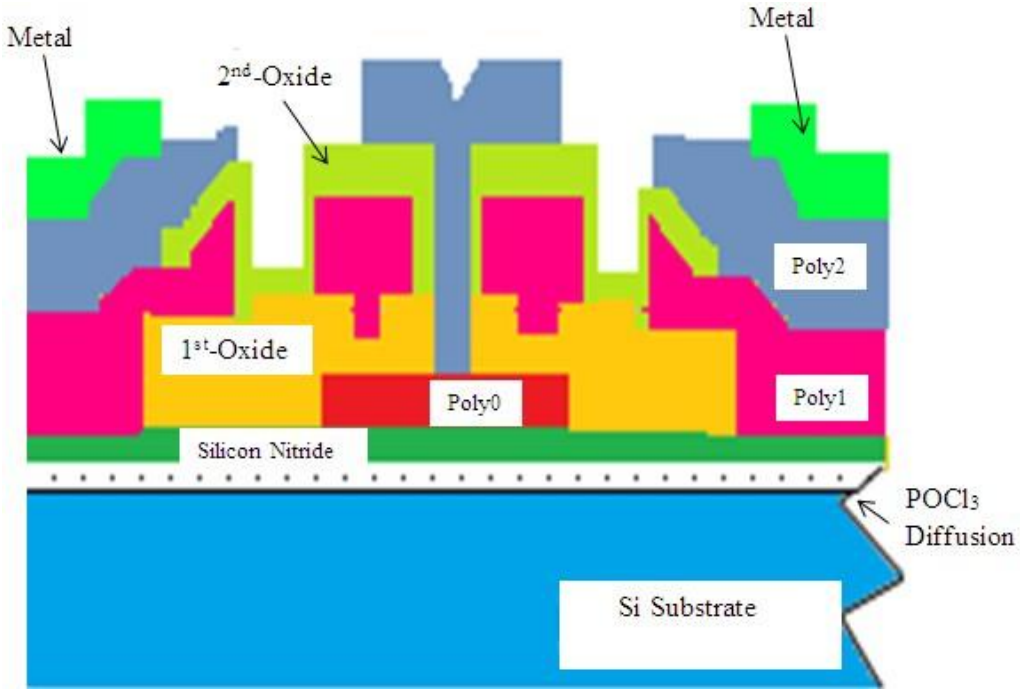

xxiii. The procedure is at this moment complete and also the substrate can be covered by a protective coating of PR and ready for diced.

xxiv. The structures are unconfined by dipping the diced chips in a hydrogen fluoride (HF) 49% solution. The Poly1 stators can be realized nearby the stable Poly2 center. The loads

of Metal, Poly1 as well as Poly2 taking place the sides signify the stators preferred to electrostatically drive the motor.

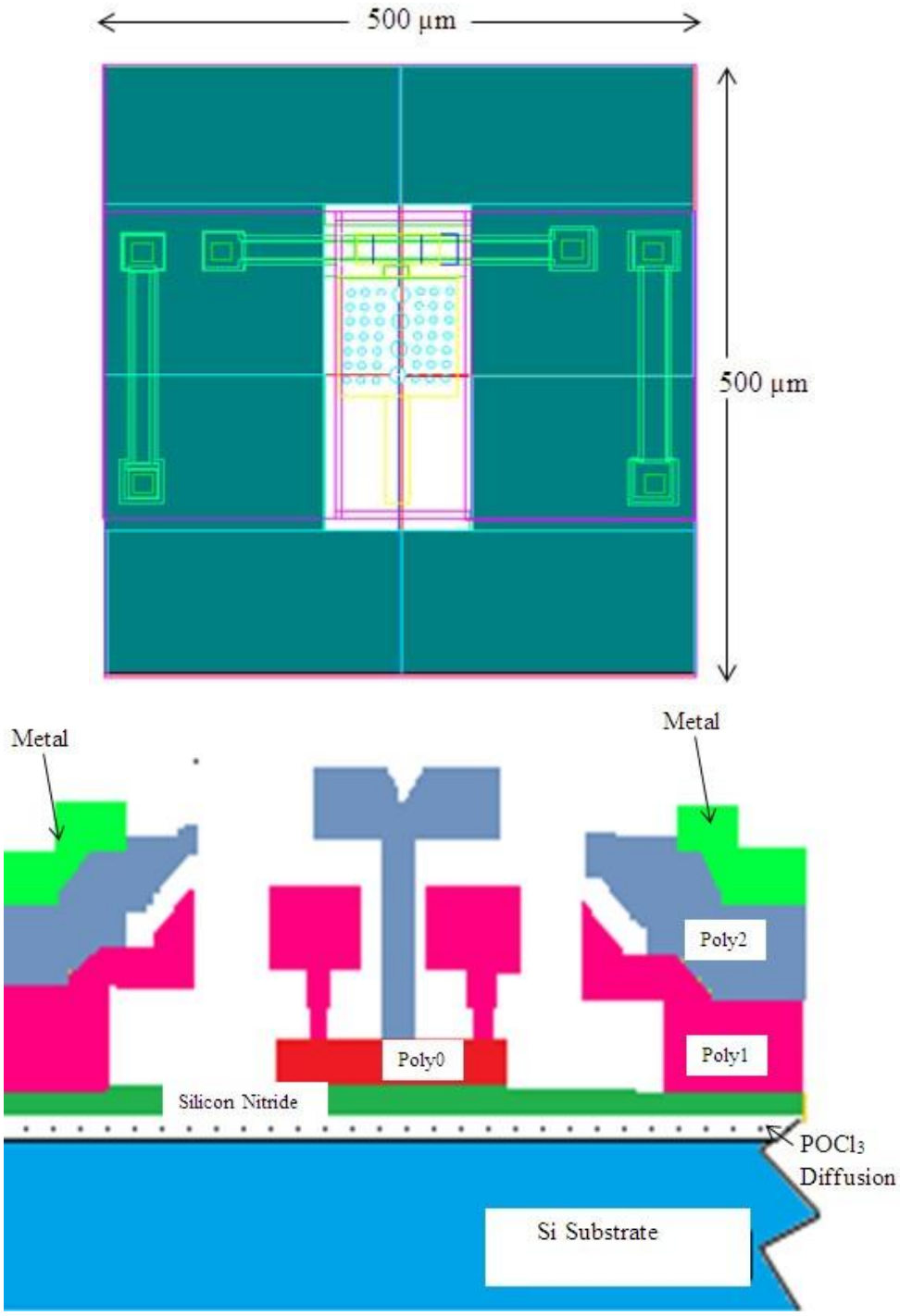

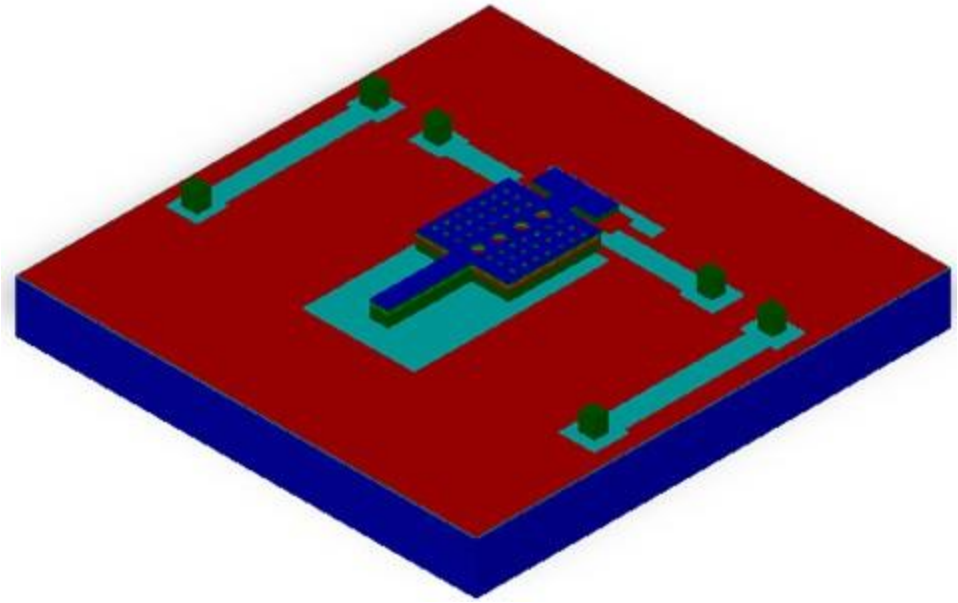

Final size of the chip is 0.5 mm × 0.5 mm

Appendix - B

PCB of Power Supply circuit to control RF MEMS switches on Antenna

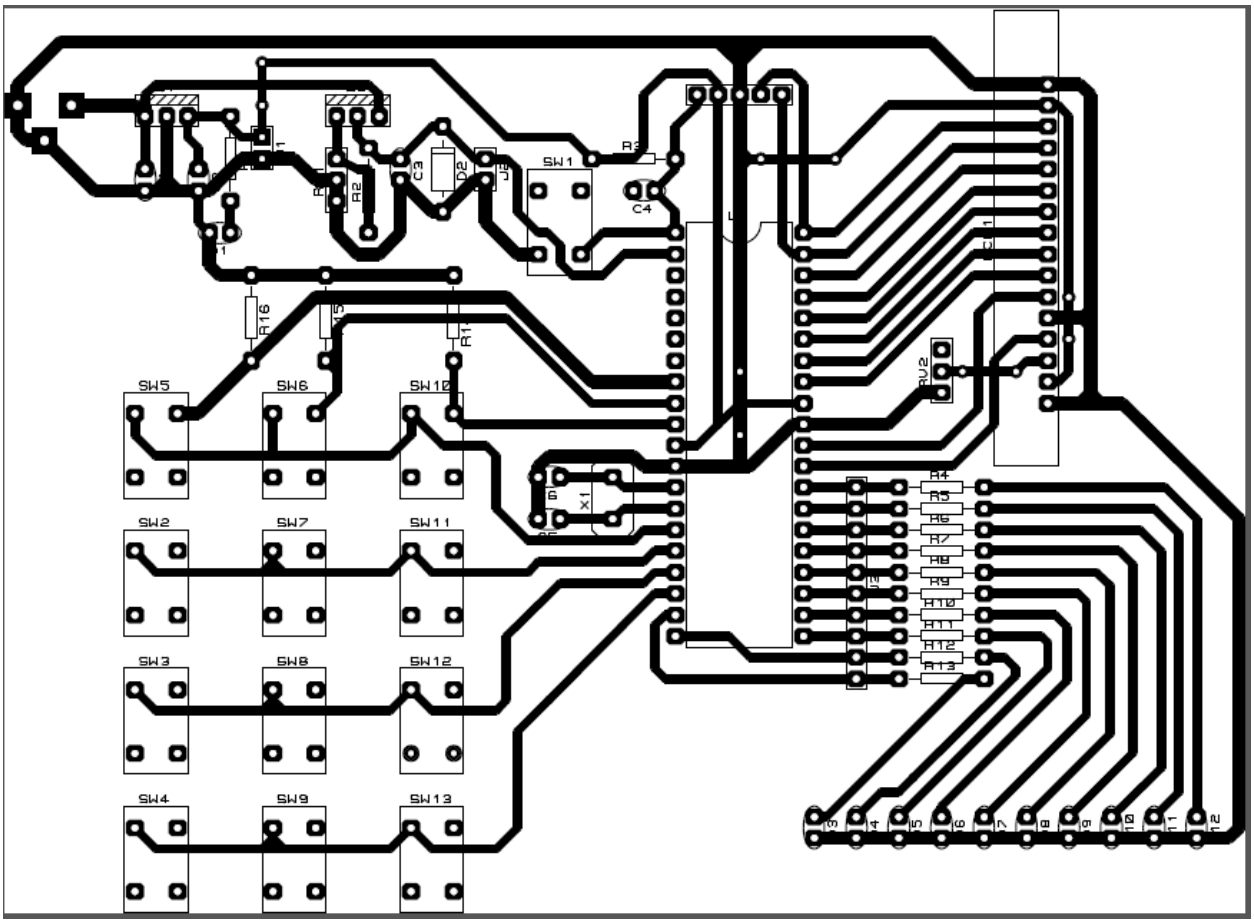

Microcontroller Programing (C-language code) - Power Supply circuit to control RF switches on Antenna

```
#include<pic.h>

#define LCD PORTB
#define RS RD6
#define EN RD7
#define LED1 RD0
```

```
#define LED2 RD1
#define LED3 RD2
#define LED4 RD3
#define LED5 RC4
#define LED6 RC5
#define LED7 RC6
#define LED8 RC7
#define LED9 RD4
#define LED10 RD5
#define col1 RC0
#define col2 RC1
#define col3 RC2
#define col4 RC3
#define row1 RE0
#define row2 RE1
#define row3 RE2
//-----------------------------------------------
unsigned int b=0,v=0;
void delay(unsigned long int);
void lcd_cmd_send(unsigned char);
void lcd_char_send(unsigned char);
void lcd_display(unsigned char *,unsigned char,unsigned char);
void lcd_num_dis(unsigned int,unsigned char);
//---------------------------------
void main(void)
{
        ANSEL=0X01;
        ANSELH=0X00;
        TRISC=0X00;
        TRISB=0x00;
        TRISD=0x00;
```

```
        TRISE=0xFF;
        TRISA0=1;
        ADCON0=0X03;
        ADCON1=0X80;
        PORTC=0x00;
        PORTD=0x00;
        lcd_cmd_send(0x38);
        lcd_cmd_send(0x01);
        lcd_cmd_send(0x0C);
        lcd_cmd_send(0x80);
//-----------------------
lcd_display("Voltage=     V ",1,0);
//---------------------------------
while(1)
{
GO=1;
while(GO==1);
b=(256*ADRESH)+ADRESL;
v=(b/1024.0)*4925;
lcd_num_dis(v,0x88);
col4=0;
col3=0;
col2=0;
col1=1;
if(row1==1)
{
while(row1==1);
LED1=~LED1;
delay(7000);
}
else if(row2==1)
```

```
{
while(row2==1);
LED2=~LED2;
delay(7000);
}
else if(row3==1)
{
while(row3==1);
LED3=~LED3;
delay(7000);
}
col1=0;
col4=0;
col3=0;
col2=1;
if(row1==1)
{
while(row1==1);
LED4=~LED4;
delay(7000);
}
else if(row2==1)
{
while(row2==1);
LED5=~LED5;
delay(7000);
}
else if(row3==1)
{
while(row3==1);
LED6=~LED6;
```

```
delay(7000);
}
col2=0;
col1=0;
col4=0;
col3=1;
if(row1==1)
{
while(row1==1);
LED7=~LED7;
delay(7000);
}
else if(row2==1)
{
while(row2==1);
LED8=~LED8;
delay(7000);
}
else if(row3==1)
{
while(row3==1);
LED9=~LED9;
delay(7000);
}
col3=0;
col2=0;
col1=0;
col4=1;
if(row1==1)
{
while(row1==1);
```

```
LED10=~LED10;
delay(7000);
}
else if(row2==1)
{
while(row2==1);
LED1=1;LED2=1;LED3=1;LED4=1;LED5=1;LED6=1;LED7=1;LED8=1;LED9=1;LED10=1;
delay(7000);
}
else if(row3==1)
{
while(row3==1);
LED1=0;LED2=0;LED3=0;LED4=0;LED5=0;LED6=0;LED7=0;LED8=0;LED9=0;LED10=0;
delay(7000);
}
}
}
//---------------------------------
void delay(unsigned long int mdelay)
{
        while(mdelay--);
}
void lcd_cmd_send(unsigned char mcmd)
{
        LCD=mcmd;
        RS=0;
        EN=1;
        delay(25);
        EN=0;
        delay(100);
}
```

```
void lcd_char_send(unsigned char mchar)
{
        LCD=mchar;
        RS=1;
        EN=1;
        delay(25);
        EN=0;
        delay(100);
}
void lcd_display(unsigned char *slcd,unsigned char lcd_line,unsigned char lcd_posi)
{       unsigned char ilcd=0;
        if(lcd_line==1)
        {
        lcd_cmd_send(0x80+lcd_posi);
        }
        if(lcd_line==2)
        {
        lcd_cmd_send(0xC0+lcd_posi);
        }

        while(slcd[ilcd]!='\0')
        {
                lcd_char_send(slcd[ilcd]);
                ilcd++;
        }
}
void lcd_num_dis(unsigned int lnum, unsigned char lposi)
{
unsigned int lunit,lten,lhun,ltho,lttho;
        lunit=lnum%10;
        lnum/=10;
```

```
        lten=lnum%10;
    lnum/=10;
        lhun=lnum%10;
    lnum/=10;
        ltho=lnum%10;
        lcd_cmd_send(lposi);
        lcd_char_send(ltho+0x30);
        lcd_char_send('.');
        lcd_char_send(lhun+0x30);
        lcd_char_send(lten+0x30);
        lcd_char_send(lunit+0x30);
}
```

References

[1]. Jeffrey L. Hilbert, "RF-MEMS for Wireless Communications", Topics in Design and Implementation, IEEE Communications Magazine, pp. 68-74, August 2008.

[2]. H. Okazaki, A. Fukuda, K. kawai, T. Furuta and S. Narahashi, "MEMS based Reconfigurable RF Circuits for future mobile terminals", Proceeding of International Microwave Conference, Bangkok, 11-14, December, 2007.

[3]. A. Tasic, Su-T. Lim, W. A. Serdijn and J. R. Long, "Design of Adaptive Multimode RF Front-End Circuits", IEEE Journal of Solid-State Circuits, Vol. 42, No. 2, February 2007.

[4]. M. Feng, Shyh-C. Shen, D. C. Caruth and Jian-J. Huang, "Device Technologies for RF Front-End Circuits in Next-Generation Wireless Communications", Proceeding of Asia-Pacific Microwave Conference, APMC 2008, 16-20, December, 2008.

[5]. C. T.-C. Nguyen, L. P. B. Katehi, and G. M. Rebeiz, "Micromachined Devices for Wireless Communications," Proceedings of the IEEE, Vol. 86, No. 8, pp. 1756–1768, Aug. 1998.

[6]. E. R. Brown, "RF-MEMS switches for reconfigurable integrated circuits", IEEE Trans. Microwave Theory Tech., Vol. 46, No. 11, pp. 1868–1880, 1998.

[7]. Hung-P. Chang, J. Qian, B. A. Cetiner, F. De Flaviis, M. Bachman and G. P. Li, "Low Cost RF MEMS Switches Fabricated on Microwave Laminate Printed Circuit Boards", International Journal of RF Microwave & Computer-Aided Engineering, Vol. 9, pp. 348–61, 1991.

[8]. L. E. Larson, R. H. Hackett, M. A. Melendes, and R. F. Lohr, "Micromachined microwave actuator (MIMAC) technology- a new tuning approach for microwave integrated circuits", Microwave and Millimeter-Wave Monolithic Circuits Symposium Digest, Boston, MA, pp. 27-30, 1991.

[9]. X. Guo, J. Cui, M. Cai, L. Liu, Z. Lai and P. Xin, "Re-Configurable Kμ Dual-bands slot Antenna using MEMS Switches", Microwave and Optical Technology Letters , Vol. 48, No. 12, 2006.

[10]. M. F. Barnsley, "Fractals Everywhere", Second Edition, Morgan Kaufmann, Academic Press, An imprint of Elsevier, 1993.

[11]. B. B. Madelbrot, "The Fractal Geometry of Nature", Henry Holt and Company, ISBN 0716711869, New York, 1983.

[12]. K. J. Falconer, "Fractal Geometry: Mathematical Foundations and Applications", New York, Wiley, 1990.

[13]. B. Ghosh, S. Sinha, M. V. Kartikeyan, "Fractal Apertures in Waveguides, Conducting Screens and Cavities", Analysis and Design Series: Springer Series in Optical Sciences, ISBN 978-3-319-06535-9, Vol. 187, 2014.

[14]. S. Lucyszyn, "Advanced RF MEMS", Cambridge University Press, ISBN: 978-0-521-89771-6, Cambridge, Aug. 2010.

[15]. S. K. Lahiri, H. Saha and A. Kundu, "RF MEMS SWITCH: An overview at- a glance", Proceedings of 4th IEEE Conference on Computers and Devices for Communication, Kolkata, CODEC 2009, 14-16 December, 2009.

[16]. G. M. Rebeiz and J. B. Muldavin, "RF MEMS Switches and Switch Circuits", IEEE Microwave Magazine, pp. 59-71, 2001.

[17]. Thesis on "Design and Analysis of Series and Shunt MEMS Switches" by Jeremy Bert Muldavin, The university of Michigan, 2001.

[18]. A. Persano, A. Cola, G. D. Angelis, A. Taurino. P. Siciliano and F. Quarant, "Capacitive RF MEMS switches with Tantalum-Based Materials", Journal of MEMS, IEEE, Vol. 20, No. 2, pp. 365-370, 2011.

[19]. Z. J. Yao, S. Chen and S. Eshelman, "Micromachined Low-Loss Microwave Switches", IEEE Journal of Microelectromechanical Systems, June 1999, Vol. 8, No.2, 1999, pp.129-134, 1999.

[20]. W. Wu, Bing-Z. Wang, Xue-S. Yang and Y. Zhang, "A Pattern-Reconfigurable Planar Fractal Antenna and its Characteristic-Mode Analysis", IEEE Antennas and Propagation Magazine, Vol. 49, No. 3, 2007.

[21]. M. Ding, R. Jin, J. Geng, X. Guo and J. Chen, "A High-Gain Dual-Band Directional/Omnidirectional Reconfigurable Antenna for WLAN Systems", Wiley Periodicals, Inc. International Journal, RF and Microwave CAE 18, pp. 225–232, 2008.

[22]. D. E. Anagnostou, G. Zheng, M. T. Chryssomallis, J. C. Lyke, G. E. Ponchak, J. Papapolymerou, and C. G. Christodoulou, "Design, fabrication, and measurements of an RF-MEMS-based self-similar Reconfigurable Antenna", IEEE Transaction on Antennas and Propagation, Vol. 54, No. 2, pp. 422–432, 2006.

[23]. L. Zhou, S. K. Sharma and S. K. Kassegne, "Reconfigurable Microstrip Rectangular loop Antennas using RF MEMS switches", Microwave and Optical Technology Letters, Vol. 50, No. 1, 2008.

[24]. G. H. Huff, J. Feng, S. Zhang and J. T. Bernhard, "A novel radiation pattern and frequency reconfigurable single spiral microstrip antenna", IEEE Microwave Wireless Component Letter 13, pp. 57-59, 2003.

[25]. J. C. Chiao, Y. Fu, I. M. Chio, M. D. Lisio and L.Y. Lin, "MEMS reconfigurable Vee antenna", IEEE MTT-S International Microwave Symposium Digest, Vol. 4, pp. 1515–1518, 1999.

[26]. Comsol, www.comsol.com.

[27]. Intellisense, www.intellisense.com.

[28]. Ansys, www.ansys.com.

[29]. Coventorware, Release by Coventorware Inc., 2010.

[30]. Ansoft Corporation, Ansoft Maxwell HFSS, www.ansoft.com.

[31]. Agilent Technology Inc., ADS 2011, Palo Alto, CA, www.agilent.com.

[32]. J. R. Reid, "An Overview of micro-electro-mechanical systems (MEMS)," Tutorial Session on MEMS for antenna applications antenna applications symposium, Allerton Park Monticello, Illinois, 1999.

[33]. A. Kundu, S. Sethi, N. C. Mondal, B. Gupta, S. K. Lahiri and H. Saha, "Analysis and optimization of two movable plates RF MEMS switch for simultaneous improvement in actuation voltage and switching time", Microelectronics Journal, Vol. 41, pp. 257–265, 2010.

[34]. M. Daneshmand and R. R. Mansour, "RF MEMS Satellite Switch Matrices", IEEE microwave magazine, pp. 92-109, August, 2011.

[35]. N. Setter, V. Sherman, K. Astafiev & A.K. Tagantsev, "Polar Ceramics in RF-MEMS and Microwave Reconfigurable Electronics: A Brief Review on Recent Issues", Journal of Electroceramics, Vol. 13, pp. 215–222, 2004.

[36]. Hee-C. Lee, Jae-H. Park and Yong-H. Park, "Development of shunt type ohmic RF MEMS switches actuated by piezoelectric cantilever", Sensors and Actuators A, Vol. 136, pp. 282–290, 2007.

[37]. A.V. Ganesan, K. K. Deepan, R. R. Varun, Swaminathan S., "Novel low cost powerless MEMS based Osscicular System", ASME 2013 International Mechanical Engineering Congress and Expo (IMECE), 2013.

[38]. Yo-T. Songa, Hai-Y. Lee and M. Esashi, "A corrugated bridge of low residual stress for RF-MEMS switch", Sensors and Actuators A, Vol. 135, pp. 818–826, 2007.

[39]. F. Ke, J. Miao and Z. Wang, "A wafer-scale encapsulated RF MEMS switch with a stress-reduced corrugated diaphragm", Sensors and Actuators A, Vol. 151, pp. 237–243, 2009.

[40]. Y. Lee, S. Ganguly, J. Yeo, and R. Mittra, "A Novel Conformal Multiband Antenna Design Based on Fractal Concepts", Proceeding of IEEE Symposium on Antennas and Propagation Society, Vol. 1, pp. 92 - 95, 2002.

[41]. C. Varadhan, J. K. Pakkathillam, M. Kanagasabai, R. Sivasamy, R. Natarajan and S. K. Palaniswamy, "Triband Antenna Structures for RFID Systems Deploying Fractal Geometry", IEEE Antennas and Wireless Propagation Letters, Vol. 12, 2013.

[42]. S. S. Patel, H. B. Soni, Y. P. Kosta and S. K. Patel, "E-shaped Patch Antenna Analysis for Multiple Applications", Proceeding of IEEE Conference on Electronics Computer Technology, 2011.

[43]. A. Patnaik, D. Anagnostou, C. G. Christodoulou and J. C. Lyke, "Neuro computational Analysis of a Multiband Reconfigurable Planar Antenna", IEEE Transactions on Antennas and Propagation, Vol. 53, No. 11, pp. 3453-3458, 2005.

[44]. A. Razavi and K. Forooraghi, "Thinned arrays using pattern search Algorithms", Progress in Electromagnetics Research, Vol.78, pp. 61–71, 2008.

[45]. F. Gunes and F. Tokan, "Pattern Search optimization with applications on synthesis of linear antenna arrays", Expert Systems with Applications, Vol. 37, pp. 4698–4705, 2010.

[46]. S. K. Jain, A. Patnaik and S. N. Sinha, "Neural Network Based Particle Swarm Optimizer for Design of Dual Resonance X/Ku Band Stacked Patch Antenna", Proceeding of IEEE conference on AP-S/URSI 2011, pp. 2932-2935, 2011.

[47]. S. P. Gangwar, R. P. S. Gangwar, B. K. Kanaujia and Paras, "Resonant frequency of circular microstrip antenna using artificial neural networks", Indian Journal of Radio & Space Physics, Vol. 37, pp. 204-208, 2008.

[48]. D. E. Skinner, J. D. Connor, S. Y. Foo, M. H. Weatherspoon and N. Powell, "Optimization of a Multi-Band Reconfigurable Microstrip Line-Fed Rectangular Patch Antenna using Self-Organizing Maps", Proceeding of IEEE conference, 2009.

[49]. B. Abolhassani, J. E. Salt and D. E. Dodds, "A two-phase genetic K-means algorithm for placement of radioports in cellular networks", IEEE Trans. Syst Man Cybern B Cybern, 34(1):533-8, February, 2004.

[50]. H. A. Majid, M. K. A. Rahim, M. R. Hamid, M. F. Ismail and F. Malek, "Frequency reconfigurable wide to narrow band monopole with slotted ground plane antenna", Journal of Electromagnetic Waves and Applications, Vol. 26, Nos. 11–12, pp. 1460–1469, August 2012.

[51]. M. A. Al-alaa, H. A. Elsadek, E. A. Abdallah, and E. A. Hashish, "Pattern and Frequency Reconfigurable Monopole Disc Antenna using PIN Diodes and MEMS Switches", Microwave and Optical Technology Letters, Vol. 56, No. 1, pp. 187-195, January 2014.

[52]. H. A. Majid, M. K. A. Rahim, M. R. Hamid and M. F. Ismail, "Frequency and Pattern Reconfigurable Yagi Antenna", Journal of Electromagnetic Waves and Applications, Vol. 26, pp. 379–389, 2012.

[53]. M. S. Parihar, A. Basu and S. K. Koul, "Transient Analysis of Reconfigurable Polarization Antenna", EuMA International Journal on Microwave Technologies, pp. 521-527, Vol. 5 No. 4, August 2013.

[54]. A. Zohur, H. Mopidevi, D. Rodrigo, M. Unlu, L. Jofre, and B. A. Cetiner, "RF MEMS Reconfigurable Two-Band Antenna", IEEE Antennas and Wireless Propagation Letters, Vol. 12, pp. 72-75, 2013.

[55]. W. H. Chen, J. W. Sun and Z. G. Feng, "A novel compact reconfigurable polarization and pattern antenna," Microwave and Optical Technology Letters, Vol. 49 pp. 2802-2805, Nov. 2007.

[56]. X. S. Yang, B. Z. Wang and H. L. Liu, "Reconfigurable Yagi Patch Array by Utilizing Odd even-Mode Method", Journal of Electromagnetic Waves and Applications, Vol. 20, No. 13, pp. 1725–1738, 2006.

[57]. P. Lotfi, M. Azarmanesh, and S. Soltani, "Rotatable Dual Band-Notched UWB/Triple-Band WLAN Reconfigurable Antenna", IEEE Antennas and Wireless Propagation Letters, Vol. 12, pp. 104-107, 2013.

[58]. C. Y. Lee, S. J. Ha, C. W. Jung and Y. J. Kim, "A CPWG-fed reconfigurable 3D beam steering antenna with directive radiation pattern", Journal of Electromagnetic Waves and Applications, Vol. 27, No. 1, pp. 59–65, 2013.

[59]. A. N. Kulkarni and S. K. Sharma, "Frequency Reconfigurable Microstrip Loop Antenna Covering LTE Bands With MIMO Implementation and Wideband Microstrip Slot Antenna all for Portable Wireless DTV Media Player", IEEE Transactions On Antennas And Propagation, Vol. 61, No. 2, pp. 964-968, February, 2013.

[60]. L. Pazin and Y. Leviatan, "Reconfigurable Slot Antenna for Switchable Multiband Operation in a Wide Frequency Range", IEEE Antennas and Wireless Propagation Letters, Vol. 12, pp. 329-332, 2013.

[61]. J. Ouyang, F. Yang, Z. P. Nie and Z. Q. Zhao, "A Novel Frequency Reconfigurable Microstrip Antenna for Wideband Application", Journal of Electromagnetic Waves and Applications, Vol. 22, pp. 1403–1410, 2008.

[62]. M. F. Jamlos, O. A. Aziz, T. A. Rahman, M. R. Kamarudin, P. Saad, M. T. Ali and M. N. Md Tan, "A Beam Steering Radial Line Slot Array (RLSA) Antenna with Reconfigurable Operating Frequency", Journal of Electromagnetic Waves and Applications, Vol. 24, pp. 1079–1088, 2010.

[63]. T. Aboufoul, C. Parini, X. Chen and A. Alomainy, " Pattern-Reconfigurable Planar Circular Ultra-Wideband Monopole Antenna", IEEE Transactions on Antennas and Propagation, Vol. 61, No. 10, 4973-4980, 2013.

[64]. T. Aboufoul, A. Alomainy and C. Parini, "Polarization reconfigurable ultrawideband antenna for cognitive radio applications", Microwave and Optical Technology Letters, Vol. 55, No. 3, 501-506, 2013.

[65]. X. Ding and B. Wang, "A millimeter-wave pattern reconfigurable antenna with a reconfigurable feeding network", Journal of Electromagnetic Waves and Applications, Vol. 27, No. 5, pp. 649–658, 2013.

[66]. X. Yang, A. Rahman, Q. H. Abbasi and Y. Hao, "Electrically Coupled Tapered Slot Ultra Wideband Antenna with Tunable Notch", Microwave and Optical Technology Letters, Vol. 53, No. 7, 1558-1561, 2011.

[67]. J. Choi and S. Lim, “Frequency and Radiation Pattern Reconfigurable Small Metamaterial Antenna using its Extraordinary Zeroth-Order Resonance”, Journal of Electromagnetic Waves and Applications, Vol. 24, pp. 2119–2127, 2010.

[68]. V. K. Varadan, K. J. Vinoy and K. A. Jose, “RF MEMS and Their Applications” John Wiley & Sons, Inc., 2003.

[69]. B. A. Cetiner, G. P. Li, “Monolithic Integration of RF MEMS Switches with a Diversity Antenna on PCB Substrate”, IEEE Transactions on Microwave Theory and Techniques, Vol. 51, No. 1, pp. 332-335, 2003.

[70]. R. Al-Dahleh, and R. R. Mansour, “ High-Capacitance-Ratio Warped-Beam Capacitive MEMS Switch Designs, Journal Of Microelectromechanical Systems”, 2010, Vol. 19, No. 3, pp. 538-547, June 2010.

[71]. R. L. Liboff and G. C. Dalman, “Transmission lines, waveguide and smith chart”, New York, pp. 237-238.

[72]. S. Fouladi and R. R. Mansour, “Capacitive RF MEMS switches fabricated in standard 0.35-µm CMOS technology”, IEEE Trans. on Microwave Theory and Techniques, Vol. 58, No.2, pp. 478-486, 2010.

[73]. K. Kuwabara, K. Takagahara, H. Morimura and Y. Sato, “RF MEMS switches integrated with sealed suspended coplanar waveguides for reconfigurable RF circuits”, IEEE Transducers, Beijing, China, pp. 5-9, 2011.

[74]. K. V. Caekenberghe, “Modeling RF MEMS Devices”, IEEE Microwave Magazine, Vol.13, No. 1, pp. 83-110, 2012.

[75]. M. N. Spasos, “RF-MEMS switches for reconfigurable antennas”, Brunel University School of Engineering and Design PhD Thesis, 2011.

[76]. R. Stefanini, M. Chatras, P. Blondy and G. M. Rebeiz, “Miniature MEMS Switches for RF Applications”, Journal of Microelectromechanical Systems, Vol. 20, pp. 1324–1335, 2011.

[77]. C. D. Patel and G. M. Rebeiz, “A High-Reliability High-Linearity High-Power RF MEMS Metal-Contact Switch for DC–40-GHz Applications” IEEE Transaction on Microwave Theory and Techniques, Vol. 60, pp. 3096-3112, 2012.

[78]. Jae-H Park, K. Singh, K. Nagachenchaiah and D. Bhatnagar, "Fabrication and measurements of direct contact type RF MEMS switch", IEICE Electronic Express, Vol. 4, pp. 319-325, 2012.

[79]. G. M. Rebeiz, "RF MEMS Theory, design, and technology", New Jersey: John Wiley & Sons, Inc., 2003.

[80]. P. Chawla and R. Khanna, "Optimization Algorithm of Neural Network on RF MEMS Switch for Wireless and Mobile Reconfigurable Antenna Applications", Proceedings of Second IEEE International Conference on Parallel, Distributed and Grid Computing, PDGC-2012, pp. 735-740, 06-08 December, 2012.

[81]. J. Sharma, N. Krishanapura and A. D. Gupta: Fabrication of low pull-in voltage RF MEMS switches on glass substrate in recessed CPW configuration for V-band application, Journal of Micromechanics and Microengineering, IOP Publishing, Feb. 2012.

[82]. F. Giacomozzi, C. Calaza, S. Colpo, V. Mulloni, A. Collini, B. Margesin, P. Farinelli, F. Casini, R. Marcelli, G. Mannocchi and L. Vietzorreck, "Technological and Design Improvements for RF MEMS Shunt Switches", Proceedings of IEEE International Semiconductor Conference, pp. 263-266, 2007.

[83]. Il-J. Cho, T. Song and Sang-H. Baek, "A Low-Voltage and Low-Power RF MEMS Series and Shunt Switches Actuated by Combination of Electromagnetic and Electrostatic Forces", IEEE Transactions on Microwave Theory and Techniques, Vol. 53, No.7, pp. 2450-2457, 2005.

[84]. F. Giacomozzi, C. Calaza, S. Colpo and V. Mulloni, "Development of High Con Coff Ratio RF MEMS Shunt Switches", Romanian Journal of Information Science and Technology, Vol. 11, No.2, pp.143-151, 2008.

[85]. J. B. Muldavin and G. M. Rebeiz, "High isolation MEMS shunt switches; Part 1: Modeling", IEEE Trans. on Microwave Theory and Techniques, Vol. 48, No.6, pp. 1045-1052, June 2000.

[86]. A. Q. Liu, M. Tang, A. Agarwal and A. Alphones, "Low-loss lateral micromachined switches for high frequency applications," Journal of Micromechanics and Microengineering, Vol. 15, pp. 157–167, 2005.

[87]. A. Q. Liu, A. B. Yu, M. F. Karim and M. Tang, "RF MEMS Switches and integrated switching circuits", Journal Semiconductor Technol. Sci. Vol. 7, No. 3, pp. 166–176, 2007.

[88]. A. Q. Liu, W. Palei, M. Tang and A. Alphones, "Microstrip lateral RF MEMS switch integrated with multi-step CPW transition," Microwave Optical Technology Letter, Vol. 44, No. 1, pp. 93–95, 2005.

[89]. F. M. Guo, Z. Q. Zhu, Y. F. Long, W. M. Wang, S. Z. Zhu, Z. S. Lai, N. Li, G. Q. Yang and W. Lu, "Study on low voltage actuated MEMS RF capacitive switches", Sensors & Actuators: A. Physical, Vol. 108, No. 1-3, pp. 128-133, 2003.

[90]. H. Jaafar, O. Sidek, A. Miskam, S. Korakkottil, "Design and Simulation of Microelectromechanical System Capacitive Shunt Switches", American Journal of Engineering and Applied Sciences, Vol. 2, No.4, pp.655-660, 2009.

[91]. J. B. Muldavin and G. M. Rebeiz, "High isolation MEMS shunt switches; Part 2: Design", IEEE Trans. on Microwave Theory and Techniques, Vol. 48, No.6, pp. 1053 - 1056, June 2000.

[92]. M. El Hassan, C. P. Moreira, A. A. Shirakawa, E. Kerherve, Y. Deval, D. Belot and A. Cathelin, "A Multistandard RF Receiver Front-End Using a Reconfigurable FBAR Filter" Proceedings of IEEE conference, ISSN- 1-4244-0417-7/06, 2006.

[93]. P. Yun-Kwon, N. Kuang-Woo, Y. Seok-Chool, H. Byeoung-Ju, H. Seog-Woo, K. Chul-Soo, S. Jea-Shik and S. In-Sang, "Fabrication of Monolithic 1-Chip FBAR Duplexer for W-CDMA Handsets", Proceedings of IEEE conference on MEMS 2007, Kobe, Japan, 21-25 January, 2007.

[94]. O. Menendez, P. de Paco, E. Corrales and J. Verdu, "Procedure for the Design of ladder BAW Filters taking Electrodes into account" Progress In Electromagnetics Research Letters, Vol. 7, 127–137, 2009.

[95]. F. Matta, "MEMS For Wireless: FBAR and LiMMS", 23rd NATIONAL RADIO CONFERENCE (NRSC2006), Faculty of Electronic Engineering, Menoufya Univ., Egypt, March 14-16, 2006.

[96]. A. K. Sahu and B. K. Sarkar, "A novel low actuation voltage RF MEMS shunt capacitive switch", Proceedings of IEEE conference on Applied Electromagnetics Conference (AEMC), pp. 1-3, 2009.

[97]. P. Chawla and R. Khanna, "A New Spiral Frequency Reconfigurable Antenna with RF-MEMS Switches for Mobile RF Front End", Applied Electromagnetics and Mechanics, ISSN 1383-5416. (Accepted for publication-In press).

[98]. A. Q. Liu, "RF MEMS Switches and Integrated Switching Circuits", Springer, ISSN-978-0-387-46261-5, 2010.

[99]. http://www.memscap.com/aboutmems.html

[100]. P. Chawla, R. Khanna, "A Novel Design and Optimization Approach of RF MEMS Switch for Reconfigurable Antenna using ANN Method", IEEE Conference on Communications, Devices and Intelligent Systems, CODIS-2012, Kolkata, India, pp. 188-191, 2012.

[101]. J. Singh, A.P. Singh, and T.S. Kamal, "Design of Circular Microstrip Antenna Using Artificial Neural Networks", Proceedings of the World Congress on Engineering 2011 Vol. II, London, U.K, July 2011.

[102]. N. Turker, F. Gunes, T. Yildirim, "Artificial Neural Design of Microstrip Antennas", Turkish Journal of Electrical Engineering & Computer Sciences, Vol. 14, pp. 445-453, 2006.

[103]. C. Puente, J. Romeu, R. Pous, X. Garcia and F. Benitez, "Fractal multiband antenna based on the Sierpinski gasket", IEEE Electronics Letters, Vol. 32, No. 1, pp. 1–2, 1996.

[104]. P. W. Tang and P. F. Wahid, "Hexagonal Fractal Multiband Antenna", IEEE Antennas and Wireless Propagation Letters, Vol. 3, pp. 111-112, 2004.

[105]. N. A. Saidatul, A. A. H. Azremi and P. J. Soh, "A hexagonal fractal antenna for multiband application", Proceedings of the IEEE International Conference on Intelligent and Advanced Systems, pp. 361–364, 2007.

[106]. D. K. Neog, S. S. Pattnaik, D. C. Panda, S. Devi, B. Khuntia and M. Dutta, "Design of a Wideband microstrip Antenna and the Use of Artificial Neural Networks in Parameter Calculation", IEEE Antennas and Propagation Magazine, Vol. 47, No.3, pp. 60-65, June 2005.

[107]. S. Lucyszyn and S. Pranonsatit, "RF MEMS for antenna applications", Proceedings of the 7th EurAAP European Conference on Antennas and Propagation (EUCAP 2013), Gothenburg, Sweden, pp. 1988-1992, Apr. 2013.